Near-net Shaping of Simple and Complex Ceramic Parts by 3D Printing and Investigations on the Physico-Chemical, Thermal, Mechanical and Microstructural Properties

Thesis

Submitted in Partial Fulfilment of the Requirements

for the Award of the Degree of

DOCTOR OF PHILOSOPHY

in

MATERIALS ENGINEERING

by

S Mamatha

(Regn. No. 18ETPM02)

Under the supervision of

Dr. Dibakar Das
Professor & Dean
School of Engineering Sciences and Technology (SEST), University of Hyderabad (UOH)
Hyderabad, Telangana State, India

Dr. Roy Johnson
Scientist - G & Associate Director
International Advanced Research Centre for Powder Metallurgy and New Materials (ARCI)
Hyderabad, Telangana State, India

DEPARTMENT OF MATERIALS ENGINEERING

SCHOOL OF ENGINEERING SCIENCES AND TECHNOLOGY, UNIVERSITY OF HYDERABAD, HYDERABAD – 500 046, TELANGANA STATE, INDIA

September - 2021

CERTIFICATE

This is to certify that the thesis entitled, **"Near-Net Shaping of Simple and Complex Ceramic Parts by 3D Printing and Investigations on Physico-Chemical, Thermal, Mechanical and Microstructural Properties"** submitted by **S. Mamatha**, bearing registration number **18ETPM02** in partial fulfilment of the requirements for the award of Doctor of Philosophy in **School of Engineering Sciences and Technology**, is a bonafide work carried out by her under my supervision and guidance.

This thesis is free from plagiarism and has not been submitted previously in part or in full to this or any other University or Institute for the award of any degree or diploma.

Parts of this thesis have been:

A. Published in the following publications:

1. **S. Mamatha,** P Biswas, P Ramavath, D Das, R Johnson, 3D-Printing of complex shaped alumina parts, Ceramic International, 2018;44:19278–19281.

2. **S. Mamatha**, P Biswas, D Das, R Johnson**,** Complex Shaped Ceramic Fabrication From 3D Printed Poly Lactic Acid Templates Through Replication Process, Ceramic International, 2019; 45: 19577-19580.

3. **S Mamatha**, P Biswas, D Das, R Johnson**,** 3D Printing of Cordierite Honeycomb Structures and Evaluation of Compressive Strength under Quasi-static Condition, International Journal of Applied Ceramic Technology, 2020;17:211-216.

4. **S Mamatha,** P Biswas, P Ramavath, D Das, R Johnson**,** Effect of parameters on 3D printing of alumina ceramics and evaluation of properties of sintered parts, Journal of Asian Ceramic Societies, 2021;9:858-864.

5. P Biswas, **S Mamatha**, S Naskar, Y S Rao, R Johnson, G Padmanabham, 3D Extrusion Printing of Magnesium Aluminate Spinel Ceramic Parts Using Thermally Induced Gelation of Methyl Cellulose, Journal of Alloys and Compounds, 2019;770:419-423.

6. P Biswas, **S Mamatha**, K Varghese, R Johnson, R Vijay, R Kumar, 3D printing of high surface area ceramic honeycombs substrates and comparative evaluation for treatment of sewage in Phytorid application, Journal of Water Process Engineering Technology, 2020; 37: 101503-101508**.**

7. A Adumbumkulath, C Shin, G Acharya, P Biswas, **S Mamatha**, R Johnson, G Padmanabham**,** 3D printing of $MgAl_2O_4$ spinel mesh and densification through Pressure-less sintering and hot-isostatic pressing, 3D Printing and Additive Manufacturing, (Ahead of Print), 2021.

B. Parts of this thesis have presented at the following conferences:

a. Poster presentation on "**Mechanical Behaviour of 3D Extrusion Printed Alumina Specimens**", S Mamatha, Papiya Biswas, Dibakar Das, Roy Johnson, 83rd Annual Session of Indian Ceramic Society (ICS) and National conference on Innovation and Technologies for Ceramics (InTec-2019), on December 11-12, 2019, Trivandrum, Kerala, India.

b. Oral presentation on "**Fluoride Removal Studies in Potable Water using gamma-Alumina Coated 3D Printed Ceramic Honeycomb Substrates**". S Mamatha, Shiv Prakash Singh, Papiya Biswas, Y. Srinivasa Rao, Dibakar Das, Roy Johnson, at 84th Annual Session of Indian Ceramic Society (ICS) and National seminar on "Propelling Innovations in Glass and Ceramics for Atma Nirbhar Bharat" held on 10-12th December, 2020, organized by CSIR-CGCRI, Kolkata, India.

c. Flash Talk on "**3D Printing of Ceramics-An Emerging Technology**" at National Science Day celebrations at ARCI on 28th February 2020, Hyderabad.

d. Talk on "**3D printing of Ceramics-An Emerging Technology**", S Mamatha, Papiya Biswas, Dibakar Das, Y Srinivasa Rao, Roy Johnson at Science Technology and Innovation Talks (STIN-2021) as a part of National Science Day celebrations organized by International Advanced Research Centre for Powder Metallurgy and New Materials (ARCI), 26th February-2021, Hyderabad.

e. Poster presentation on "**Investigations on 3D Printing of Complex Shaped Alumina Parts**", S Mamatha, S Naskar, P Biswas, Y S Rao, Roy Johnson at 81st Annual Session of Indian Ceramic Society (ICS) and International Conference on "Expanding Horizons of Technological Applications of Ceramics and Glasses (EH-TACAG'17), 14-16th December, 2017, Pune.

The student has passed the following courses towards the fulfilment of the course work requirement for Ph.D.

Course code	Name	Credits	Pass/Fail
PD801	Research Methodology	4	Pass
PD802	Advanced Materials Processing and Characterization	4	Pass
PD803	Advanced Engineering Mathematics	2	Pass
PD804	Materials Characterization- I	4	Pass

Supervisor 21/10/21

Prof. Dibakar Das
DEAN
School of Engineering Sciences and Technology
University of Hyderabad, Hyderabad 500 046.

Dean of School 21/10/21

Prof. Dibakar Das
DEAN
School of Engineering Sciences and Technology
University of Hyderabad, Hyderabad 500 046.

ए आर सी आई
ARCI
डॉ.रॉय जॉनसन
Dr. Roy Johnson
सह - निदेशक / Associate Director

इंटरनेशनल एडवांस्ड रिसर्च सेंटर फॉर पाउडर मेटलर्जी एंड न्यू मटेरियल्स
INTERNATIONAL ADVANCED RESEARCH CENTRE FOR
POWDER METALLURGY AND NEW MATERIALS (ARCI)
(विज्ञान एवं प्रौद्योगिकी विभाग, भारत सरकार का स्वायत्त अनुसंधान एवं विकास केन्द्र)
(An Autonomous Research & Development Centre of Department of Science & Technology, Govt. of India)
डाक घर: बालापुर, हैदराबाद 500 005. तेलंगाना, भारत.
P.O: Balapur, Hyderabad - 500 005, Telangana, INDIA.

CERTIFICATE

This is to certify that the work presented in the thesis entitled **"Near-net Shaping of Simple and Complex Ceramic Parts by 3D Printing and Investigations on Physico-Chemical, Thermal, Mechanical and Microstructural Properties"** which is being submitted by **Mrs. S Mamatha (Regn. No. 18ETPM02),** is a bonafide work submitted to University of Hyderabad in partial fulfillment of the requirements for the award of the degree of **Doctor of Philosophy** in **Materials Engineering Department.**

To the best of my knowledge, the work incorporated in the thesis has not been submitted to any other university or institute for the award of any other degree or diploma.

डॉ. रॉय जॉनसन / Dr. ROY JOHNSON
सह-निदेशक / ASSOCIATE DIRECTOR
एआरसीआई / ARCI
विज्ञान एवं प्रौद्योगिकी विभाग, भारत सरकार
Dept. of Science & Tech., Govt. of India
डाकघर: बालापुर/Balapur P.O., हैदराबाद/Hyderabad
(तेलंगाना/Telangana), भारत/INDIA

Dr. Roy Johnson

Thesis External Supervisor
Scientist-G & Associate Director
International Advanced Research Centre for
Powder Metallurgy and New Materials (ARCI)
Hyderabad

ई पी ए बी एक्स/EPABX : 0091-040-2444 1077, 2445 2306 (30 लाइनें/Lines) फैक्स/Fax : 0091-040-2444 2699.
ई-मेल/E-mail : royjohnson@arci.res.in, वेबसाईट/Website: www.arci.res.in

Thesis Approval for Ph.D.

This Thesis entitled **"Near-net Shaping of Simple and Complex Ceramic Parts by 3D Printing and Investigations on Physico-Chemical, Thermal, Mechanical and Microstructural Properties"** by **Mrs. S Mamatha (Regn. No. 18ETPM02),** is approved for the degree of Doctor of Philosophy.

Examiners

_____

_____

_____

Internal Supervisor

_____

_____

_____

External Supervisor

_____

_____

_____

Date : _____

Declaration

This is to certify that the research work presented in the thesis entitled **"Near-net Shaping of Simple and Complex Ceramic Parts by 3D Printing and Investigations on Physico-Chemical, Thermal, Mechanical and Microstructural Properties"** is a bonafide work done by me under the supervision of **Prof. Dibakar Das,** UOH and **Dr. Roy Johnson,** ARCI and was not submitted elsewhere for the award of any degree. I declare that this written submission represents my ideas in my own words and where others' ideas or words have been included, I have adequately cited and referenced the original sources. I also declare that I have adhered to all principles of academic honesty and integrity and have not misrepresented or fabricated or falsified any idea / data / fact / source in my submission. I understand that any violation of the above will be a cause for disciplinary action by the Institute and can also evoke penal action from the sources which have thus not been properly cited or from whom proper permission has not been taken when needed.

S. Mamatha

(Signature)

S Mamatha
Regn. No. 18ETPM02

Date: 22-09-2021

Acknowledgements

First and foremost, I wish to express my heartful thanks to the **Late G. Padmanabham, DIRECTOR,** ARCI for providing me an excellent opportunity, facility and advice time to time throughout my research work.

I am truly indebted and I express my earnest gratitude for my research supervisor **Dr. Roy Johnson**, Scientist-G and Associate Director, ARCI, Hyderabad for his immense support and guidance without which I could not have been completed my work successfully. His unabated enthusiasm, which stems from his absolute command over the subject, has been a constant source of inspiration for me to work hard and the outcome is expressed in the form of this thesis.

I express my deep and sincere gratitude to my research supervisor **Dr. Dibakar Das**, Professor & Dean, School of Engineering Sciences and Technology, University of Hyderabad for his inestimable expertise and able guidance and valuable suggestions and relentless advice which were much needed to complete this piece of research work during my doctoral research.

I am thankful to **Dr. Papiya Biswas**, Sc-'E', ARCI, for technical support and encouragements throughout this work and completion of the proposed research work in time.

I express my gratitude to the Doctoral Review Committee member: **Dr. Jai Prakash Gautam**, Professor, SEST for the detailed review, constructive suggestions and excellent advice during the progress of this research work. I take this opportunity to thank all my co-scholars for their help and encouragement

I express my heartiest regards to Dr. Y. S. Rao, Sc. 'F' and Team Leader, Centre for Ceramic Processing for his support to me in research related issues. I am grateful to scientists Dr. M B Suresh, Sc. 'E', Dr. Pandu Ramavath, Sc. 'D' for extending their cooperation.

I also express my thanks to technical staff Mr. V Mahendar, Technical Officer-C, Mr. A Rajashekar Reddy, Technical Officer-B, Mr E. Yadagiri, Technician-C, Mr G Anjanbabu, Technician-C, Mr A Satyanarayana, Technician-D, Mr Sushanta Mukhopadyay, Technician-C, who helped me in this endeavor as and when required.

Last but not least, I express my immense gratitude to my parents, husband and daughter for their encouragement, support, understanding and cooperation extended to me in carrying out this research endeavor successfully.

S Mamatha

S Mamatha

Abstract

3D printing of ceramics is an emerging area due to the flexibility and advantages for complex prototyping of the components/parts with the micro-features for versatile applications as revealed by recent increasing trends not only in publications but also in patents. In the current study, four advanced ceramic formulations such as alumina, magnesium aluminate spinel, cordierite and kaolinite clay has been established starting from the powder characterization through printing of various configurations. An indigenously supplied 3D printer was modified to suite a ram type/screw type extruders designed and fabricated in the current study. A naturally occurring environmentally friendly cellulose derivative (Methylcellulose) and its thermal gelation property in the temperature range of 35-42^{o}C was used for the first time in 3D printing process. A pseudo-plastic paste was prepared with proper additives for each ceramic formulation and printing parameters such as printing speed, length to Diameter (L/D) ratio and self-standing distance are found to be critical to minimize the defects. The various configurations such as honeycombs, corrugated monoliths, discs, cylinders etc., were sintered to achieve the acceptable theoretical densities for various applications targeted. Collaborative research was also carried out at Baylor College of Medicine, USA and 3D printed fine spinel mesh for the possible applications in cranioplasty. The printed specimens were characterized for their physico-chemical, thermal, mechanical and microstructural properties using advanced ceramic characterization techniques and correlated with the processing parameters. Additionally, highly porous ceramic honeycomb structures were also prepared for the first time using the 3D printed poly lactic acid based (PLA) template replication process. Hot isostatic pressing (HIPing) of encapsulated green alumina compact is demonstrated for minimization of defects originating from layer by layer deposition while printing. The current study have also explored for the applications of various 3D printed ceramic formulations as high surface area substrates for wetland phytorid sewage treatment system and also corrugated monolith substrates for de-fluoridisation of potable water and have shown encouraging results.

CONTENTS

Chapter-4: 3D Printing of Magnesium Aluminate Spinel Ceramics and the Evaluation of Physico-Chemical, Microstructural and Mechanical Properties

Chapter-5: 3D Printing of Ceramic Honeycomb Structures and the Property Evaluation

List of Figures

List of Tables

CHAPTER - 1

INTRODUCTION

1.1 Additive Manufacturing

Additive Manufacturing (AM) is generally known as 3D Printing (3DP), Rapid Prototyping (RP), Rapid Manufacturing, Solid Free Forming (SFF), Layer Manufacturing (LM), Additive Fabrication etc. [1-3]. The 3DP process was first invented and patented by W. Chuck Hull in 1984 for plastic materials and named as stereolithography. The evolution of the process over the period of years till date is depicted in Fig.1.1.

Fig.1.1 Evolution of additive manufacturing (AM) techniques

AM process enable to create a three-dimensional object gradually from the pre-designed 3D model, by adding raw material layer by layer, which is opposed to conventional subtractive manufacturing. Conventional subtractive manufacturing follows a top-down approach based on the removal of material from the bulk solid sample until one gets desired geometry or shape which consumes more time. Unlike the conventional fabrication processes, the AM process provides advantages in reducing the time to arrive an optimum prototype design including savings on cost with minimum waste generation.

The basic principle of three-dimensional printing is well documented and involves generation of 3D model with the help of the Computer Aided Design (CAD) followed by conversion of 3D model to Standard Tessellation Language (STL) format. The converted STL file is then used to develop 3D structures in layers by layer fashion by the printing machine. The typical process is represented in Fig.1.2.

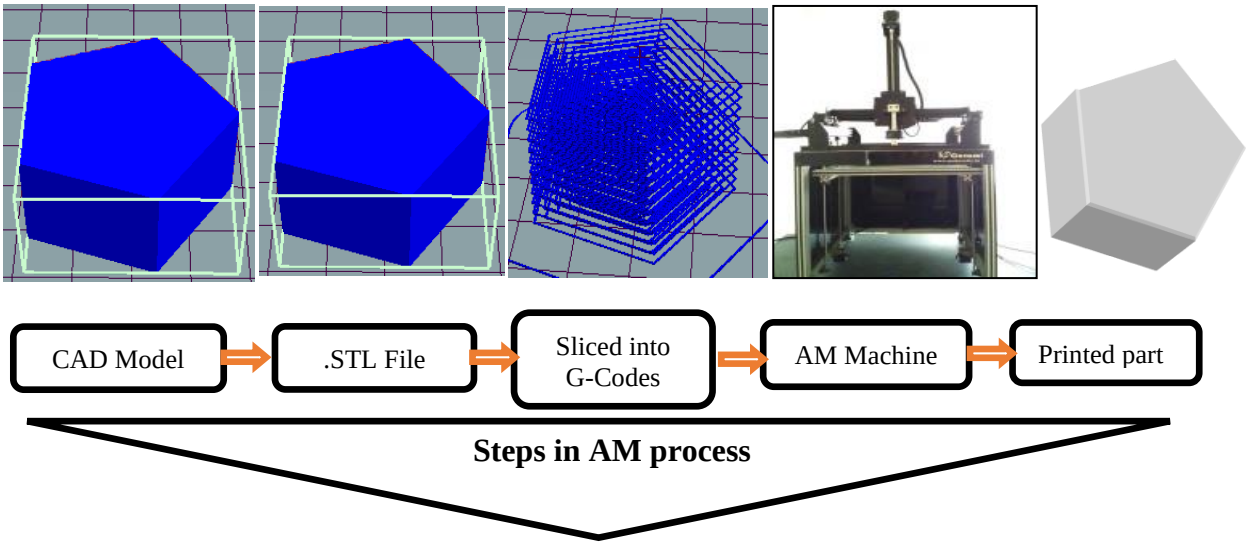

Fig.1.2 Process flow chart of Additive Manufacturing

Thickness of layer printed during the fabrication process varies from a few microns to millimeter depending on the particular technology used. Surface quality and resolution of the printed object depend on the layer thickness and speed. Hence the fine layer thickness and optimized speed for specific material results good resolution and surface quality [4-5]. Any solid form or intricate, complex shaped components or objects can be manufactured by this method. AM process is specific with respect to materials, though they overlap in many phases. A typical classification of AM process in general is shown in Fig.1.3.

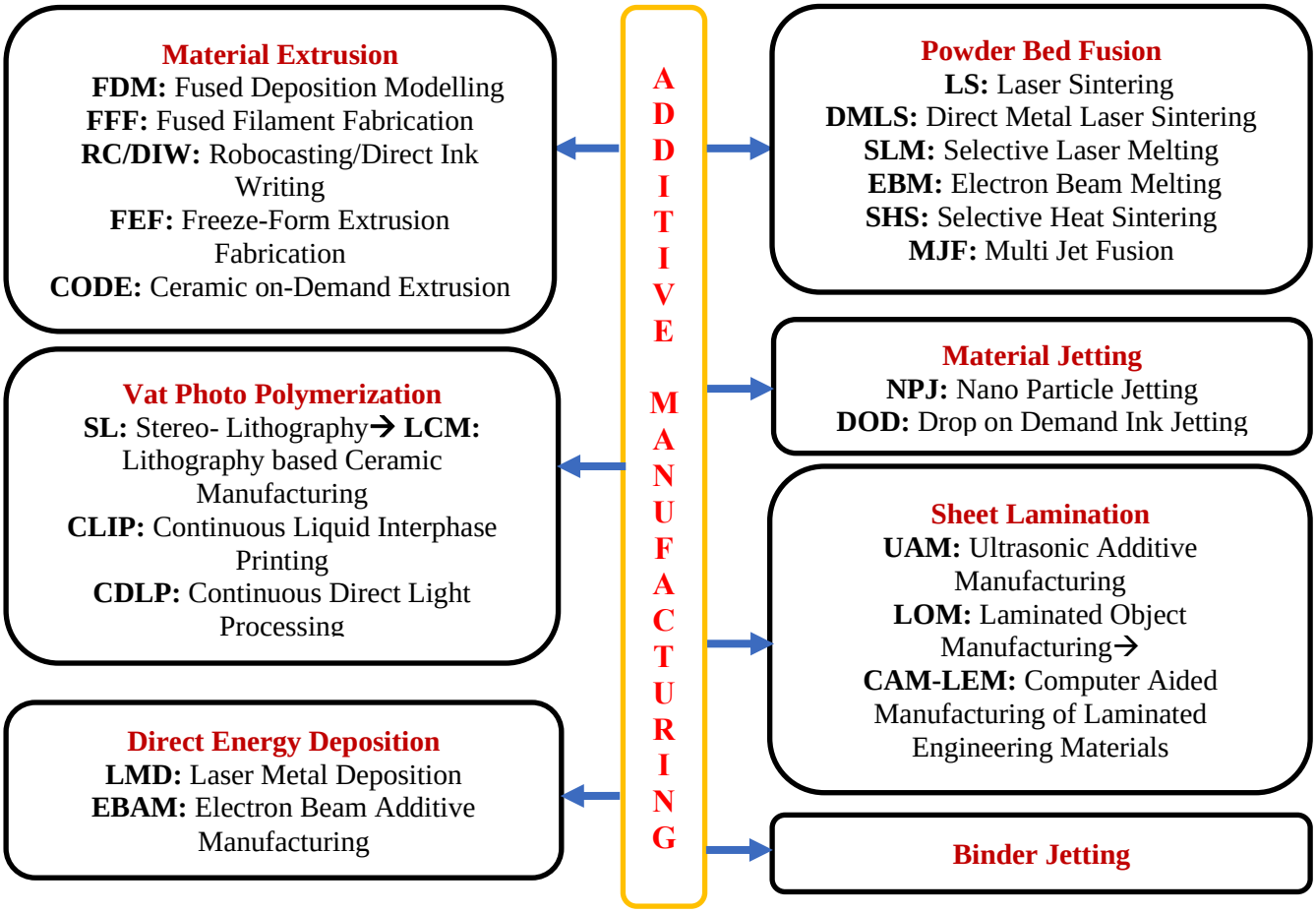

Fig.1.3 Classification of additive manufacturing (AM) techniques

As it is evident from Fig.1.3, the additive manufacturing is classified into 7 categories which are 1. Material Extrusion, 2. Powder Bed Fusion, 3. Vat photo Polymerization, 4. Material Jetting, 5. Direct Energy Deposition, 6. Sheet Lamination and 7. Binder Jetting.

1.1.1 Material Extrusion

Material extrusion is an additive manufacturing technology where it uses continuous filament of thermoplastic material which is feed into the heated nozzle. The resulted molten feed filament is extruded through the nozzle layer by layer according to the virtual 3D CAD model to fabricate the physical 3D object. This method applies to thermoplastics, ceramics and composites. Material extrusion is sub-classified into Fused Deposition Modelling (FDM), Fused Filament Fabrication (FFF), Direct Ink Writing (DIW) or Robocasting, Freeze Form Extrusion (FEF) and

Ceramic on-demand Extrusion (CODE). FDM and FFF methods use thermoplastics filament which is fed through the heated nozzle and extruded on the printer platform and get solidified as per the 3D model.

1.1.2 Powder Bed Fusion

In Powder Bed Fusion a laser, heat or electron beam is used to fuse the powder particle together according to the 3D CAD model to build the object. Three types of energy sources are used to fuse the powder particles namely laser light, electron beam energy and thermal energy. Depending upon the kind of energy used to fuse the powder particles, powder bed fusion is sub classified into Direct Metal Laser Sintering (DMLS), Selective Laser Melting (SLM), Electron Beam Melting (EBM), Selective Heat Sintering (SHS) and Multi Jet Fusion (MJF). Though the above mentioned methods use different energy sources, but all these methods follow the same procedure. Powder bed fusion printers usually have 2 chambers, i.e., Powder chamber and build chamber. Powder chamber consists of powder roller which is used to spread the powder on the platform for each layer. Build chamber allows the energy to fuse the powder particles according to the virtual 3D CAD model which is imported to the machine software and build the object under vacuum which is filled with inert gases to prevent corrosion of molten metal. This method applies to metals and plastics to prepare 3D objects.

1.1.3 Vat Photo Polymerization

Photo polymerization is well known method of additive manufacturing technique where it uses ultraviolet (UV) light to cure the liquid resins and forms hard body with the help of polymerization. This process involves the feedstock (liquid photo-polymer resin) to flow through the nozzle as per the desired 3D model and UV light cure the liquid resin by conducting the polymerization reaction. Photo-polymers are light activated resin which is turned into hard material by changing its properties when exposed to light. Other methods which are sub classified under this technique is Stereo-lithography (SL), Digital Light Processing (DLP), Lithography based Ceramic manufacturing (LCM) and Direct Light Processing (DLP). This method allows to use high concentrations (i.e., 25%, approximately) of photo polymers to prepare resins with the raw materials. UV photo-polymerization causes high emissions of hazardous gases into the environment, which is not environmentally friendly.

1.1.4 Material Jetting

The material Jetting printing method involves the selective deposition of feedstock (liquid) dropwise or continuous through the nozzle layer by layer on the surface of printer platform, as per the 3D model and allows to cool to solidify. Some setups use an exposure of UV light also to solidify the printed layers. Material Jetting includes Nano Particle Jetting (NPJ) and Drop-on Demand Ink jetting.

1.1.5 Direct Energy Deposition

This is one of the 7 categories of additive manufacturing processes. Direct energy deposition forms 3D objects by melting the material as it is being deposited using focused thermal energy such as laser, electron beam or plasma arc. Both the energy source and the material feed nozzle are manipulated using a gantry system or a robotic arm. Direct energy deposition is increasingly used in hybrid manufacturing where the bed also can be moved to generate complex shapes. This method is used to make 3D complex shapes with metals, ceramics and polymers. Depending on the energy source to melt the feedstock, this method further classified into Laser Metal Deposition (LMD) and Electron Beam Additive Manufacturing (EBAM).

1.1.6 Sheet Lamination

Sheet lamination additive manufacturing process involves the fabrication of 3D object by stacking the thin layer sheets on a platform of printer. These thin laminated sheets are bonded by using ultrasonic welding or brazing while the final shape is achieved either by laser cutting or CNC machining. Sheet lamination method produces the parts with low additive layer resolution. Depending on the kind of bonding source used to bond the sheets such as adhesive bonding, thermal bonding and ultrasonic welding, further it has been classified into Ultrasonic Additive Manufacturing (UAM), Laminated Object manufacturing (LOM) and Computer Aided Manufacturing of Laminated Engineering Materials (CAM-LEM). CAM-LEM allows to form the layers and then bond. Other methods like UAM, bond the laminar layers and form the desired shapes by cutting the excessive material.

1.1.7 Binder Jetting

As the name indicates binder jetting process allows to form 3D object by depositing the binding liquid on spread layer of powder according to the 3D CAD model. This binding liquid which is deposited on the powder layer helps to join the powder particle. Among the all other additive manufacturing technologies, binder jetting is unique as it is not employing heat or other energy sources to fuse the powder particles to form dense body. This method is available for range of materials like polymers, metals and ceramics.

1.2 Publication Trends in AM of Ceramics

Publications available in the public domain are surveyed by using Science Direct in the reputed ceramic journals such as Journal of American Ceramic Society (JACS), Journal of European Ceramic Society (JECS) and Ceramic International (CI). A trend of publication on Additive Manufacturing (AM) of ceramics is shown in Fig.1.4 which reveals an increasing trend in the research and development of 3D Printing technology in the area of ceramics from 2014 to 2021.

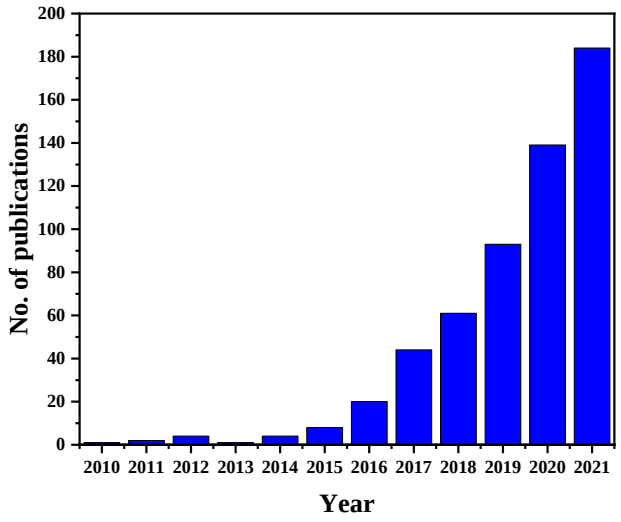

Fig.1.4. Status of publications (JACS, JECS, Ceramic International on AM ceramics)

1.3 Patent Filing and Publication Trends

There are 949 patents shortlisted on the subject of the 3D printing of ceramics from 2008 to 2018 [6-22]. As it is evident from Fig.1.5 that, though the innovation on the 3D printing of

ceramics is rather slow in the beginning, the gradual shift to rapid growth has been observed during 2015 to 2017. This signifies the potential growth in this area as an emerging technology.

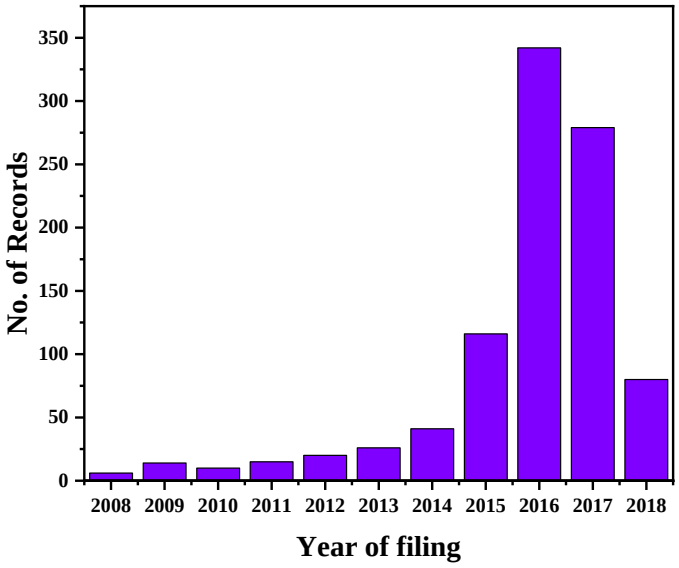

Fig.1.5 Filing of patents from 2008-2018

The number of patent applications during the year 2018 is expected to be much higher than the previous year, as most of the applications filed during 2018 will be available in the public domain after the completion of the prescribed publication timeline.

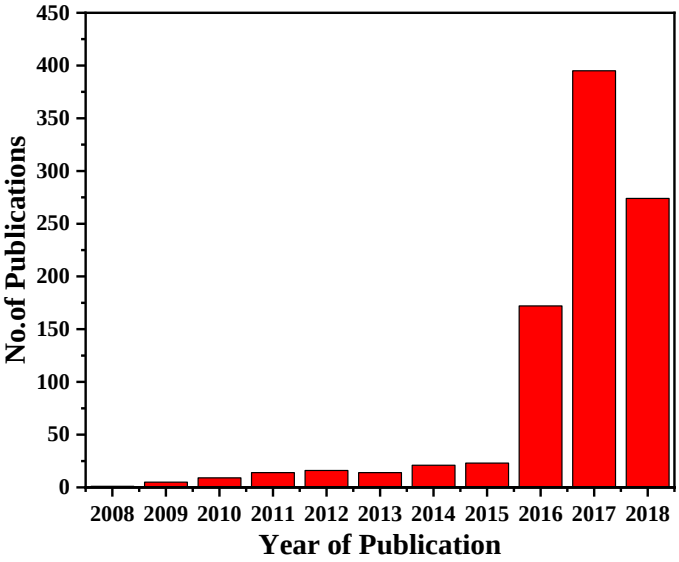

Fig.1.6 Status of publications from 2008-2018

1.4 General Steps of an Additive Manufacturing Process:

A schematic diagram for additive manufacturing is already represented in Fig.1.2 in section 1.1. As per the block diagram the manufacturing process involves the design of the CAD model, conversion of CAD model to .STL file, slicing of 3D model into layers and printing process as described below.

1. Design of CAD model:

In order to produce 3-Dimensional object by using Additive Manufacturing (AM) techniques, the first step follows the designing the 3D model with accurate dimensions. 3D object can be designed by using Computer Aided Design (CAD) or Computer Aided Three-Dimensional Interactive Application (CATIA) by giving the exact dimensions of model and simulate the object to observe under various conditions.

2. Conversion of CAD model to .STL file:

CAD and CATIA designing software allow to save the file in .IGES (Initial Graphics Exchange Specification), .STEP (Standard for the Exchange of Product Data), .VRML (Virtual reality modeling language) and .3DS (3D System) etc**.** Designed CAD model usually saved in .IGES format by default. Further the designed model has to be converted into Standard Tessellation Language (.STL) which is a most common suitable file format for 3D printer. Other than .STL file format, .3DS, .amf and .obj 3D file formats will also be suitable to most of the 3D printers.

3. Slicing of 3D model into layers and printing process

Designed CAD model should be imported to the computer which is connected to 3D printer. Imported 3D model will be subjected to various printing conditions such as thickness of layer, number of perimeters, number of solid layers needed, percentage of infill, fill pattern, direction of filling-in of imported model, diameter of nozzle, printing speed, temperature, and X-Y-Z offset positions from home position. Further the imported 3D object will slice into layers with the selected printing conditions by using Slicing (slice3r, Cura engine, matter control, simplify 3D etc.) software and generate Geometrical codes (G-Code) of X, Y, Z and extruder position in a layer fashion. Generated G-Codes can be saved in a micro-processor or model can print directly from the computer which is connected to 3D printing machine. According to the G-codes, the 3D printing machine will

build the 3D object. Later the printed object will be dried in particular atmospheric conditions followed by very minimal post machining.

1.5 Literature Survey and Technical Challenges in Ceramic Additive Manufacturing

Ceramic materials are playing prominent role and have a wide range of applications because of their unique combination of properties such as high hardness, mechanical strength, chemically inert and electrical insulating. Generally, ceramic components are fabricated by conventional ceramic shaping processes such as slip casting, gel casting, die pressing, tape casting and extrusion. Conventional ceramic shaping techniques proceeds through several iterations of fabrication of die and mold during prototype fabrication, which is time consuming and expensive. From last three decades additive manufacturing technology is gaining prominence in the field of ceramic materials, though it is well established for the plastics and metals. By considering the processing requirements (preparation of feedstock, sintering), ceramics are not easy to fabricate through the additive manufacturing technology. However, so many additive manufacturing technologies were developed for processing ceramic materials to suit various applications. Since ceramic 3D printing is currently an emerging area and a number of publications are increasing to a greater extent but the total availability with respect to a number of publications are limited.

Rueschhoff et al, [23] reported on the fabrication of dense alumina ceramics by the direct ink writing of highly loaded aqueous alumina suspension in layer-by-layer fashion at room temperature. They have studied the effect of solid loading of alumina suspension by characterizing slurry for the viscosity with varying shear rates, density, homogeneity, mechanical and microstructural properties. Rheological studies proved that slurry possess yield pseudo-plastic behaviour according to the Herschell-Buckley model, yield stress and viscosity of the slurry was increased with an increase in the solid loading of the suspension.

Patrike H warnke et al, [24] investigated on the fabrication of ceramic scaffolds of tricalcium phosphate and hydroxyapatite by using computer assisted 3D printing process and sintered. Study mainly focused on the investigations on biocompatibility of printed scaffolds using scanning electron microscope and reveals that the more cells were observed on hydroxyapatite scaffold than tricalcium phosphate scaffold.

M Faies et al, [25] developed extrusion based additive manufacturing system using ultraviolet curable suspensions. This study investigated on commercially available different UV

suspensions containing various concentrations (22.5 to 55% Vol) of Zirconia for their characteristics such as homogeneity, rheological properties and printability. Further study has reported that the printed samples were sintered and achieved 92% of theoretical density.

U Scheithauer et al, [26] investigated on thermoplastic 3D printing to produce dense ceramic parts with alumina and zirconia. The study reported that preparation of homogeneous suspension with alumina and Zirconia with optimized rheological parameters and printed. Printed samples were characterized and shown 99% density and microstructure of printed samples shows homogeneous bonding between layers.

R He et al, [27] reported on the fabrication of complex shaped Zirconia triangle cutting tool with a withdrawal tool by using digital light processing -stereolithography method. Sintered samples were analyzed for shrinkage, phases, hardness, fracture toughness and density. The study reported that all measured values of specified properties are close to structural properties of conventionally processed common Zirconia ceramics.

H Wu et al, [28] reported on developing of rapid prototyping process to fabricate the alumina based complex ceramic core by using the combination of stereo-lithography and gel casting. Integral sacrificial resin mold prepared by stereolithography and ceramic core green body was fabricated by gel casting process by polymerizing the aqueous ceramic slurry. Freeze drying was used as an alternate to conventional drying, which helps in less shrinkage which has resulted in good structural integrity of prepared complex shaped ceramic core. Sintering conditions were optimized by adding magnesium oxide as a mineral.

M L Griffith et al, [29] has investigated on preparation of ceramic slurry by dispersing the ceramic powder (silica and alumina) in ultraviolet curable acrylamide resin to form the structural parts through stereo-lithography. As a preliminary study prepared ceramic slip, tape casted on a substrate and cured under high intensity UV light.

G Mitteramskogler et al, [30] studied on light curing strategies for lithography based additive manufacturing to fabricate complex shaped ceramics. Digital Light Processing (DLP) has been used to print complex zirconia structures, by stacking the zirconia (solid loading of 45 vol%) layers with photo-curable resin with good dimensional accuracy. Prepared sample was thermally debinded and sintered to achieve high density. Further the study also reported various methods to improve the structural properties and geometrical accuracy for final 3D printed components.

S P Gentry et al, [31] reported on characterizing printed layers (silica, mullite, alumina, and zircon powders) after photo polymerization for its layer width and depth. The study also reports the effect of energy of UV light on layer width and depth, the experimental studies revealed that cure depth follows semilogarithmic behavior as the dose of energy increases and fitted by using the Beer-Lambert absorption, further it describes the depth sensitivity and depth critical energy dose. Broadening depth of cured layers was decreased with the normalized refractive index.

Y D Hazan et al, [32] testified on photo-polymerization mechanism of 3D printed SiC ceramic rich polymers and developed photopolymerizable compositions for stereolithography desktop 3D printer. The study also describes the proposed method can be used to print preceramic polymers containing Allyl/Vinyl compounds with acrylates. High definition structures and complex geometries can be printed successfully using this desktop STL 3D printing AMHPCS (Allyl/methyl hydride polycarbosilane). Printed preceramic polymers were converted to ceramics by pyrolysis process at 1300^{o}C. Type and concentration of preceramic polymer affect the composition and final structure of the ceramic component. Addition of solvents does not affect the pore size and distribution other than the surface area of the final ceramic structure.

P Gonzalez et al, [33] conveyed the experimental work related to the 3D printing of functionally graded ceramic parts using the stereolithography method by mixing of aluminum oxide powder to polymers. Study also describes the importance of rheological behavior of prepared ceramic mixture and proper handling of ceramic paste during printing process.

M Zhou et al, [34] investigated on fabrication defect free alumina cutting tool by using stereolithography additive manufacturing method and for the preparation of the sintered body several drying processes and debinding procedures has been followed to optimize the process. The study also reports that drying process using liquid desiccant (PEG 400) results in less deformation of the printed part at green stage and optimization of debinding process is also helps in shape integrity of 3D printed parts.

A D B Romero et al, [35] study reports on the development of different micro-textured device using lithography based additive manufacturing method. The study also provides information on obtaining a high aspect ratio and surface topography for complex geometries. Structures with controlled surface texture explore possible applications in biomedical industry.

M C Leu et al, [36] investigated on fabricating ceramic composite by printing different ceramic materials (alumna, zirconia) prepared into paste and using triple extruder one solid body

printed by using Freeze-form Extrusion method. The study reported additives provides sufficient adhesion of the ceramic particles and optimized concentration of additives converts paste's rheological behavior to pseudoplastic behavior with high yield stress which is suitable for printing process.

M L Griffith et al, [37] reported on the fabrication of ceramic parts by using a Freeform fabrication process which works based on the principle of stereolithography method. Ceramic suspensions prepared with the acrylamide photo polymer in both aqueous and non-aqueous media were investigated for viscosity and cure depth. The higher cure depth was observed during the printing of non-aqueous diacrylamide suspension, which have shown higher viscosity than aqueous acrylamide suspensions. The study also applied the Beer-Lambert law to analyze the effect of the curing depth of layers and observed that cure depth is inversely proportional to the volume percentage of ceramic powder and the square of the refractive index difference between the ceramic powder and the liquid medium.

G A Brady et al, [38] reported on the fabrication of ceramic green parts using the stereolithography method of preparing the UV-curable ceramic suspension. Further the green ceramic parts solidified and sintered in a furnace. The study used alumina ceramic suspension prepared by adding of hexanediol diacrylate and rheological and curing characteristics of resin was challenging parameters which were measured by photo-theology and photo calorimetry.

J W Halloran et al, [39] investigated on the photopolymerization behavior of ceramic suspension, which is a basic step in shaping the ceramic component. The properties of monomer and photo initiator determine the photopolymerization behavior. The curing and rheology characteristics of ceramic suspension were made with photopolymers.

C-J Bae et al, [40] explored the method to determine the quantity of sedimentation occur during the formation of layers in ceramic additive manufacturing. The study provides the information that use of Fast Fourier Transforms (FFTs), helps in identifying the generation of flaws occurred due to the sedimentation of the ceramic layer to layer fabrication.

W Zimbeck et al, [41] has reported on the flexural strength of metal and ceramic specimens fabricated through rapid prototyping process where the optimized concentrations of photo-sensitive polymeric resins were added to ceramic or metal powder and formed suitable suspension for prototyping process. Further the samples were cured under UV light followed by the debinding of polymers and sintered in furnace to achieve high mechanical properties.

M Wozniak et al, [42] studied on preparation of highly photo curable silica suspensions for rapid prototyping process. Silica microreactors were fabricated with low viscous suspensions contain high concentration of solid loading and transparency using the stereolithography process. The high solid loading of silica particles provides the ability to reduce the Van der Waal forces by matching the refractive index of nano silica and UV curable polymers which leads to high curing depths.

H Xing et al, [43] evaluated for physical and mechanical properties of Zirconia ceramic parts produced through the laser scanning stereolithography process. Physical properties include surface roughness of printed body and warpage were measured with respect to printing sizes of Zirconia bar along with the studies on the effect of microstructure on mechanical properties.

C-J Bae, [44] and W Z Zhou et al, [45] proposed the direct fabrication of ceramic shell molds and the steps involved in the process by the ceramic stereolithography method as an alternate method to lost wax process, for producing small and complex designs and patterns. The preparation of ceramic suspension with photopolymers should be characterized for its photosensitive parameters such as curing depth and rheology of ceramic suspensions.

Chen et al, [46] investigated on the optimization of printing parameters for producing the ceramic parts through stereolithography method. Taguchi method was applied to determine the effect of stereolithography based printing parameters such as layer thickness, laser energy beam scanning speed etc. and also sintering conditions like temperature, soaking time and heating rate.

T N Nguyen et al, [47] used stereolithography technique to fabricate ceramic antennas with alumina. The micro - stereolithography process enables fabrication of three-dimensional micro sensors using polymeric resin prepared with magnetite nano particles investigated by S J Leigh et al, [48].

S Kirihara et al, [49] reported on the printing of diamond like structures and photonic crystal with alumina using stereolithography method. Alumina powder particles were dispersed in acrylic resin and fabricated a micro-lattice and complex structures with high accuracy. This method enables to fabricate ceramic components for bio-medical applications. D Du et al, [50] studied on the fabricated artificial bone using the stereolithography process and this can be useful for defect repair for bone and bone engraftment. Surgical templates and dental implants were fabricated through stereolithography and it allows precise translation in the surgical field as reported by D P Sarment et al, [51].

Q Lian et al, [52] investigated on the fabrication of zirconia ceramic bridges using stereolithography. Light curable Zirconia suspension was subjected to stereolithography followed by vacuum freeze drying. The scanning speed and sintering conditions were important parameters which can influence the mechanical and microstructural properties.

C J Bae et al, [53] analyzed the curing behavior of the photopolymers present in the formed ceramic body by stereolithography method. The photopolymer resins were not cured fully and few portions were remained with uncured resins which lead to the initiation and propagation of microcracks during the heat treatment. However, the complete removal of photopolymer resins is required to avoid the crack initiation.

P Colombo et al, [54] reviewed the polymer derived ceramics (PDC). The transformation from polymer to ceramics is done by ceramic coatings on polymers and producing ceramic fillers. Additive manufacturing also provides the ability to produce ceramic components from the printing of preceramic polymers. Complex geometries and cellular structures can be 3D printed and pyrolyzed to ceramic structures with high density and uniform shrinkage. Honeycomb cellular structures with silicon oxycarbide were printed and pyrolyzed which can exhibit the superior mechanical properties than the ceramic foams as reported by Z C Eckel et al, and E Zancheta et al, [55-56].

P Colombo et al, [57] used preceramic polymers to produce ceramic parts through additive manufacturing techniques. The study also investigated that, the altering the chemistry and molecular properties of preceramic polymers results in the improvement of the properties of final ceramic components. A Zocca et al, [58] have investigated on the printing of preceramic polymers to produce hardystonite bio ceramic scaffold through direct ink writing technique. Rheological behavior as well as the heat treatment schedule for forming the hardystonite phase is very essential. After pyrolyzed samples were characterized for effect of heat treatment and rheological behavior of fluids on morphology, crystalline phase and mechanical properties.

R He et al, [59] reports on the fabrication of dense and complex ceramic parts made of Zirconia and alumina through digital light processing (DLP) - stereolithography method. A triangular cutting tool was printed with zirconia and alumina reported by M Zhou et al, [60] and M Schwentenwein et al, [61] and also the mechanical properties of cutting tool was relatively comparable with conventionally processed zirconia samples. Optimized debinding and sintering process were adapted to produce defect free ceramic part. Two-step debinding step allows to

minimize the formation of defects during drying and also results to get densified ceramic body as same as in conventional ceramic shaping processes.

R Felzmann et al, [62] opted lithography based stereolithography process to produce cellular structures with alumina, bioactive glass and tricalcium phosphate. The rheological parameters for ceramic suspensions should be optimized to obtain dense ceramic components. Ceramic bio devices for cell culture also printed using stereolithography method and proper control of surface topography results in obtaining the surfaces with controlled microstructure explained by R Gmeiner et al, [63].

M Schwentenwein et al, [64] studied on the fabrication of dense ceramic parts with high efficiency with respect to physical and mechanical properties produced through Lithography based ceramic manufacturing process (LCM). LCM involves the printing of ceramic suspension which in turn get hardened when it is exposed to light and this process enables to get highly dense ceramic component with precise dimensional accuracy to the CAD model.

U Scheithauer et al, [65] investigated for use of the LCM method to print tailor-made structures such as ceramic micro-reactors and heat exchangers made with alumina and Zirconia [66] contains modified honeycomb pattern with wall openings where it offers low pressure drop used as a catalytic support.

M Hatzenbichler et al, [67] proposed the study for the fabrication of light engine from Digital Light Processing (DLP) stereolithography technique. The DLP - stereolithography process provides the flexibility to form the layers by exposing photosensitive resins to light. This system can be able to print ceramic components with higher density and resolution.

P Blazdell et al,[68] studied on the fabricating ceramic structures using Multilayer Jet printing, which includes the dispersion of powder particles in liquid binder. This process has the capability to disperse the particles uniformly in binder liquid. The preparation of ceramic ink is a strong function of the selection of thermoplastics and dispersants. Solid Freeform fabrication of complex ceramic structures can be obtained through drop-on-demand multilayer jet printing, which is gaining importance in producing the monolithic ceramic structures, solid oxide fuel cells and circuits as reported in Q Xiang et al, [69].

M Singh et al, [70] reported on applications and process development of Inkjet Printing technique to produce complex structures for light-emitting-diode (LED), thin-film transistors, solar cells sensor and memory devices. Drop on demand ink jetting process uses actuated

piezoelectrical transducer printhead with nozzle orifice in micrometer. It consists of several steps such as ejection of liquid drop, stretching, pinch-off of the liquid thread from the orifice end, contraction and breakup of the liquid to form a primary drop and satellites. The drop formation characteristics, mainly depend on the driving voltage of piezoelectric transducer, liquid and system parameters [H Dong et al, [71]]. Green ceramic structures were produced by ink Jet printing using alumina slurry prepared with paraffin as reported by N C Reis et al,[72]. The study investigated on the effect of fluid parameters on printing behavior of the prepared ink by computational fluid dynamics (CFD) to optimize the printing conditions for ink jet printing process.

R Noguera et al, [73] studied on the printing of ceramic fine structures through an inkjet printing process by modifying the fluid properties as well as printing conditions. The modified fluid exhibiting the Newtonian behavior with a low viscosity. Formation of drop and liquid thread, ejecting parameters such as volume and velocity of the droplet are affected by pulse amplitude of the transducer.

B Derby [74] discussed about the processing parameters of fluid and the printing conditions. The study states that fluids used for ink jet printer should fall in the range of ohnesorge number(Z) between 1 to 10 and this limit of fluid consistency shows the flowability through piezoelectric ink jet printers. Drop formation and spreading characteristics of fluid will determine the minimum dimension of printed body that can be achieved. The coffee staining method was addressed to reduce the defect formation during the drying of printed drops.

R Dou et al, [75] studied in preparation of ink with 10 Vol% of Zirconia aqueous ink for Ink Jet printing. The study has reported that applying of coffee staining method to observe the defect formation during the process. The study also states that on adding of PEG to the prepared zirconia ink, the coffee staining was restrained.

A Friederich et al, [76] reported on the preparation of ceramic ink with suitable flow behavior to form droplets in smaller sizes. The coffee staining effect was observed during the printing formation which is caused by the particle migration from center to edges during the drying leads to defects in layers and it is the main function of rheological parameters and drying time. However, the study reported that it can be prevented on the mixing of binder and fast drying agent resulted in the improvement in viscosity after deposition and decrease the drying time. Further, it also helped in suppressing the coffee staining behavior.

M A Sukheshini et al, [77] explored the process for producing solid oxide fuel cells using an Ink Jet process. The author has prepared anode interlayer with composite consisting 55 wt% of Nickel oxide and 45 wt% of YSZ, which were printed on anode support made by tape casting. A cathode interlayer was also fabricated using strontium doped lanthanum manganite (LSM) ink jet printer and integrated in a single cell. These single cells and LSM printed layers were characterized by DC polarization and AC- impedance methods. The study observed the reduction in efficiency due to incorporation of single cells and that phenomena was attributed to the microstructure of the composite cathode which can be supervised by modifying the formulation of ink and printing parameters.

G D Han et al, [78] was demonstrated the fabrication of cathodes from high pure Lanthanum strontium cobalt ferrite (LSCF) for the application of solid oxide fuel cells using the ink jet printing process. The aqueous based ink was prepared with LSCF by dissolving it into the aqueous based solvents with other surfactants. The author also mentioned that a LSCF cathode which is printed with optimal conditions are resulting in high peak density.

P Miranda et al, [79] reported on fabricating the scaffolds with beta-Tricalcium phosphate through robocasting 3D printing method. The author developed the viscoelastic inks, which are suitable to fabricate the complex structures by robocasting. Optimum rheological properties and heat treatment schedule to obtain dense scaffold which helps in controlling the microstructure and performance of scaffolds.

F J Martinez-Vazquez et al, [80] demonstrated the fabrication of beta-tricalcium phosphate through robocasting technique and analyzed the compressive strength behavior of scaffolds based on the polymer infiltration. Prepared viscoelastic ink of tricalcium phosphate was printed to tetragonal 3D mesh porous structures of interpenetrating rods which are further infiltrated with biodegradable polymer melt such as polylactic acid (PLA) and poly ε-caprolactone (PCL) by immersing into polymer melt. The compressive strength of scaffolds was significantly increased by a factor of 3 for PCL and 6 for PLA. Further the study also reported that, the mechanical strength and load bearing capacity of the scaffold structures were improved and this was attributed to the sealing of flaws on the rod surface and minimum transfer of stress to the polymer.

T Schlordt et al, [81] investigated on the fabrication of lattice cellular ceramics by robocasting technique. An aqueous colloidal gel was prepared with α-alumina of 50 Vol% and characterized for rheological properties. Author fabricated lattice truss with free spanning

filaments, a circular and rectangular type tubular filament were deposited in oil bath followed by freeze drying and sintering at 1550^{o}C. The continuity of the filaments was also characterized by micro-X-ray μ-CT and critical conditions were discussed to avoid capillary collapse.

S Eqtesadi et al, [82] demonstrates the process for fabricating the B4C complex structures using robocasting in combination with pressureless spark plasma sintering. To print these parts, the prepared ink with suitable rheological behavior was printed through robocasting method. After printing the samples were pressureless spark plasma sintered to attain required mechanical properties. Further the samples were cold isostatic pressed to improve the density of the printed parts. The author also discussed the production of large B_4C structures.

T Huang et al, [83] have used freeze-form extrusion-based 3D printing technique to fabricate the ceramic structures. The study used alumina paste with optimum rheological behavior and printed ceramic parts by depositing material in a layer fashion in aqueous medium. The study also examined the effect of process parameters on the printed geometry.

A Li et al, [84] investigated on the printing of functionally graded composite structures using freeze-form extrusion process. The authors have prepared the colloidal sol with composite consisting of zirconium carbide and tungsten and printed to complex structures. Further the sintered samples were characterized for its mechanical and microstructural properties.

G Franchin et al, [85] discussed about the printing of complex ceramic matrix composite using Direct Ink writing technique. A suitable ink with optimum rheological behavior was prepared using preceramic polymer. Rheology of the ink is to be optimized for printing the various complex structures. The author has reported that prepared ink was able to print finer filaments less than 1mm and it contains high amount (>30%) of fibers. The orientation of fibers depends on the extrusion direction where the shear stresses generated at the nozzle. This orientation of fibers provides flexibility to enhance the mechanical and microstructural properties by alignment of filler layers to layer and can be extended to many other types of fillers.

G Pierin et al, [86] reported on the printing of SiOC micro ceramic components using the direct ink writing of preceramic polymer. The preceramic polymer was prepared by dissolving the preceramic polymer with siloxane in a solvent. The author also added the low concentration of graphene oxide to the prepared polymeric mixture to attain structural stability during the pyrolysis process. The printed micro SiOC components results in good compression strength with 64 vol% porosity.

A Butscher et al, [87-89] discussed about the printing of scaffolds with calcium phosphate using powder-based 3D printing method. This includes the depowdering step where the remaining powder will be removed from the printed structure after printing and it is very critical and challenging task. The author has used mobile fillers in which the distance of the fillers was changed and these are glued to the scaffold cage or it can move freely after depowdering from the structure. The author reported that using of mobile fillers enhances the depowdering and applicable print large scaffold structures. The study further reviewed the material developments in powder-based 3D printing method to fabricate ceramic scaffolds for bone tissue engineering applications.

J Grau et al, [90] investigated on the printing of ceramic components with higher green density using slurry-based 3D printing method. This method involves the deposition of a powder layer by spraying the slurry of the component onto a piston. The author experimented the printing trails with alumina, lead zirconate titanate and silicon nitride and achieved the 67% of theoretical density. Further, this process resulted in improved surface finish of the components over the other powder-based 3D printing methods.

E Sachs et al, [91] discussed about the printing of alumina complex structures using Ink-jet 3D printing technique. An alumina component was built to a height of 50 layers and layer thickness of 0.005 in using alumina as a powder and colloidal silica as a binder. After printing the sample was characterized for its dimensional deviations with respect to the initial model. The method was also used to fabricate the injection molding tools with cooling channels using stainless steel as the powder and binder [92] and printed ceramic shells [93].

G Cesaretti et al, [94] investigated on the fabrication of building components using lunar soil on the moon through the patented D-shape 3D printing technology. The components were printed under both in air and vacuum to observe the occurrence of any reticulation in the structure. Printed test pieces were characterized for their mechanical properties.

D Ke et al, [95] demonstrated the effect of pore size distribution and material chemistry on the properties of the scaffolds fabricated by binder jet 3D printing process. Scaffolds were printed with tricalcium phosphate (TCP), MgO and Zno-TCP materials using binder jet 3D printer according to the predesigned porosity and size and sintered. After sintering the samples were characterized for the mechanical and biological properties. The study reports the dense scaffolds are shown an increase in surface area due to MgO and ZnO, density and compressive strength. The study reports the flexibility of 3D printing process to fabricate dense and porous structures with

high surface roughness, good mechanical and biological properties provides application in dental and orthopedic fields.

A Zocca et al, [96] discussed the printing of bio ceramic silicate (wollastonite ($CaSiO_3$)) parts from powder-based 3D printing method. In this glass powder was mixed with the preceramic polymer. The silicone resin present in the preceramic polymer will behave as a non-sacrificial binder and reaction between the fillers and binder results in desired phase formation of bio ceramics. Printed bio ceramic parts were characterized for porosity, compressive strength and in-vitro test.

J Moon et al, [97] demonstrated the preparation of binders which play a critical role during the fabrication of ceramic parts through ink-jet printing. The surface properties of printed body, such as surface finish, resolution of layers and dimensional accuracy mainly decided by the binder. The author has investigated various polymeric solution phase binders and characterized for its rheological and printing behavior. The literature reports the binder solution with the molecular weight of less than 15000 will penetrate strongly into the dense powder compacts. Physical properties such as viscosity of the binder solution and surface tension will also influence the binder infiltration kinetics and the width of the printed layer.

A Lauder et al, [98] used ink-jet printer to fabricate components with different chemistries of material. The printing parameters mainly raster scan pattern as well as the layer thickness affects the surface finish and microstructure of the printed body. To optimize printing process parameter such as printing speed, layer thickness and powder density were experimented.

M Lanzetta et al, [99] investigated on effect of particle size distribution of powder on the surface finish of the printed body. The author has used powder by bimodal distribution which is mixed uniformly and spread on a powder bed before starting the printing. Later the binder liquid deposited on the powder bed, according to the model. The study reports finer particles were found on the surface of line and coarse particles are found in the interior of the line, thus improved the surface finish of the printed body and this phenomenon was attributed to the displacement of finer particles to the surface after bounded by the binder.

G A Fielding et al, [100] studied the effect of dopants in the mechanical and biological performance of the TCP scaffold structure fabricated by 3D printing process. The author used silica and zinc oxide as a dopant into the TCP scaffolds. On addition of silica and zinc oxide to the TCP scaffolds, the density and compressive strength of the scaffolds was improved significantly.

I Gibson et al, [101] and H Zhang et al, [102] investigated on the factors which affects the laser powder bed fusion on printing oxide ceramics. The processing parameters such as printing conditions during printing, namely scanning speed, power, wavelength, diameter and scan pattern of the laser beam; material properties, namely particle size distribution, surface morphology, flowability and thickness of deposition etc.; and post processing parameters should be optimized for printing of every material. H Zhang optimized the processing parameters effect on properties of printed body by printing alumina, silica and mixtures of oxide ceramics. The study also addressed the issue that, by reducing the temperature gradient leads to reduction of the thermal stresses which further results in achieving the quality of printed body.

U Laxminarayan et al, [103-104] demonstrated the printing of alumina-ammonium phosphate bodies using selective laser sintering method. During printing the ammonium phosphate subjected to melt by laser energy and forms a glassy phase. The study reported the influence of printing and processing conditions (laser parameters, heat treatment schedule, powder properties) on the physico-chemical, mechanical and microstructural properties of sintered body.

I Lee [105] reported on the printing of alumina-aluminum borate structure using selective laser sintering method. The author has used the infiltration method as an effective way to densify the printed objects partially. Chromic acid and colloidal silica used as an infiltrate and out of these two infiltrates, the colloidal silica was found to improve the density (75% of theoretical density) and the bend strength (33 MPa) of the sintered body, whereas chromic acid as an infiltrate resulted in 80% of the theoretical density and strength of 15 MPa.

N Harlan et al, [106] investigated on the printing of ceramic structures with micro features using Zirconia powder through SLS method. Zirconia powder was subjected pre-processing to change its particle shape and size distribution. The study reported printed objects were laser sintered and resulted in relatively higher density with hole size of 180 microns.

H-H Tang [107] studied the printing of ceramic components using ceramic laser fusing (CLF) method. In this a ceramic powder mixed with the inorganic binder which is a temperature resistant to generate a layer of printing body and applied laser radiation melt the printed layer at the green stage. This process enables in fusing of the printed layers in green stage and no requirement to do conventional sintering process. The study reported that CLF has provided the flexibility to print complex structures with minimum shrinkage and distortion.

J Liu [108] investigated the influence of processing parameters on properties of dental glass ceramic parts produced by selective laser sintering method. The author has used fine dental glass ceramic powder to print parts for dental restoration application. Processing parameters related to the SLS method such as laser energy, scanning speed, pattern, preheating temperature were investigated to observe the effect on physical and mechanical properties of the sintered body. The study concludes that at an optimized conditions of SLS process parameters, the printed dental glass ceramic parts have shown high relative density and good bend strength.

K Shahzad et al, [109] demonstrated indirect selective laser sintering technique to fabricate complex alumina ceramic shapes in a two-step process. The first step includes the melting of deposit alumina/polymer composite layer using laser beam which leads to binding of ceramic particles together. Further the samples were subjected to heat treatment with lower heating rate and sintered to achieve good density. The author has used submicron alumina powder and polyamide 12 spherical particles were prepared using an inversion technique. The author characterized the powder for its powder properties and laser parameters to optimize the condition to fabricate defect free alumina parts.

J Deckers et al, [110] reported the experimental studies on the printing of alumina components using indirect selective laser sintering technique. An alumina/polyamide powder was ball milled and printed into ceramic component by indirect SLS technique and subjected for subsequent post processing steps. Sintered alumina components achieved 94% of theoretical density with an average grain size of 5 microns. The microstructure of the sintered structure has shown two types of pore morphology. The author also proposed quasi-isostatic pressing (QIP) at high temperatures as an alternative approach to cold isostatic pressing to enhance the density of the parts. Optimization of SLS parameters, deposition parameters, powder properties, QIPing schedule results in homogeneity of the pores and defect free parts.

K Shahzad et al, [111] demonstrated the indirect selective laser sintering system to produce alumina ceramic parts with high density. This author used thermally induced phase separation (TIPS) to prepare alumina-polymer composite. After investigating for the processing parameters mainly polymer concentration, stirring, cooling rate and polymer-ceramic composite, the alumina-polypropylene composite was prepared using TIPS. Printed green alumina parts through indirect SLS technique has shown 34% of density at optimum conditions of printing process parameters (scan speed, laser energy, powder preheating temperature, sintering schedule etc.,). Different post

processing methods have opted to enhance the density of the printed body. The author found that infiltrating with the alumina powder ethanol suspension in green SLS parts enhanced the density from 34% to 68 % and similar enhancement was observed in warm isostatic pressing (WIPing) method.

T Friedel et al, [112] carried out experimental studies in the fabrication of ceramic parts using preceramic polymer through selective laser curing technique. SiC incorporated with polysiloxane and used CO_2 laser to cure the polymer phase at 400^oc followed by pyrolysis at 1200^oC in inert atmosphere. The power of the laser beam and scanning speed were varied to observe the material properties. Parts containing 50 Vol% of polymers resulted in green density of 38 to 60% and decreased to 32-50% due to the polymer shrinkage occurred during pyrolysis process. After infiltrating the liquid silica resulted in improvement in the density and bend strength of the structure.

A Gahler et al, [113] printed dental ceramic components using direct laser sintering of alumina-silica powders by depositing the slurry layer wise. The author has prepared alumina silica ceramic slurry with high solid loading and characterized for its stability, flowability and viscosity for uniform layer deposition. The study also reports that optimization of laser parameters results in obtaining ceramic parts with good mechanical and microstructural properties. The microstructure of the printed parts was strongly influenced by the preheating temperature of laser beam and thermal conduction. The sintering process enables the printed components to achieve relatively high density.

V K Balla et al, [114] opted laser engineered net shaping to fabricate bulk complex structures with alumina. The author has used α-alumina to print cylinder, gear and cube with 10-25 mm size cross sectional. The printed bodies have shown mechanical anisotropy with enhanced compressive strength and the mechanical anisotropy and strength of the sintered body not changed after the heat treatment but it varied with the grain size and hardness structure.

J P Kruth et al, [115] discussed the status of the selective laser sintering towards the materials and different lasers. The initial raw material should be in a powder form or it may contain any polymer binders which can be burnt by post heating process. The chemical interaction of laser beam energy and powder spread on the powder bed determines the quality of the printed body. The author has used numerical simulation analysis to investigate this interaction between the laser and material and controlled it.

T Muhler et al, [116] have studied the application of slurry-based powder bed to fabricate silicate ceramic structures using selective laser sintering (SLS) technique. The powder-based platform in SLS uses dry powder which is spread by roller and there spread layers have lower density. But depositing the highly solid loaded slurry, the author observed the good adherence of layers and exhibiting the relatively good properties comparable to the conventionally processed ceramic parts. A focused laser beam travels on the deposited slurry bed, according to the CAD model and produce the dense ceramic part with close dimensional tolerance.

X Tian et al, [117] experimented the processing parameters of direct SLS and post processing parameters to fabricate porcelain structures by applying the Taguchi method. The author has studied the influence of SLS printing parameters, namely the power of the laser, scanning speed and scanning thickness, post heating parameters such as sintering temperature, heating rate and soaking time on printing of porcelain parts. Based on the Taguchi experimental design, it is revealed that, a higher scanning thickness and scanning speed with lower laser power along with optimum sintering temperature (1425-1475^{o}C) promotes the printed porcelain parts with good mechanical properties.

L Weisensel et al, [118] studied on printing of SiSiC composite structure using laminated object manufacturing (LOM) technique. The study reports that, printed laminar sheets with carbon, which are manufactured from pyrolyzed filter paper sheets through LOM technique and printed laminar structures were converted to SiSiC composites by sintering it under pressure less conditions using silica as infiltrate. The process parameters of LOM as well as the physical properties (density, porosity) of the biocarbon preform determine the mechanical and microstructural properties of the fabricated part.

The last three decades, research challenges and industrial needs have promoted ceramics massively to be an exciting field of application of 3D printing technologies. Complex ceramic structures have been fabricated through AM methods which are difficult to fabricate with conventional ceramic shaping processes. However, 3D printing process is used to form ceramic structures only, but the properties of the final ceramic body depend on the composition of raw material and microstructure by sintering process. Further to improve the properties of ceramic printed component at the green stage and sintered body, an appropriate feedstock preparation with optimum rheological behavior and post treatment process such as hot and cold isostatic pressing

offers possibility to heal the layer structure which further improves the mechanical properties of ceramics although the cost of operation for mentioned post processing techniques.

Powder bed fusion methods are well developed for both metals and plastics. But for ceramics it is still under development due to its high melting temperatures. Fabrication of ceramic parts with a laser or other energy sources would assistance in studying the interaction between laser and electron beam energy with the ceramic particles. Rapid heating and cooling rates caused by the laser/electron beam energy source induces residual stresses which lead to initiation of defects and cracks. Preheating of powder bed will help to reduce the cracks and distortions caused by the energy, but a high melting point of ceramics makes the process expensive.

Developed photo-polymerization process as stereolithography, DLP enables the forming of ceramic parts easily than the powder bed fusion methods. Usage of photopolymer resins in a very high concentration emitting hazardous emissions into the environment and causes pollution. As a substitute to the photopolymer curable resins, there is a necessity to develop and use environmentally friendly binder systems which will provide the good shape integrity of printed parts. Moreover, selection of raw material and optimization of process such as parameters required to prepare ceramic feedstock (slurry based/paste/powder) for each and every material is important. Production of large size (few meters) ceramic parts is difficult in 3D printing process due to characteristics of ceramics mainly brittleness and low expansion coefficients of materials. Extension of 3D printing process for the large-scale production of high-performance ceramic parts is possible in less time with low cost.

1.6 Scope of work

It is evident from the extensive literature survey discussed above that the 3D Printing technique is an emerging area in ceramic prototype fabrication as it offers complex shaping capability along with micro-features. Currently major focusing of 3D Printing process is in the shaping of traditional ceramics using UV curable monomer resins. In the present study attempts will be made to extend the process to advance ceramic materials such as Al_2O_3, Magnesium Aluminate spinel ($MgAl_2O_4$) and Cordierite. Additionally, investigation will also be carried out to replace the UV curable resins with environmentally friendly cellulose-based binders based on rheological data

analysis. The studies will also concentrate to use thermal gelation as a replacement of UV polymerization. Design and development of extrusion assembly for ram and screw type extrusion will also be undertaken as a part of the study. The printed components will further be subjected to the characterization of its physical-thermal, mechanical and microstructural properties in the intermediate and sintered conditions. Accordingly, the objectives of the study are as follows.

- To characterize the advanced ceramic powder of various properties such as Phase analysis (XRD), Particle size distribution (DLS), Morphology (SEM), Chemical analysis (EDS) and Surface area (BET).
- To prepare printable paste with environmentally friendly cellulose-based binders followed by rheological studies
- To carry out curing experiments by thermal gelation process
- To design and fabricate an extrusion assembly to suite the existing 3D printer at ARCI
- To optimize the 3D printing parameters (instrumental and rheological) based on the printing experiments
- Development of complex ceramic parts based on the 3D printed polymer replication
- Characterization of printed and sintered components for physical-chemical, thermal, mechanical and microstructural properties
- To correlate the properties of printed parts with printing parameters and comparative evaluation with a conventionally processed alumina part
- To explore the pressure assisted sintering process to produce defect free 3D printed samples
- Development of parts with respect to bio-reactor, bio-medical and environmental related applications

1.7 References

1. E M Sachs, J S Haggerty, M J Cima, P A Williams, Three-dimensional printing techniques, Google Patents, 1993.
2. J Deckers, J Vleugels, J P Kruth, Additive manufacturing of ceramics: a review, Journal of Ceramic Science and Technology, 2014;5:245–260.

3. B Utela, D Storti, R Anderson, M Ganter, A review of process development steps for new material systems in three-dimensional printing (3DP), Journal of Manufacturing Processes, 2008;10:96–104.
4. H Yang, S Yang, X Chi, J R Evans, Fine ceramic lattices prepared by extrusion free forming, Journal of Biomedical Materials Research Part B: Applied Biomaterials, 2006;79:116–121.
5. Z Xianwei, H E Zhang, W Chunwei, Z Zexiong, W Enhui, C Yiqing, Hectorite modified 3D printing ceramic clay and preparation method thereof. Chinese Patent application 108840662A, 2018.
6. Z Aili, C Longsheng, S Huimin, M Youjun, Y Shangquan, W Kun, G Xiang, Purple sand mud material suitable for LMD method 3D printing and preparation method and application. Chinese Patent application no. 108793951A, 2018.
7. L Cong, L Jialin, G Jiemei, G Honghao, H Yuming, Formula of ceramic 3D printing mud. Chinese Patent application no. 108484110A, 2018
8. Z Yue, D Lina, Y Liangliang, B Feng, Water-based ceramic slurry for free extruding and molding as well as preparation method and application thereof. Chinese Patent application no. 108191409A, 2018.
9. W Tao, W Yong, 3D (three dimensional) printing molded cation light-curing type aluminum oxide ceramic slurry composition. Chinese Patent application no. 108191410A, 2018.
10. Z Tao, Z Kun, Z Yikai, Preparation method of SiCW/SiC/SiC ceramic-based composite material. Chinese Patent application no. 108264353A, 2018.
11. Z Dongyun, Z Yan, W Weidong, Silicon carbide particle reinforced aluminum-based composite material forming method based on selective laser melting technology. Chinese Patent application no. 108480625A, 2018.
12. Q Haijun, Preparation method for ceramic composites for 3D printing. Chinese Patent application 108726977A, 2018.
13. S Wu, R Huang, H Wu, Q Jiang, Y Li, Silicon nitride ceramic and preparation method thereof. Chinese Patent application 108675798A, 2018.

14. M Qingsong, Z Kuanhong, Three-dimensional silicon carbide fiber reinforced aluminium oxide-zirconium oxide composite material and preparation method thereof. Chinese Patent application no. 108033803A, 2018.
15. S Chunxia, W Wenxin, C Jing, Self-lubrication ceramic material and preparation method thereof. Chinese Patent application no. 108555294A, 2018.
16. G Weiming,W Lixiang, N Wenbin, C Zhiwei, L Huatai, W Shanghua, Titanium diboride-based multiphase ceramic and preparation method and application thereof. Chinese Patent application no. 108610052A, 2018.
17. W Xiaofeng, Y Kai, Preparation method of 3D (three-dimensional) printing ceramic slurry. Chinese Patent application no. 108069704A, 2018.
18. C Laifei, L Xinyuan, Y Fang, F Shangwu, Y Shuyin, L Yongsheng, Z Litong, Ceramic material SiC whisker suitable for stereolithography, and preparation method thereof. Chinese Patent application no. 108395249A, 2018.
19. H Mingyang, C Xiangpeng, L Lecheng, Gypsum-based composite binding material for extruded 3D printing and preparation method thereof. Chinese Patent application no. 108383465A, 2018.
20. C Sainan, G Hai, Y Jianchun, J Jie, L Bin, Z Jie, W Guoqing, H Tiancheng, L Jinjin, Multiphase nano ceramic particle hybrid reinforced nickel-based alloy composite material and laser forming method thereof. Chinese Patent application no. 108728695A, 2018.
21. D C Hofmann, High toughness metallic glass-based composites for additive manufacturing. WIPO Patent application no. 2018223117A2, 2018.
22. B A Demuth, A R Pawloski, Ceramic support structure. US Patent application no. 2018339426A, 2018.
23. L Rueschhoff, W Costakis, M Michie, J Youngblood, R Trice, Additive manufacturing of dense ceramic parts via direct Ink writing of aqueous alumina suspensions, International Journal of Applied Ceramic Technology, 2016;1–10
24. H Patrick, H Warnke, F Seitz, S T Becker, S Sivanathan, E Sherry, Q Liu, J Wiltfang, T Douglas, Ceramic scaffolds produced by computer-assited 3D printing and sintering: Characterization and biocompatibility investigations, Journal of Biomedical Materials Research pat B: Applied Biomaterials/ 2010; 93B(1).

25. M. Faesa, H. Valkenaersa , F. Vogelera , J. Vleugelsb , E. Ferrarisa, Extrusion-based 3D printing of cermic components, Procedia CIRP, 2015;8:76 – 81
26. U Scheithauer, E Schwarzer, H-J Richter, T Moritz, Thermoplastic 3D printing- an additive manufacturing method for producing dense ceramics. International Journal of Applied Ceramic Technology, 2015;12:26-31.
27. R Hea, W Liua, Z Wua, D Anb, M Huanga, H Wua, Q Jianga, X Jia , S Wua, Z Xieb, Fabrication of complex-shaped zirconia ceramic parts via a DLP stereolithography-based 3D printing method, Ceramic International, 2018;44:3412-3416.
28. H Wu, D Li, Y Tang, B Sun, D Xu, Rapid fabrication of alumina-based ceramic cores for gas turbine blades by stereolithography and gelcasting, Journal of Materials Processing Technology, 2009;209:5886–5891.
29. M L Griffith, J W Halloran, Ultraviolet curable ceramic suspensions for stereolithography of ceramics, The International Mechanical Engineering Congress and Exposition, 1994;44:529–534.
30. G Mitteramskogler, R Gmeiner, R Felzmann, S Gruber, C Hofstetter, J Stampfl, J Ebert, W Wachter, J Laubersheimer, Light curing strategies for lithographybased additive manufacturing of customized ceramics, Additive Manufacturing, 2014;1:110–118.
31. S P Gentry, J W Halloran, Depth and width of cured lines in photopolymerizable ceramic suspensions, Journal of the European Ceramic Society, 2013;33:1981–1988.
32. Y. de Hazan, D. Penner, SiC and SiOC ceramic articles produced by stereolithography of acrylate modified polycarbosilane systems, Journal of the European Ceramic Society, 2017;37:5205–5212.
33. P Gonzalez, E Schwarzer, U Scheithauer, N Kooijmans, T Moritz, Additive Manufacturing of Functionally Graded Ceramic Materials by Stereolithography. Journal of Visualized Experiments, 2019;143:57943
34. M. Zhou, W Liu, H Wu, X Song, Y Chen, L Cheng, F He, S Chen, S Wu, Preparation of a defect-free alumina cutting tool via additive manufacturing based on stereolithography – Optimization of the drying and debinding processes, Ceramics International, 2016;42: 11598-11602.
35. A D B Romero, M Pfaffinger, G Mitteramskogler, M Schwentenwein, C Jellinek, J Homa, A D Lantada1, J Stampfl, Lithography-based additive manufacture of ceramic biodevices

with design-controlled surface topographies, International Journal of Advanced Manufacturing Technology, 2017;88:1547–1555.

36. M C Leu, L Tang, B Deuser, R G Landers, G E Hilma, S Zhang, J Watts, Freeze-form extrusion fabrication of composite structures, Reviewd article 09-2011.
37. M L Griffith, J W Halloran, Freform fabrication of ceramics via stereo-lithography, Journal of the American Ceramic Society, 1996;79:2601-2608.
38. G A Brady, J W Halloran, Stereolithography of ceramic suspensions, Rapid Prototyping Journal, 1997;3:61–65.
39. J W Halloran, V Tomeckova, S Gentry, S Das, P Cilino, D Yuan, R Guo, A Rudraraju, P Shao, T Wu, Photopolymerization of powder suspensions for shaping ceramics, Journal of the European Ceramic Society, 2011;31:2613–2619.
40. C J Bae, A Ramachandran, J W Halloran, Quantifying particle segregation in sequential layers fabricated by additive manufacturing, Journal of the European Ceramic Society, 2018;38:4082-4088.
41. W Zimbeck, M Pope, R Rice, Microstructures and strengths of metals and ceramics made by photopolymer-based rapid prototyping, Solid Freeform Fabrication Symposium, 1996; 411–418.
42. M Wozniak, T Graule, Y D Hazan, D Kata, J Lis, Highly loaded UV curable nanosilica dispersions for rapid prototyping applications, Journal of the European Ceramic Society, 2009;29:2259–2265.
43. H Xing, B Zou, S Li, X Fu, Study on surface quality, precision and mechanical properties of 3D printed ZrO_2 ceramic components by laser scanning stereolithography, Ceramics International, 2017;43:16340–16347.
44. C J Bae, Integrally cored ceramic investment casting mold fabricated by ceramic stereolithography, University of Michigan, 2008.
45. W Z Zhou, D Li, Z W Chen, S Chen, Direct fabrication of an integral ceramic mould by stereolithography, Proceedings of the Institution of Mechanical Engineers Part B- Journal of Engineering Manufacture, 2010;224:237–243.
46. Z Chen, D Li, W Zhou, Process parameters appraisal of fabricating ceramic parts based on stereolithography using the Taguchi method, Proceedings of the Institution of Mechanical Engineers, Part B: Journal of Engineering Manufacture, 2012;226:1249–1258.

47. N T Nguyen, N Delhote, M Ettorre, D Baillargeat, L L Coq, R Sauleau, Design and characterization of 60-GHz integrated lens antennas fabricated through ceramic stereolithography, IEEE Transactions on Antennas and Propagation, 2010;58:2757–2762.
48. S J Leigh, C Purssell, J Bowen, D A Hutchins, J A Covington, D Billson, A miniature flow sensor fabricated by micro-stereolithography employing a magnetite/acrylic nanocomposite resin, Sensors and Actuators A: Physical, 2011;168:66–71.
49. S Kirihara, T Niki, Three-Dimensional Stereolithography of Alumina Photonic Crystals for Terahertz Wave Localization, International Journal of Applied Ceramic Technology, 2015;12:32–37.
50. D Du, T Asaoka, T Ushida, K S Furukawa, Fabrication and perfusion culture of anatomically shaped artificial bone using stereolithography, Biofabrication, 2014;6:045002.
51. D P Sarment, K Al-Shammari, C E Kazor, Stereolithographic surgical templates for placement of dental implants in complex cases, International Journal of Periodontics & Restorative Dentistry, 2003;23:287-95.
52. Q Lian, W Sui, X Wu, F Yang, S Yang, Additive manufacturing of ZrO2 ceramic dental bridges by stereolithography, Rapid Prototyping Journal, 2018;24:114–119.
53. C J Bae, J W Halloran, Influence of residual monomer on cracking in ceramics fabricated by stereolithography, International Journal of Applied Ceramic Technology, 2011;8:1289–1295.
54. P Colombo, G Mera, R Riedel, G D Soraru, Polymer-derived ceramics: 40 years of research and innovation in advanced ceramics, Journal of the American Ceramic Society, 2010;93:1805–1837.
55. Z C Eckel, C Zhou, J H Martin, A J Jacobsen, W B Carter, T A Schaedler, Additive manufacturing of polymer-derived ceramics, Science, 2016;351:58–62.
56. E Zanchetta, M Cattaldo, G Franchin, M Schwentenwein, J Homa, G Brusatin, P Colombo, Stereolithography of SiOC ceramic microcomponents, Advanced Materials, 2016;28:370–376.
57. P Colombo, J Schmidt, G Franchin, A Zocca, J Gunster, Additive manufacturing techniques for fabricating complex ceramic components from preceramic polymers, American Ceramic Society Bulletin, 2017;96:16–23.

58. A Zocca, G Franchin, H Elsayed, E Gioffredi, E Bernardo, P Colombo, Direct ink writing of a preceramic polymer and fillers to produce hardystonite ($Ca_2ZnSi_2O_7$) bioceramic scaffolds, Journal of the American Ceramic Society, 2016;99:1960–1967.
59. R He, W Liu, Z Wu, D An, M Huang, H Wu, Q Jiang, X Ji, S Wu, Z Xie, Fabrication of complex-shaped zirconia ceramic parts via a DLP- stereolithography- based 3D printing method, Ceramics International, 2018;44:3412–3416.
60. M Zhou, W Liu, H Wu, X Song, Y Chen, L Cheng, F He, S Chen, S Wu, Preparation of a defect-free alumina cutting tool via additive manufacturing based on stereolithography – Optimization of the drying and debinding processes, Ceramics International, 2016;42:11598–11602.
61. M Schwentenwein, J Homa, Additive manufacturing of dense alumina ceramics, International Journal of Applied Ceramic Technology, 2015;12:1-7.
62. R Felzmann, S Gruber, G Mitteramskogler, P Tesavibul, A R Boccaccini, R Liska, J Stampfl, Lithography-Based Additive Manufacturing of Cellular Ceramic Structures, Advanced Engineering Materials, 2012;14:1052–1058.
63. R Gmeiner, G Mitteramskogler, J Stampfl, A R Boccaccini, Stereolithographic ceramic manufacturing of high strength bioactive glass, International Journal of Applied Ceramic Technology, 2015;12:38–45
64. M Schwentenwein, P Schneider, J Homa, Lithography-based ceramic manufacturing: a novel technique for additive manufacturing of high-performance ceramics, Advances in Science and Technology, 2014;88:60–64.
65. U Scheithauer, E Schwarzer, G Ganzer, A Kornig, W Becker, E Reichelt, M Jahn, A Hartel, H Richter, T Moritz, Micro-Reactors Made by Lithography-Based Ceramic Manufacturing (LCM), Additive Manufacturing and Strategic Technologies in Advanced Ceramics: Ceramic Transactions, 2015;258:31–41.
66. U Scheithauer, E Schwarzer, T Moritz, A Michaelis, Additive Manufacturing of Ceramic Heat Exchanger: Opportunities and Limits of the Lithography-Based Ceramic Manufacturing (LCM), J Mater Eng Perform, 2018;27:14–20.
67. M Hatzenbichler, M Geppert, S Gruber, E Ipp, R Almedal, J Stampfl, DLP-based light engines for additive manufacturing of ceramic parts, Proc. SPIE 8254. Emerging Digital

Micromirror Device Based Systems and Applications IV, International Society for Optics and Photonics, 2012; 82540E.

68. P Blazdell, J Evans, M Edirisinghe, P Shaw, M Binstead, The computer aided manufacture of ceramics using multilayer jet printing, Journal of materials science letters, 1995;14:1562–1565.
69. Q Xiang, J Evans, M Edirisinghe, P Blazdell, Solid freeforming of ceramics using a drop-on-demand jet printer, Proceedings of the Institution of Mechanical Engineers, Part B: Journal of Engineering Manufacture, 1997;211:211–214.
70. M Singh, H M Haverinen, P Dhagat, G E Jabbour, Inkjet printing process and its applications, Advanced Materials, 2010;22: 673–685.
71. H Dong, W W Carr, J F Morris, An experimental study of drop-on-demand drop formation, Physics of Fluids, 2006;18:072102.
72. N Reis, B Derby, Ink jet deposition of ceramic suspensions: Modeling and experiments of droplet formation, MRS Online Proceedings Library Archive, Symposium V-Materials Development for Direct Write Technologies, 2000;624:65.
73. R Noguera, M Lejeune, T Chartier, 3D fine scale ceramic components formed by ink-jet prototyping process, Journal of the European Ceramic Society, 2005;25:2055–2059.
74. B Derby, Inkjet printing ceramics: From drops to solid, Journal of the European Ceramic Society, 2011;31:2543–2550.
75. R Dou, T Wang, Y Guo, B Derby, Ink-Jet Printing of Zirconia: Coffee Staining and Line Stability, Journal of the American Ceramic Society, 2011; 94:3787–3792.
76. A Friederich, J R Binder, W Bauer, Rheological control of the coffee stain effect for inkjet printing of ceramics, Journal of the American Ceramic Society, 2013;96:2093–2099.
77. M Sukeshini, R Cummins, T L Reitz, R M Miller, Ink-Jet Printing: A Versatile Method for Multilayer Solid Oxide Fuel Cells Fabrication, Journal of the American Ceramic Society, 2009;92:2913–2919.
78. G D Han, K C Neoh, K Bae, H J Choi, S W Park, J-W Son, J H Shim, Fabrication of lanthanum strontium cobalt ferrite (LSCF) cathodes for high performance solid oxide fuel cells using a low price commercial inkjet printer, Journal of Power Sources, 2016;306: 503–509.

79. P Miranda, E Saiz, K Gryn, A P Tomsia, Sintering and robocasting of β-tricalcium phosphate scaffolds for orthopaedic applications, Acta biomaterialia, 2006;2:457–466.
80. F J M-Vazquez, F H Perera, P Miranda, A Pajares, F Guiberteau, Improving the compressive strength of bioceramic robocast scaffolds by polymer infiltration, Acta Biomaterialia, 2010; 6: 4361–4368.
81. T Schlordt, S. Schwanke, F Keppner, T Fey, N Travitzky, P Greil, Robocasting of alumina hollow filament lattice structures, Journal of the European Ceramic Society, 2013;33:3243–3248.
82. S Eqtesadi, A Motealleh, F H Perera, P Miranda, A Pajares, R Wendelbo, F Guiberteau, A L Ortiz, Fabricating geometrically-complex B4C ceramic components by robocasting and pressureless spark plasma sintering, Scripta Materialia, 2018;145:14–18.
83. T Huang, M S Mason, G E Hilmas, M C Leu, Freeze-form extrusion fabrication of ceramic parts, Virtual and Physical Prototyping, 2006;1:93–100.
84. M C Leu, B K Deuser, L Tang, R G Landers, G E Hilmas, J L Watts, Freeze-form extrusion fabrication of functionally graded materials, CIRP Annals-Manufacturing Technology, 2012;61:223–226.
85. G Franchin, L Wahl, P Colombo, Direct ink writing of ceramic matrix composite structures, Journal of the American Ceramic Society, 2017;100: 4397–4401.
86. G Pierin, C Grotta, P Colombo, C Mattevi, Direct Ink Writing of micrometric SiOC ceramic structures using a preceramic polymer, Journal of the European Ceramic Society, 2016;36:1589–1594.
87. A Butscher, M Bohner, N Doebelin, L Galea, O Loeffel, R Muller, Moisture based three-dimensional printing of calcium phosphate structures for scaffold engineering, Acta biomaterialia, 2013;9:5369–5378.
88. A Butscher, M Bohner, S Hofmann, L Gauckler, R Muller, Structural and material approaches to bone tissue engineering in powder-based three-dimensional printing, Acta biomaterialia, 2011;7:907–920.
89. A Butscher, M Bohner, N Doebelin, S Hofmann, R Muller, New depowdering friendly designs for three-dimensional printing of calcium phosphate bone substitutes, Acta biomaterialia, 2013;9:9149–9158.

90. J Grau, J Moon, S Uhland, M. Cima, E. Sachs, High green density ceramic components fabricated by the slurry-based 3DP process, Solid Freeform Fabrication Symposium, 1997;43:371–378.
91. E Sachs, M Cima, P Williams, D Brancazio, J Cornie, Three dimensional printing: rapid tooling and prototypes directly from a CAD model, Journal of Engineering for Industry, 1992:114: 481–488.
92. E Sachs, E Wylonis, S Allen, M Cima, H Guo, Production of injection molding tooling with conformal cooling channels using the three dimensional printing process, Polymer Engineering & Science, 2000;40:1232–1247.
93. E Sachs, CAD-casting: the direct fabrication of ceramic shells and cores by three dimensional printing, Manufacturing Revision, 1992;5:118–126.
94. G Cesaretti, E Dini, X D Kestelier, V Colla, L Pambaguian, Building components for an outpost on the Lunar soil by means of a novel 3D printing technology, Acta Astronautica, 2014;93:430–450.
95. D Ke, S Bose, Effects of pore distribution and chemistry on physical, mechanical, and biological properties of tricalcium phosphate scaffolds by binder-jet 3D printing, Additive Manufacturing, 2018;22:111–117.
96. A Zocca, H Elsayed, E Bernardo, C Gomes, M Lopez-Heredia, C Knabe, P Colombo, J Gunster, 3D-printed silicate porous bioceramics using a non-sacrificial preceramic polymer binder, Biofabrication, 2015;7:025008.
97. J Moon, J E Grau, V Knezevic, M J Cima, E M Sachs, Ink-jet printing of binders for ceramic components, Journal of the American Ceramic Society, 2002:85:755–762.
98. A Lauder, M Cima, E Sachs, T Fan, Three dimensional printing: surface finish and microstructure of rapid prototyped components, MRS Online Proceedings Library Archive,1991:249.
99. M Lanzetta, E Sachs, Improved surface finish in 3D printing using bimodal powder distribution, Rapid Prototyping Journal, 2003;9:157–166.
100. G A Fielding, A Bandyopadhyay, S Bose, Effects of silica and zinc oxide doping on mechanical and biological properties of 3D printed tricalcium phosphate tissue engineering scaffolds, Dental Materials, 2012;28:113–122.

101. I Gibson, D Shi, Material properties and fabrication parameters in selective laser sintering process, Rapid prototyping journal, 1997;3:129–136.
102. H Zhang and S LeBlanc, Processing parameters for selective Laser Sintering or Melting of Oxide Ceramics, book: Additive Manufacturing of High-performance Metals and alloys-Modelling and Optimization, 2018.
103. U Lakshminarayan, S Ogrydiziak, H Marcus, Selective laser sintering of ceramic materials, 1990 International Solid Freeform Fabrication Symposium, 1990.
104. U Lakshminarayan, H Marcus, Microstructural and Mechanical Properties of Al_2O_3/P_2O_5 AND Al_2O_3/B_2O_3 Composites Fabricated by Selective Laser Sintering, 1991 International Solid Freeform Fabrication Symposium, 1991.
105. I Lee, Densification of porous Al_2O_3-$Al_4B_2O_9$ ceramic composites fabricated by SLS process, Journal of materials science letters,1999;18:1557–1561.
106. N Harlan, S-M Park, D L Bourell, J J Beaman, Selective laser sintering of zirconia with micro-scale features, Proceedings of SFF Symposium, Austin, 1999:297–302.
107. H-H Tang, Direct laser fusing to form ceramic parts, Rapid Prototyping Journal, 2002;8:284–289.
108. J Liu, B Zhang, C Yan, Y Shi, The effect of processing parameters on characteristics of selective laser sintering dental glass-ceramic powder, Rapid Prototyping Journal,2010;16:138–145.
109. K Shahzad, J Deckers, S Boury, B Neirinck, J-P. Kruth, J Vleugels, Preparation and indirect selective laser sintering of alumina/PA microspheres, Ceramics Internationa,2012; 38:1241–1247.
110. J Deckers, K Shahzad, J Vleugels, J-P Kruth, Isostatic pressing assisted indirect selective laser sintering of alumina components, Rapid Prototyping Journal,2012;18:409–419.
111. K Shahzad, J Deckers, J-P Kruth, J Vleugels, Additive manufacturing of alumina parts by indirect selective laser sintering and post processing, Journal of Material Processing Technology,2013;213:1484–1494.
112. T Friedel, N Travitzky, F Niebling, M Scheffler, P Greil, Fabrication of polymer derived ceramic parts by selective laser curing, Journal of the European Ceramic Society,2005;25:193–197.

113. A Gahler, J G Heinrich, J Guenster, Direct Laser Sintering of Al_2O_3–SiO_2 Dental Ceramic Components by Layer-Wise Slurry Deposition, Journal of the American Ceramic Society,2006;89:3076–3080.
114. V K Balla, S Bose, A Bandyopadhyay, Processing of bulk alumina ceramics using laser engineered net shaping, International Journal of Applied Ceramic Technology, 2008;5:234–242.
115. J P Kruth, X Wang, T Laoui, L Froyen, Lasers and materials in selective laser sintering, Assembly Automation.2003;23:357–371.
116. T Muhler, C Gomes, M Ascheri, D Nicolaides, J Heinrich, J Gunster, Slurry-based powder beds for the selective laser sintering of silicate ceramics, Journal of Ceramic Science and Technology, 2015:6:113–118.
117. X Tian, J Gunster, J Melcher, D Li, J G Heinrich, Process parameters analysis of direct laser sintering and post treatment of porcelain components using Taguchi's method, Journal of the European Ceramic Society,2009;29:1903–1915.
118. L Weisensel, N Travitzky, H Sieber, P Greil, Laminated object manufacturing (LOM) of SiSiC composites, Advanced Engineering Materials, 2004;6:899–903.

****

CHAPTER-2

EXPERIMENTAL METHODOLOGIES

2.1 Importance of Powder Properties

Forming or processing of any ceramic part generally begins with the powder as a basic building unit. Further, the physico-chemical properties (density, purity, porosity and pore size), mechanical properties (hardness, compressive strength, flexural strength and fracture toughness) and microstructural properties (grain size and their distribution) of the formed parts are a strong function of the characteristics of the starting powder. These properties which in turn determines the performance, reliability and durability of the ceramic components under various service conditions.

Hence selection of raw material and its properties such as particle size and its distribution, morphology (particle shape and shape distribution), surface area, the chemical composition of the powder and phase will play a crucial role in ceramic processing techniques. Particle size and its distribution along with morphology and surface area will primarily determine the formability of the parts. The major controlled parameters generally include its ability to flow with adaptability to higher packing densities under shear forces.

2.2 Characterization of Powder

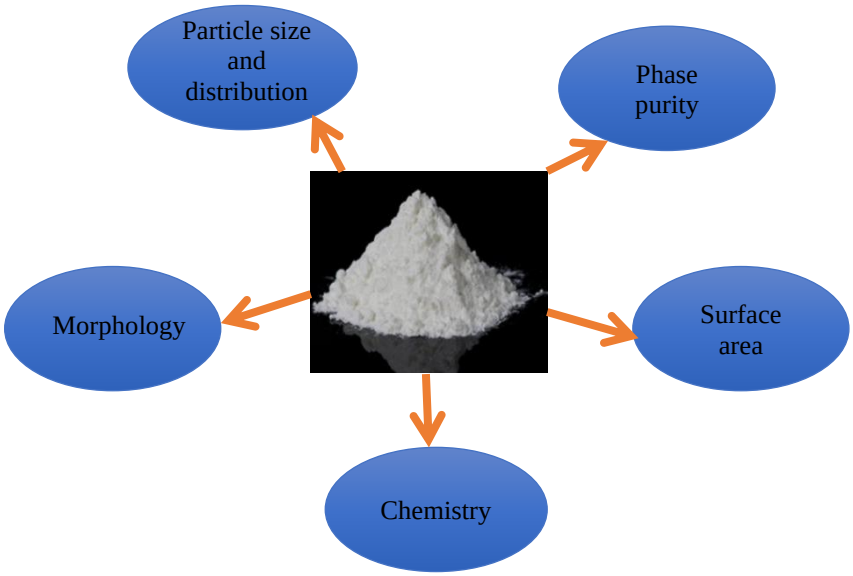

Fig: 2.1 Important properties of ceramic powders

Table 2.1: Properties of powder and measuring techniques

S. No	Property	Technique
1	Particle Size and Distribution	Laser Diffraction/Dynamic Light Scattering (DLS)
2	Phase Purity	X-Ray Diffraction (XRD)
3	Specific Surface area	Brunauer-Emmett-Teller (BET) theory
4	Chemistry	Energy Dispersive Spectroscopy (EDS/EDAX)
5	Particle shape and Distribution (morphology)	Scanning Electron Microscopy (SEM)

2.2.1 Particle size and Distribution

Advanced ceramic powders are generally characterized for particle size and distribution by Laser Diffraction (LSD) or Dynamic Light Scattering (DLS) technique, whose principles and basic procedure are as described below [1-3].

2.2.1.1 Laser Diffraction

Laser Diffraction is the most commonly used technique to measure the particle size range from hundreds of nanometers to several millimeters. It measures particle size by measuring the angular variation in the intensity of light scattered from the dispersed sample. Diffraction is phenomenon of waves where the incident light bends due to obstacles faced during the path of motion.

It is an analytical technique to measure the particle size from the dispersed powder in solvent. Main working principle of the laser diffraction technique is inverse relation of angular

variation and particle size. Less angular variation of diffracted light indicates the large particle size and high angular variation results from small particle size. He-Ne Laser used as analysis source for such experiments, hence method known as laser diffraction. In practice to measure particle size, the measuring size of particle should be in the range of wavelength of laser light.

Fraunhofer and Mie theory are used to detect and analyze the diffracted beam. Fraunhofer theory is simple and it works well for opaque particles and consider optical properties of particle, but Mie theory considers both optical and scattering properties of the particles. Size distribution of particle has one or more sizes of particles which are indicated by D_{mode}. The cumulative distribution curve size D_{mode} represents from 0 to 100%. D_{50} is the most commonly used referring point in laser diffraction and it defines where 50% of particles smaller and 50% of particles bigger than certain diameter.

Laser diffraction allows measuring the particle size in dry method which means a required amount (3-5 gms) of powder in chamber. During the process the incident laser beam will be diffracted with different angles according to the size of particles, further all diffraction angles are detected and recorded in diffraction pattern on the screen. The diffraction pattern is analyzed by complex algorithm and measures the values of particle size and distribution.

2.2.1.2 Dynamic Light Scattering

Dynamic Light Scattering technique is another well-known technique to measure particle size and it is also known as Quasi-elastic scattering or Photon correlation spectroscopy. The analysis of particle size is done by the measurement of velocity of particles dispersed in liquid medium caused by motion of a particle randomly. This motion is called Brownian motion. When monochromatic light hit the particle, it gets scattered in all directions. Due to random motion of particle, there is a fluctuation in local particle suspended in the liquid leads to resulting in in-homogeneity in refractive index of material. Further it leads to spectrum of Rayleigh scattering with line width Γ (half width at half maximum) and it is proportional to the diffusion coefficient (D).

$$\Gamma = DK^2 \text{ ----------} \rightarrow 1$$

Where, $K = \left(\frac{4n\pi}{\lambda}\right) * \sin\left(\frac{\theta}{2}\right)$

n is the refractive index,

θ = scattering angle,

λ = Wavelength of laser

Assuming that particles are spherical and non-interacting, the mean radius of the particle is obtained from the Stokes-Einstein equation (equation 2)

$$R = \left(\frac{kT}{6\pi\eta D}\right) \text{----------} \rightarrow 2$$

Where k = Boltzmann constant,

D = Diffusion coefficient

T = Absolute temperature and

Ɲ = coefficient of viscosity of the medium

To measure particle size and size distribution, the required amount (0.05 gm) of powder was dispersed in aqueous medium by adding ammonium polyacrylate dispersant (Darvan 821A, R.T Vanderbilt Co.Inc. USA). Further the resultant solution was ultrasonicated for 20 minutes using Sonics ultrasonicator (VCX 750, Sonics and Materials Inc., Newtown CT, USA) to obtain homogeneous solution. A 5ml of resultant solution was filled in cuvette and placed between the light source and detector present in the Nanosizer.

2.2.2 X-Ray Diffraction:

Phase purity of the powder is very important in view of the properties especially associated with the functionalities. X-ray Diffraction (XRD) is an effective tool to identify the major and minor phases in the starting material. XRD works on the fundamental principle of Braggs Law $n\lambda = 2dsin\theta$, where n = order of reflection, λ = Wavelength, d = Interplanar spacing, θ = Angle of diffraction. In this investigation, an advanced diffractometer D8 advanced system of Bruker AXS GMbH, Karlsruhe, Germany was used for recording X-ray diffraction data. Cu-Kα (λ=1.5418 A^o) radiation was used as a source and analysis is carried out by using LynxEye^{TM} silicon strip detector. The powder to be characterized is placed in a sample holder and inserted in the Bragg-Brentano diffractometer setup. The sample was scanned from angle (2θ) from 10 to 90^o. The recorded data was standardized to 100% with respect to the individual phases incorporating background correction. Phase analysis was carried out using search-match program with ICDD-PDF4+ database.

2.2.3 Specific Surface Area (SSA)

Specific surface area is the total surface area to mass of material expressed in m^2/gm and is measured based on the Brunauer-Emmett-Teller (BET) adsorption method. The assumptions of BET theory are – (a) An infinite layer of gas molecules is found on the surface of solid, (b) Negligible or nil interaction occurred among the adsorbed layers. A plot based on equation-1 is a straight line i.e., 1/ [Q (P_0/P-1)] versus P/P_0.

$$\frac{1}{\left[\vartheta\left(\left(\frac{p_0}{p}\right)-1\right)\right]} = \frac{c-1}{\vartheta_m c} * \left(\frac{p}{p_0}\right) + \left(\frac{1}{\vartheta_m c}\right) \qquad \text{----------} \rightarrow \mathbf{3}$$

Where,

p & p_0 are equilibrium and saturation pressure of adsorbates,

$\boldsymbol{\vartheta}$ is the adsorbed gas quantity

$\boldsymbol{\vartheta_m}$ is the monolayer adsorbed gas quantity and

c is the BET constant ,

$$c = exe^{((E1-EL)/(RT))}$$

Where E_1 is the heat of 1st adsorption layer, E_L is the heat of the last adsorption layer of layer of liquefaction

R is universal gas constant and

T is temperature

The powders used in the study were subjective to BET surface area measurement using BET surface area analyser (Micromeritics Instruments Corp, ASAP 2020, Norcross GA, USA). The equipment operates based on the static volumetric principle. A known dose of adsorbate (nitrogen) is consecutively added to the sample holder containing the sample which is kept at liquid nitrogen temperature (77K). The liquid nitrogen temperature is essential to facilitate the adsorption of injected gas on sample surface and resulting in the decrease of pressure gradually till an equilibrium pressure was established. Generally, the measurement is carried out by placing 0.5 gm of the powder which was degassed at a 300^{o}C to remove all adsorbed gases. BET analysis was carried out at liquid nitrogen temperature. Quantity of adsorbed nitrogen, relative pressure (P/P_0) and {1/ [ϑ (P_0/P)-1]} obtained from BET analysis data and the plot of 1/ [ϑ (P_0/P-1)] against (P/P_0). From the linear plot the y-axis intercept (I) and slope (A) are derived and ϑm was calculated using the equation 4 and 5, where C is BET constant.

$$\vartheta_m = \frac{1}{A+I} \quad \text{---------- 4}$$

And $$c = \frac{I+A}{I} \quad \text{----------5}$$

Hence total surface area (S_{total}) can be estimated by using an equation 6 and 7.

$$S_{total} = \frac{\mathbb{[}(\vartheta_m N s)}{V} \text{ -------- 6}$$

$$S_{BET} = (S_{total}/a) \text{--------- 7}$$

Where, N is Avogadro's number (6.02 x10^{23} mol^{-1}), ϑ_m is volume of adsorbed gas for monolayer, s is adsorption gas cross section (16(A^o)^2), V is molar volume of gas adsorbate and a is mass of adsorbent or solid.

2.2.4 Morphology and EDS analysis

Surface morphology and composition of the raw material under investigation was carried out by dispersing in the water medium using dispersant Darvan 821 A. The slurry was ultrasonicated for 30 minutes and the SEM studies were conducted with highly dispersed slurry followed by drying. Morphology of the powder particles observed by scanning electron microscope and chemical analysis was carried out by Energy dispersive spectroscopy (EDS).

2.3 Determination of Powder Processing Regimes

The ceramics are generally processed by compaction, viscous plastic processing (VPP) or by casting. The additives required for processing is estimated by the Critical Additive Volume Concentration (CAVC). In this process 60 gm of ceramic powder was titrated against the additive in a sigma kneader and the torque was measured using torque meter. An indigenous assembly for estimating the CAVC is shown in Fig.2.2 (a) and a typical plot of torque against the additive volume concentration is shown in Fig.2.2 (b).

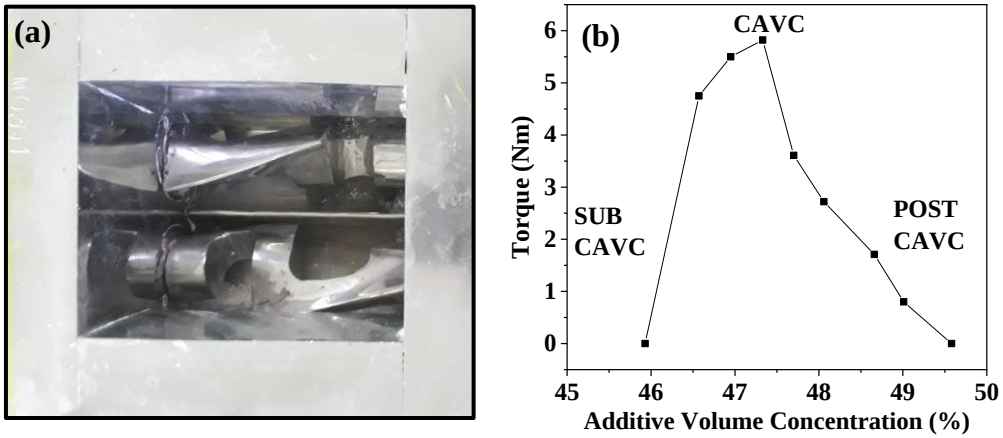

Fig.2.2 (a) Indigenous assembly for estimating CAVC and (b) Torque vs. additive volume concentration, showing the region of Sub-CAVC, CAVC, Post-CAVC

In this mixing experiment (in sigma kneader), the binder containing water was added in installments to the raw material and recorded the mixing torque by means of a specially contoured rotating blades in the sigma kneader. The volume of the additive added and the equilibrium torque value achieved after each addition was monitored and plotted. It is evident from the plot that, initially, when the additives are minimum, the additive replaces the powder-air interface forming an adsorbed monolayer of the additive on the particles as shown in Fig. 2.3

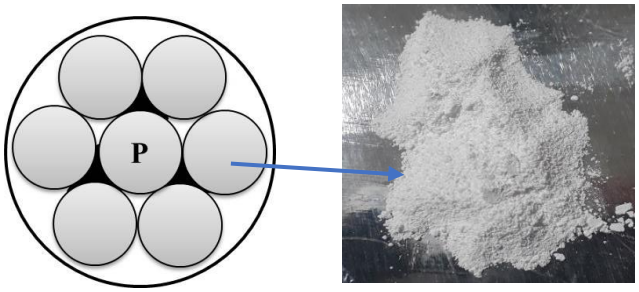

Fig.2.3 Particles with monolayer coating

As the additives are increased, the pendular bonds begin to form and bridge the particles forming clusters. On shearing and mixing continuously, it leads to a dynamic equilibrium, breaking the clusters and interlocks the particles and can be considered as compaction processing region. On further addition of binder, it gets distributed and partly fills the voids. On further shear mixing with the addition of liquid, bigger clusters form by the growth of smaller ones and ultimately the

mass becomes a coherent paste at the point of CAVC, which is the capillary state suitable for extrusion processing (VPP) as shown in Fig.2.4.

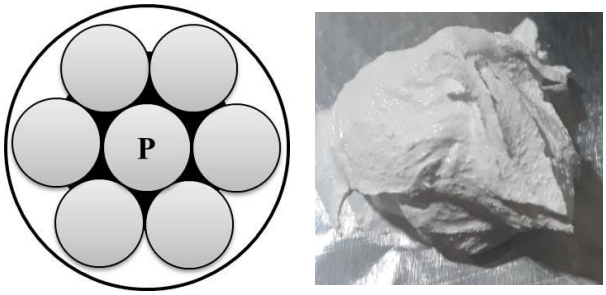

Fig. 2.4 Particles forming coherent paste

After CAVC, on further addition of liquid medium, the particle gets distanced and remains in the entrapped state. In such conditions the mixing torque will fall and homogeneous slurry formation takes place which is suitable for casting operation shown in Fig.2.5

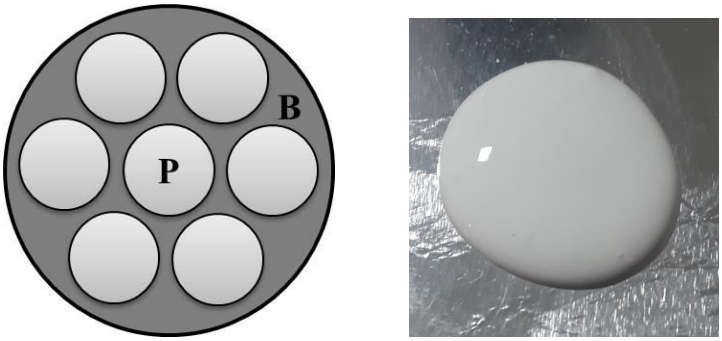

Fig 2.5 Particles forming slurry

2.4 Rheological studies

Rheology and flow behavior play a very important role in the shaping of ceramics [4]. In the current research the rheological behavior of the ceramic paste is characterized and analyzed using Anton Paar rheometer, MCR 51, Austria Preparation of ceramic paste includes mixing of ceramic powder with a binder solution and is homogenized in sigma kneader for 30-40 minutes. Later the resultant paste is placed on the parallel plate of rheometer setup and spindle attached to the rheometer is then moved downwards and placed on top of the paste. Shear rate was varied from 10 to 1000 1/s using computer control program. A typical plot of shear stress vs. shear rate and viscosity vs. shear rate is shown in Fig.2.6 (a) and (b).

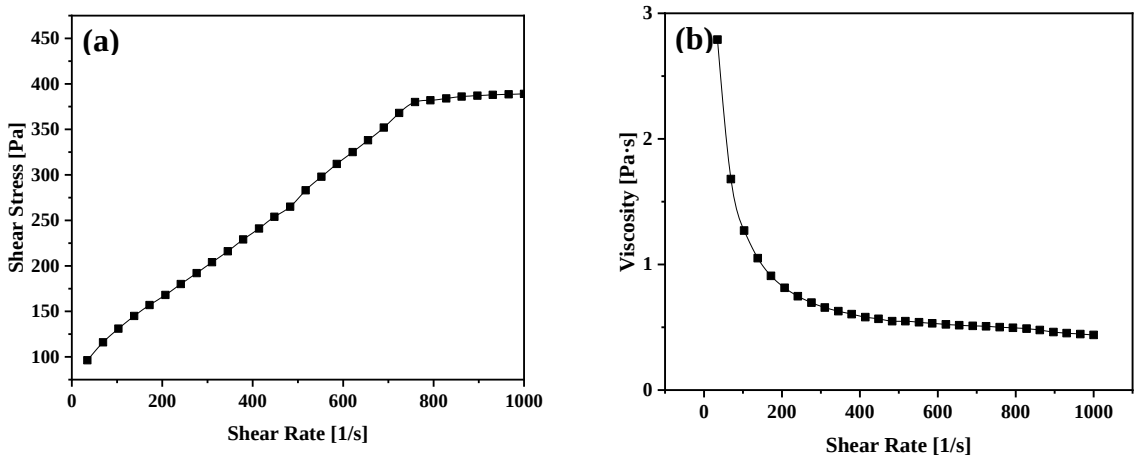

Fig. 2.6 A typical plots of (a) shear stress vs. shear rate and (b) viscosity vs shear rate

2.5 Extrusion shaping of ceramics

Extrusion is one of the ceramics forming process which is used extensively to fabricate long symmetrical structures such as tubes, bricks, pipes, honeycombs, heat exchangers, catalyst supports etc. Extrusion process involves the pressing of high viscous plastic dough which is prepared with mixing of ceramic powder with additives pressed through shaped die. Key characteristics of prepared ceramic paste are:

- The paste should be plastic and flow through the shaped die
- Ceramic paste should have sufficient rigid wet strength to resist deformation during handling
- The paste should not stick to the wall of die and must yield smooth surface after extrusion
- Ceramic powder and solvent used to prepare ceramic paste should not separate under applied pressure
- The paste should have reproducible porosity so that shrinkage of extruded sample is predicted during drying and sintering
- Ceramic paste should have low ash content to leave minimal residue.

Depending on the equipment and operation wise extrusion is two types 1. Ram type extrusion and 2. Auger type screw extrusion

2.5.1 Ram type extrusion

Ram type extruder consists of a barrel, piston, die and die fixture and generally used for batch type extrusion process is shown in Fig. 2.7. High viscous ceramic paste is filled in barrel and forced through the die which is designed and fabricated as per the required geometry to fabricate ceramic components. The paste is loaded into the barrel without air pockets usually achieved through vacuum and the piston translates the paste under pressure consolidating the paste. When the pressures reach the extrusion pressure, the paste flow through the die entry and die land of the die and shaping take place within the die assembly according to specific geometries. Further the extrudate is received on channels or specially designed fixtures and post processing will be carried out.

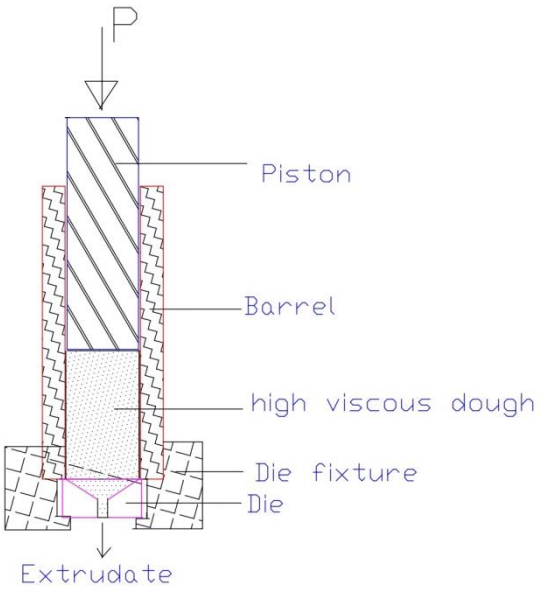

Fig 2.7 Schematic of piston type extruder [5]

2.5.2 Auger type screw extrusion

Unlike the ram type extruder, the auger type screw extruder as shown in Fig. 2.8 contains several sections which are able to produce ceramic parts continuously. It consists of feed hopper, pug mill, deairing chamber, compaction chamber and shaped die. Feed hopper is input to the material which is premix of ceramic powder with additives (binders, plasticizers, deflocculants, lubricants) and organic or inorganic solvents. Pug mill is designed with mounting of two rows of screw on auger shafts and the two auger shafts rotates in opposite direction, results a passage to material feeding from hopper. Opposite rotation of both auger shafts, screws mounted on

shafts and parameters of screw such as depth, pitch and helical angle of screw provides high shear thinning or pseudo plastic behavior to fed material by squeezing between screws. Pug mill acts as a kneading unit of premix by providing homogeneity, plasticity and removes the trapped air. Further the ceramic paste enters deairing chamber removes air present in it with help of applied vacuum and auger motion. Finally, the paste enters into compaction chamber where it pre compacts the paste to remove void space as much as possible before to the extrusion. Further this paste forced through the shaped die at high pressures. Extruded components will cut at desired length prior to the drying and subjected to sintering.

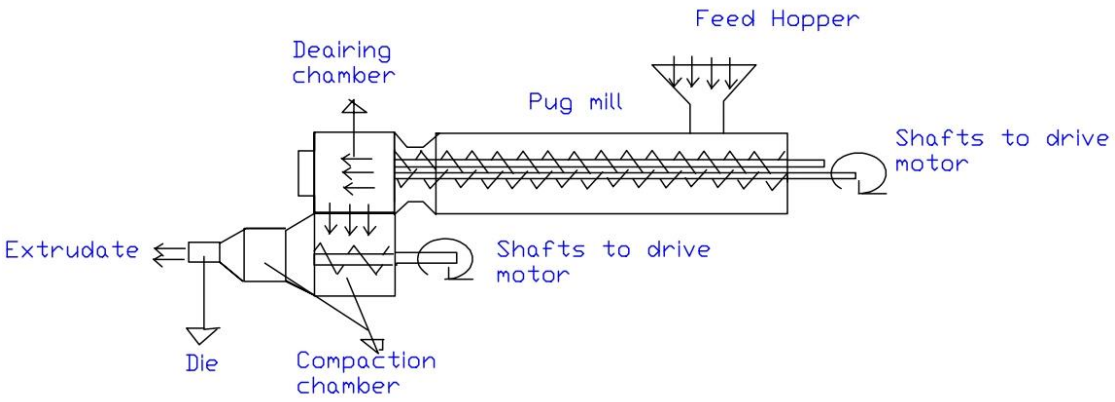

Fig 2.8 Schematic of screw type extruder [5]

2.5.3 Characterization of extrudates

Extrudates need to be inspected for their quality and defects. Common extrusion defects found in an extrusion process is distortion or warpage, laminar defects, tearing, cracking, inclusions, porosity and segregation. Warpage or distortion occurs due to the density variations or improper alignment of die. Improper alignment of die results in applying of pressure in one side of die causes more material to extrude from one side which leads to bending of extruded component. Laminar defects are in the form of orientation, which are occurring due to the incomplete knitting. Tearing contains cracks on the surface while material extruded from the extruder. These surface cracks can be extended to inside of the material due to friction and contact stresses between die wall and material. Segregation is also one of common extrusion defect which is defined as a separation of solid and liquid portions of ceramic paste during extrusion. Segregation defect leads in cracking or distortion during drying or sintering.

2.6 3D Printer at ARCI

Based on the ceramic extrusion processing expertise available at ARCI for the fabrication of ceramic honeycombs, concentric tubes etc., an FDM based 3D printing process is selected for the establishment of AM process. Accordingly, the specification was drawn and a 3D printer was fabricated by an indigenous manufacturer (3D Cerami, Trivandrum, India) of the machine. The machine designed and fabricated as per the specification is shown in Fig. 2.9.

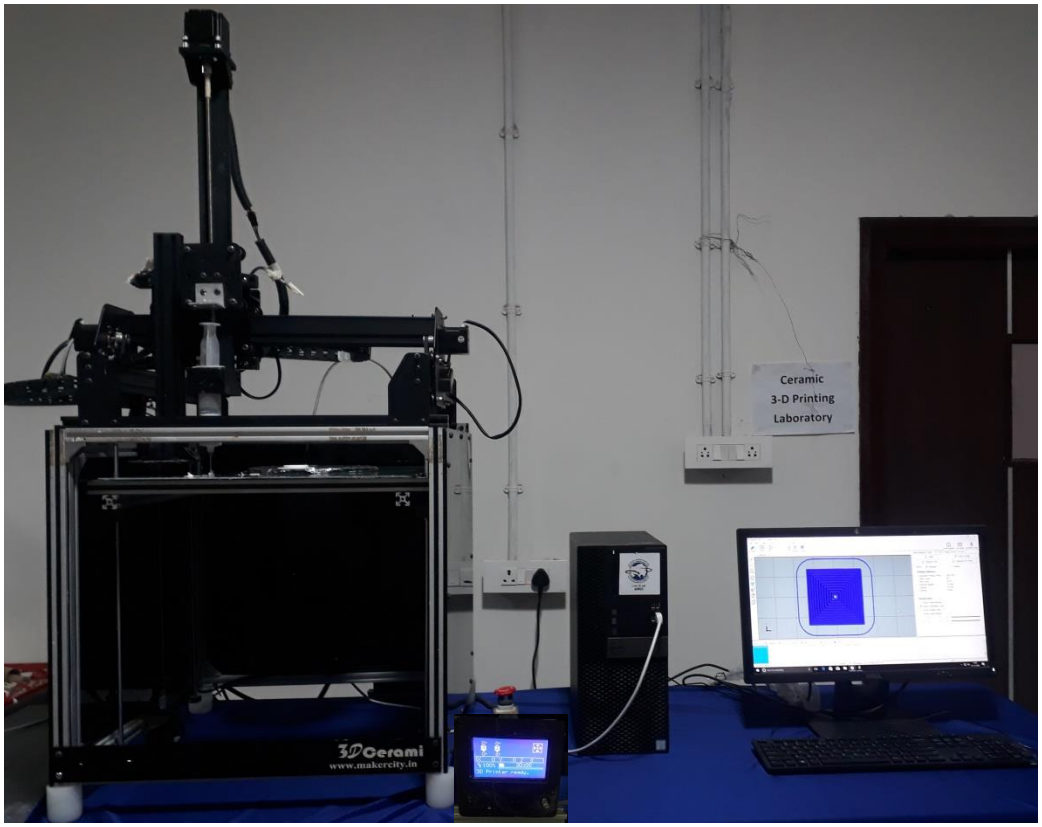

Fig 2.9 3D Printer, interface and computer installed at ARCI

As is evident from the Fig.2.9, the 3D printer system consists of stepper motor, transmission screw, plunger, barrel, barrel holder and platform as base support to print the object. The movement of every axis and rotation of transmission screw caused by stepper motor. Stepper motors are direct current (DC) electric motor, which split the number of rotations to equal number of points and moves in discrete steps. Stepper motor includes multiple coils which are arranged in groups called phases. Further with the help of the electrical connections, each phase of the stepper motor will

energize in sequence which results in the rotation of motor to one step at a time. The stepper motor is controlled by computer and one can achieve a very accurate position of the motor speed.

3D Printing system depicted in Fig 2.9 consists of 2 stepper motors for each axis responsible for the movement Y and Z and a stepper motor in combination with driver motor for X-axis. The driver motor placed at the top of the machine and rotates precisely by computer control. Stepper motor converts the electrical energy to rotational energy and transmits the required power to the transmission rod, which results in translational movement of the plunger head. Rotation of transmission screw applies pressure on the top surface of the plunger leads to forcing the plunger into the barrel to extrude the inside feedstock material through the attached nozzle on the platform. Barrel in the 3D printing system was fixed in extruder holder. The movement of X, Y, Z is done through the rack and pinion arrangement with belt and drive. Another two stepper motors are fixed at the bottom of the printer to control the movement of Z axis and its translational movement depends on the layer thickness. Two stepper motors were placed at the side of the printer to control the Y axis and one stepper motor placed at the backside of the extruder holder to translate X axis.

CAD model using CATIA software was used for designing the printing parts. The computer was installed with the Repetier Host software which is compatible to any 3D printer and user friendly. This software allows the person to operate the 3D printing machine directly from the computer which includes importing the CAD design to the software, slicing with predesigned printing parameters and giving print command to the 3D printer from the computer. Additionally, a micro controller unit is also connected to 3D printing machine, where it follows the steps as (a) importing the CAD model to repetier host software, (b) Slicing operation with the given printing conditions, (c) Generating the G-codes, (d) Saving the G-codes in data card, (e) providing in the micro controller unit and also give (f) Give the print command from microcontroller. The sequence of operation depicted in flow chart below section.

2.6.1 Design of Ram type Extruder Compatible to 3D printer

In addition to the plastic syringes provided by the machine manufacturer for carrying out the extrusion in the current study, the extrusion assembly has been designed and fabricated according to the engineering design shown in Fig. 2.10(a). A typical extruder fabricated as per the

design is shown in Fig.2.10 (b). The extrusion assembly was provided with a detachable ring at the bottom which provides the flexibility in assembling nozzles of different diameter.

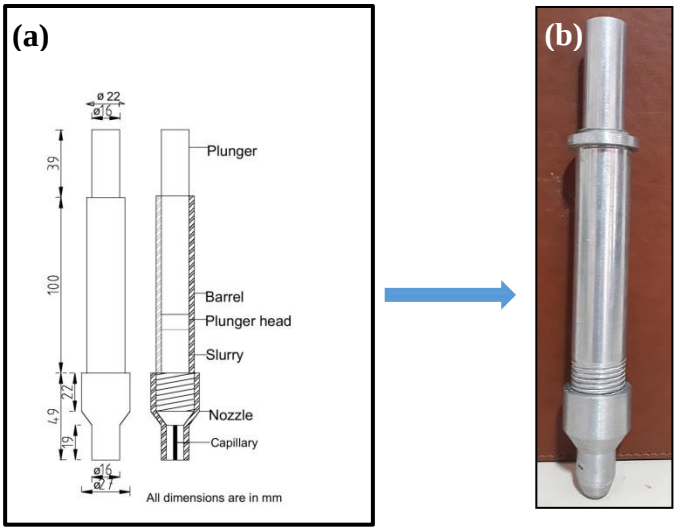

Fig 2.10 (a) Engineering drawing and (b) Fabricated piston type extruder

Designing of piston type extruder and selection of material for fabricating the extruder will play crucial role in extruding the material. Flow characteristics of ceramic feedstock are depending on the design of extruder. To prevent buildup of residue material along the wall of barrel and plunger, the clearance between barrel and plunger should be minimum. High clearance between barrel and plunger allows the material to stagnate on some areas of the walls and also it decreases the extrusion pressure which is not desirable. Hence high clearance and dead spots should be eliminated from the walls of the barrel during the manufacturing process. Hence the minimum clearance results in higher efficiencies of the flow. Surface finish of the inner wall of the barrel is important, because the wall friction between the barrel and material will affect the life of extruder. Designing of nozzle is also a key parameter during extrusion of ceramic paste. Nozzle characteristics such as diameter, length and cone angle should be optimum. Low cone angle results in high requirement of load due to frictional forces offered by the wall lead to inhomogeneous deformation. High cone angle results negligible shear on the paste. According to the printing process, the diameter of nozzle affects the time of printing as it depends on the given layer thickness for the model. The small diameter of nozzle provides a good surface finish of the printed part, although it increases the time of printing. The length to diameter (L/D) ratio of nozzle is also an important factor to decide the quality of printing. High L/D ratio of nozzles

provide additional wall shear and intermixing of paste leads to better homogeneity of the feedstock which results in higher green strength of the printed component. However, ram type extruder enables to print components with limited height due to its limited filling capacity of feedstock. Barrel with bigger size can be able to print bigger size components, which creates overload to the extruder holder, more heat and pressure to the stepper motors and it led to failure of motor due to thermal relay.

2.6.2 Design of Pneumatic Screw Type Extruder Assembly Compatible to 3D Printer

In addition to the ram type extruder a screw type extruder has also designed and fabricated and the engineering drawing of screw, nozzle and barrel is shown in Fig. 2.11 (a) (b) and (c)**.** Earlier 3D printer (described in the above section) consisting of a ram type extruder which is fixed to the frame of the axis. Since ram type extruder has limitations on quantity (batch type) of paste which is fed inside of the barrel, thus leads to print components with smaller heights. Hence screw type extruder is designed and fabricated as per the dimensions to suit the existing 3D printer for semi-continuous operation.

In screw type extrusion process the paste is fed into horizontal twin screw type of mixer and the paste is continuously fed through the hopper. The paste is kneaded thoroughly and translates into the extruder as shown in the Fig.2.12 (a). However, the current study is only aimed at the proof of concept a ram type barrel and piston assembly with higher capacity (in comparison to the ram type extruder described above) where operated with a screw type extruder the engineering drawing and schematic assembly is shown in Fig. 2.12 (a) and (b) respectively. 3D printer consists of an extruder assembly and barrel with plunger. Extruder assembly further contains stepper motor attached with screw by coupler motor, casing cover, inlet for the material and nozzle. Barrel is used to load with ceramic paste which is forced by the plunger with the help of the compressed air. Compressed air supplied from the air compressor. Compressed air forces the filled stock material into the screw chamber. The screw is fixed to the stepper motor through a coupler. Stepper motor rotates the screw very accurately. Rotation of screw decides the direction of paste flow, such as rotation of screw in anticlockwise direction leads to downward flow of material through the nozzle and upward flow caused by the clockwise rotation of the screw.

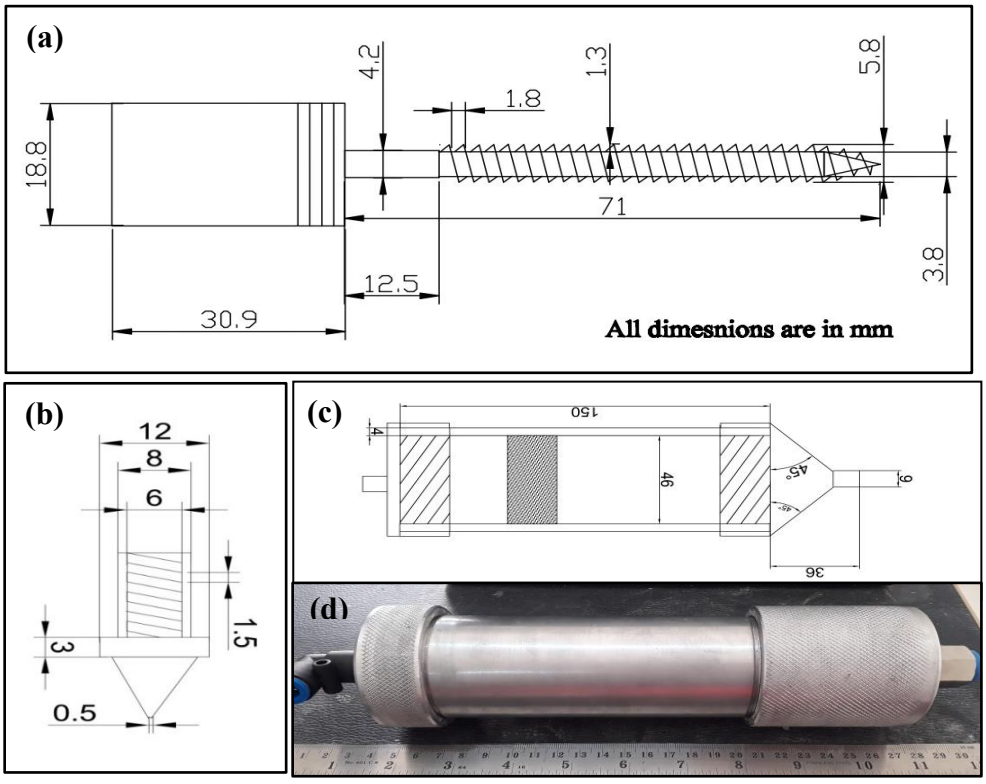

Fig. 2.11 Engineering drawing of (a) screw, (b) nozzle, (c) barrel and (d) fabricated barrel

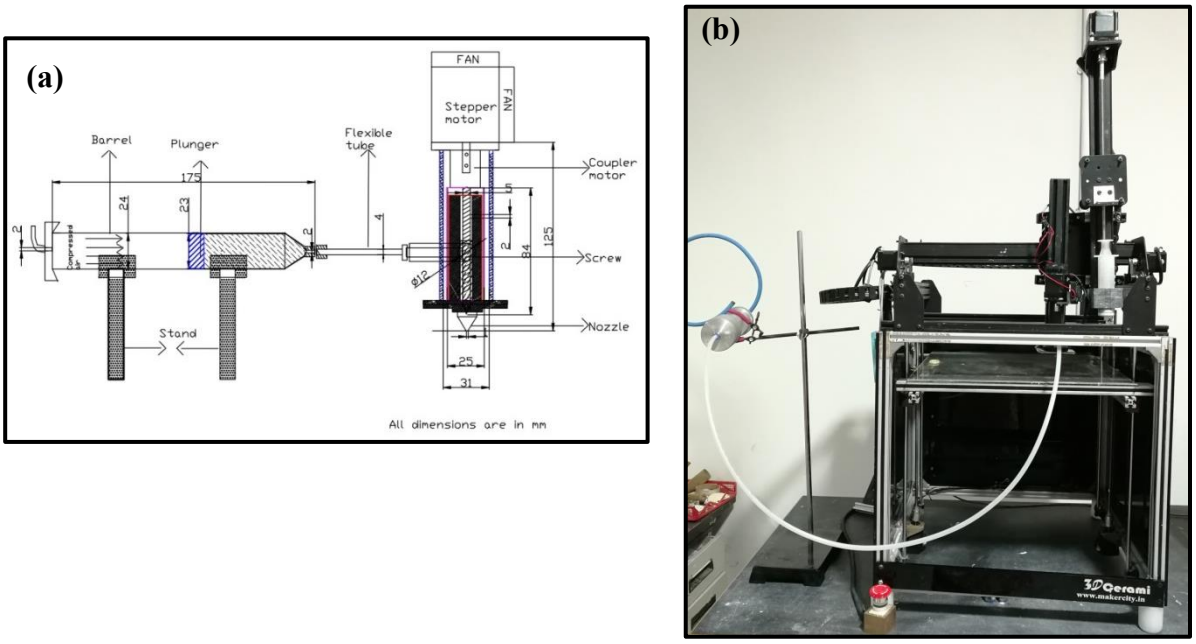

Fig. 2.12 (a) Cross-section view and (b) Pneumatic screw type extruder assembly integrated to 3D Printer

2.6.3 Extrusion Printing Process Development and Optimization

The standard operating procedure for printing of parts in the current study is detailed in the flowchart depicted in Fig.2.13.

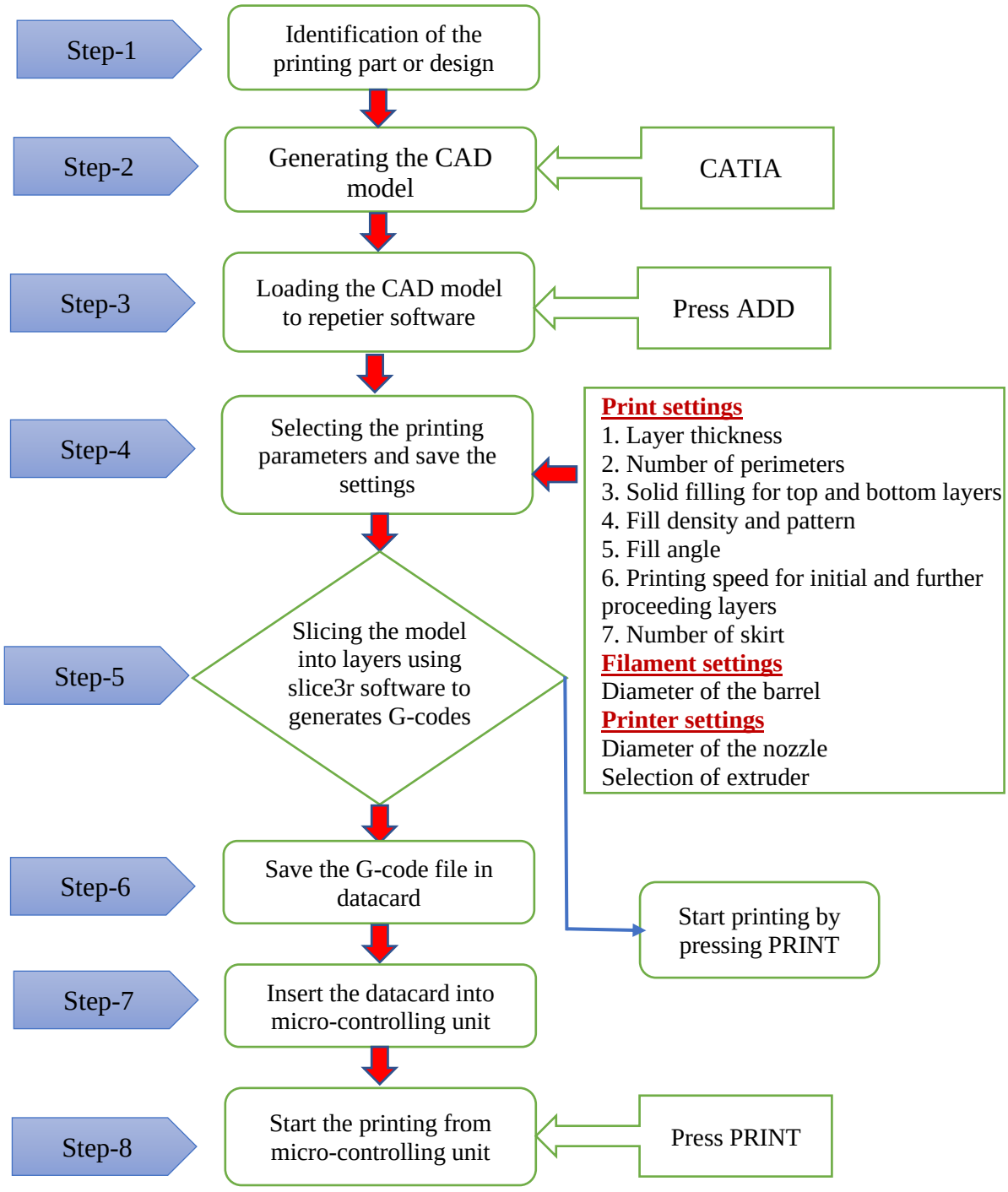

Fig. 2.13 Flow chart of 3D Printing process

2.6.4 3D printing of ceramic parts

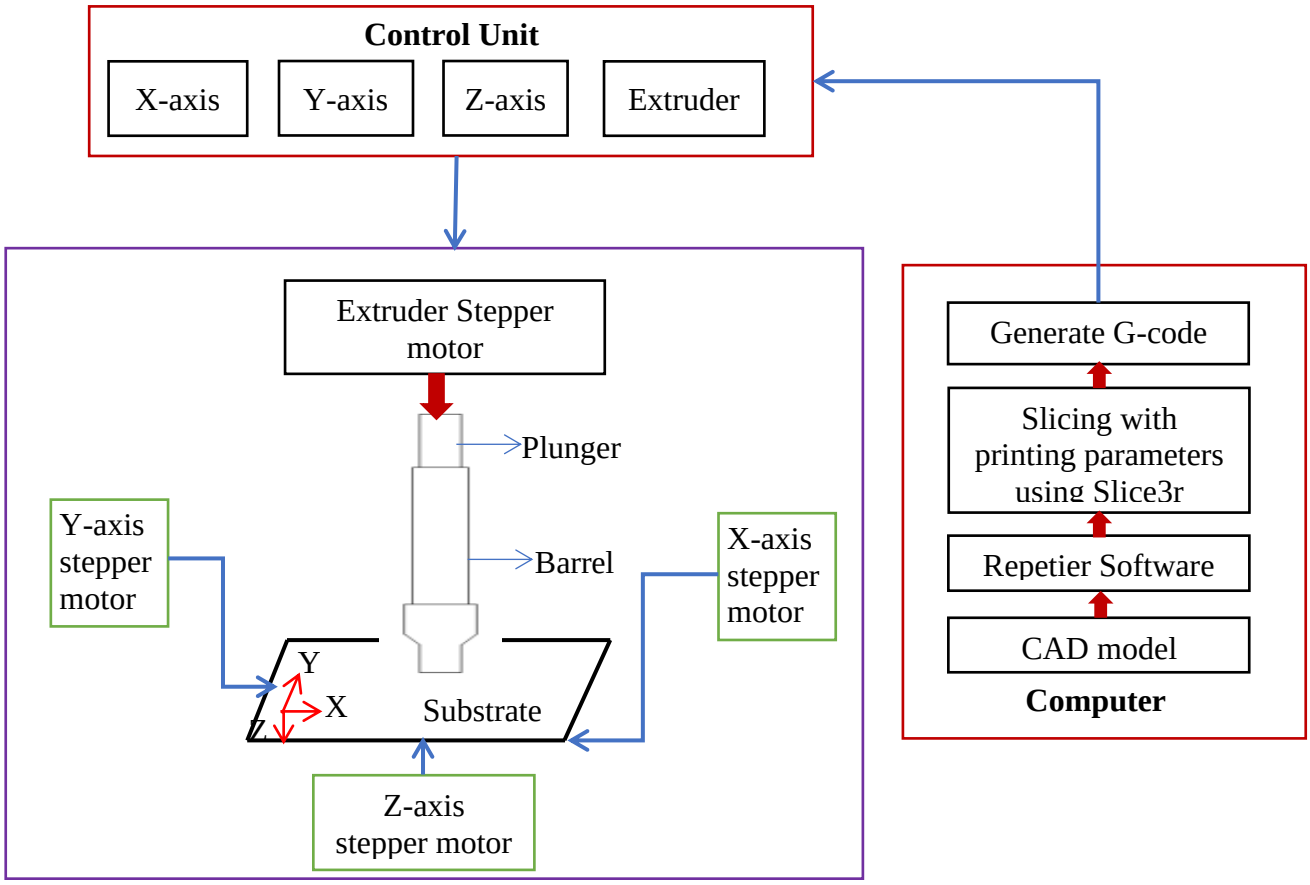

Fig. 2.14 Block diagram of the ram extrusion-based 3D Printing process

The block diagram of 3D printer used in the present study is shown in Fig. 2.14. The printer is provided with a ram type extruder with a cylinder and piston fitted with an interchangeable nozzle. 3D printing process involves the flow of the paste through a barrel which stores the mix, a cone at the end channelizes the flow of paste into a nozzle of the diameter typically 22 times smaller than the diameter of the barrel. During this process the paste is compressed within the barrel which peaks up a load to overcome the initial resistance and started flow as extrudate through the nozzle and printing occurs at the preset control printing parameters.

2.6.5 Optimization of Printing Parameters

Printing parameters play a major role in determining the quality and the properties of the printed parts. The list of printing parameters optimized under the study is as follows.

1. Self-standing distance

2. Surface properties of substrate on which the printed parts are received
3. Length to diameter (L/D) ratio of the nozzle
4. Printing speed
5. Filling pattern
6. Filling angle

2.6.5.1 Effect of Self standing distance on flow of paste

Self-standing distance is a vertical distance between the nozzle and substrate as shown in Fig.2.15. To study the effect of self-standing distance on printing process and quality of the samples, the self-standing distance was varied from 0.5 to 1.5mm

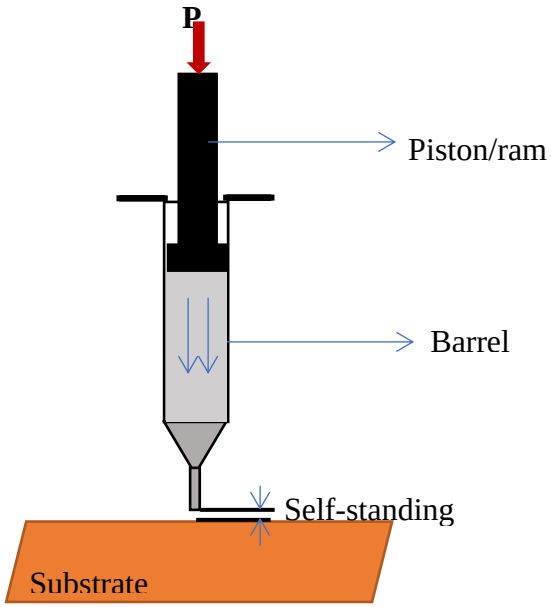

Fig.2.15 Schematic illustration of self-standing distance of extrudate

To study the effect of self-standing distance on quality of the printed part, the following printing conditions were maintained as constant,

1. Layer thickness= 1mm,
2. Printing speed for 1st layer: 4mm/s and 2nd to last layer: 6mm/s
3. Flow rate: 4mm/s for 1st layer and 2nd to last layer :6mm/s
4. Filling pattern = concentric
5. Fill direction =90^{o}
6. Nozzle diameter = 1mm were selected.

Experiment-1: Self-standing distance = 0.5mm

For this, the self-standing distance was set to be 0.5 mm but layer thickness of extrudate is 1mm. The gap between the nozzle tip and substrate is lower than the layer thickness. For the given preset printing conditions the flow of the extrudate was smeared through the nozzle path due to compressive forces exhibited by substrate. Because of the smearing, the layer width was uneven than predesigned layer thickness. Further the extrudate paste blocking the nozzle holes partially and often resulted in blocking of the nozzle opening. The printed part obtained under the experiment is shown in Fig.2.16

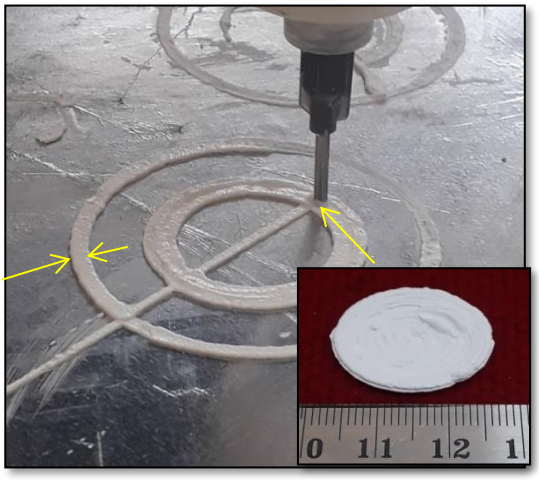

Fig. 2.16 printing of extrudate with self-standing distance 0.5mm

Experiment-2: Self-standing distance =0.75mm:

In this experiment the self-standing is set as 0.75mm (self-standing distance lower than the nozzle diameter) to evaluate the effect of printing of extrudate maintaining all other parameters identical. Similar printing behavior was observed as in Case 1. Though it is close to the layer thickness, the smearing of the layer occurred throughout the nozzle path, however the smearing less than in experiment-1 and represented in Fig.2.17.

Fig. 2.17 Printing of extrudate with self-standing distance 0.75mm

Experiment-3: Self-standing distance = 1 mm

The self-standing distance was kept as 1mm which is equal to the nozzle diameter. In this case the flow of the extrudate was continuous and it is following the nozzle path thus leads to get printed part with in tolerances of the pre-designed CAD model. Fig. 2.18 represents the printing of extrudate with self-standing distance 1.00 mm.

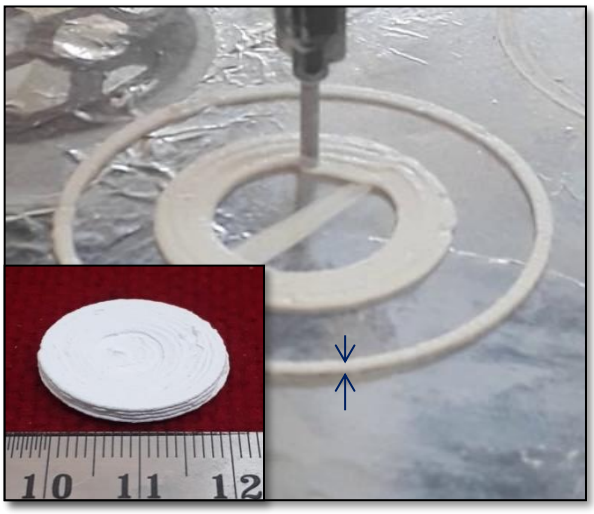

Fig. 2.18 Printing of extrudate with self-standing distance 1.00 mm

Experiment-4. Self-standing distance 1.5mm:

The self-standing distance is higher than the nozzle diameter, but there was no obstruction for the flow of paste to form the extrudate. The printed parts are found to be according to the pre-

designed and simultaneously maintaining the designed tolerances of the part printed as shown in the Fig.2.19.

Fig. 2.19. Printing of extrudate with self-standing distance 1.50 mm

Experiment-5 Self standing distance = 2mm:

In this case given self-standing distance was high between nozzle tip and substrate than the nozzle diameter. Though the flow of paste is continuous but it is not following the path of nozzle predesigned through CAD model. This can be attributed to the overhanging of the paste in combination with more exposure to the atmosphere leading to skin hardening as a result of preferential drying. A typical printing process at self-standing distance of 2mm is shown in Fig. 2.20.

Fig. 2.20. Printing of extrudate with self-standing distance 2.0 mm

A summary (dimensional tolerances to the self-standing distance) of the effect of self-standing distance on the printing of extrudate is represented in Fig. 2.21. A distance of 0.5 and 0.75 mm, less than the nozzle diameter the surface of the extrudate layer was smeared and part was printed out of the tolerance. When the self-standing distances is increased to 1 mm and 1.5 mm printed, extrudate is found to maintain the designed layer thickness and the printed parts were well within the tolerance limit. Further, a self-standing distance beyond 1.5 mm, the extrudate was overhanging and deviated from the designed print path with discontinuities throughout the printed parts.

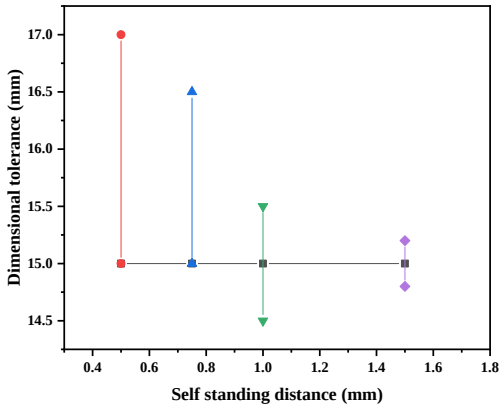

Fig. 2.21 Self-standing distance versus dimensional tolerances

Though the self-standing distance is a function of the material chemistry and the rheology of the paste the present study provides an outline of the 3D printing process.

2.6.5.2 Effect of L/D ratio of the Nozzle on Printed Samples

The nozzle with constant diameter of 1 mm and various lengths of 10, 15 and 25 mm were fabricated to study the effect of L/D ratio of the nozzle on the printed samples. The printed samples with identical rheology printed through the nozzle with L/D ratios of 10, 15 and 25 and the green density are correlated. A plot of green density versus L/D ratio of the nozzle is shown in Fig. 2.22. Length to diameter ratio (L/D ratio) of 10 and 15 have shown an identical green density of 2.10 g/cc however, the green density have shown a marginal increase to 2.14 g/cc at an L/D ratio of 25. The relatively high-density values can be attributed to the additional wall shear and intermixing of the paste due to the increased length of the nozzle leading to a better homogeneity of the paste.

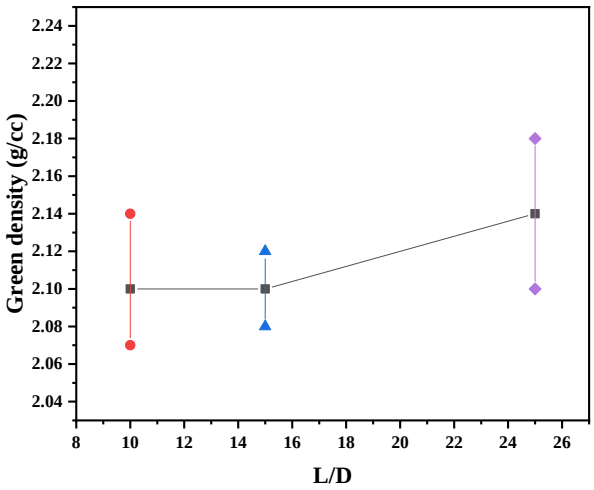

Fig. 2.22 Plot of green density versus L/D ratio of alumina samples

2.6.5.3 Effect of Printing Speed and Flow rate:

Printing speed can be defined as a speed of X, Y and Z axes. Flow rate is the delivery of material through the nozzle with respect to time. Printing speed and flow rate are dependent on each other. If the printing speed increases the flow rate will also increase. Hence, a good control on printing speed will results in improvement of material flow, which further leads to get a defect free printed part with in the dimensional tolerances. So, to optimize the Printing speed, the layer thickness is kept constant for first layer and further printing layers, and fill pattern and infill density have preset to perimeter and 100% respectively

The selection of low printing speed for 1st layer and enhanced speed for further printed layers will provide a homogeneous flow of material along the nozzle for the first layer. If the discontinuity is generated in the first layer due to the enhanced speed the defects will be generated in the subsequent layers resulting from improper support. A typical sample printed with printing speed of 4-6 mm/s and beyond 6 mm/s is shown in Fig. 2.23 (a) and (b).

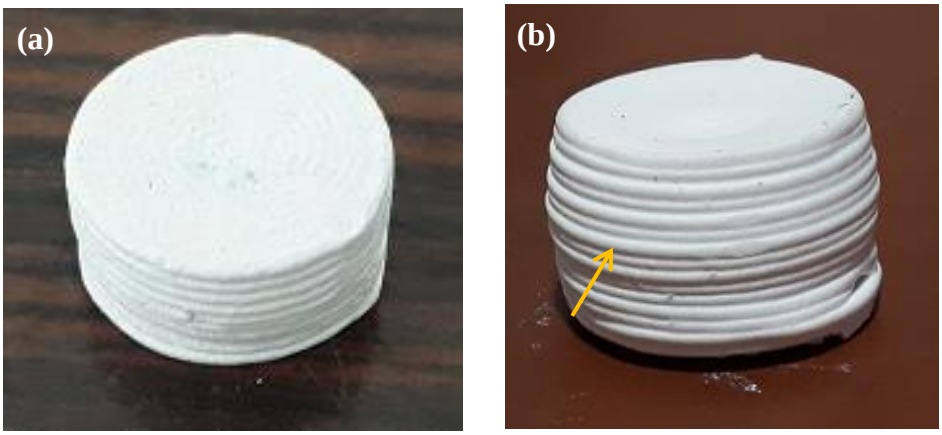

Fig: 2.23 3D printed samples (a) Printing speed at between 4-6mm/s (b) printing speed beyond 6mm/s

Printing speed less than 4mm/s results in extended duration of printing, which further leads to the loss of moisture within the layers and results in inhomogeneity. Printing speed beyond 6mm/s resulted in overflow of the paste leading to deformations beyond the tolerance specified.

2.6.5.4 Effect of filling pattern and filling angle

To study the effect of filling pattern and filling angle, the samples were printed with concentric, rectilinear, and aligned rectilinear pattern along with fill density of 100% (i.e., it will fill the whole area of given part). Here fill pattern give the flexibility to make solid body according to the selection by arranging the layers in different manner.

The filling pattern such as rectilinear, concentric and aligned rectilinear are experimented in the current study and the typical filling patterns are shown in Fig. 2.24 (a), (b) and (c). Based on the optimized printing conditions obtained from the previous experiments, the layer thickness of 1mm, printing speed of 4-6mm/s and self-standing distance of 1mm was selected to print the cylindrical samples with concentric, rectilinear and aligned rectilinear patterns. It is evident from Table.3 that the duration of printing as well as the green density of the printed samples is similar and no significant or minimum effect on printed samples. Experiments were also conducted to study the effect of filling angle for the rectilinear filling pattern and the angle was varied from 30-90°. A schematic of the filling angle used for printing of specimens is schematically shown in Fig.

2.25. Green density of the alumina samples is shown in Table 2.2 signifying minimum effect on density values

Table. 2.2 Properties of printed samples with rectilinear pattern with different filling angles

Properties	Filling pattern			Filling angle (Rectilinear)			
	Rectilinear	Concentric	Aligned rectilinear	30º	45º	60º	90º
Green density (g/cc)	2.01	2.04	2.08	2.03	2.02	2.03	2.00

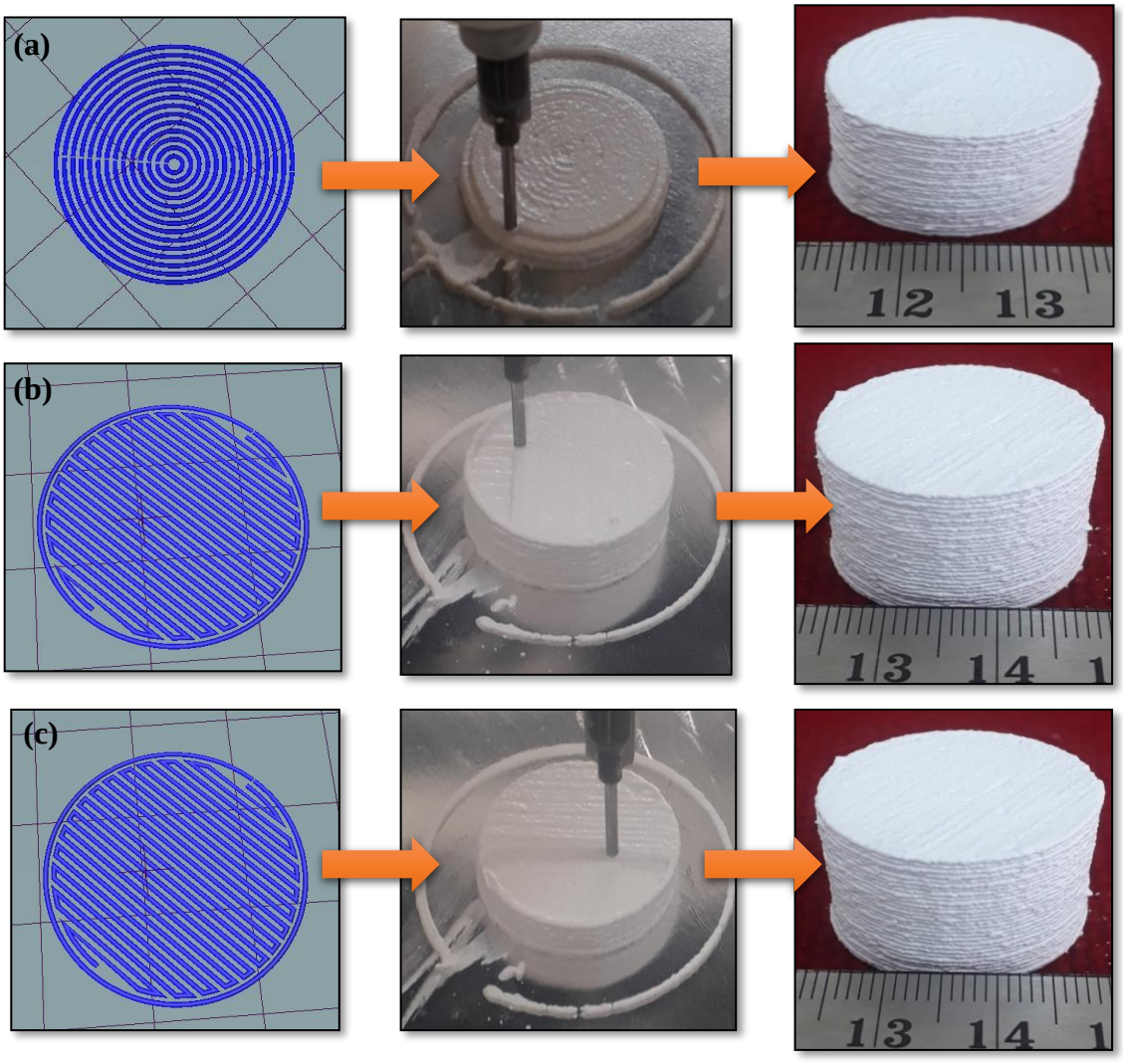

Fig.2.24 Fill patterns of (a) concentric, (b) rectilinear and (c) aligned rectilinear along with the sample during printing and green condition

Fig. 2.25 Schematic of filling angle of rectilinear patterns

2.6.5.5 Effect of substrates on the printed part tolerance:

To study the effect of receiving substrate on the printed part tolerances, three substrates namely glass plate, aluminum foil and plaster of paris were employed. After printing the samples on each substrate, the samples were examined for predesigned tolerances.

Fig. 2.26(a) shows sample printed on glass plate. Glass plate being chemically inert and smooth, the printed first layer could not adhere properly displacing further layers leading to deformation. A typical deformation from the predesigned parameters is shown in the figure along with the printed sample.

Fig.2.26 (b) shows sample printed on aluminum foil. It is evident that the printed samples have exhibited close tolerance with respect to the predesigned parameters. This can be attributed to the chemical interaction between the methylcellulose with the nascent aluminum foil surface leading to adhesion and providing strong base to the further printed layers.

Fig. 2.26(c) shows the sample printed on Plaster of Paris (POP) block. The POP being highly porous, the printed layers though adhere initially, due to the capillary action the moisture dries up fast from the first printed layer leading to further deformation. Additionally, the differential drying with in the sample and separation of the layers is also evident from the sample as shown in Figure.

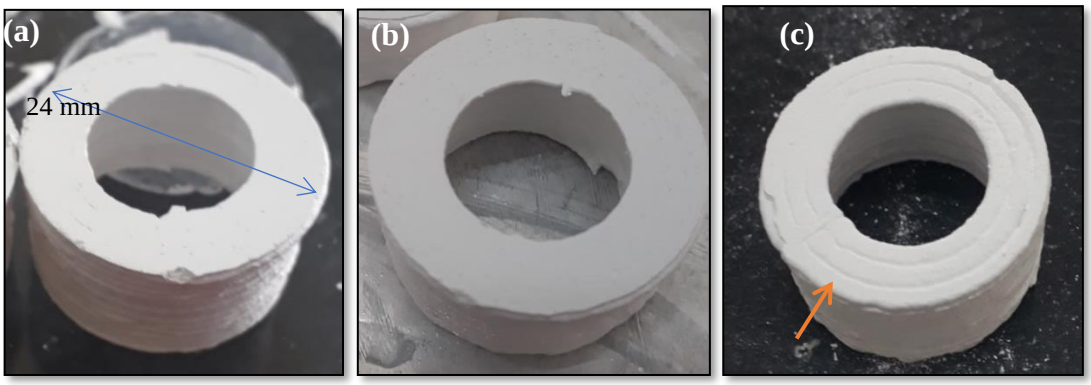

Fig.2.26 Samples printed on (a) Glass plate (b) Aluminum foil and (c) POP surface

Table: 2.3 Optimum parameters for 3D printing alumina parts based on the above experiments

S. No	Parameters	Optimum values
1	Printing Speed (mm/s)	4-6
2	L/D ratio	25
3	Self-standing distance (mm)	1.25±0.25
4	Filling angle (^{o})	90
5	Filling pattern	Rectilinear
6	Substrate	Aluminum foil

Based on the above experiments the optimum parameters are found to be as tabulated in Table 2.3 for alumina paste. However, printing parameters cannot be generalized with respect to composition and geometries of the printed parts.

2.7 Characterization of printed part

All printed samples after drying were subjected to visual inspection using magnifying glass, dimensional measurement using metrological measurements (vernier calipers) and green density measurement through dimensional method. An electronic balance was used for the accurate weighing and green density of the sample was estimated using mass/volume. Fig. 2.27 represents the flow chart of post processing and quality control of printed parts.

Post processing and quality control of printed parts:

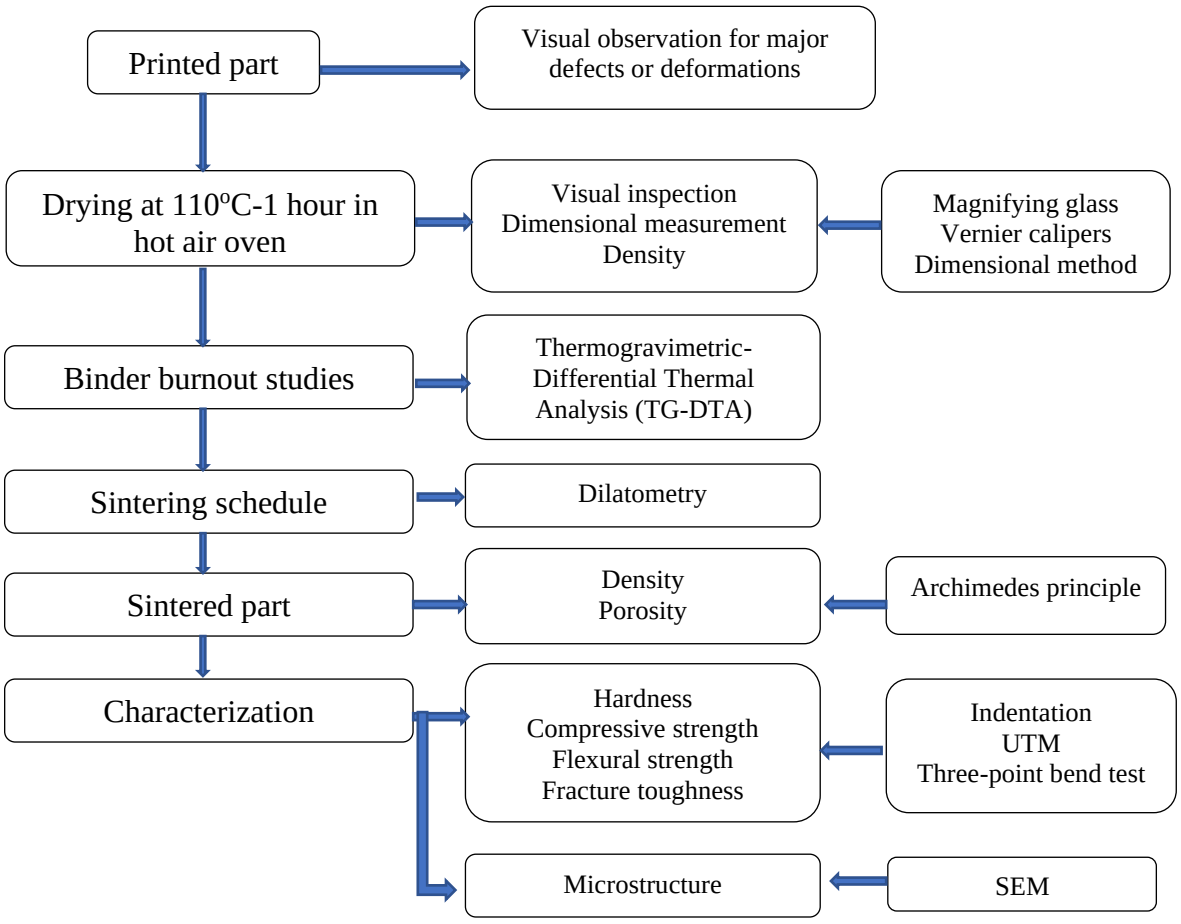

Fig.2.27 Flow chart for post processing and quality control of printed parts

2.7.1 Binder Removal and Sintering

2.7.1.1 Simultaneous (Thermogravimetry- Differential Thermal (TG-DTA)) Analysis

Thermogravimetry (TG) in combination with Differential thermal analysis (DTA) is used for the organic burnout and identification of associated thermal (endo and exothermic) events. The sample is subjected to heating as per the predesigned heating schedule and the weight of the sample is determined by the analytical balance. Thermocouples placed on the crucible measures the temperature changes and recorded as exo and endo with respect to the base line. A simultaneous thermal analyzer (STA 449 F3, Netzsch, Germany) used for the typical TG-DTA curve which is recorded for a green 3D printed part is shown in Fig. 2.28

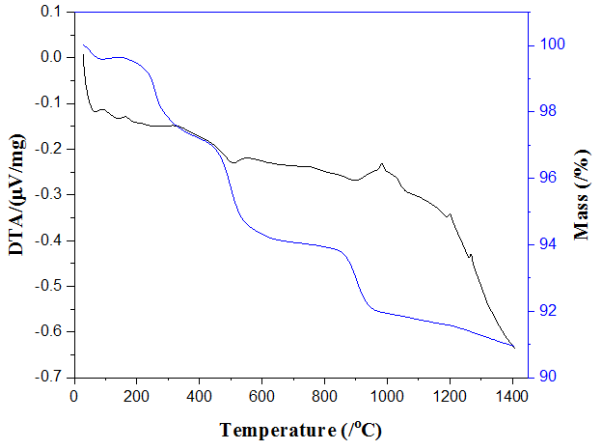

Fig.2.28 A typical TG-DTA plot of 3D printed green sample

2.7.1.2 Dilatometer

Dilatometry determines linear variation in the dimensions of the sample while the sample is subjected to a programmed temperature schedule. A push rod-based dilatometer [6] with linear variable displacement transducer (LVDT) has been used for monitoring the shrinkage pattern of the printed samples. Based on the dilatometric plots L/L_0 versus temperature, the sintering schedule/ sintering mechanisms are evolved. A dilatometer (NETZSCH, DIL 402 C) has been used for the analysis and typical plot of L/L_0 versus temperature for green 3D printed sample is shown in Fig.2.29

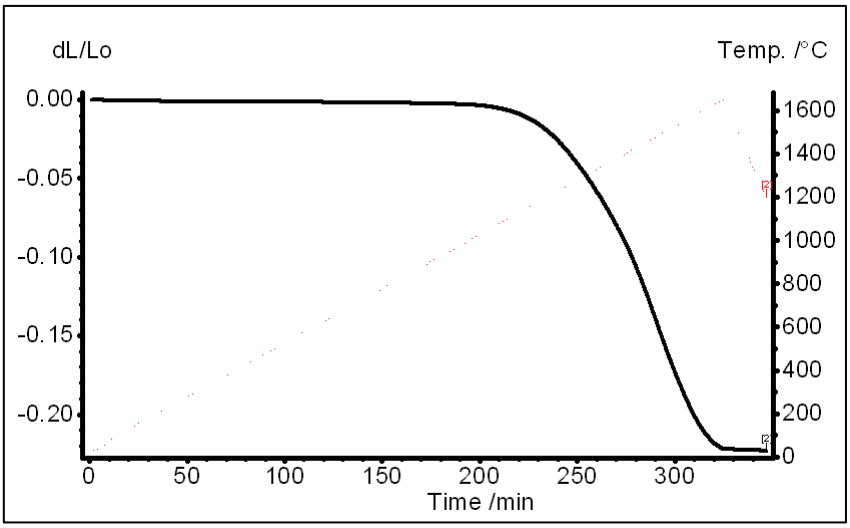

Fig.2.29 A typical plot of L/L_0 vs time and temperature vs time

2.8 Characterization of Sintered Part

Based on the data of thermogravimetric-differential thermal analysis (TG-DTA) and dilatometer of the 3D printed green samples, a sintering schedule was evolved and subjected to sintering in a muffle furnace. The sintered specimens were further characterized for the physico-chemical, thermal and mechanical properties and the details as shown in Table 2.4.

Table.2.4 Characterization techniques of sintered 3D printed parts

S. No	Property	Characterization technique	ASTM Standard
1	Sintered Density	Archimedes principle	ASTM 792
2	Compressive strength	Universal Testing Machine (UTM)	ASTM C1424 [7-8]
3	Hardness	Vickers Hardness test	ASTM C1327 [9-10]
4	Flexural strength	Three-point bend test	ASTM C1161 [11-12]
5	Fracture toughness	Three-point bend test	ASTM C1421 [13-14]
6	Microstructure	Scanning Electron Microscope (SEM)	
7	Fractography	Scanning Electron Microscope (SEM)	

2.8.1 Sintered Density

After sintering the samples are subjected to measure the sintered density by using Archimedes principle (ASTM 792). The principle which states about the upward buoyant force exerted on a center of mass of the body, whether it is fully or partially immersed in fluid or liquid, it is equal to the fluid mass that is displaced by the body. The sintered density of the ceramic samples is determined by taking dry weight, saturated and suspended weight of the ceramic specimen. Ceramic samples have porosity which is caused during processing stage. Due to porosity, ceramic samples will undergo for boiling process in which samples are immersed in deionized water for 30 minutes after taking dry weight of them.

The density of sintered samples is determined by using the formula (equation 8)

$$\rho = \left(\frac{Wd}{Wst - Wss}\right) * Density\ of\ liquid\ or\ fluid \text{ -------8}$$

Where W_d - dry weight of the sample in air

W_{st} – Saturated weight of the sample

W_{ss} – Suspended weight of the sample

Sintered samples were subjected to the above procedure for determining the density.

2.8.2 Compressive Strength Measurement

As per the ASTM C 1424 standards, the samples were printed to cylindrical (Diameter=15mm, height=15mm) or cuboid (15mm x 15mm x 15mm) geometry and subjected to compression test using Universal Testing Machine (UTM). A ram rate of 0.5mm/min is used for loading the samples. A typical compressive load versus compressive extension curve recorded using UTM (Instron 8854, UK) is shown in Fig 2.30.

$$\sigma = \left(\frac{F}{A}\right) \qquad \text{---------- 9}$$

Where σ is the Compressive strength

F is Uniaxial load applied on surfaces and

A is Surface area

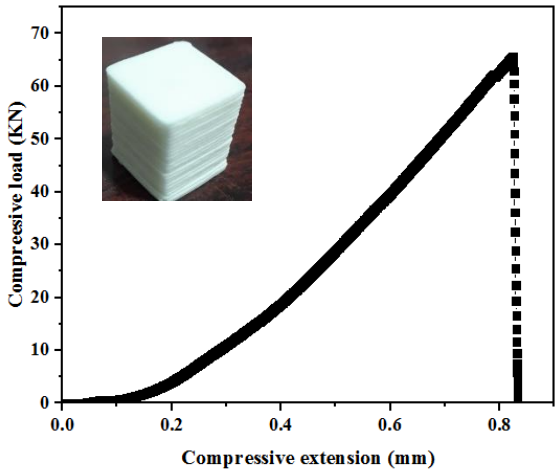

Fig. 2.30 A typical compressive load vs compressive extension curve of 3D printed sintered sample

2.8.3 Hardness Measurement

As per the ASTM C-1327, the hardness of the 3D printed sintered sample was measured by Vickers indentation. A Vickers hardness tester (Leco, St. Joseph, MI) was used for the hardness determination. The sintered samples were grounded and polished as per ceramographic procedure using variable speed grinder-polisher (BUEHLER, Ecomet 4, USA). The polished sample was positioned and focused using microscope which is connected to the Vickers hardness tester. During the test a 500 gm load was selected and applied on a polished surface of the sample for a dwell

time of 15 sec. After the dwell time indenter goes to its home position by leaving impression of indenter on surface of the sample. A typical impression of the Vickers indenter captured during the hardness test is represented in Fig. 2.31. The diagonals of the indent impression were measured by optical microscope and calculated the hardness value using equation 10.

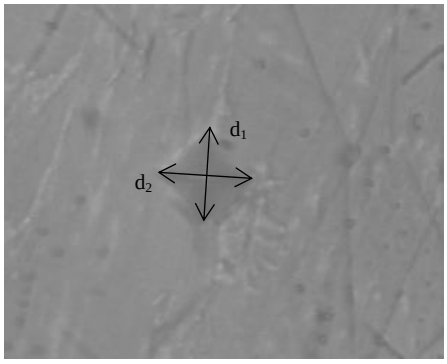

Fig 2.31 Impression of the Vickers indenter recorded during the hardness measurement

$$HV = \left(\frac{F}{A}\right) = \left(\frac{1.8544F}{d^2}\right) \qquad \text{---------- 10}$$

Where HV is the Vickers hardness value in kgf/mm^2

F is applied load (kg)

D is length of the impression diagonally in mm

2.8.4 Flexural Strength

According to ASTM C-1161, the flexural strength of 3D printed ceramic samples was measured by three-point bend test using Universal Testing Machine (UTM) (5584, Instron, UK). To measure flexural strength of 3D printed parts, a bar sample (60x40x30 mm^3) was printed and sintered. Further, the sample was cut into 45 mm x 4 mm x 3 mm using isomet cutter as per the ASTM specifications and subjected to the flexural strength measurement. These rectangular samples were placed on the two supporting pins of the three-point bend test fixture fixed in the UTM. A load was applied on the middle of the sample length with a ramp rate of 0.5mm/min and the load versus displacement curve was recorded. When the load applied on rectangular specimen increases, the specimen tends to bend and fracture as the load attains the fracture strength of the sample. For a rectangular specimen, the stress under axial force is calculated using formula (equation 12).

$$\sigma = \frac{3FL}{2bd^2} \qquad \text{----------12}$$

Where F is the axial load at the fracture point (N)

L is length of the specimen (mm)

B is the width of specimen (mm)

d is the depth of specimen (mm) and

σ is flexural strength (MPa)

The schematic illustration of the Three-point bend test is represented in Fig 2.32(a) and typical Flexural stress vs flexural strain curve recorded for the ceramic specimen is shown in Fig. 2.32(b)

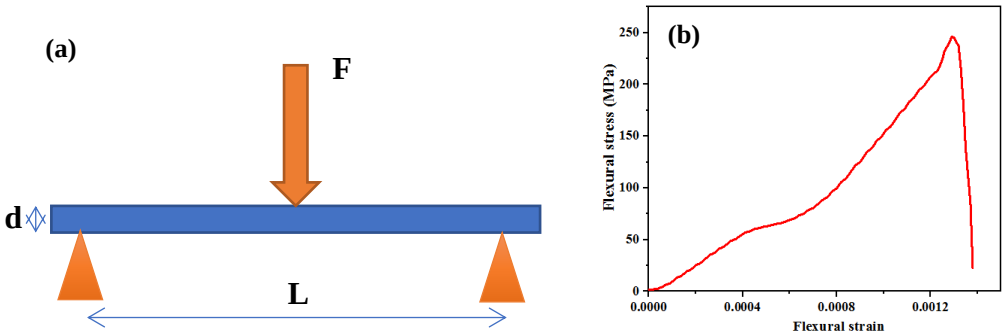

Fig. 2.32(a) Schematic illustration of three-point bend test and (b) plot of Flexural stress vs Flexural strain

2.8.5 Fracture Toughness

As per the ASTM C-1421-18, the fracture toughness of 3D printed sintered samples measured by three-point bend test by applying mode-1(K_{IC}) equation [15]. For experiment a v-notched rectangular specimen is used and these notches were created by standard wafer blade fitted on a low-speed isomet cutter. According to standard procedure ASTM C 1421-18, the specimen is sized to 45mm X 4mm X 3mm of length, breadth and height respectively. Prior to the testing, a V-notch will be created which is a 35-55% of breadth of sample. The specimen will be placed on the three-point bend fixture and very low load rate applied on specimen through load pin at ambient conditions. Deflection of the sample is recorded with respect to load and K_{IC} is calculated by using following formula (equation 13).

$$\mathbf{K_{IC} = Y\sigma c/ (\pi a)^{½}} \text{ ---------- } \mathbf{13}$$

Where

$Y = 1.93\text{-}3.07(a/w) + 13.66(a/w)^2\text{-}23.98(a/w)^3+25.22(a/w)^4$

K_{IC} – stress-intensity factor, measured in MPa.m½

σ_C– the critical stress applied to the specimen

a – the crack length for edge crack or half crack length for internal crack

Y – geometry factor

2.8.6 Fractography

The fractured samples obtained from the flexural strength test/ fracture toughness test the sample was subjected to fracture surface analysis using Field Emission Scanning Electron Microscope (FESEM) (Gemini 500, Carl Zeiss, Germany). To analyze the fractography, the fracture surface of the sample was sputtered for 60 sec with the current of 10mA using Ion sputtering device (JEOL, JFC-1100E) to provide conductivity of electrons during the FESEM analysis. Further the sample was loaded in FESEM chamber; a focused beam of electrons scans the surface of small area and capture the surface. The images and information obtained from the SEM micrographs of the fracture surface is known as fractographs. These fractographs provides the information about the propagation of crack and different fracture mechanisms associated with it [16-18].

2.8.7 Microstructure

The 3D printed sintered parts were characterized for microstructure by Field Emission Scanning Electron Microscope (FESEM) (Gemini 500, Carl Zeiss, Germany). A sintered 3D printed specimen was cold mounted in mounting cups having a diameter of 25 to 30mm by pouring thermosetting solid and resins and dried for 30 minutes at room temperature. Mounting process enables to hold the specimen tightly during the grinding and polishing process. After removing the sample from the mounting cups, the samples were grounded and polished using standard ceramography practices [19-24]. After ensuring that the sample does not consists any visible scratches or polishing defects, the sample was thermally etched in a furnace at a temperature of 100-150^{o}C less than the sintering temperature. The etched sample further subjected to sputtering for 60 seconds and characterized for the microstructure analysis using FESEM.

2.9 Summary and Conclusion

Based on the experiment methodologies for extrusion 3D printing process a flow chart of the process, quality control and respective techniques are summarized in Fig.2.33.

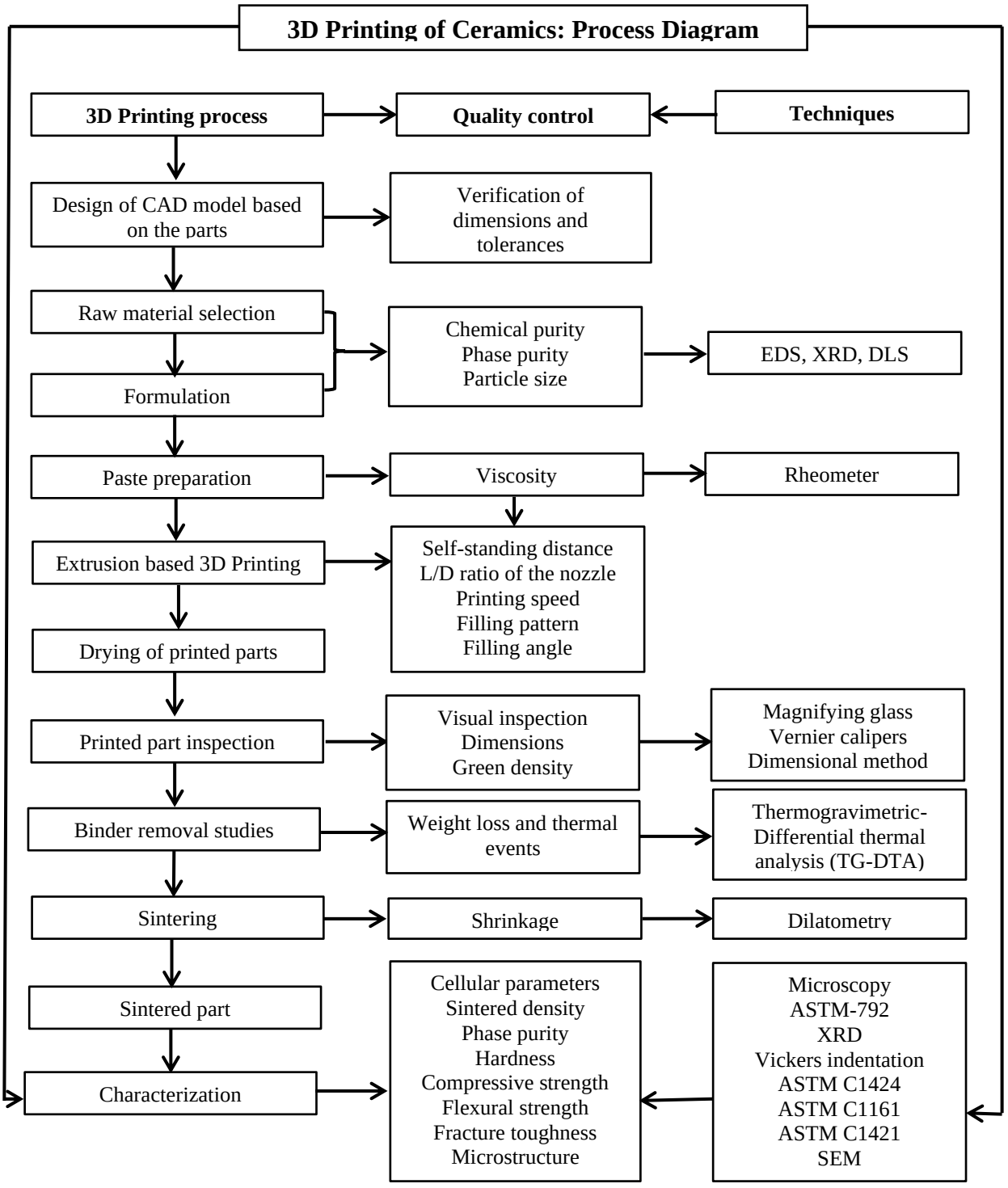

Fig.2.33 3D Printing process flow chart

2.10 References

1. H Merkus, Particle Size Measurements, Dordrecht: Springer Netherlands, 2009:259-285.
2. C Bohren and D Huffman, Absorption and Scattering of Light by Small Particles, Weinheim Wiley-VCH Verlag GmbH & Co. KGaA, 2007:381-428.
3. ISO 13320:2009, Particle size analysis - Laser diffraction methods, 2009.
4. H Myung, Kim and James, L White, A Non-Newtonian Model Of Flow In Forward And Backward Pumping Screw Regions Of A Modular Tangential Counter-Rotating Twin-Screw Extruder, Journal of Non-Newtonian Fluid Mechanics, 1990;37:37-53.
5. D W Richerson, W E Lee, Modern Ceramic Engineering: Properties, Processing and Use in Design, ISBN:1498716911, 9781498716918.
6. ASTM E228-17, Standard test method for linear thermal expansion of solid materials with a push-rod dilatometer, ASTM International, West Conshohocken, PA, 2017.
7. ASTM Standard C 1424, Standard Test Method for Monotonic Compressive Strength of Advanced Ceramics at Ambient Temperature, Drawing is copyright ASTM International, West Conshohocken, PA, 2004.
8. Compressive Strength of Concrete & Concrete Cubes | What | How | CivilDigital |". 2016-07-07. Retrieved 2016-09-20.
9. Wredenberg, Fredrik, PL Larsson, Scratch testing of metals and polymers: Experiments and numerics. Wear.266 (1–2): 76, 2009
10. W D Callister, Materials Science & Engineering an Introduction, John Wiley & Sons, U.S.A, ISBN 0-471-22471-5, 2003
11. ASTM C1161-18, Standard Test Method for Flexural Strength of Advanced Ceramics at Ambient Temperature, ASTM International, West Conshohocken, PA, 2018.
12. L Ćurković, A Bakić, Janoš K, Tatjana H, Flexural Strength Of Alumina Ceramics: Weibull Analysis, Transactions Of Famena, January 2010
13. ASTM C1421-18, Standard Test Methods for Determination of Fracture Toughness of Advanced Ceramics at Ambient Temperature, ASTM International, West Conshohocken, PA, 2018.

14. D George, L Quinn, T Brian, Sparenberg, P Koshy, L K Ives, S Jahanmir and D D Arola, Flexural strength of ceramic and glass rods, Journal of Testing and Evaluation, Vol. 37, No. 3
15. M Moeser, V Schmidt, Fractographic analysis of failures, Proc. 7th Congress Materials Testing, Budapest 1978;II:851-855.
16. T S Yen, J A Pask, Microstructure and properties of ceramic materials. United States, 1984.
17. R F Cook, B R Lawn and C J Fairbanks, Microstructure-Strength Properties in Ceramics: I, Effect of Crack Size on Toughness, Journal of American Ceramic Society, 1985;68:604-615.
18. C P Bergmann, A Stumpf, Microstructure of Ceramic Materials. In: Dental Ceramics. Topics in Mining, Metallurgy and Materials Engineering. Springer, Berlin, Heidelberg, 2013.
19. R E Chinn, Ceramography, ASM International and the American Ceramic Society, 2002, ISBN 0-87170-770-5.
20. C S Smith, A History of Metallography, University of Chicago Press, 1960:169–185.
21. S Binkowski, R Paul & M Woydt, Comparing Preparation Techniques Using Microstructural Images of Ceramic Materials, Structure, 2002;39:8–19.
22. H Mörtel, Microstructural Analysis, Engineered Materials Handbook, Volume 4: Ceramics and Glasses, ASM International, 1991:570–579, ISBN 0-87170-282-7.
23. G Petzow, Metallographic Etching, 2nd Edition, ASM International, 1999, ISBN 978-0-87170-633-1.
24. U Täffner, V Carle & U Schäfer, Preparation and Microstructural Analysis of High-Performance Ceramics, ASM Handbook Volume 9: Metallography and Microstructures, ASM International, 2004:1057–1066, ISBN 0-87170-706-3.

****

CHAPTER-3

PREPARATION OF ALUMINA PASTE AND EXTRUSION 3D PRINTING OF PARTS

3.1 Introduction

Aluminum oxide (Al_2O_3) or alumina is one of the advanced ceramic materials widely used by the ceramic industry for the fabrication of various components for application in vital sectors. Alumina exists in five polymorphic phases such as γ, δ, θ, κ, α with high temperature α –phase being the most thermodynamically stable phase. Alumina exhibits outstanding properties which makes it one of the candidate materials for high temperature and corrosion applications. Typical properties of alumina is shown in Table 3.1 Alumina is industrially synthesized by Bayer's process from naturally occurring ore of aluminum known as bauxite.

Table 3.1 Properties of aluminum oxide

Properties	Value	Units
Molecular weight	101.96	g/mol
Density	3.987	g/cm^3
Melting point	2072	^oC
Solubility	Insoluble in water & other solvents	-
Thermal conductivity	30	$W.m^{-1}K^{-1}$
Crystal structure	Hexagonal	-
Coefficient of thermal expansion (CTE)	8.20	$\mu m/m.^oC$
Hardness	1800	HV
Flexural strength	350	MPa
Youngs modulus	370	GPa
Compressive strength	2600	MPa
Fracture toughness	4.00	$MPa.\sqrt{m}$

Alumina is adaptable for various conventional and advanced ceramic shaping process such as compaction, casting, extrusion, injection molding etc. Recently the additive manufacturing or 3D printing processes is also explored widely for shaping of alumina by various R& D groups across

the globe. A brief survey of the published work of 3D printing of alumina is conducted as a part of the study and is presented below in addition to the data presented in chapter-1.

3.2 Literature Survey

Rueschhoff, et al, [1] fabricated dense alumina ceramic parts by direct ink writing of highly loaded aqueous alumina suspension in layer-by-layer fashion at room temperature. They have studied the effect of solid loading of alumina suspension by characterizing the slurry for the viscosity with varying shear rates and homogeneity and further correlated with density, mechanical and microstructural properties. The Rheological studies proved that slurry possess pseudo-plastic behaviour according to the Herschell-Buckley model. Yield stress and viscosity of the slurry was increased with increase in solid loading of the suspension.

Y Li et al, [2] investigated on Laser engineered net shaping (LENS) additive manufacturing technology to produce dense alumina ceramics as it has many advantages over traditional manufacturing methods. They have studied the effect of LENS deposition variables on deposition quality of the ceramic product. With increasing laser power length of the deposition layer, powder efficiency and micro hardness of the deposited layers were increased and surface roughness of the deposited layer was decreased. With increasing deposition head scanning speed, length of the deposition layer, powder efficiency and micro hardness was decreased and surface roughness got increased. Powder feeding rate also had effect on properties of the deposited layers. By using LENS alumina bulk samples were fabricated successfully.

H. Wu et al, [3] investigated on fabrication of alumina ceramics by stereolithography based 3D printing process. The authors have used alumina with different particle size and studied the effect of particle size on mechanical properties and debinding process of alumina parts through traditional thermal heating and vacuum debinding process. They suggested that particle size with bimodal distribution would exhibit good packing density in combination with superior mechanical properties.

A. Zocca et al. [4] studied on improved method of additive manufacturing technology i.e., layer-wise slurry deposition (LSD). This process is combined with the binder jetting process. They observed that a submicron powder can be processed through a LSD process and the properties of samples were comparable with the conventionally compacted samples. S. Maleksaeedi et al. [5] reported on production of alumina ceramics by powder-bed ink jet method. Printed samples were

vacuum infiltrated with high solid loading slurries to produce a good density at green and sintered stages. They studied the effect of solid loading concentration of infiltrant on mechanical properties of alumina samples. Slurry with higher solid loading demonstrated the enhancement of properties like density and surface finish.

Alumina-polypropylene composite was prepared by thermally induced phase separation (TIPS) method by K Shahzad et al [6] and resultant powder was used to produce parts by selective laser sintering technique at optimized conditions of laser power, scanning speed and temperature before printing. They have studied the post processing techniques such as warm isostatic pressing (WIP), infiltration to get alumina ceramic parts with good physical and mechanical properties. M. Schwentenwein et al [7] investigated fabrication of dense alumina ceramic parts by using one of the additive manufacturing technology i.e. Lithography based ceramic manufacturing (LCM) and used curing of photosensitive slurry by using dynamic mask exposure process. The study also reports that the LCM method produces dense ceramic parts with negligible geometrical limitations. The study stated that the alumina specimens produced from the LCM method had the 99.3% of the theoretical density, and four-point bend strength of 427 MPa with smooth surfaces relatively similar to other conventional ceramic shaping methods.

M Zhou et al. [8] has explored the fabrication of defect free alumina parts by stereolithography process and also examined various debinding and drying profiles to optimize the conditions for the sintered body. The study reports that use of Polyethylene glycol (PEG 400) as a desiccant resulted in lower deformation of the printed body during drying process. To minimize the defect formation during debinding process, the author has used vacuum debinding or air debinding and also two-step debinding which includes air debinding followed by vacuum debinding. Optimized parameters of debinding process enables the alumina specimens to achieve 99.3% of the theoretical density and hardness of 17.5 GPa similar to the traditional ceramic manufacturing methods.

J Wilkes et al. [9] developed one of the additive manufacturing technologies., selective laser melting to produce ceramics with high density and better mechanical properties. For the experimental studies, alumina, zirconia and mixture of both were melted by focused laser beam and also to minimize the thermal residual stresses during the printing process, the materials were pre-heated at 1600^{o}C. The study claims the possibility of fabricated specimens to achieve the density of 100% without any requirement of sintering and post-machining processes. Fabricated

samples have shown pure alpha phase and tetragonal in case of alumina and zirconia respectively. The fabricated specimens achieved a flexural strength of 500MPa. The study also reported the poor surface finish of the specimens which can be improved by the deposition of cold powder on preheated ceramic component.

J.A Gonzalez et al. [10] reported on fabrication of aluminum oxide specimens by binder jetting method. The author has studied the fabrication of alumina components by varying parameters alternatively such as layer thickness, particle size and powder distribution to achieve relatively good mechanical properties. High amount of powder distribution, lower layer thickness and increase in sintering time resulted in improvement of density and compressive strength of the specimens.

K Shahzad et al. [11] examined on fabricating the complex ceramic structures by using indirect selective laser sintering (SLS) in two-step process. A homogeneous composite mixture with good flowability and formability was prepared by phase inversion technique. As the study reports, first step involves the deposition of composite prepared by using polyamide and alumina in a layer manner and melts by scanning laser beam having an energy of 0.0176 and 0.37 J/mm^3. Further, the polymer present in the specimen slowly heated up to sintering temperatures to improve the density of the specimens. The study also reported the effect of laser scanning energy on the quality of specimens. The prepared samples were achieved with only 50% of the theoretical density due to debinding of polyamide which was seen to form interlayer porosity.

M Hotta et al., [12] fabricated alumina parts by forming powder layers of alumina on a platform by spraying water to the alumina granules which contains organic methylcellulose as the binder. The spraying of water enables the powder particles to get bonded and provides good shape retention to the parts. Further, the study also reported the debinding and sintering process for the prepared green ceramic part. After sintering the specimens showed no visible interface between the stacked layers.

L-K Tsui et al., [13] used extrusion based additive manufacturing technique to fabricate the alumina components by extruding UV-cured paste. The author investigated the printing process by varying solid loading of alumina paste from 70-81.5 wt.% mixed with UV curable resin. The layers were deposited using syringe head of the extruder and cured under UV LEDs fixed on the printing head with optimum printing conditions namely printing speed, layer thickness, deposition rate and force. The author printed components with alumina precursors (commercial grade A15

and submicron A16 of Almatis) and achieved the densities of 91% and 96% of the theoretical density. It was found that the alumina precursor with smaller particles have shown the higher density and X-ray tomography was performed to locate the defects to correlate with the density.

T Huang et al., [14] printed alumina components through solid freeze form extrusion process using alumina paste with high solid loading (≥ 50 vol%) with organic binder (Aquazol 50, 2 vol.%). The layers were printed according to the CAD model at freezing temperature of the paste and performed freeze drying technique to prevent deformation at green stage. The author experimented rheological properties of the paste and post processing conditions strongly influenced the properties of the final component. It was found that the lower deposition angle results in high amount of paste extrusion leading to the fabrication of component with overhanging layers. The sintered components were achieved with ~98% of the theoretical density and measured flexural strength for longitudinally and transversely deposited parts of 219 and 198 MPa respectively.

Based on the literature studies, though several researchers have attempted to 3D print alumina ceramics the studies have used UV curable resins or higher binder concentrations and further resulted in limitations in achieving theoretical densities. In the current study attempt has been made to employ an environmentally friendly thermal gelation process of methylcellulose in very low concentration for 3D printing of complex parts. The printed samples are sintered under pressureless and pressure assisted condition to study the effect of pressure on 3D printed samples in achieving the theoretical density. The samples Hot Isostatically Pressed (HIP) under vacuum encapsulation have resulted in 99.5% of theoretical density.

3.3 Experimental Studies

3.3.1 Characterization of Alumina Powder

Alumina powder was procured from Rohini industries, Pune and it was characterized for its properties such as particle size and its distribution, phase identification, chemical quantitative analysis, particle shape and specific surface area.

3.3.1.1 Particle Size Distribution

Particle size of alumina powder was measured using Dynamic Light Scattering technique which is described in the previous chapter in 2.2.1.2. The recorded data of intensity of the laser

light versus particle diameter is shown in Fig 3.1. It is evident from the particle size distribution plot, the alumina have an average particle size of D_{50} 330 nm.

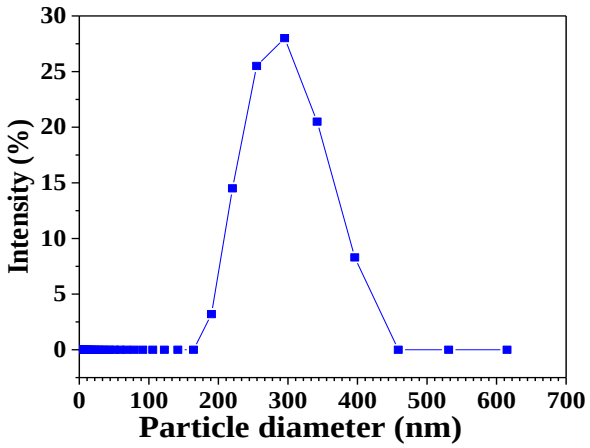

Fig.3.1 Particle size distribution of alumina powder

3.3.1.2 Phase Identification by X-Ray Diffraction

Alumina powder was characterized for its phase identification and purity by X-Ray Diffraction (XRD) technique (D8-Bruker, Germany) as described in previous chapter 2.2.2. The XRD pattern recorded for alumina powder with reference file is shown in Fig 3.2. The recorded diffraction pattern with respect to intensities and diffraction angle (2θ) is matched with the International Centre for Diffraction Data (Match entry no: C 96-900-9784). The resulting diffraction patten proves that alumina powder is showing pure α- phase.

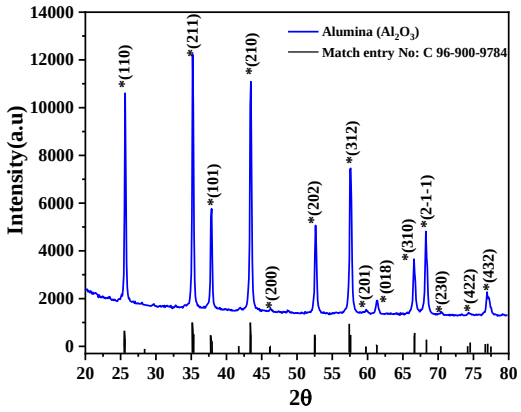

Fig.3.2 X-Ray Diffraction pattern of alumina powder

3.3.1.3 Chemical Quantitative Analysis

Alumina powder in the present study was also characterized for its chemical composition by Energy Dispersive Spectroscopy (EDS/EDAX) as mentioned in the previous chapter 2.2.4. EDS spectrum of alumina powder and quantitative analysis are shown in Fig.3.3 and Table 3.2 respectively. Based on the EDS spectrum, the powder have shown 62.79 wt% of Aluminum (Al) and 37.21 wt% of Oxygen (O). Except Al and O no other elements were traceable.

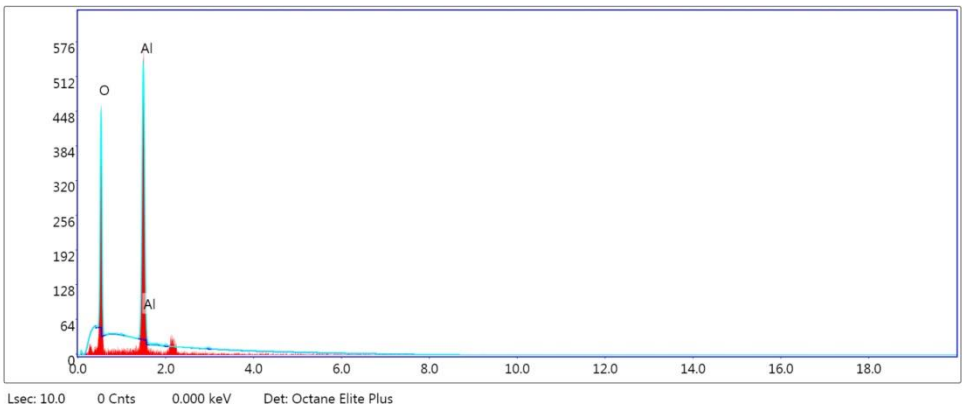

Fig 3.3 EDS pattern of Alumina powder

Table 3.2 EDS report of Alumina powder

Element line	Weight (%)	Atom %	Atom % Error	Net Int.	K_{ratio}	Z	A	F
O K	37.21	49.99	8.13	412.54	0.2510	1.0867	0.6207	1.0000
Al K	62.79	50.01	4.46	763.21	0.5530	0.9472	0.9296	1.0003

3.3.1.4 Particle Morphology

The alumina powder was characterized for the identification of particle shape and distribution using FESEM which is described in previous chapter 2.2.5. Fig 3.4 represent the morphology of alumina powder showing irregular particle shape.

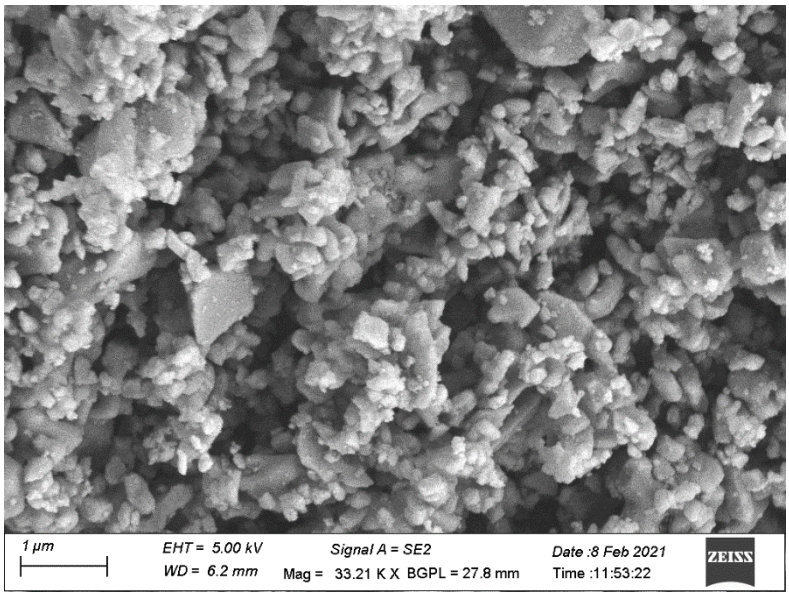

Fig. 3. 4 Morphology of alumina powder

3.3.1.5 Specific Surface Area

The specific surface area of alumina powder was measured by Breunaur-Emmett-Teller (BET) method as described in previous chapter 2.2.3. It is evident from the BET isotherm plot represented in Fig. 3.5, the specific surface area of alumina powder found to be 9.87 m^2/gm.

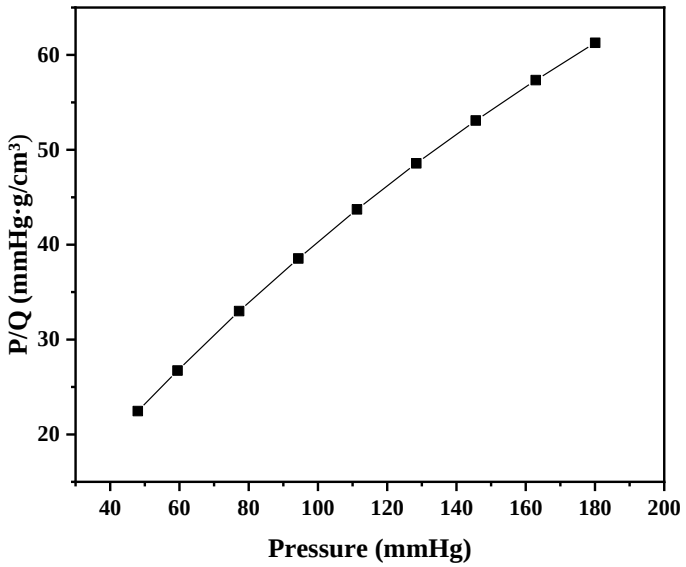

Fig 3.5 Langmuir isotherm plot of alumina powder

3.3.2 Preparation of Alumina Paste

3.3.2.1 Selection of Binder Based on Thermal Gelation Process

Methylcellulose (MC) ($C_{17}H_{32}O_{11}$, Molecular weight=412.4 g/mol) is an environmentally friendly binder which is derived from natural cellulose and the molecular structure of the MC is represented in Fig. 3.6. It is usually not soluble in solvents due to high crystallinity. This is mainly because of the hydrogen bonds formed by the hydroxyl groups in glucose residues. But on substituting of methyl group (-CH_3) to 1.6-2.0 will enhance the dissolution of the same in cold water. The aqueous solution of MC forms gel network on increasing the temperature primarily because of hydrophobic interaction of the molecules containing methoxyl substitution.

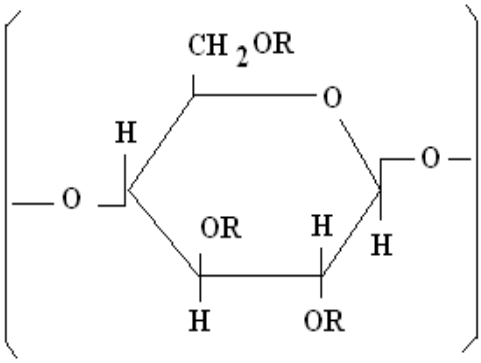

Fig.3.6 Structure of methylcellulose R=CH3

The gelation process of methylcellulose has been studied by several researchers [15-16]. It is evident from Fig. 3.7 that at low temperatures polymer-polymer interaction is minimum however with increase of temperature polymerization takes place forming a gel as indicated by the increase in the viscosity. On cooling the gel formed due to polymerization is transformed into its original state forming a hysteresis.

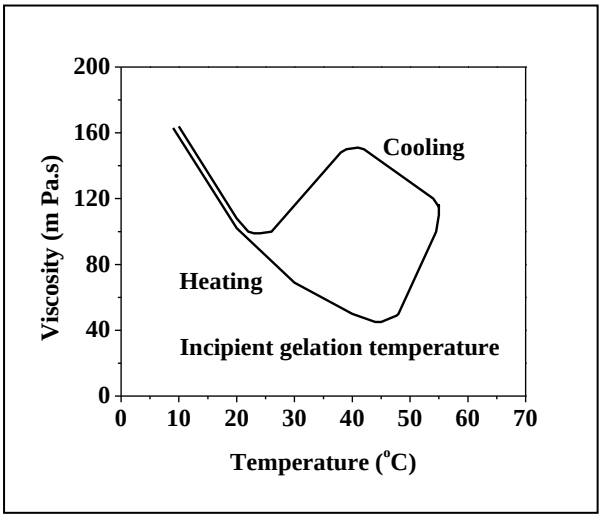

Fig.3.7 Gelation of 2% aqueous solution of MC, having normal viscosity of 100mPa.s, when heated at 0.25°C/min; rate of shear 86s^{-1} [17]

In the present study, the methylcellulose is procured from Loba chemie and used as a binder for printing of alumina ceramics. The thermal gelation behavior was studied using 0.25 wt.% of aqueous MC solution and subjected to elevated temperature. a MC solution was prepared with 0.25 wt.% of binder dissolved in cold deionized water. Fig. 3.8 (a) depicted in the figure shows a clear solution of 0.25 wt.% of MC in water at room temperature which was turned into turbid when exposed to 35°C (Fig.3.8 (b)). On further increasing the temperature to 42°C intensive polymerization takes place leading to gel formation as is evident from Fig. 3.8(c).

The observations are complimented by the rheological measurements recorded with respect to the temperature. It is evident from the Fig. 3.9, the viscosity of the solution is remained constant till the 30°C and there is slight increase in viscosity after 35°C. As the solution reached to 38-45°C, a steep increase in the viscosity of 50000 Pa.s was observed signifying the formation of polymer gel network.

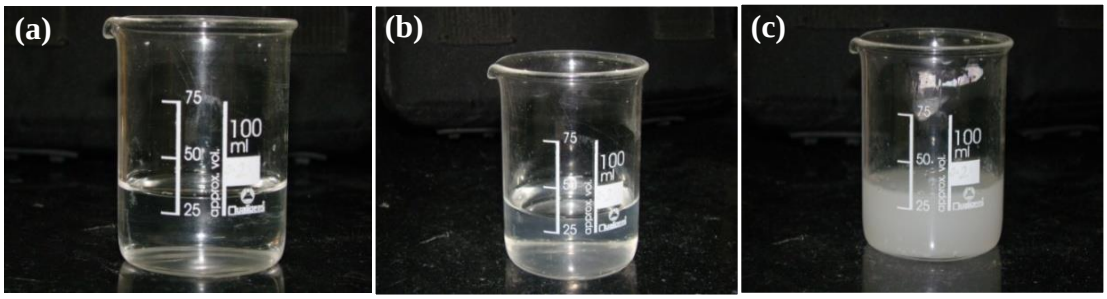

Fig.3.8 MC solution at (a) room temperature (30°C), (b) 35°C and (c) 42°C

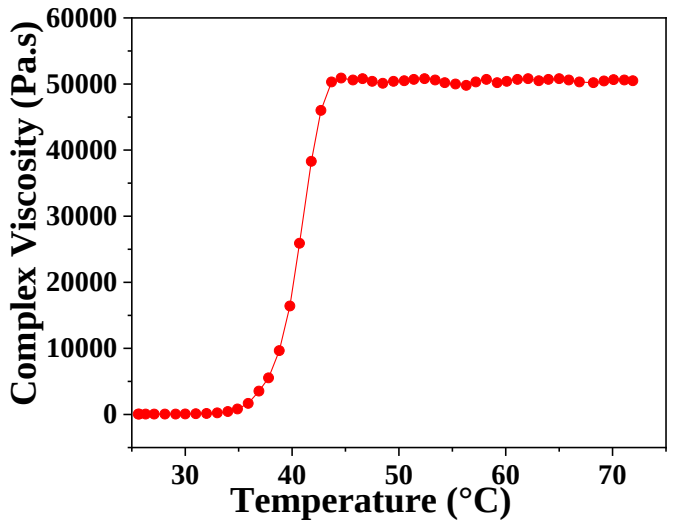

Fig.3.9 Plot of Complex viscosity vs Temperature of the MC solution

3.3.2.2 Preparation of Alumina Paste

The alumina paste was prepared with three selected concentration of MC 0, 0.25, 0.5 and 0.75 wt.% in order to study the effect of MC concentration on 3D printing.

In this study, the methylcellulose used as a binder as a substitution to the UV-curable resins to fabricate the green ceramic parts by 3D printing as it exhibits the following advantages.

- It is synthesized from the naturally occurring cellulose
- Lower thermal gelation temperature ~45^{o}C results in shaping of simple and complex ceramic parts
- Low binder concentration i.e., 0.2 wt.%
- It permits 100% organic burn out
- It is adaptable for common ceramic powders.

To prepare feedstock/paste with any advance ceramic powder, it requires an additives/binder due to lack of plasticity. Selection of type and concentrations of additives plays a major role while preparing the paste. In present study methylcellulose (MC) used as a binder to prepare paste. The steps involved in the pate preparation is represented in flowchart depicted in Fig. 3.10.

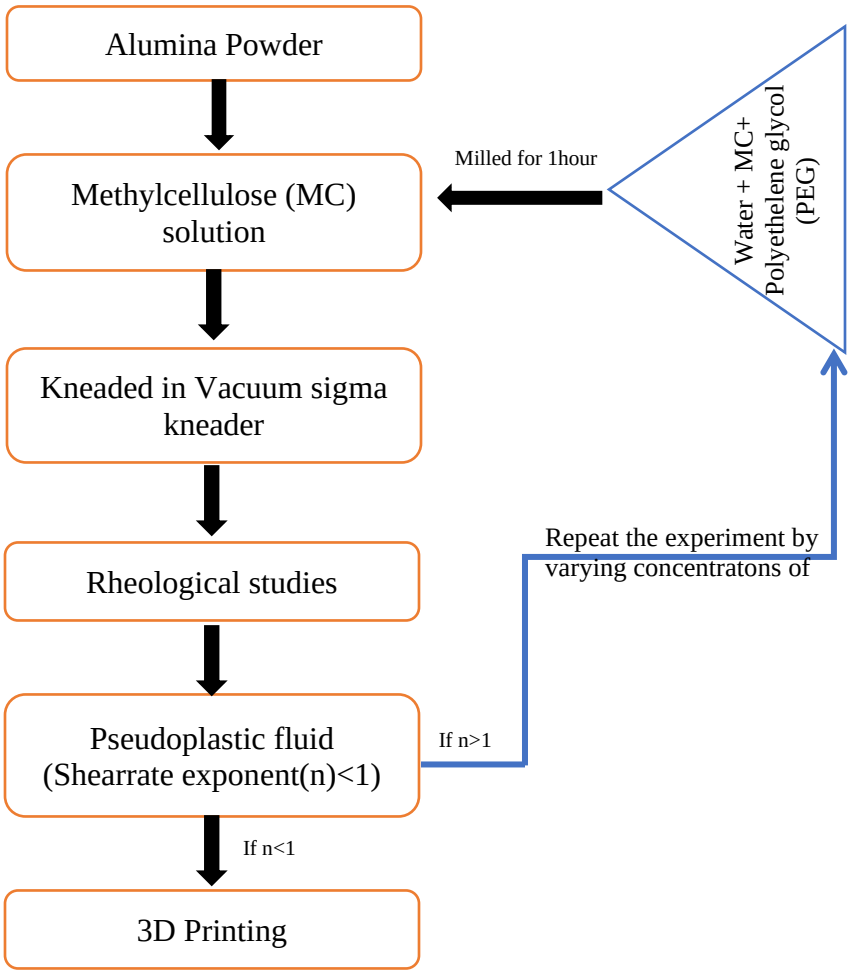

Fig 3.10 Flow chart for preparation of alumina paste

To prepare alumina paste, the alumina powder is added to the methylcellulose (MC) solution. To optimize the concentrations of water, binder and plasticizer, the traditional approach was opted. Polyethylene glycol is used as a plasticizer in the current study. The concentrations of binder were varied from 0.25 to 0.75 wt.%, water from 33 to 38 wt.% and plasticizer from 0 to 2 wt.% of powder. General steps in the preparing of alumina paste are mentioned in flowchart (Fig.3.10) which follows the first step as a preparing the MC solution by adding 0.25 wt.% of MC to the cool deionized water (33 wt.% of powder) in a bottle consisting alumina balls and no plasticizer were added. Further the resultant mixture is kept for milling for 30 minutes until MC powder particles get dissolves. Later, the alumina powder is added to the milled MC solution and again milled for 15 minutes. To removes clusters and agglomerates which are formed during the adding of powder to MC solution, the mixture was kneaded in vacuum sigma kneader for 30 minutes. Further the prepared homogeneous mixture was measured for its viscosity under varying

shear rates from 1 to 1000 s^{-1} using rheometer (MCR 51, Anton Paar, Austria) as described in 2.4 by placing it on parallel plate-spindle arrangement.

3.3.2.3 Effect of Additives on Viscosity

To study the effect additives on viscosity and flow of paste, the alumina paste was prepared by maintaining water and plasticizer concentrations constant as refer in the Table 3.3.

Table 3.3 Concentration of additives and optimization

S.No	Methylcellulose (MC) (wt.%)	Water (wt.%)	Polyethylene glycol (PEG) (wt.%)
1	0.25	33	1
2	0.5	33	1
3	0.75	33	1
4	0.25	35	1
5	0.5	35	1
6	0.75	35	1
7	0.25	38	1
8	0.5	38	1
9	0.7	38	1

The paste prepared from first three formulations which are mentioned in above Table 3.3 The prepared MC solution (with 0.25 wt.% MC, 33 wt.% water and 1% PEG) was slowly added to the powder to ensure the homogeneous mixing of powder and MC solution. Though the concentration of binder is low in the water, it is unable to form homogeneous paste and formed the agglomerates. Such agglomerates will object the flow of paste during rheological measurement as well as during the 3D Printing process. Similarly, the MC solution with 2^{nd} and 3^{rd} formulation (Table:3.3), was also formed agglomerates. Though these agglomerates can be removed by the improving the kneading time in Sigma kneader, but it forms coherent paste, which requires a high amount of pressure during the printing process. Then to avoid agglomerates the amount of water is increased from 33 to 35 wt.%. The formulation 4, 5 and 6 (Table: 3.3) were prepared with respective concentrations of MC, water and PEG. For the 4^{th} formulation, the amount of liquid increases, the powder particles moves to the region where it can partially or fully filled the void space. By kneading the mix for 15-20 minutes results in homogeneous paste. At this point the

binder and water concentrations were sufficient to make a printable paste. For the 5th formulation, at the same concentration of water, the 0.5 wt.% MC also forms the paste and the viscosity of the formulation is more than the 4th formulation. Further the binder concentration was increased to 0.75 wt.% with 35 wt.% of water, the amount of water is not sufficient to form paste and the agglomerates present in it leads to irregular flow and increase in viscosity during rheological measurement. In the case of 7, 8 and 9th formulation, the more amount of water (38 wt.%) was added to the powder with different MC concentrations. The more amount of water in formulation, decreases the interparticle friction and allows a particle to flow freely without any shear. This kind of paste is not suitable as it is results poor shape retention to 3D Printed parts. At 0.5 wt.% MC and 38 wt.% water results in a paste with optimum viscosity, but the more concentrations of binder lead to more porosity during binder burnout process. Finally for 0.75 wt.% binder, the mentioned water is not sufficient to form a homogeneous paste. Overall, based on the experiments by varying amount of binder and water to prepare a paste for 3D printing process, the 4th formulation was selected as a optimum to prepare alumina paste after characterized for the rheological parameters as it contains minimum binder.

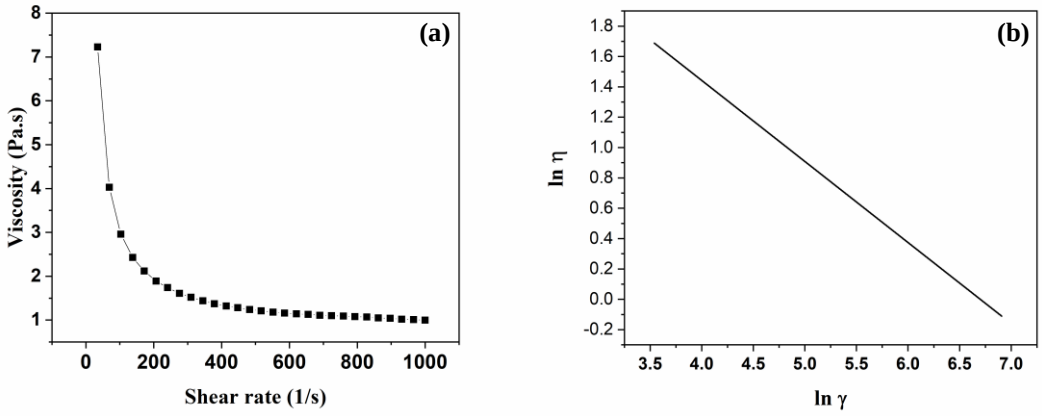

Fig 3.11 Plot of (a) Shear rate vs Viscosity and (b) lnγ vs lnŋ for alumina paste

Shear rate vs viscosity plot for the optimum formulation is shown in Fig. 3.11 (a). The plot represents the viscosity of alumina paste is decreasing as the shear rate increases which proves the paste is showing pseudoplastic (shear thinning) behavior. Further to confirm the rheological behavior of the paste, the shear rate exponent of the measurement was calculated using Power law model (Refer in previous chapter, 2.4). Logarithm of shear rate and viscosity values were plotted in X and Y-axis and plotted (Fig. 3.11 (b)). The linear fit of the curve provides a straight line and

slope of the curve is known as shear rate exponent(n). The shear rate exponent for the formulation is 0.55 (n<1) proves the pseudoplastic behavior. The lower concentration of binder and water provides the good shape retention as well as good green and sintering densities.

3.3.3 3D Printing of Alumina parts

The prepared alumina paste was subjected to 3D printing process using ram type extruder assembled in 3D printer described in chapter 2.6. The paste was filled in the barrel of extruder assembly shown in previous chapter in Fig. 2.10(b). By the application of pressure, the filled paste will flow under pressure applied through the plunger and further print through the nozzle according the design path.

3.3.3.1 Effect of printing parameters on the quality of the printed sample

As described in chapter 2. the parameters used for printing have shown in this Table 3.4

Table 3.4 Optimum parameters for 3D printing alumina parts

S. No	Parameters	Optimum values
1	Printing Speed (mm/s)	4-6
2	L/D ratio	25
3	Self-standing distance (mm)	1.25 ± 0.25
4	Filling angle (^{o})	90
5	Filling pattern	Rectilinear
6	Substrate	Aluminum foil

3.3.4 Characterization of 3D Printed Green Alumina Samples

Using the optimum printing speed and other conditions different geometries and complex structures were printed. After completion of printing, the samples were dried for 4-5 hours in oven at 30-40^{o}C temperature. After drying the specimen was observed for its structural integrity, visual defects and initiation of crack in the sample. Dried samples were measured for shrinkage by dimensional method. In green stage the samples have shown 7-10% shrinkage. Further the green specimen sample is also sized to 25mm x 8mm x 8mm to characterize for linear shrinkage with the heating rate of 5^{o}C/min using Dilatometer and recorded plot of $\Delta L/Lo$ versus time with respect

to temperature is represented in Fig. 3.13. It is evident from the Fig.3.13, a total shrinkage of 22% was observed.

Green density of the samples was calculated by taking weight and dimensions of the sample using dimensional method. The samples have shown green density from 1.92-2.02 gm/cm^3 which is 48 to 50% of theoretical density. After the samples are completely dried, these samples (Fig. 3.12) are sintered at atmospheric pressure in muffle furnace (Deltech, USA) according to the sintering schedule represented in Fig 3.14(a) to 1650^{o}C for 1hr soaking. Samples were heated from room temperature to 500^{o}C with the heating rate of 2^{o}C/min and soaked for 1hour, with the same heating rate samples are again heated from 500 to 1650^{o}C, soaked for 1 hour. The sample was furnace cooled to room temperature and sintered samples are shown in Fig. 3.14(b).

Fig. 3.12 3D Printed green alumina structures

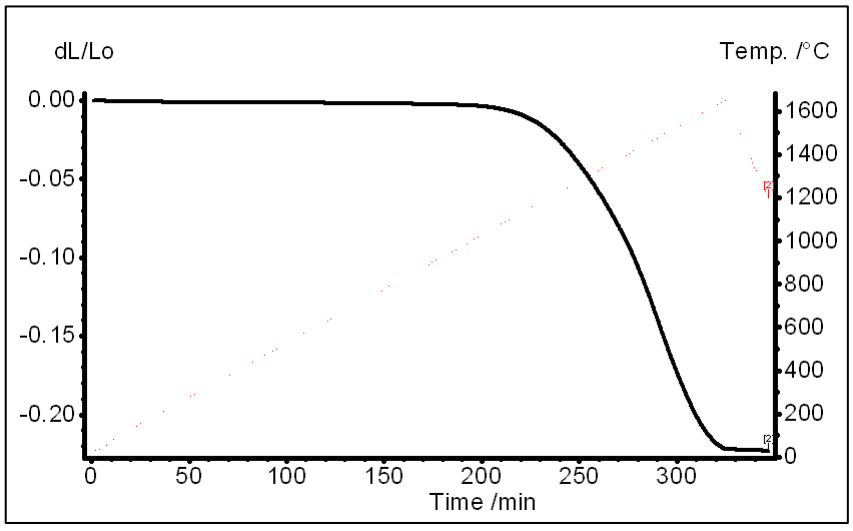

Fig 3.13 A Plot of ΔL/Lo vs Time vs Temperature for 3D printed alumina sample

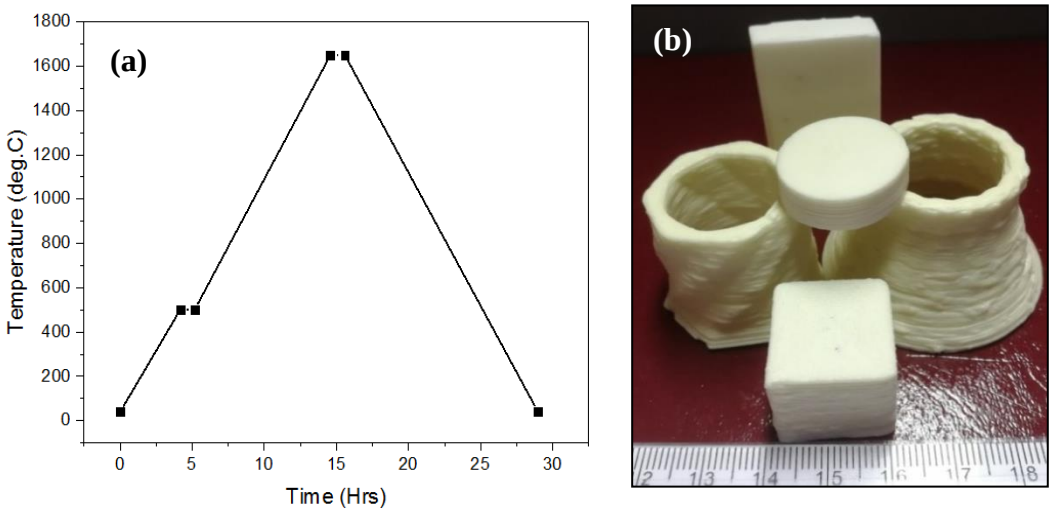

Fig 3.14 (a) Sintering schedule and (b) Green alumina 3D Printed specimens

3.3.5 Characterization of 3D Printed Sintered Parts

Sintered samples shown in Fig 3.14(b) were measured for its sintering density using Archimedes Principle, which is explained in chapter 2.8.1. The density of the samples was achieved to 3.88 g/cc which is 97.4% of theoretical density. Further the sintered samples were also measured for its flexural strength using Three-Point bend test in UTM as described in previous chapter at 2.8.4.

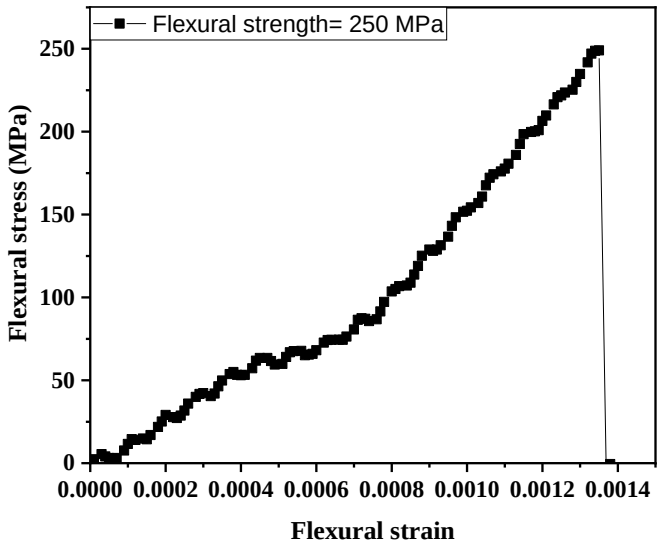

Fig.3.15 Flexural Stress vs Flexural strain of sintered specimen

The deflection occurred in the sample has been recorded as the load applied on it. The flexural stress versus flexural strain curve was shown in Fig 3.15 and it is evident that 3D printed sintered specimen has been failed at strength of 250 MPa. The fracture surface of broken specimen during the 3-Point bend flexural test was sputtered for 1 minute at 10 mA current. The fractography of sputtered specimen recorded using Scanning Electron Microscope (SEM) is shown in Fig 3.16. Fracture surface reveals that the sample failed through both intergranular and intragranular fracture.

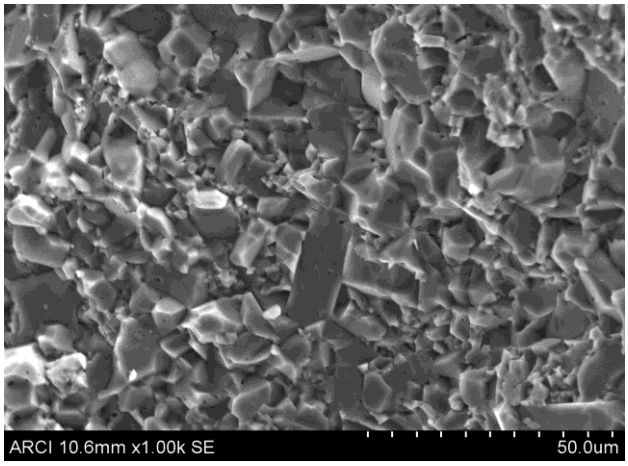

Fig. 3.16 Fractography of 3D Printed sintered sample

Further the sintered sample was polished as per the ceramograhy procedures and measured the hardness using Vickers hardness test. Initially a load of 0.5 kg is applied on polished sample for a dwell time of 15 seconds. The diagonals of the impression of the indenter are measured and calculated the hardness of the sample. On an average of 10 measurements, the hardness of sintered specimen was found to be 15 GPa.

The printed rectangular bar samples were scanned for detection of the surface and sub-surface flaws present in the specimen by X-Ray Radiography. It is the one of non-destructive test which is used to inspect sub-surface flaws by using X-rays which is having shorter wavelength and high energy photons. These high energy photos have an ability to penetrate inside the material and passes through it and intensity of the x-rays are captured by radiation sensitive film.

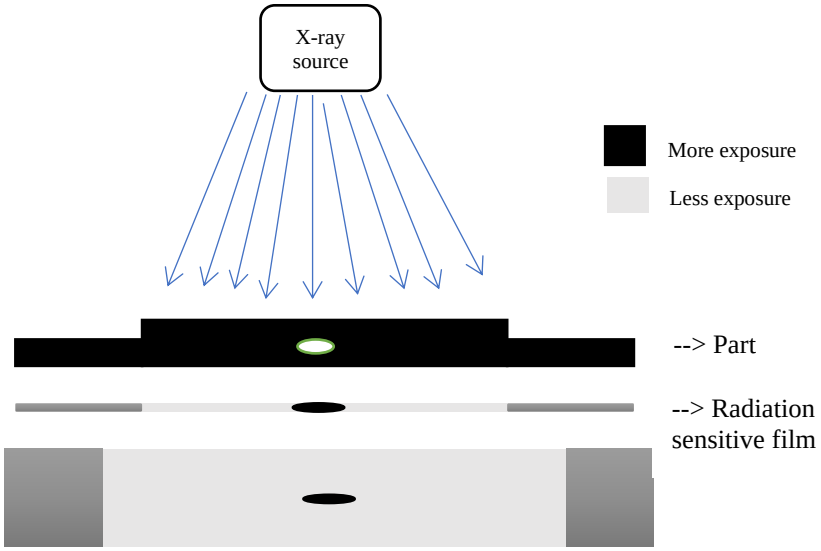

Fig. 3.17 Schematic of X-Ray Radiography

General working procedure in X-ray radiography is that, the sample which is to be tested is placed between the radiation source and radiation sensitive film. The source to generate x-rays by either x-ray machine or Co-60, Ir-192 will be used. The x-rays will pass through the object, thicker regions of the part will allow less radiation and thinner regions will allow more radiation and the radiation that passes through the different regions of part will expose the film as shadow graphs. The film darkness intensity will vary with the amount of radiation reach to the film. Area which is more exposure to the amount of radiation will show a dark region and area exposed to the less amount of radiation will give light color regions. The variation in darkness reveals whether any defects present in that or not.

3D Printed green and sintered alumina samples were screened by radiography test. Radiography images of green and pressureless sintered samples have shown in Fig 3.18 (a) and (b) respectively. The green alumina sample was showing randomly placed laminar defects caused due to the layer structure. Further these defects reduced in pressure less sintered sample.

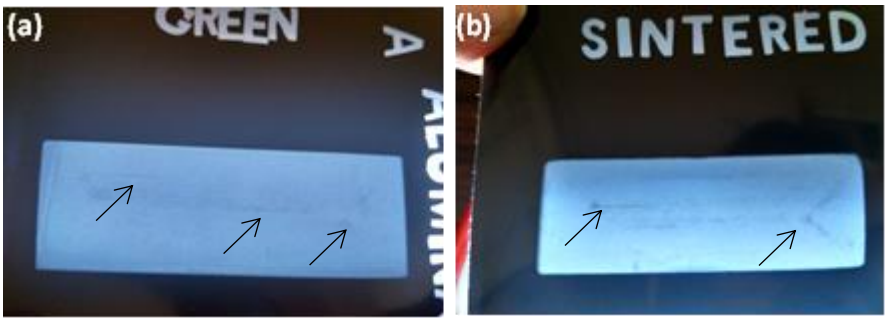

Fig 3.18 X-Ray radiography image of 3D Printed (a) green and (b) pressureless sintered sample

3.3.6 Hot Isostatic Pressing (HIP)

Since the density and measured mechanical properties could not achieve theoretical values of alumina due to processing defects occurred during the building the object layer by layer. Conventional sintering process at atmospheric pressure was unable to heal the interlayer defects. Hence to heal the interlayer defects of printed specimen the printed samples were sintered in Hot Isostatic Pressing (HIP) after encapsulation where the densification of specimen occurs due to the application of temperature and pressure simultaneously. HIP process involves the densification of object under pressure at high temperature which is relatively lower than conventional sintering temperature. Argon (Ar) is used as pressure medium as it is chemically stable during the process. 3D Printed green samples cannot be hot isostatically pressed as the green body exists with inherent porosity. Direct HIPing of green sample results filling of the pores of the sample with pressure media. Leading to ballooning effect and restrict densification. In such cases the samples are encapsulated in a metallic capsule and created a vacuum around 10^{-3} Torr.

Encapsulation based capsule process generally applied in the powder form as well as shaped components. Capsule method involves the enclosing powder or shaped body in a container or capsule. The material of this container is made up of with the material which is resistant to penetrate to the gaseous pressure medium. Further the air present in the container will removed and creates vacuum. After evacuation the container will be sealed by welding process. Then the material present in the capsule is compressed at high temperature and pressure, thus the densification of the object achieved.

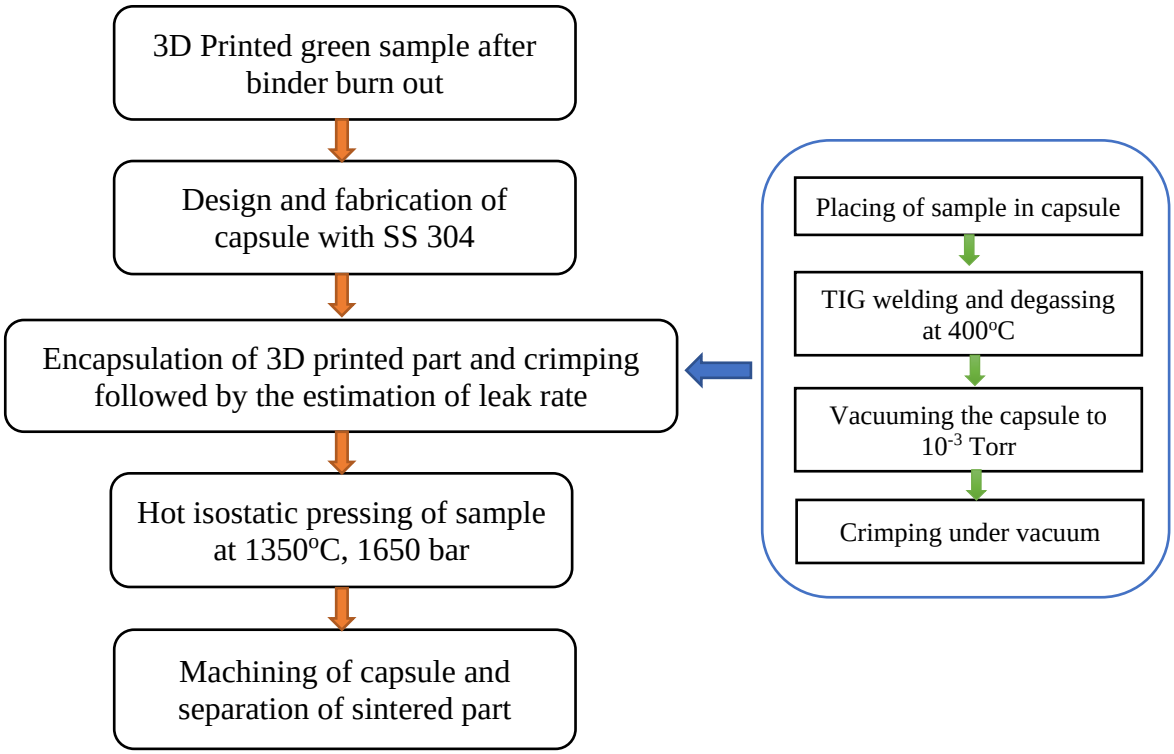

Fig 3.19 Flowchart for HIPing of vacuum encapsulated 3D printed green sample

Fig 3.19 represents the steps involved in the HIPing of vacuum encapsulated 3D Printed green sample. In the current study to heal the interlayer defects and to achieve the higher density, the 3D Printed green cylindrical samples were enclosed in container made with stainless steel (SS 304) after binder removal and pre sintering at 1000°C for 1 hour soaking period. The selection of capsule material is based on the chemical reactivity, metal and processing cost and weldability of material. The recrystallization temperature of steel is less than 1500°C . Hence, mostly the capsule container for ceramics HIPing is made up of with mild steel or stainless steel. The 3D printed green ceramic sample after binder burnout and schematic of the capsule design is represented in Fig 3.20 (a) and (b) respectively.

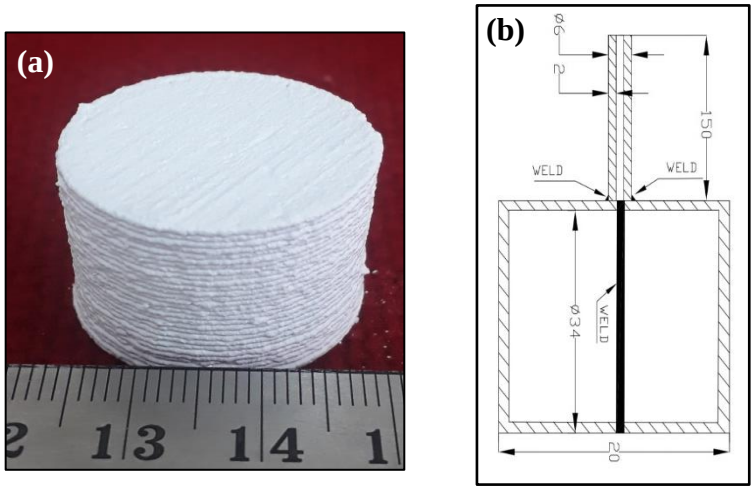

Fig 3.20 (a) 3D Printed green ceramic sample after binder burnout and (b) Schematic of capsule

As the schematic of capsule represents, it has a two capsule which is joined together by Tungsten Inert Gas Arc welding (TIG) welding after placing the sample between those capsules. Further the capsule was degassed at 400^{o}C to remove atmospheric gases adsorbed by the surface of sample. This encapsulation process was done by facility available at ARCI represented in Fig 3.21. Fabricated SS 304 capsule along with the 3D printed green specimen and encapsulated capsule/can is shown in Fig. 3.22 (a) and (b) respectively.

Fig 3.21 Encapsulation facility at ARCI

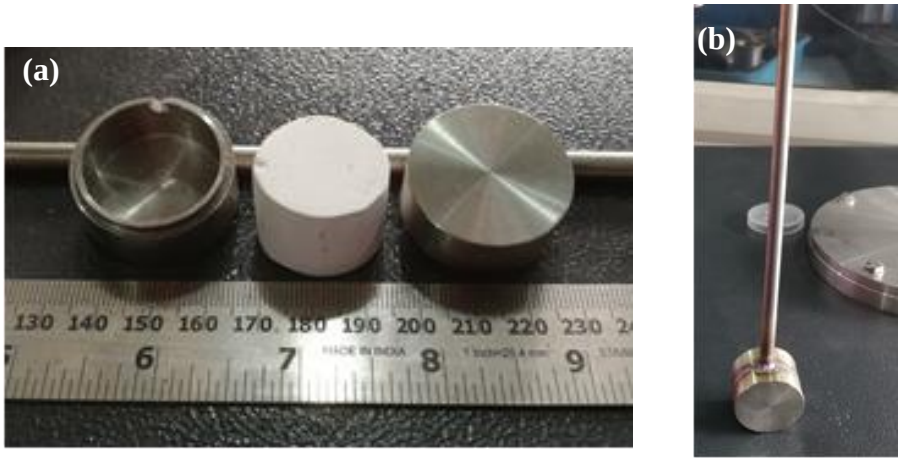

Fig 3.22 (a) Fabricated SS 304 capsules along with printed sample and (b) Encapsulated SS 304 container

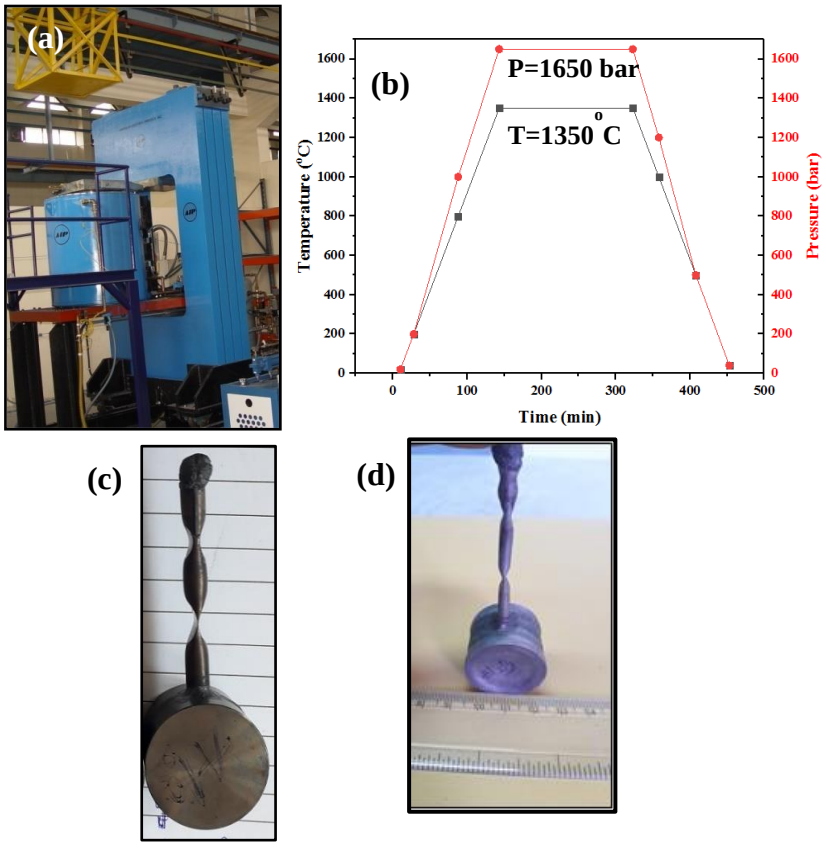

Fig 3.23 (a) Hot isostatic Press (HIP) facility, (b) HIP schedule, (c) Capsule after welding, (d) Deformed capsule after HIPing

Later, the helium gas leak test was conducted at 10^{-3} Torr level. After ensuring that there is no leakage of helium gases from the welded can/capsule, the SS304 cans were degassed and crimped under 10^{-3} Torr vacuum level. Crimping is the action of joining of two materials by deforming the both materials to hold together.

After crimping the samples were kept in pressure vessel in HIP furnace shown in Fig. 3.23 (a). The pressure vessel was pumped with Argon gas to the 1650 bar pressure and increase the temperature to 1350^{o}C as shown in Fig 3.23 (b). The increased temperature is very less than the conventional sintering temperature. After HIPing the capsule was deformed (Fig 3.23 (d)) and the compressed sample is removed by breaking the capsule. Due to the combination of pressure and temperature the diffusion of grains is enhanced and the healing of porosity present between the layers was also increased which is proven by radiography image of HIPed sample shown in Fig 3.24. The density of pressure assisted sinteried sample was measured by Archimedes principle. The density of the HIPed sample was enhanced to 3.94 g/cc which is 99% of theoretical density due to application of pressure. The fracture surface of the sample was shown in Fig 3.25, which have shown both intergranular and intragranular fracture. Fractography image proves the healing of interlayer defects and porosity and Hardness of HIPed sample is improved from 15 to 18 GPa.

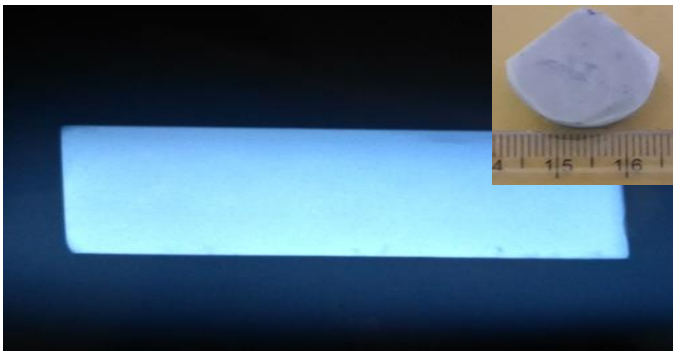

Fig 3.24 X-Ray radiography image of HIPed sample

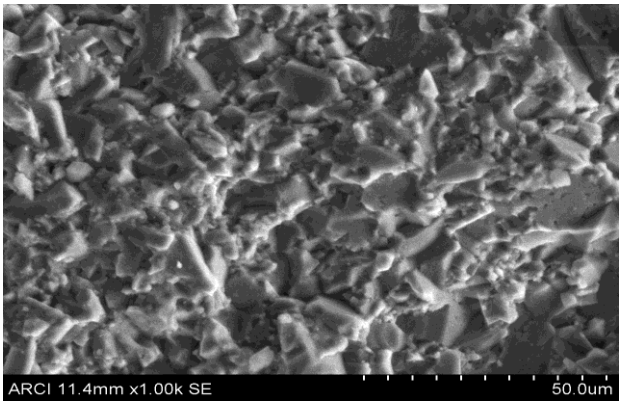

Fig 3.25 Fracture surface of HIPed sample

3.4 Conclusions

Commercially available alumina was characterized for its particle size, size distribution, phase purity, chemical characterization, morphology and specific surface area. The particle size of alpha-alumina is found to be 330nm. The rheological regime for alumina feedstock was achieved by optimizing the additives, plasticizer and water concentrations. Ram type extrusion-based 3D printing has been successfully applied to print the simple and complex shaped alumina ceramics.

The printing speed of 4- 6mm/s was optimized to print alumina structures with better structural integrity, defect free specimen with in the dimensional tolerances. Dried green 3D printed samples have shown 48-50% of theoretical density with a shrinkage of 22-25%.

The dried samples were sintered at 1650^{o}C with heating rate of 2^{o}/min, soaked for 1 hour. 3D printed green and sintered samples were subjected to X-ray radiography and the observed lamination defects can be attributed to inherent layer by layer formation of the parts while printing. Though the sintering under pressureless conditions results in the eliminations of most of the printing defects, randomly oriented flaws are evident from the radiographic studies which resulted in the deteriotion of the mechanical properties.

HIPing of 3D printed green samples results in elimination of flaws and also finer grained microstructure due to the low temperature sintering leading to the higher density and superior mechanical properties. Pressureless sintered samples have shown a maximum density of 3.88 g/cc at 1650°C against the HIPed samples exhibiting density of 3.94 g/cc even at low temperature of 1350°C revealing the effect of pressure assisted sintering. HIPed sample has shown a higher hardness of 18 GPa against 15 GPa observed for pressureless sintering samples.

3.5 References

1. L Rueschhoff, W Costakis, M Michie, J Youngblood, R Trice, Additive manufacturing of dense ceramic parts via direct ink writing of aqueous alumina suspension, International Journal of Applied Ceramic Technology, 2016;13:1–10
2. Y Li, Y Hu, W Cong, L Zhi, Z Guo, Additive manufacturing of alumina using laser engineered net shaping: Effects of deposition variables, Ceramics International, 2017; 43:7768-7775.
3. H Wu, Y Cheng W Liu, R He, M Zhou, S Wu, X Song, Y Chen, Effect of the particle size and the debinding process on the density of alumina ceramics fabricated by 3D printing based on stereolithography, Ceramics International, 2016;42:17290-17294.
4. A Zocca, P Lima, J Gunster, LSD-based 3D printing of alumina ceramics, Journal of Ceramic Science and Technology, 2017;08:141-148.
5. S Maleksaeedi, H. Eng, F E Wiria,T M H Ha, Z He, Property enhancement of 3D-printed alumina ceramics using vacuum infiltration, Journal of Materials Processing Technology, 2014;214:1301-1306.
6. K Shahzad, J Deckers, J-P Kruth, J Vleugels, Additive manufacturing of alumina parts by indirect selective laser sintering and post processing, Journal of Materials Processing Technology, 2013;213:1484-1494.
7. M Schwentenwein, J Homa, Additive manufacturing of dense alumina ceramics, International Journal of Applied Ceramic Technology, 2015;12,1-7.
8. M Zhou, W Liu, H Wu, X Song, Y Chen, L Cheng, F H Shixim, Preparation of defect free alumina cutting tool via additive manufacturing based on stereolithpgraphy-Optimization of the drying and debinding process, Ceramic International, 2016;10:1598-11602.
9. J Wilkes, Y C Hagedorn, W Meiners, K Wissenbach, Additive manufacturing of ZrO_2-Al_2O_3 ceramic components by selective laser melting, Journal of Rapid Prototyping, 2013;19:51-57.
10. J A Gonzalez, J Mireles, Y Lin and R B. Wicker, Characterization of ceramic components fabricated using binder jetting additive Manufacturing technology, Ceramics International, 2016;42,10559-10564.

11. K Shahzad, J Deckers, S Boury, B Neirinck, J P kruth, J Vleugels, Preparation and indirect selective laser sintering of alumina/PA microspheres, Ceramics International, 2012;38:1241-1247.
12. M Hotta, A Shimamura, N Kondo, T Ohji, Powder layer manufacturing of alumina ceramics using water spray bonding, Journal of the Ceramic Society of Japan, 2016;124:750-752.
13. L-K Tsui, E Maines, L Evans, D Keicher, J Lavin, Additive Manufacturing of alumina componenets by Extrusion of in-situ UV cured pastes, Solid Freeform Fabrication 2018: Proceedings of the 29th Annual International Solid Freeform Fabrication Symposium – An Additive Manufacturing Conference, Reviewed Paper.
14. T Huang, M S Mason, X Zhao, G E Hilmas, M C Leu, Aqueous-based freeze-form extrusion fabrication of alumina components, Rapid Prototyping Journal, 2009;15:88-95.
15. M Takahashi, M Shimazaki, J Yamamoto, Thermoreversible gelation and phase seperation in aqueous methylcellulose solutions, Journal of Polymer Science: Part B: Polymer Physics, 2001;39:91-100
16. K Kobayashi, C-I Huang, T P Lodge, Thermoreversible gelation of aqueous methylcellulose solutions, Macromolecules, 1999;32:7070-7077.
17. N Sarkar, Thermal gelation properties of methyl and hydroxylpropyl methylcellulose, Journal of Applied Polymer Science,1979;24:1073-1087.

****

CHAPTER – 4

3D PRINTING OF MAGNESIUM ALUMINATE SPINEL CERAMICS AND THE EVALUATION OF PHYSICO-CHEMICAL, MICROSTRUCTURAL AND MECHANICAL PROPERTIES

4.1 Introduction

Magnesium aluminate ($MgAl_2O_4$) spinel is a high strength advanced ceramics consists of combination of the high temperature mechanical properties, corrosion resistance in harsh environment as well as the unique optical properties. This makes spinel a candidate material for versatile application especially in refractory, strategic and associated areas [1-9]. The typical properties of polycrystalline spinel are tabulated in Table.4.1 [10].

Spinel is well known and potential material for refractory applications. Though it is expensive in developing spinel for refractory applications, but it is gaining an interest in the applications where spinel used as replacement for refractory brick material for magnesia chrome-based bricks containing hexavalent chrome. It is also a suitable material as an alternative for magnesium chromite-based refractories and major applications in burning and transient chambers in cement rotary kilns and side and bottom wall of the steel ladles. Further it has another major application in carrying out the checker work of glass tank furnace regenerators. It is also used as catalyst and catalyst support for various organic reactions mainly in petroleum processing, Oleflex process which does the dehydrogenation of the propane and Star process for dehydrogenation of the butane [11-18]. Spinel is gaining interest as a potential material due to its inherent cubic crystallography and transparency in the strategic sector [19-23]. Additionally, spinel also is proposed as core insulation in fusion reactor due to its good resistance in radiation induced swelling and strength degradation during irradiation [24-26]. Spinel is also explored as a material for environmental barrier coating for the blades and vanes in the hot section components for gas turbines [27].

Table 4.1 Typical properties of polycrystalline spinel ceramics [10]

Properties		Value
Physico-chemical properties	**Chemistry**	**$MgAl_2O_4$**
	Density (g/cm^3)	**3.58**
	Crystal structure	**Cubic**
	Melting point (^oC)	**2135**
Mechanical properties	**Elastic Modulus (GPa)**	**277**
	Flexural strength (MPa)	**250**
	Compressive strength (GPa)	**2.69**
	Fracture Toughness (K_{1C}) ($MPa.m^{1/2}$)	**1.9**
	Hardness (GPa)	**12.1**
Thermal properties	**Coefficient of Thermal Expansion (/K, (at 25-1000^oC))**	**7.9×10^{-6}**
	Thermal Conductivity (W/m.K) at 25^oC)	**24.7**
Optical properties	**Dielectric Constant**	**8.2**
	Dielectric loss	**0.00025**
	Range of transmission (µm)	**0.2-6**
	Refractive index at 3 µm	**1.69**
	Theoretical transmission (%) at 3 µm	**87**

4.1.1 Spinel Crystallography

The name of magnesium aluminate spinel structure was taken from the mineral spinel with the general formula of AB_2O_4 and arranges atoms in cubic crystal structure. General formula of spinel represents A^{2+} and B^{3+} with the divalent and trivalent cations occupying tetrahedral and octahedral sites respectively and O atoms arranged in a cubic close-packed lattice [28]. Schematic of magnesium aluminate spinel unit cell structure is shown in Fig. 4.1.

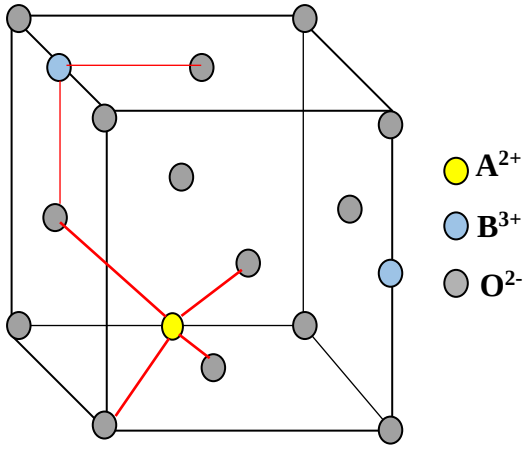

Fig. 4.1 Magnesium aluminate spinel ($MgAl_2O_4$): unit cell structure

4.1.2 Spinel Phase Diagram

The phase diagram of MgO–Al_2O_3 is represented in Fig.4.2. It is evident from the phase diagram that 71.8 wt. % Al_2O_3 and 28.2 wt. % MgO to form stoichiometry and correspondingly melts at 2135^{o}C. Other than the spinel, the presence of precursor oxides results in reduction of melting point of the composition. The solubility of MgO and Al_2O_3 is 2 and 6% respectively at 1600^{o}C and further it is increased to 3 and 10% respectively on increasing the temperature to 1700^{o}C.

Spinel can be classified in two groups such as magnesia rich spinel which contains excess MgO and alumina rich spinel which contain excess Al_2O_3 which form either side of the stoichiometry. Due to the spinel phase region, at high temperatures up to 1900°C a spinel phase containing 90% Al_2O_3 can be produced and maintained by rapid cooling. At lower temperatures, i.e., 1600°C during steel production, this high alumina content in alumina rich spinel becomes unstable and a mixture of spinel and free corundum (Al_2O_3) is formed. Alumina rich spinel phase remains stable at temperatures around 1600°C.

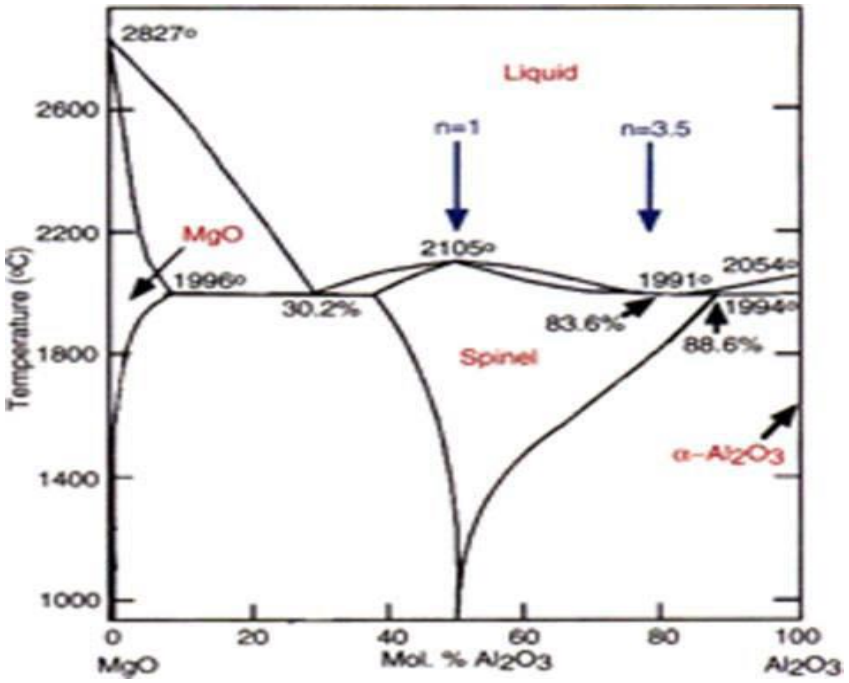

Fig. 4.2 MgO – Al_2O_3 phase diagram [29]

4.2 Literature Survey

Literature survey was conducted on magnesium aluminate spinel structures fabricated through conventional shaping methods and additive manufacturing techniques for refractory applications and described below.

G Wu et al, [30] investigated 5 lightweight periclase-$MgAl_2O_4$ spinel structures consists of porous spinel groups with different concentrations of spinel. These lightweight structures were analyzed for adherence and cement clinker resistance properties by sandwich and static crucible test. The authors investigated the effect of spinel content present in the porous spinel aggregates on the resistance of cement clinker and adherence properties using SEM and EDS. It was reported that the liquid phase occurred due to the reaction between the spinel and cement clinker which affected the resistance of the cement clinker. Also, the resistance of the corrosion of the spinel refractories were increased and adherence between cement clinker and spinel refractory was good at spinel concentration of 0-25 wt.%. On increasing the spinel concentration on porous aggregates resulted in excessive formation of liquid phase which reduced the corrosion resistance and adherence capability.

J M Pappas et al, [31] fabricated transparent spinel structures using laser direct deposition which is a one of the additive manufacturing techniques. Spinel structures were printed with 0.3% porosity and achieved the highest optical transmittance of 82% at a wavelength of 632.8 nm. The authors also investigated on silica dopants spinel structures to prevent cracking in the 3D printed spinel structures. It was observed that increasing silica dopants resulted in reduction of average total crack length by 79% and average crack density by 71%. The study also observed that higher concentration of dopant limits the optical transmission which is attributed to increase of porosity and secondary phase. Further the study reports the decreased fracture toughness of spinel and silica doped spinel structure from 2.4 $MPa.m^{1/2}$ to 1.9 $MPa.m^{1/2}$. The study also demonstrated the possibility of laser direct deposition method to fabricate transparent spinel structure and addition of dopants helped in solving cracking issues.

H Wang et al, [32] reported on the fabrication of transparent spinel ceramics samples using stereolithography based 3D printing process. Various spinel complex structures such as micro lattices and lenses were printed with high resolution of 100-200 μm and transparency of the printed samples achieved 97% of the transmittance limit. The authors have investigated the effect of parameters which governs the transparency of spinel ceramics which includes concentration of dispersant (3%), debinding schedule and sintering temperatures. The printed samples were pre-sintered at 1650^{o}C followed by HIPing at temperatures of 1800^{o}C to achieve the density close to theoretical value. Spinel micro lattices and lens have exhibited good optical imaging capability and transparent spinel micro lattices were used as photocatalyst support for TiO_2 which enhanced the photocatalytic efficiency compared to the opaque parts.

J M Pappas et al, [33-34] investigated on direct fabrication of transparent spinel structures from micrometer size magnesium aluminate spinel powder using laser direct deposition method. The author also studied the effect of parameters such as residual porosity and cracking on optical transparency of the printed spinel structures. Transmission analysis of fabricated spinel structures has exhibited 82% of maximum transmittance at 632.8 nm. Residual porosity and cracking of the printed samples were the key issues in achieving the transparency of the printed samples. Various processing parameters such as scan speed, laser power, powder flow rate and particle size of powder was studied by J M Pappas et al, [35]. Bulk samples have shown density of 98% at powder flow rate of 0.58 g/min. Grain size and total crack length of the samples were increased with the increase of laser power. Increase in scan speed resulted in increase in density initially and

decreased at the scan speed greater than the 2000 mm/min. Also, the authors observed that the residual porosity of the samples was decreased with increase of laser power. Lower powder flow rates (<0.1 g/min) resulted in decrease in the residual porosity which further led to high transparency of the printed spinel structures.

E Y Sako et al, [36-37] studied the in-situ formation of spinel and physical reactions associated with it such as various volume changes which results in pore generation. The authors were focused on the possible reasons for in-situ formed spinel castable exhibiting good corrosion resistance in industrial applications. The authors investigated cement-bonded magnesia-alumina castable which are designed using different particle sizes of dead-burnt magnesia. These castables were evaluated for microstructure and it has reported that, the fast migration of Mg^{2+} ions lead to vacancy accumulation followed by pore generation during the formation of spinel as result of Kirkendall effect. Volumetric expansion of castables affect by sintering efficiency and chemical interactions of MgO-Al_2O_3 in the mixture which generally do not exhibit any effect on the corrosion resistance of the spinel castables in industrial application.

P G Lampropoulou et al, [38] reported on investigations on mineral composition, microstructure, strength and thermal expansion of periclase-spinel refractories prepared from high purity magnesite and other synthetic compositions. Samples were prepared from sintered magnesite at 1600^{o}C and synthesized three compositions based on spinel at 1700^{o}C. After sintering final parts contain 8-11 wt. % Al_2O_3 and 19-21 wt. % Al_2O_3. Specimens with 19-21 wt.% alumina consists of more magnesia-alumina spinel and exhibited low linear thermal expansion coefficient (LTEC) due to the dimensional stability and thermal shock at high temperatures. Authors have reported that synthesized refractories have shown high apparent density and found as a suitable material for industrial application.

J Meng et al, [39] prepared the magnesium aluminate spinel refractories from chromium slag. It was reported that spinel refractories produced by traditional sintering process resulted in density of 3.14 g/cc and porosity of 9.16%. By adding more amount of MgO powder to the spinel could not met the requirements of refractory materials. For spinel parts produced by electric melting process, samples were achieved with density of 3.27 g/cc and porosity of 8.78%. Density and porosity volume of spinel parts were affected by concentration of magnesia and it was reported that adding of lower concentration of magnesia to spinel has satisfied the required properties for refractory raw materials.

Several researchers have published processing of spinel for high temperature and refractory application and very few literatures are found in the data base on printing of magnesium aluminate spinel structures using laser direct energy deposition method which uses powder to be deposited on platform of the printer and laser energy melt the particle according the virtual model. Also, available literature is more focused on 3D printing of transparent spinel structure, but no work has been reported on the fabrication of spinel structures through 3D printing technique for refractory and high temperature applications. Hence the study was focused on fabrication of magnesium aluminate spinel structures through ram type extrusion-based 3D printing process for high temperature and refractory applications.

In this study, magnesium aluminate spinel structures were printed into simple to complex shapes using ram type extrusion-based 3D printing process. Spinel powder was formulated with suitable rheological regime by adding optimum concentrations of water, binder and plasticizer and printed. Thermal gelation property of methylcellulose was applied successfully during the printing process to retain the shape of 3D printed parts. For comparative evaluation of the properties of 3D printed samples, spinel specimens were also prepared by slip casting process. All samples prepared by both the processing techniques were sintered and evaluated for the physico-chemical, mechanical and microstructural properties.

4.3 Experimental Procedure

4.3.1 Characterization of Magnesium Aluminate Spinel Powder

Magnesium aluminate spinel powder (S30CR, Baikowski, France) in the study was subjected to thermal passivation [40] and characterized for phase purity by X-Ray diffraction (XRD) (D8-Bruker, Germany) technique. Diffraction pattern recorded for the spinel powder is shown in Fig. 4.3 and represents the high phase purity of the powder.

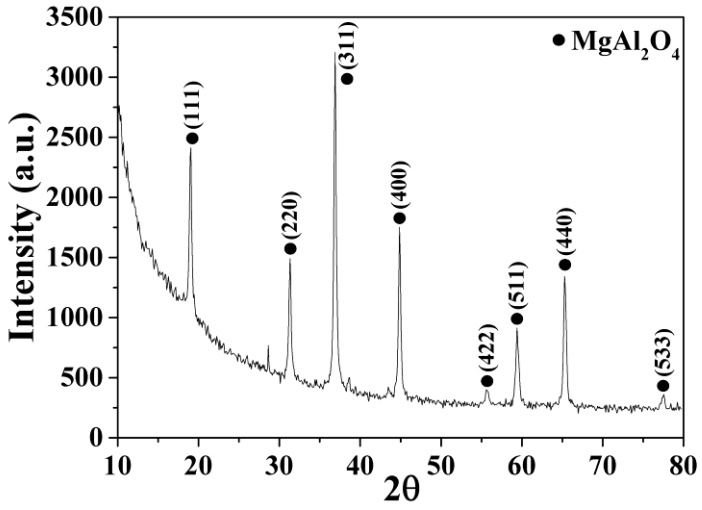

Fig 4.3 X-Ray Diffraction pattern of magnesium aluminate spinel powder

Spinel powder was characterized for particle size and its distribution by Laser Diffraction method (Malvern Instruments, UK). Recorded Intensity versus particle diameter data plotted and represented in Fig. 4.4. It is evident from the figure that, the spinel powder has an average particle size of 250 nm.

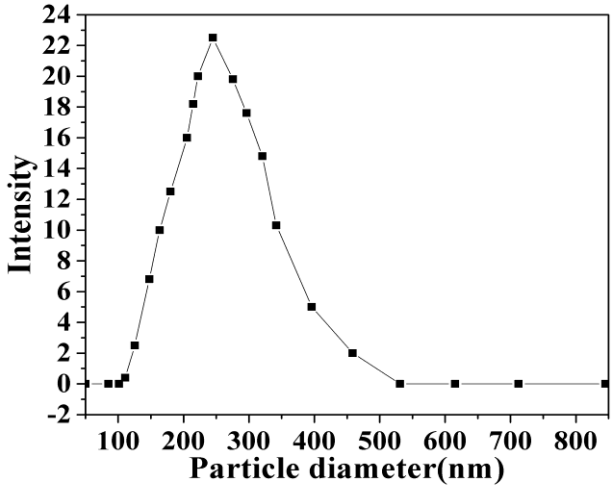

Fig 4.4 Particle size distribution of magnesium aluminate spinel powder

Magnesium aluminate spinel powder was also characterized for the chemical composition by Energy Dispersive Spectroscopy (EDS) and morphology by Scanning Electron Microscope (SEM). The EDS pattern and the morphology of spinel powder are shown in Fig.4.5 (a) and (b) respectively. It is evident from the EDS pattern that, the spinel powder exhibited 72% of aluminum

oxide and 28% of magnesium oxide which correlates well with the stoichiometry of spinel formulation. The morphology of spinel powder was found as irregular which is evident from the SEM micrographs.

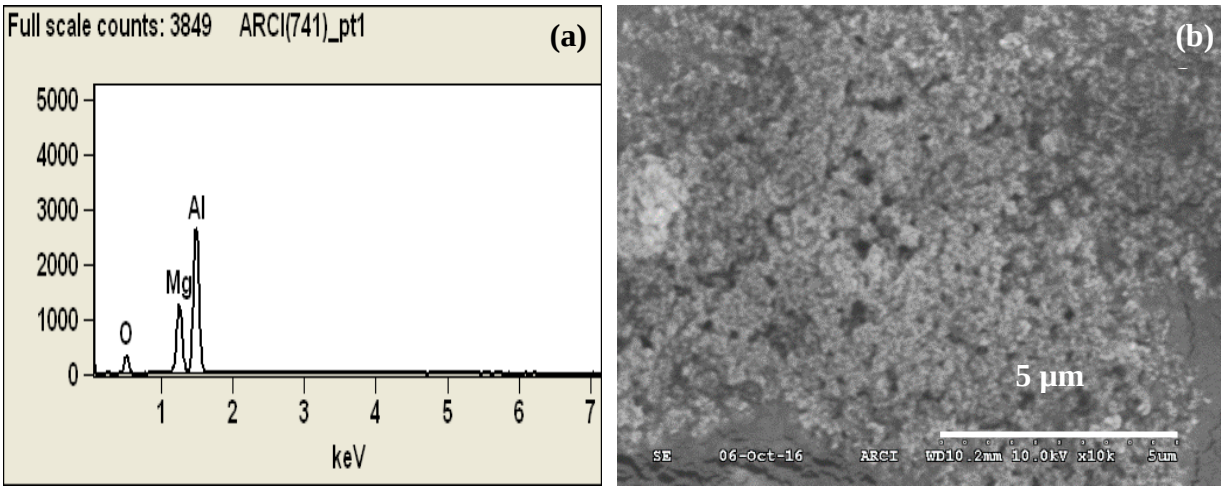

Fig 4.5 (a)EDS pattern and (b) Morphology of magnesium aluminate spinel powder

4.3.2 Preparation of Paste with Magnesium Aluminate Spinel Powder

Magnesium aluminate spinel powder was made into printable paste by using methylcellulose (MC) solution as a binder and water as liquid medium. First, the MC solution was prepared by dissolving 0.25 wt. % of MC in 40 wt. % of water using ball milling for 30 minutes. The spinel powder was added to prepared aqueous MC solution slowly and kneaded in vacuum sigma kneader for 30 minutes. Further resulted paste was characterized for rheological properties using rheometer (MCR 51, Anton Paar, Austria). Recorded data of shear rate (γ) versus viscosity (η) of the spinel paste was plotted and shown in Fig.4.6 (a) and Shear rate exponent calculated using Power law model by plotting $\ln\gamma$ versus $\ln\eta$ which is represented in Fig.4.6 (b). It is evident from the shear rate versus viscosity plot that, the viscosity of the paste was decreased with the increase in shear rate and exhibited a shear thinning behavior. Calculated shear rate exponent (n) = 0.45 also confirmed the shear thinning behavior of spinel paste.

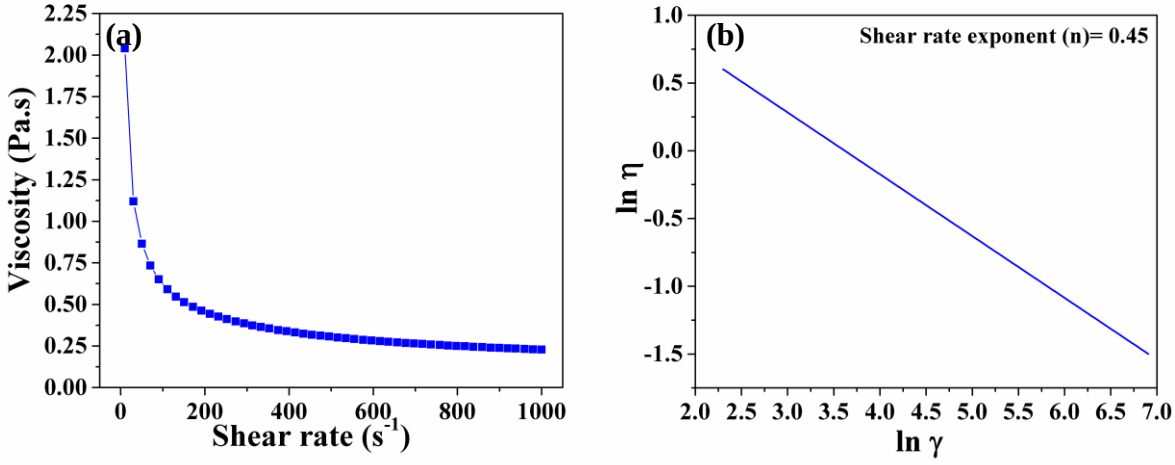

Fig.4.6 Plots of (a) shear rate vs. viscosity and (b) lnγ vs. lnη of spinel paste

In order to study the thermal induced gelation behavior of MC, the prepared spinel pastes with MC and without MC were subjected to viscosity measurement at constant shear rate of 10 s^{-1} and at varying temperatures ranges from 25-72^{o}C with heating rate of 1^{o}C/min. Recorded complex viscosity vs temperature data plotted and shown in Fig 4.7 (a) and (b). It is evident from Fig 4.7 (a) that, initial viscosity of the paste at 25^{o}C was 52 Pa. s, and as the temperature increased from 35^{o}C to 45^{o}C, the viscosity of the paste was suddenly raised from 242 Pa. s to 50,300 Pa.s. This can be attributed to the crosslinking of monomers due to the dehydration of methoxy groups present in the methylcellulose compound followed by hydrophobic association of the monomers resulted in polymerization. Hence the viscosity of the paste with MC exhibited great difference from 35 to 45^{o}C and further, the viscosity of the paste remained constant from 50-70^{o}C due to the evaporation of the water molecule present in the paste. During cooling, this reaction was irreversible as the polymer network hold ceramic particles together and forms a rigid body. In the case of paste without MC represented in Fig.4.7 (b), the viscosity of the paste was 26 Pa.s at 25^{o}C and it is increased gradually to 2000 Pa.s with the increase in the temperature to 70^{o}C due to the evaporation of water.

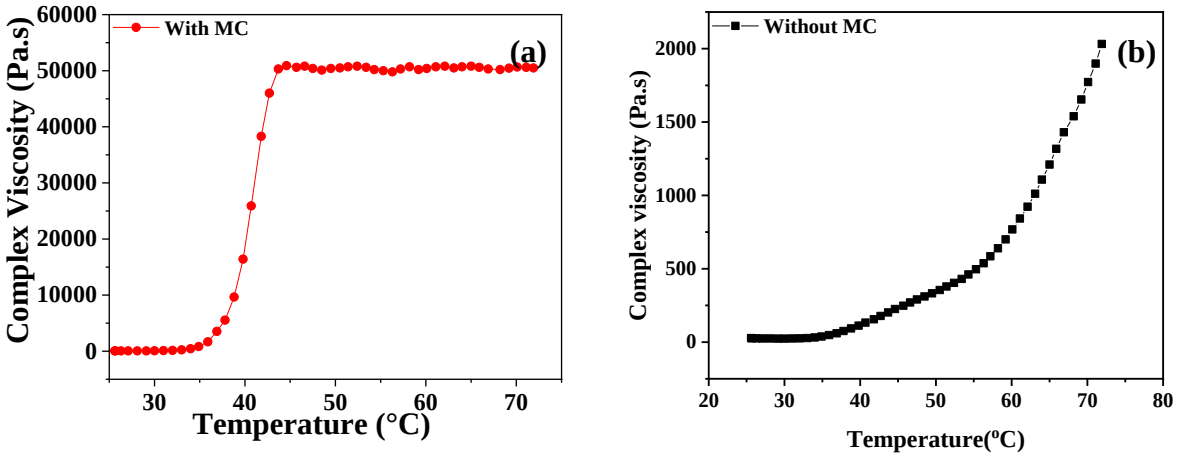

Fig 4.7 Plot of complex viscosity vs. temperature for paste (a) with MC and (b) without MC

4.3.3 3D Printing of Spinel Parts

General steps involved in the printing of physical objects from 3D CAD model have been described in the chapter.2. Similarly, in this study 3D CAD models were designed for simple and complex shaped geometries and converted into .STL files. These files were further subjected to slicing operation with the selected printing conditions such as printing speed and layer thickness. The generated sliced files were saved as G-codes and saved in micro controller unit of the 3D printer. The spinel paste with suitable rheological behavior was used to fill in the barrel of the ram-based extruder without any air gap and placed in the holder of the 3D printer (3D Cerami, Maker city, India) fitted with 1.00 mm nozzle. Printing speed of 9 mm/s was found optimum for printing of spinel structures with good structural integrity and the sample with in the dimensional tolerances. During the printing process, the samples were exposed uniformly to the hot air (35-45^{o}C) which initiates the polymerization by crosslinking of monomers of methylcellulose molecule. Due to the polymerization, it forms gel network which holds the ceramic particles together and forms a rigid body. Typical spinel 3D printed green samples are shown in Fig.4.8.

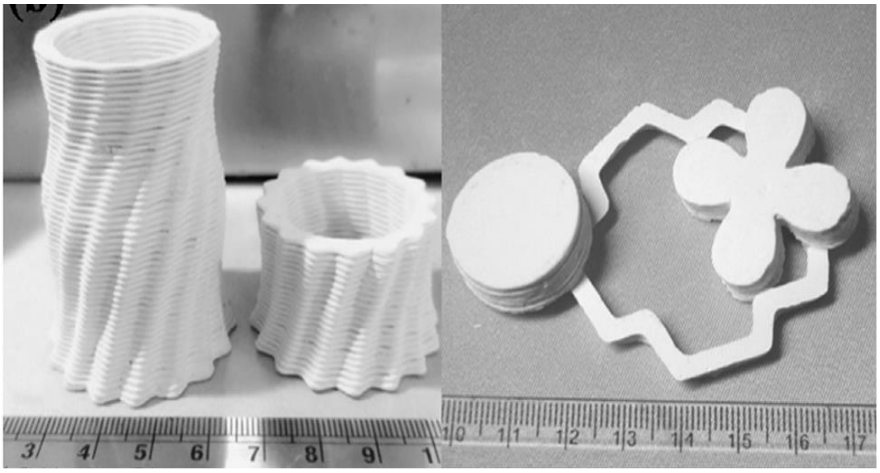

Fig 4.8 3D printed magnesium aluminate green samples

Additionally, spinel samples were prepared using slip casting process for comparative evaluation of properties of 3D printed parts. Spinel slurry was prepared by dispersing spinel powder using Darvan 821 A in 40 wt.% of water. This mix was milled for 4 hours in a pot jar mill with alumina balls as a milling medium. The obtained stable and homogeneous spinel slurry was poured into preselected shape of porous plaster of paris mold. After removing the samples from porous mold, the samples were dried in oven at 40^{o}C.

4.3.4 Sintering of 3D Printed and Slip Cast Samples

Spinel samples fabricated through ram type extrusion-based 3D printing process and slip cast samples were subjected to binder removal by heating the samples to 550^{o}C at a heating rate of 1^{o}C/min. Further theses samples were sintered at 1650^{o}C at a heating rate of 100^{o}C/h in a muffle furnace (Deltech, USA) and soaked for 1 hour to achieve the theoretical density. These sintering conditions were found optimum based on several trials at our laboratory. The schedule used for the sintering of all the spinel samples is shown on Fig.4.9 and the 3D printed and slip casted sintered samples have been shown in Fig.4.10 (a) and (b) respectively.

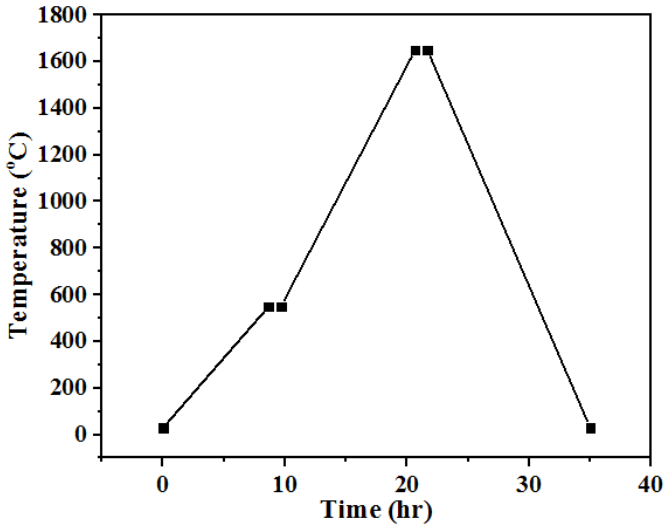

Fig 4.9 Sintering schedule for magnesium aluminate spinel 3D printed and slip cast samples

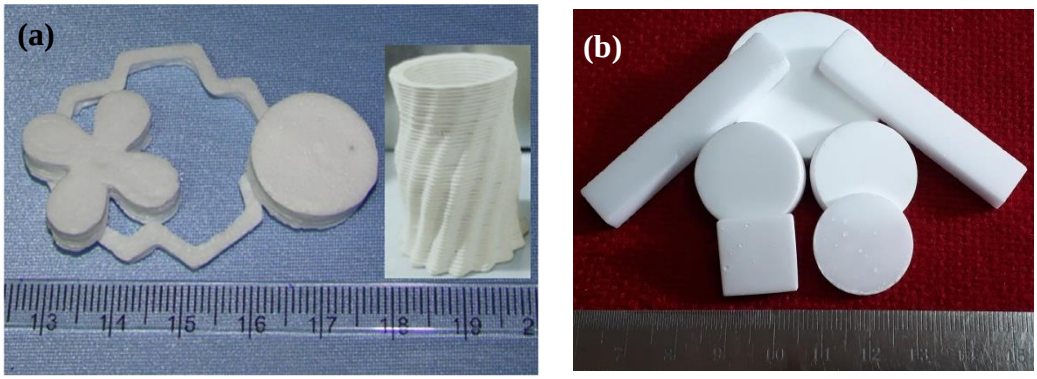

Fig 4.10 Magnesium aluminate spinel sintered samples (a) 3D printing process and (b) Slip casting process

4.3.5 Characterization of 3D Printed and Slip Casted Spinel Specimens

Spinel samples processed by both 3D printing and slip casting process were subjected to evaluation of physico-chemical, mechanical and microstructural properties. Sintered density of all the samples was measured using Archimedes principle (ASTM C792). The sintered density of 3.47 g/cc for the 3D printed sintered samples and 3.51 g/cc for sintered slip cast specimens were measured. Further, both the samples were polished using ceramographic procedures and measured the hardness using Vickers hardness tester (Leco, St. Joseph, MI). Ten indentations were recorded for each specimen at 500 gm load and found the hardness of 11.5 GPa and 12.5 GPa for 3D printed

and slip cast sintered samples respectively. Also, the 3D printed and slip cast specimens were measured for flexural strength using three-point bend test (ASTM C1161) in Universal Testing Machine (UTM) (Instron-5584). All the samples were shaped to size of 45 mm x 4 mm x 3 mm and placed at the fixtures of three-point bend test in UTM. Load was applied on the mid-point of the test specimens with ramp rate of 0.5 mm/min. Recorded load vs. displacement data were plotted and shown in Fig. 4.11 and the flexural strength of both 3D printed and slip cast spinel samples were found to be 182 MPa and 205 MPa respectively. Further, the specimens failed through three-point bend test were analyzed for the fracture surface using Scanning Electron Microscope (SEM) (S-4300SE/N, Hitachi, Tokyo, Japan). It is evident from the SEM micrographs, fracture surface of the 3D printed spinel sample has shown layered structure which is formed during 3D printing process. Fracture surface of both specimens have shown intergranular and intragranular fracture. Measured properties of 3D printed spinel and slip cast specimen is tabulated in Table 4.2

Table 4.2 Properties of sintered 3D printed and slip cast specimens

Properties	3D printed specimens	Slip cast specimens
Density (g/cc)	**3.47**	**3.51**
Hardness (GPa)	**11.5**	**12.5**
Flexural strength (MPa)	**182**	**205**

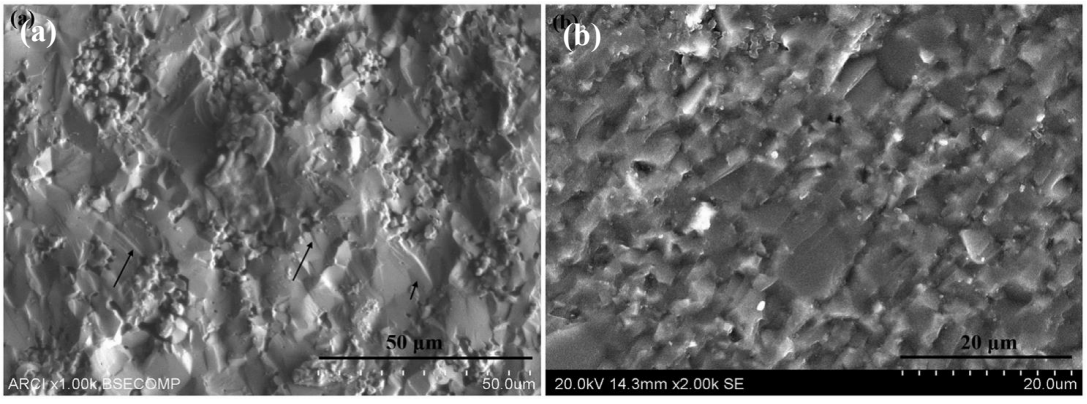

Fig. 4.11 Fracture surface of (a) 3D printed and (b) slip cast specimens

4.4. Fabrication of Magnesium Aluminate Spinel Mesh Structures using Fused Deposition Modeling (FDM) in Collaboration with Baylor College of Medicine, USA

Finer mesh focusing on the application of cranioplasty surgery could not be printed using existing facility at ARCI due to the inherent limitation of the equipment. In view of the above, collaborative research was initiated with Baylor College of Medicine, USA where such facilities were available. Spinel powder was supplied by ARCI for 3D printing process. In order to prepare a printable paste, the binder was prepared by dissolving 10 gms of Polyvinyl Alcohol (PVA) in 100ml water under stirring for overnight. One gram of spinel powder was added to 40 ml of prepared PVA solution and subjected to stirring for 1 day. The obtained homogeneous solution was transferred to cartridge (10 ml) and extruded through 30-gauge needle on glass slide. Complex spinel mesh structures were designed using BioCad software (regenHU) and printed through 3D bioprinter (3D Discovery, regenHU, Switzerland). Printing parameters such as layer thickness, gauge and pressure of the needle and pore size were optimized to print the mesh structures and found 30-gauge needle (Inner Diameter=0.15 mm, length 6.35 mm), needle pressure of 0.145 MPa and printing velocity of 10mm/s optimum. Temperature (40^{o}C) of the platform of the 3D printer maintained constant for in-situ drying of the structures.

4.4.1 Characterization of 3D Printed Green Spinel Mesh

Dried green 3D printed spinel mesh samples are shown in Fig. 4.12 were tested under optical microscope to characterize for cellular parameters and shown in Fig.4.13. It is clear from Fig. 4.13 that, the mesh have a unit cell length (l) of 980 μm, wall thickness (t) of rib was 420 μm and cell density of 18 PPI (pores per inch).

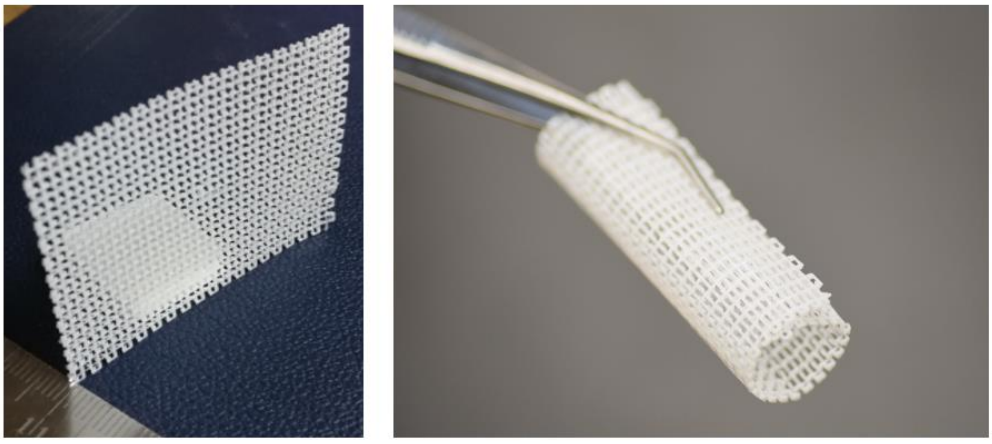

Fig.4.12 Green spinel mesh 3D printed at Baylor College of Medicine, USA

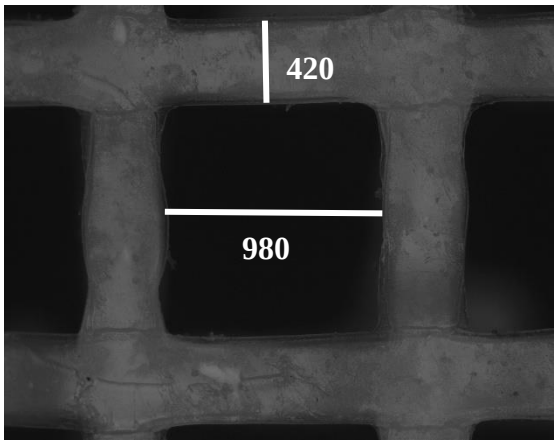

Fig.4.13 Optical micrograph of 3D printed green spinel mesh

Further, 3D printed green spinel mesh samples were characterized for Thermo-gravimetric (TG)-Differential Thermal Analysis (DTA) and recorded mass change and various thermal events with respect to temperature. Fig.4.14 represents the TG-DTA plot of 3D printed green spinel mesh. It is evident from the TG-DTA plot that, a total weight loss of 60% was occurred from room temperature to 1000^{o}C along with two major thermal events. Thermal event occurred in TG-DTA curve at 350-400^{o}C is due to the thermal decomposition of poly vinyl alcohol (PVA) which was used for the preparation of ink and another thermal event occurred at 450-600^{o}C due to the complete decomposition of the PVA. Higher concentration of PVA resulted in the flexibility of the printed spinel mesh structure at green stage.

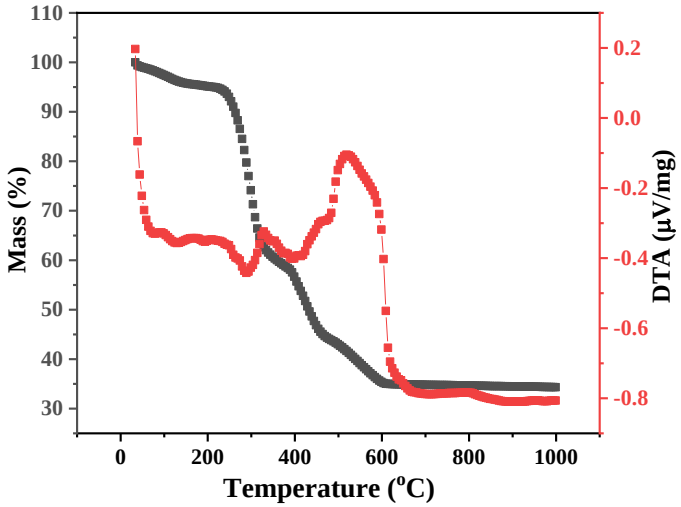

Fig.4.14 TG-DTA curve of 3D printed green spinel mesh

4.4.2 Sintering and HIPing Schedule for 3D Printed Green Spinel Mesh

3D printed green spinel mesh structure has shown good flexibility and integrity of the shape due to higher concentration of PVA. Based on the TG-DTA studies, sintering schedule for printed spinel mesh was optimized. Initially green spinel mesh was subjected to heating with low heating rate of 0.5^{o}C/min till 400^{o}C with soaking period of 30 minutes and again heated to 600^{o}C hold for 30 minutes. Further this spinel mesh structure was heated to 1500^{o}C with the heating rate of 2^{o}C/min followed by heating to 1650^{o}C with heating rate of 0.5^{o}C/min and soaked for 1 hour. The need for providing low heating rate is to remove the binder slowly which enables the shape retention of the printed parts with in the dimensional tolerances as well as the prevention of microcracking. Higher heating rate results in faster binder burnout leading to generation of non-uniform stresses which further results in micro cracking of the sample. 3D printed green spinel mesh samples were also subjected to Hot Isostatic Pressing (HIPing) to achieve the theoretical densities with good mechanical properties. HIPing schedule was optimized based on the several trials at our laboratory. Spinel mesh structures were HIPed at temperature of 1800^{o}C and at pressure of argon gas of 195 MPa. Schedule of pressure less sintering and HIPing process have shown in Fig.4.15 (a) and (b) respectively.

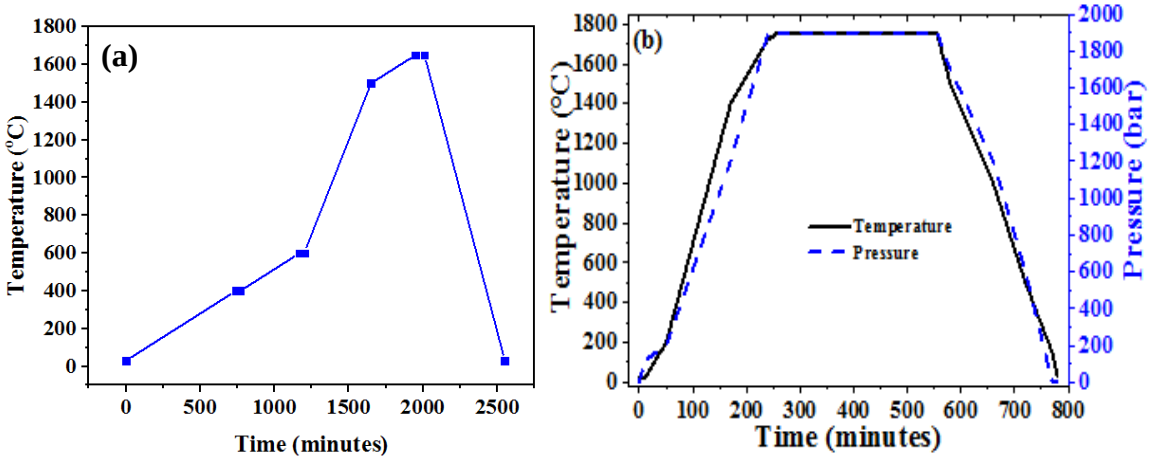

Fig 4.15 Sintering schedule of (a) Pressureless and (b) Hot isostatic pressing for 3D printed spinel mesh

4.4.3 Characterization of Sintered Spinel Mesh Structures

Spinel mesh structures sintered under both pressurerless and HIPed conditions were measured for its density by Archimedes principle (ASTM B962) using high precision weighing

balance (ME204 E/A04; Mettler –Toledo AG, Switzerland). The density of the sintered sample was found to be 3.51 g/cc which is 98% of theoretical density and 3.57 g/cc for HIPed sample which is 99.7% of theoretical density of magnesium aluminate spinel. Further these structures were measured for cellular parameters using optical microscope and tabulated in Table.3. It is evident from Table.4.3 that, edge length (l) and wall thickness of pressureless sintered and HIPed spinel mesh samples have shown 58% and 40% reduction in size from green stage respectively.

Further pressureless sintered and HIPed samples were characterized for microstructural anlaysis using Scanning Electron Microscope (SEM) (Gemini 500, Carl Zeiss, Germany). Microstructure of pressureless sintered spinel structure is shown in Fig.4.16 and it is evident from the microstructure that, it has shown graded microstructure with in the ribs of sintered samples. Grain size of pressure less sintered samples was calculated using SEM micrographs by linear intercept method. It was observed that size of grains was large in the center of the rib comparing to the grain size calculated along the edges of the rib. An average grain size of 5.2 μm at the center and 0.7 μm at the edges of the rib was found for pressureless sintered samples. The difference in the grain structure across the samples is attributed to the segregation of binders near the edges during the printing, which results in generation of residual pores because of binder burnout. These residual pores are retained by lower heating rate provided during the sintering and act as obstacle for grain growth. Similarly, the SEM micrographs of HIPed spinel mesh structures are shown in Fig.4.17 which also exhibited the graded grain structure and grain growth. HIPing of the spinel structures resulted in achieving the higher density by eliminating residual pores and average grain size of 2 μm at edges and 12.5 μm at center of the rib.

Table 4.3 Cellular parameters and density of the 3D printed magnesium aluminate spinel mesh structures

Spinel mesh	Cell length (μm)	Rib thickness (μm)	PPI	Density
Green	**980**	**420**	**18**	**-**
Sintered	**410**	**250**	**30**	**3.51**
HIPed	**410**	**250**	**30**	**3.57**

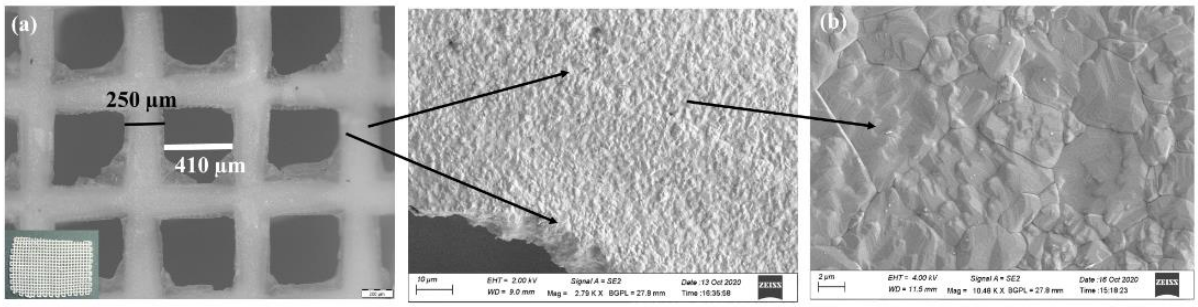

Fig.4.16 (a) Optical image and (b) Microstructure of sintered magnesium aluminate ($MgAl_2O_4$) spinel mesh sample

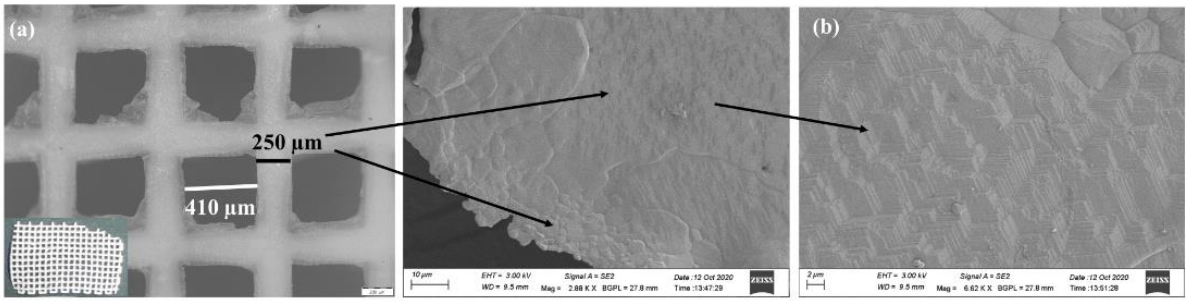

Fig.4.17 (a) Optical image and (b) Microstructure of HIPed magnesium aluminate ($MgAl_2O_4$) spinel mesh sample

Further HIPed samples were polished using ceramography procedure and measured the hardness using Vickers hardness tester (VMHT; Walter UHL, Germany). A load of 100 gms was applied on the sample to indent for a dwell time of 15 sec. Ten indentations were recorded on the HIPed sample and found the average hardness of 12.95 GPa. Additionally, elastic modulus of the HIPed spinel mesh structures was measured using Nano-indentation (iNano; KLA Corporation) method by applying highest load of 45 mN to take measurements and recorded the data as elastic modulus with respect to indenter depth. The elastic modulus of the HIPed structures was found to be 238±15 GPa.

4.5 Conclusions

Magnesium aluminate ($MgAl_2O_4$) spinel powder was characterized for phase purity, particle size distribution, morphology and chemical quantitative analysis. Spinel paste was prepared using methylcellulose in low concentration and its thermal gelation property applied successfully to print simple to complex geometries. Printing speed of 9 mm/s was found optimum

to print the spinel structures with in the dimensional tolerance and in-situ drying of 3D printed spinel specimens resulted in substantial reduction in the drying time compared to the slip cast samples. 3D printed samples were sintered and exhibited density of 3.47 g/cc, hardness of 11.5 GPa and flexural strength of 180 MPa. The properties of 3D printed sintered samples exhibited marginal variation compared to sintered slip cast specimens.

Spinel powder supplied by ARCI was made into printable paste and printed flexible and fine mesh with edge length of 980 μm and rib thickness of 420 μm at Baylor College of Medicine, USA. 3D printed green spinel mesh samples were conventionally sintered based on the TG-DTA studies and exhibited the density of 98% of theoretical density. 3D printed spinel structures were HIPed at temperature of 1800^{o}C and pressure of 195 MPa. Density of the HIPed 3D printed spinel specimens have shown enhancement of density from 98% to 99.7% of theoretical density due to application of pressure and temperature simultaneously. Microstructure of the pressureless sintered and HIPed mesh samples exhibited graded grain structure with finer grains at edges and coarser grains at center of the rib. Hardness and Nano-indentation tests were conducted for ceramographically polished HIPed 3D printed spinel samples and found the hardness of 12.95 GPa and elastic modulus of 238 ±15 MPa.

4.6 References

1. C Baudin, R Martinez, P Pena, High-temperature mechanical behavior of stoichiometric magnesium spinel, Journal of American Ceramic Society, 1995;78:1857-1862.
2. T E Mitchell, Dislocations and Mechanical properties of MgO-Al_2O_3 spinel single crystals, Journal of American Ceramic Society, 2004;82:3305-3316.
3. I Ganesh, G Jangantha Reddy, G Sundarajan, S M Olhero, P M C Torres, J M F Ferreira, Influence of processing route on microstructure and mechanical properties of $MgAl_2O_4$ spinel, 2010;36:473-482.
4. O Tokariev, L Schnetter, T Beck, J Malzebender, Grain size effect on the mechanical proeprties of transparent spinel ceramics, 2013;33:749-757.
5. A F Dericioglu, A R Boccaccini, I Dlouhy, Y Kagawa, Effect of chemical composition on the optical properties and fracture toughness of transparent magnesium aluminate spinel ceramics, Materials Transactions, 2005;46:996-1003.

6. K Waetzig, A Krell, The effect of composition on the optical properties and hardness of transparent Al-rich Mgo-nAl_2O_3 spinel ceramics, 2015;99:946-953.
7. C Gajdowski, J Bohmler, Y Loguoilloux, S Lemonnier, S d'Astorg, E Barraud, A Leriche, Influence of post-HIP temperature on microstructural and optical properties of pure $MgAl_2O_4$ spinel: From opaque to transparent ceramics, Journal of the European Ceramic Society, 2017;37:5347-5351.
8. G Glide, P Patel, P Patterson, D Blodgett, Donald Duncan, D Hahn, Evaluation of hot pressing and hot isostatic pressing parameters on the optical properties of spinel, Journal of American Ceramic Society, 2005;88:2747-2751.
9. P Ramavath, P Biswas, K Rajeswari, M B Suresh, R Johnson, G Padmanabham, C S Kumbhar, T K Chongdar, N M Gokhale, Optical and mechanical properties of compaction and slip cast processed transparent polycrystalline spinel ceramics, Ceramics International, 2014;40:5575-5581.
10. I Ganesh, A review on magnesium aluminate ($MgAl_2O_4$) spinel: synthesis, processing and applications, International Materials Reviews, 2013;58:63-112
11. W Yan, G Wu, S Ma, S Schaffoner, Y Dai, Z Chen, J QI, N Li, Energy efficient lightweight periclase-magnesium alumina spinel catastables containing porous aggregates for the working lining of steel ladles, Journal of European Ceramic Society, 2018;38:4276-4282.
12. I Ganesh, S Battacharjee, B P Saha, R Johnson, K Rajeshwari, R Sengupta, M V R Rao, Y R Mahajan, An efficient $MgAl_2O_4$ spinel additive for improve slag erosion and penetration resistance of high-Al_2O_3 and MgO-C refractories, Ceramics International, 2002;28:245-253.
13. W Peng, Z Chen, W Yan, S Schaffoner, G Li, Y Li, C Jia, Advanced lightweight periclase-magnesium aluminate spinel refractories with high mechanical properties and high corrosion resistance, Construction and Building Materials, 2021;291:123388.
14. R Salomao, M O C V Boas, V C Pandolfelli, Porous alumina-spinel ceramics for high temperature applications, Ceramics International, 2011;37:1393-1399.
15. A Feltz, W Polzl, Spinel forming ceramics of the system $Fe_xNi_yMn_{3-x-y}O_4$ for high temperature NTC thermistor applications, Journal of the European Ceramic Society, 2000;20:2353-2366.

16. M C L Patterson, A A DiGiovanni, L Fehrenbacher, D W Roy, Spinel: gaining momentum in optical applications, Proceedings SPIE 5078, Window and Dome Technologies VIII, 2003.
17. R Sarkar, Refractory applications of magnesium aluminate spinel, International Ceramic Review, Refractories Manual 2010.
18. D Schmidtmeier, G Buchel, A Buhr, Magnesium aluminate spinel raw materials for high performance steel ladles, Materialy Ceramiczne, 2009;61:223-227.
19. Z Shi, Q Zhao, B Guo, T Ji, H Wang, A review on processing polycrystalline magnesium aluminate spinel ($MgAl_2O_4$): Sintering techniques, material properties and machinability, Materials & Design, 2020;193:108858.
20. P Biswas, R Johnson, Y R Mahajan, G Padmanabham, Processing of infrared transparent magnesium aluminate spinel, Handbook of Advanced Ceramics and Composites, 2019;1-37.
21. M Ramisetty, S Sastri, U Kashlikar, L M Goldman, N Nag, Transparent polycrystalline cubic spinels:protect and defend, Americal Ceramic Society Bulletin, 2013;92:20-25.
22. A Krell, K Waetzig, J Klimke, Influence of the structure of $Mgo.nAl_2O_3$ spinel lattices on transparent ceramics processing and properties, Journal of the European Ceramic Society, 2012;32:2887-2898.
23. J Sanghera, S Bayya, G Villalobos, W Kim, J Frantz, B Shaw, B Sadowski, R Miklos, C Baker, M Hunt, I Aggarwal, F Kung, D Reicher, S Peplinski, A Ogloza, C Lamar, P Varmette, L D Sandre, Transparent ceramics for high-energy laser systems, Optical Materials, 2011;33:511-518.
24. G Cevlkbas, A B Tugrul, U Onen, T Boyraz, B Buyuk, An investigation on aluminium titanate-spinel composites behavior in radiation, AIP conference proceedings 1653, 2015:020029.
25. H-E Kim, S J Zinkle, W R Allen, Preparation of Magnesium aluminate spinel containing controlled amounts of ^{17}O isotope, Journal of American Ceramic Society, 1991;74:1442-1444.
26. E Feldbach, I Kudryavtseva, K Mizohata, G Prieditis, J Raisanen, E Shablonin, A Luschik, Optical characteristics of virgin and proton irradiated ceramics of magnesium aluminate spinel, Optical Materials, 2019;96:109308

27. W X Zhang, Y L Sun, T J Wang, Effect of spinel growth on the delamination of thermal barrier coatings, Key Engineering Materials, 2011;462-463:389-394.
28. K E Sickafus, J M Wills, N W Grimes, Structure of spinel, Journal of the American Ceramic Society, 2004;82:3279-3292.
29. B Hallstedt, Thermodynamic assessment of the system MgO-Al2O3, Journal of American Ceramic Society, 1992;75:1497-1507
30. G Wu, W Yan, S Schaffoner, X Lin. S Ma, Y Zhai, X Liu, L Xu, Effect of magnesium aluminate spinel content of porous aggregates on cement clinker corrosion and adherence properties of lightweight periclase-spinel refractories, Construction and Building Material, 2018;185:102-109.
31. J M Pappas and X Dong, Direct 3D Printing of silica doped transparent magnesium aluminate spinel ceramics, Materials,2020;13:4810.
32. H Wang, L Y Liu, P Ye, Z Huang, A Y R Ng, Z Du, Z Dong, D Tang, C L Gan, 3D printing of transparent spinel ceramics with transmittance approaching the theoretical limit, Advanced Materials, 2021;33:2007072
33. J M Pappas, A R Thakur, E C Kinzel, X Dong, Direct 3D printing of transparent magnesium aluminate spinel ceramics, Journal of Laser Applications,2021;33:012018.
34. J M Pappas, E C Kinzel, X Dong, Laser direct deposited transparent magnesium aluminate spinel ceramics, Manufacturing letters; 2020;24:92-95.
35. J M Pappas, X Dong, Porosity characterization of additively manufactured transparent MgAl2O4 spinel by laser direct deposition, Ceramics International, 2020;46:6745-6755.
36. E Y Sako, M A Braulio, E Zinngrebe, S R Vander Lann, V C Pandolfelli, Fundamentals and applications on in situ spinel formation mechanisms in Al2O3-MgO refractory castables, Ceramics International, 2012;382243-2251.
37. E Y Sako, M A L Braulio, V C Pandolfelli, Insights on in situ MgAl2O4 formation mechanism and its correlation with the corrosion resistance of pinel-containing refractory castables, Refractories Worldforum, 2014;6:1
38. P G Lampropoulou, C G Katagas, I.Iliopoulos, D Papoulis, New periclase-spinel refractories from densely sintered high purity magnesite and new synthetic compositions based on spinel. Part 1: Study if mineral composition, microstructure, thermal expansion

and ultimate strength in compression, Refractories and Industrial Ceramics, 2013;53:310-316.

39. J Meng, W Chen, J Zhao, L Liu, Study of the high-temperature synthesis of $MgAl_2O_4$ spinel refractory raw materials from chromium slag, Article in High Temperature Materials and Processes, 2017.
40. K Rajeswari, P Biswas, R Johnson, S Prabhudesai, V K Sharma, S Mitra, R Mukhopadhayay, Effect of surface passivation in spinel slurry towards hydrolysis: neutron scattering and rheological studies, Journal of Dispersion Science Technology, 2014;35:1442-1448.

****

CHAPTER- 5

3D PRINTING OF CERAMIC HONEYCOMB STRUCTURES AND THE PROPERTY EVALUATION

5.1 Introduction

5.1.1 Honeycomb Structures

Ceramic honeycombs are manmade cellular structures that resembles the bees honeycomb exist in nature. Ceramic honeycombs are composites in which one is solid and the other one is an empty space generally filled with air. They are made up of regular array of cells with triangular, circular, square and hexagonal geometries. Due to its inherent features, they can be engineered with various relative densities by tailoring unit cell parameters such as wall thickness(t) and edge length(l) for a given material as depicted in Fig.5.1

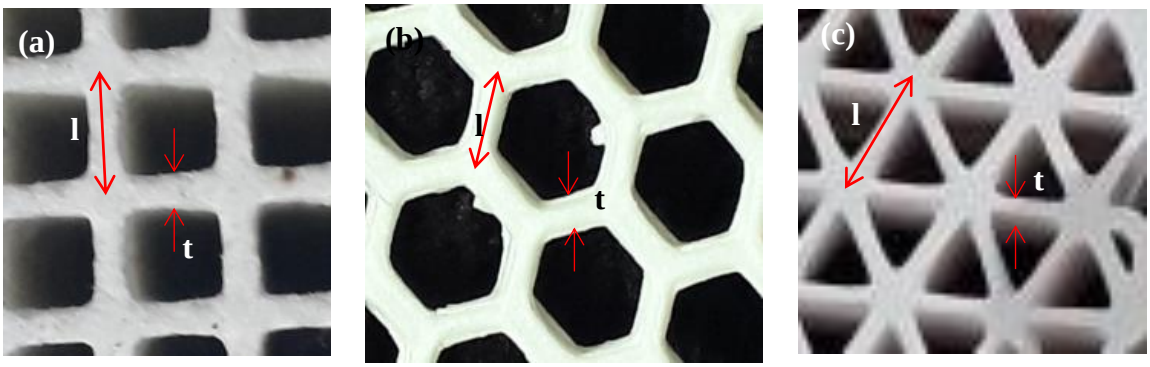

Fig.5.1 Unit cell parameters for (a) Square (b) Hexagonal and (c) Triangle channel

Ceramic honeycombs are generally fabricated by extrusion process using a very complex die manufactured through advanced machining techniques from special alloys. During extrusion process the ceramic formulation formed in the form of cohesive paste under pressure flow laterally through the die slits and extrude as a single monolith of honeycomb [1-3]. This method permits mass manufacturing of honeycombs however every geometry needs a specific die tailored for the desired geometry.

The cellular properties of honeycomb structures are described by M.F Ashby [4] in his classical book on Cellular Solids-Structure and Properties. Table. 5.1. shows estimation of various cellular parameters based on their unit cell dimensions.

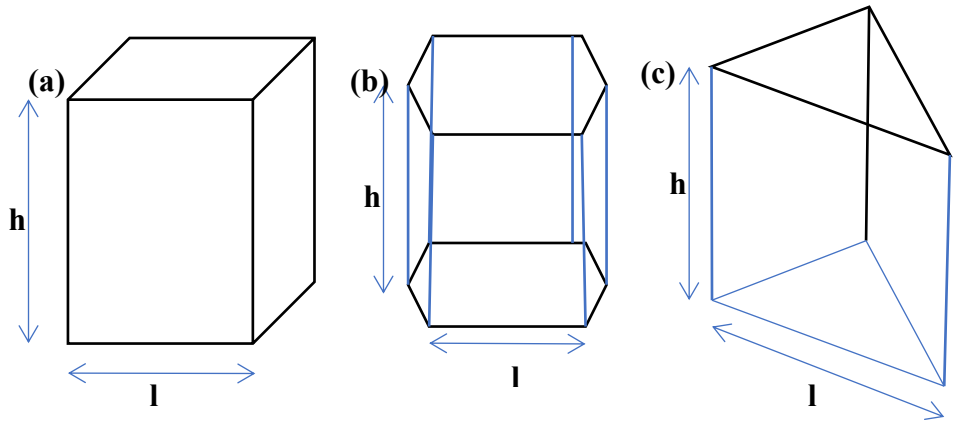

Fig.5.2 Three-dimensional structures of (a) Square (b) Hexagonal and (c) Triangle cells

Table. 5.1 Cellular parameters of square, hexagon and Triangle geometries

Cell shape	No. of faces(f)	No. of edges(n)	No. of vertices(v)	Cell volume (V)	Surface area (A)	Edge length(l)
Square channel	6	12	8	$l^3 * A_r$	$2l^2 * (1 + 2A_r$	$8l * (1 + \frac{A_r}{2})$
Hexagonal channel	8	18	12	$\frac{3\sqrt{3}}{2} l^3 A_r$	$3\sqrt{3}\, l^2 (1 + \frac{2A_r}{\sqrt{3}})$	$12l(1 + \frac{A_r}{2})$
Triangular channel	5	9	6	$\frac{\sqrt{3}}{4} * l^3 A_r$	$\frac{\sqrt{3}}{2} * l^2 (1 + 2\sqrt{3}A_{r)}$	$6l(1 + \frac{A_r}{2})$
	Relative density (ρ*/ρs)			**Open Frontal Area (OFA)**		
Square channel	$\left(\frac{\rho *}{\rho s}\right) = \left(2\frac{t}{l}\right)\left(1 - \left(\frac{t}{2l}\right)\right)$			$\left(\frac{(l-t)^2}{l^2}\right)$		
Hexagonal channel	$\left(\frac{\rho *}{\rho s}\right) = \left(\frac{2t}{\sqrt{3}l}\right)\left(1 - \left(\frac{t}{l(2\sqrt{3})}\right)\right)$			$\left(\frac{(l-0.577t)^2}{l^2}\right)$		
Triangular channel	$(\frac{\rho *}{\rho s}) = (\frac{2\sqrt{3}t}{l})(1 - \sqrt{3}\frac{t}{2l})$			$\left(\frac{(l-1.732t)^2}{l^2}\right)$		

Where A_r is the aspect ratio= h/l ratio,

h- height of the channel

l is the length and t is the thickness.

5.2 Literature Survey

Unlike the extrusion process as mentioned above which require dies with specific geometries, 3D printing permits the printing of several simple to complex configurations with the same infrastructure. A few reports are available in public domain which discusses the additive manufacturing of cellular structures as detailed in this section. Z Chen et al [5] have used Digital Light Processing technique to fabricate bulk parts including honeycomb structure with cordierite formulation and investigated for its mechanical and microstructural properties. The author has examined the printed parts for quality in terms of physical (shrinkage, dimensional tolerance and porosity) and mechanical properties. Printing parameters such as layer thickness and exposure time of layer) and the particle size of cordierite slurries were optimized using orthogonal array of experiments. The study observed that printing of bulk parts with cordierite slurry consisting smaller particle size results in more shrinkage and thus lead to lower porosity.

S Couck et al [6] used direct ink writing method to fabricate zeolite SAPO-34 based honeycomb structured adsorbents. The author has used methylcellulose as a binder and graphite as a lubricant for preparing zeolite SAPO-34 ink and printed honeycomb adsorbents were characterized for SEM and Mercury (Hg)-porosimeter. Adsorption isotherms were recorded using gravimetric technique at high pressure and different temperatures by determining the CO_2 adsorption capacity, its affinity and heat of adsorption. Adsorption studies were carried out by separation potential of CO_2 and N_2 mixture was investigated. CO_2 and N_2 separated were analyzed with the Ideal Adsorbed Solution Theory (IAST). The study reports that capacity of the zeolite honeycombs was decreased due to the binder added in honeycomb structures during the experiment and also due to the effect of temperature as well as the material degradation.

J Maurath et al [7] has investigated on fabrication of high specific strength open-porous cellular structures by direct ink writing technique. A homogeneous capillary suspension was prepared with alumina which has been used as ink to print highly porous hexagonal honeycomb structure using filament-based ink writing with nozzle diameter less than or equal to 200 μm. Cellular structures were conventionally dried, debinded and sintered without any crack formation. The study reports that printed open porous structure with strut porosity of 45-60% and pore size

of $X_{50,3}$< 6 μm. The specific strength of open porous structure is increased by factor of 2-3 times larger than the density. Anisotropy behavior of honeycomb structures in-plane under compression load is larger than out-of-plane conditions. The investigation claims filament-based ink writing technique offers an opportunity to fabricate cellular porous structure with high mechanical strength.

C Minas et al [8], proposed the study in which the macroporous cellular structure can be fabricated by direct ink writing technique. In this study, direct ink writing of emulsions in the form of ceramic gels/suspension results in macroporous hierarchical structure with pore size in micrometer. The size of pore determined solvent droplet used in preparing the emulsions. Rheological behavior of emulsions is important parameter during the direct ink writing process. Surface modification of powder particles and stabilized emulsions (polyvinyl alcohol) are the key parameters to achieve the structure with either open or closed porosities. Further the study also states that the use of surface modified powder and emulsion together allows fabricating the object with bulk porosity which is difficult in conventional shaping methods.

B G Compton et al [9], described about the first cellular composites made by 3D printing process. These composites are light in weight and these are collection of fiber filled epoxy with unique mechanical properties. The alignment of fillers with high aspect ratio and control of printing direction determines the orientation of layers in the part. The approach will be applicable to fabricate various bio-ceramic composites with optimized printing conditions.

C Wu et al [10] investigated on the preparation of uniform calcium silicate ($CaSiO_3$) scaffolds for the first time for bone regeneration application with controlled pore size, structure and better mechanical properties. The compressive strength of prepared calcium silicates by modifying the 3D printing process is almost 120 times more than conventional scaffolds made by polyurethane foam using template honeycombs process. The study suggests that the calcium silicate scaffolds prepared by 3D Printing method can be an alternative for beta-tricalcium phosphate scaffolds in vivo osteogenesis.

A Ortona et al [11], have described about the process to produce silicon carbide cellular ceramic structure by rapid prototyping and replication methods. The preceramic structures were printed by using stereolithography and selective laser cutting followed by the pyrolyzation of preceramic articles and infiltration with molten silicon. The study introduces the hybrid method to fabricate cellular structures with engineered porosity, better surface finish, excellent mechanical

properties and microstructure as compared to the other rapid prototyping technologies. The structures produced by the replicated rapid prototyping structures have exhibited more strength than foams due to regularity of struts.

R Felzmann et al [12] investigated on the fabrication of ceramic cellular structures using lithography based additive manufacturing technology. The fabrication of cellular ceramic structure by layer wise printing of liquid photopolymer resins on platform followed by the solidification using ultraviolet/visible or infrared light. The suspensions with higher solid loading can be processed even though the viscosity of resin is high. Alumina and Bio active ceramic powder such as beta-tricalcium phosphate were printed for bone tissue applications. Printing of alumina with 50 vol% solid loading of filled resin helps to achieve the fully dense parts (>99%) with high fracture strength of 516 MPa.

B Leukers et al [13] has reported on preparation of hydroxyl apatite scaffolds by 3D Printing technique. The sintered samples were characterized for its biocompatibility and cytotoxicity. 3D Printing process provides flexibility to fabricate patient specific implants with hydroxy apatite powder for bone repairing applications.

J T Muth et al [14], studied the significance of direct foam writing technique during the fabrication of architected cellular ceramic structures with customized geometry, microstructure and mechanical properties. By varying the dimensions of cellular structure, hexagonal and triangular configured honeycombs were composed, and elastic modulus of struts of hexagonal and triangular honeycombs were tuned to 1 to 27 GPa approximately. The study reveals that the stiffness of these configured honeycombs was more than 10^7 Pa.

Though several works have been carried out in producing honeycomb structures as reported above, no work has been reported in producing the honeycomb structures through extrusion of paste-based 3D printing method followed by conventional heat treatment procedures on which the current study is focused. Three formulations such as Cordierite (Magnesium Aluminate Silicate ($Mg_2Al_4Si_5O_{18}$), Alumina (Al_2O_3), and Aluminum silicate ($Al_2Si_2O_5(OH)_4$ (Clay)) were formulated with additives to achieve printable paste and processed to obtain the honeycomb structures. The chemistry and configuration of designed honeycombs is shown in Table. 5.2. These green honeycombs are further sintered or heat treated to achieve desirable properties for specific applications.

Table. 5.2 Design of ceramic honeycomb structures

S. No	Process	Cordierite Honeycomb structures								
	3D extrusion printing process	**Square channel**			**Triangular channel**			**Hexagon channel**		
1.		l (mm)	t (mm)	OFA (%)	l (mm)	t (mm)	OFA (%)	l (mm)	t (mm)	OFA (%)
		11.18	1.00	80±5	14.38	1.00	80±5	6.37	1.00	80±5
2.		**Porcelain clay honeycomb structures**								
	3D extrusion printing process	**Square channel**			**Triangular channel**			**Hexagon channel**		
		l (mm)	t (mm)	OFA (%)	l (mm)	t (mm)	OFA (%)	l (mm)	t (mm)	OFA (%)
		3.49	1.00	50	6.09	1.00	51	4.06	1.00	73
		6.52	1.00	71	13.40	1.00	75	5.53	1.00	80
3.		**Alumina honeycomb structures**								
	3D extrusion printing process	**Square channel**								
		l (mm)			t(mm)			OFA (%)		
		4			1			56		

Where l is edge length, t is wall thickness and OFA is open frontal area of honeycomb channel.

5.3 3D Printing of Cordierite Honeycomb Structures

5.3.1 Cordierite Chemistry

Cordierite is a naturally occurring mineral with the chemical name of magnesium aluminum silicate with the formula $Mg_2Al_4Si_5O_{18}$. Technically cordierite is termed as ternary or tri-axial system composed of chemical compounds such as $2MgO.2Al_2O_3.\ 5SiO_2$.

This ternary system helps to understand the various compounds during the cordierite formation. The phase diagram of $MgO\text{-}Al_2O_3\text{-}SiO_2$ [18] is shown in Fig 5.3. The cordierite consists of various binary compounds such as Mullite ($3Al_2O_3.2SiO_2$), Enstatite ($MgO.SiO_2$), spinel ($MgO.Al_2O_3$) and Forsterite ($2MgO.SiO_2$) along with ternary compounds mainly cordierite ($2MgO.2Al_2O_3.5SiO_2$) and sapphirine ($4MgO.5Al_2O_3.2SiO_2$). Different raw materials are used to prepare the cordierite powder. Hence it contains different types of impurities namely iron oxide,

alkaline oxides etc., during the formation of cordierite at sintering stage. Fig 5.4 represents cordierite region is surrounded by six crystalline phases. Those are Tridymite-Mullite-Cordierite, Protoenstatite-Tridymite-Cordierite, Forsterite-Protoenstatite-Cordierite, Sapphirine-Spinel-Cordierite, Mullite-Sapphirine-Cordierite and Forsterite-Sapphirine-Cordierite. The impurities present in the raw materials lead to decrease in sintering temperature of cordierite and increase the amount of liquid phase in fired body. Cordierite is the only stable compound in tri-axial phase diagram which melts at 1460ºC by forming the Mullite and liquid [1 and 15].

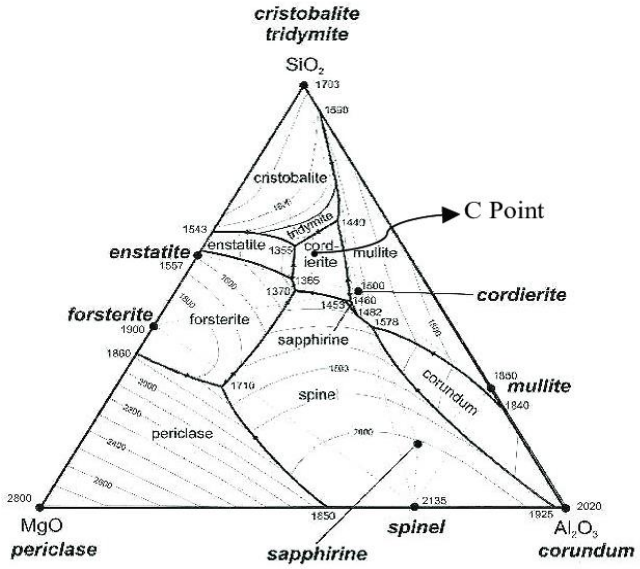

Fig 5.3 Phase diagram of $MgO.SiO_2.Al_2O_3$

Conventionally, cordierite is prepared from naturally occurring precursor oxides such as kaolinite clay (Aluminum silicate), talc (Magnesium silicate) and alumina. These precursor oxides (talc and clay) have a short fusion range which is practically not possible and unable to produce 100% cordierite phase. Hence it is difficult to produce cordierite ceramics with high strength, high density due to its short and narrow firing range.

Cordierite formation by using precursor oxides such as clay, talc and the reactions associated with it is represented by following equation [16-20].

$$\underset{\text{(Kaolin)}}{Al_2O_3.2SiO_2.2H_2O} \xrightarrow{800^oC} \underset{\text{(Metakaolin)}}{Al_2O_3.2SiO_2} + H_2O \qquad (1)$$

$$\underset{\text{(Talc)}}{3MgO.4SiO_2.H_2O} \xrightarrow{800^oC} \underset{\text{(Protoenstatite)}}{3(MgO.SiO_2)} + \underset{\text{(Amorphous silica)}}{SiO_2} + H_2O \qquad (2)$$

$$(Al_2O_3.2SiO_2) \xrightarrow{1000^oC} 3Al_2O_3.2SiO_2 + 4SiO_2 \quad (3)$$
(Metakaolin) (Mullite) (Cristobalite)

$$2(3Al_2O_3.2SiO_2) + 5SiO_2 + 6(MgO.\ SiO_2) \xrightarrow{1150^oC} 3\ (2MgO{:}2Al_2O_3 : 5SiO_2) \quad (4)$$
(Mullite) (Crystobalite) (Protoenstatite) (Cordierite)

Among the three raw materials, the talc and clay exist with more structural water than alumina. These integral structural water present in the clay is removed by dehydration process at 800^{o}C and loss of hydroxyl group from the water. Further, it results in transformation of phase to γ-Alumina at high temperature. Similarly for talc (Magnesium silicate), after dehydration process and dehydroxylation, it is converted into protoenstatite and amorphous silica. Metakaolin at higher temperature (1000^{o}C) leads to formation of Mullite and crystobalite. Further at 1150^{o}C, the reaction 4 represents the formation of cordierite. The properties of cordierite ceramics are tabulated in Table. 5.3.

Table. 5.3 Properties of cordierite ceramics [21]

Property	**Value**	**Units**
Density	2.5	gm/cm^3
Hardness	5.8	GPa
Modulus of Elasticity	82	GPa
Compressive strength	206-351	MPa
Flexural strength	55-117	MPa
Coefficient of Thermal Expansion at 25-600^{o}C	$1.7\text{-}2.4*10^{-6}$	/^{o}C
Thermal conductivity at 25^{o}C	3	W/mK

Cordierite ceramic exhibits the unique electrical and thermal properties such as low dielectric constant (ε=5-6), good resistant to thermal shock, low thermal expansion coefficient, chemically inert and high resistivity (ρ $>10^{12}$ Ωcm). Due to the inherent properties of cordierite mentioned above, they found many applications in the form of cordierite solid as well as the honeycomb structures. One of the most significant products in ceramic world i.e., cordierite ceramic honeycomb structures which is used for auto-exhaust emission control, generally produced by extrusion process. In the current study, two approaches have been attempted to

fabricate ceramic honeycomb structures. 1. 3D extrusion printing process and 2. Replication of parts using 3D printed poly lactic acid (PLA) templates.

5.3.2 Experimental Process Flowchart

The flowchart represented in Fig.5.4 depicts the steps involved in fabrication of cordierite honeycomb structures using extrusion-based 3D printing process.

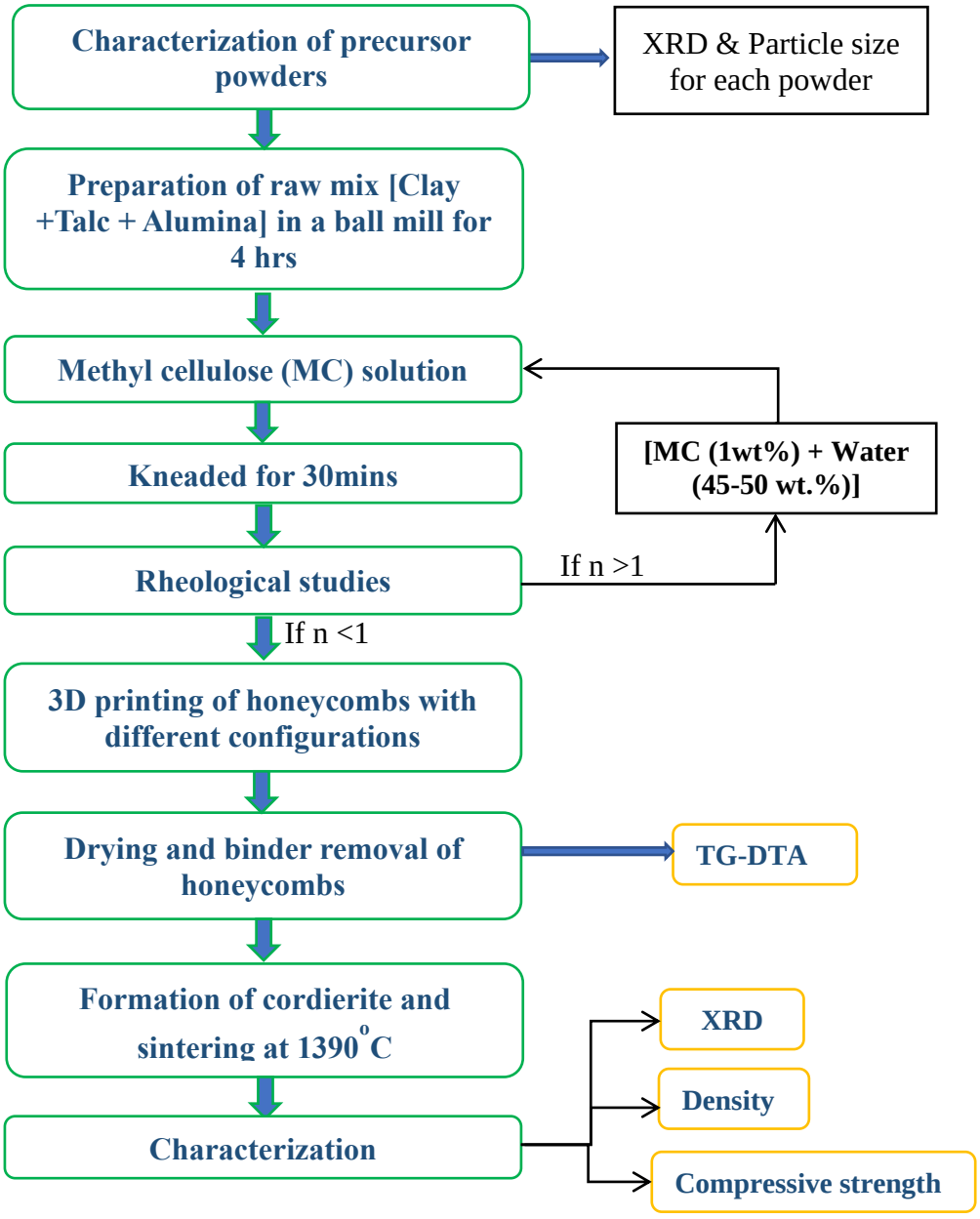

Fig 5.4 Process flowchart for fabricating cordierite honeycomb structures by 3D Printing

5.3.2.1 Characterization of Raw Materials

In the current study, raw materials used for preparing the cordierite raw mix, such as the clay (aluminum silicate), talc (magnesium silicate) and alumina powders were characterized individually for its phase identification and purity by X-Ray Diffraction (XRD) and particle size distribution by Dynamic Light Scattering (DLS) technique. The XRD patterns recorded for the cordierite precursors such as clay, talc and alumina powders are shown in Fig 5.5(a), (b) and (c) respectively. The XRD pattern of clay shows kaolinite as the major phase, magnesium silicate as the major phase for talc and α-phase for alumina powder.

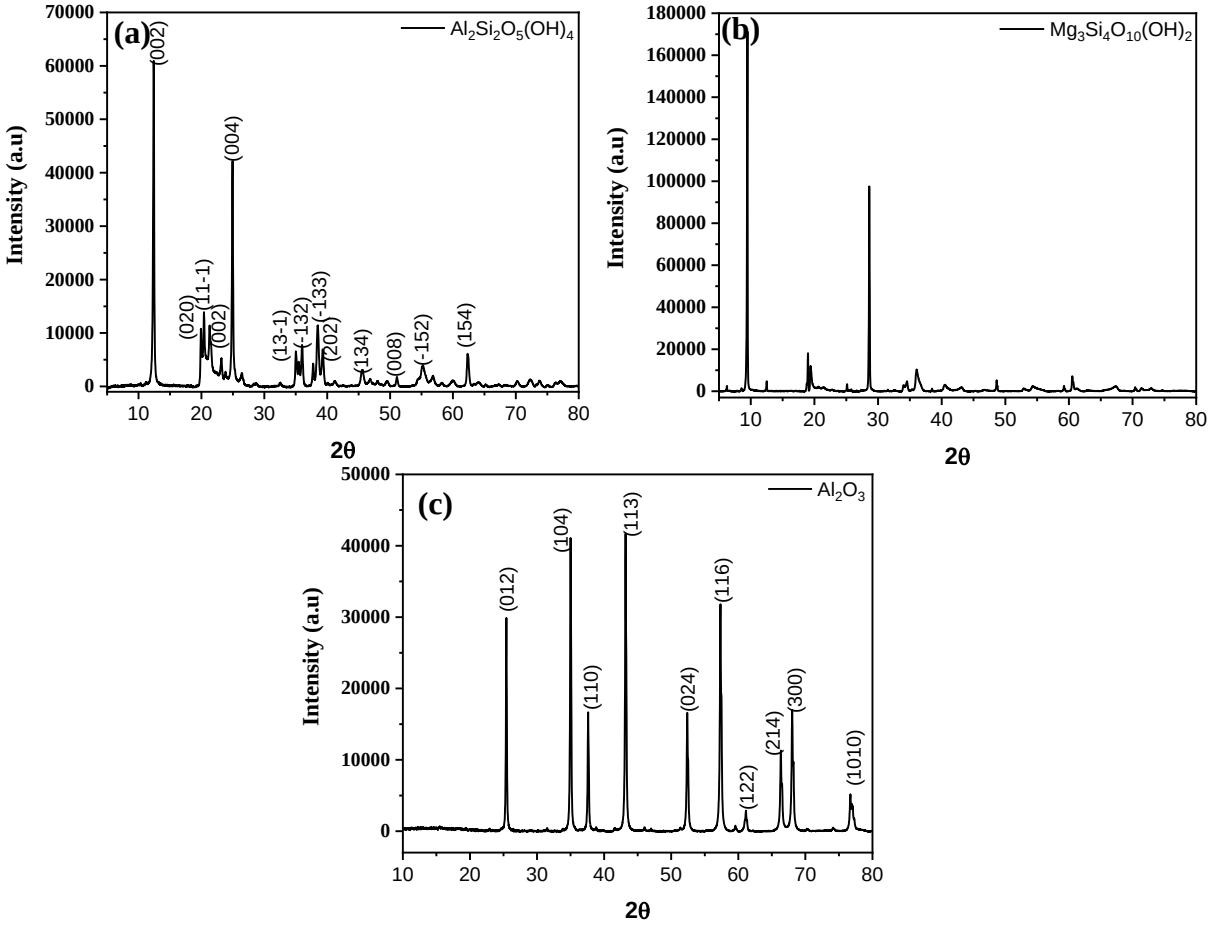

Fig 5.5 XRD patterns of (a) Clay (b) Talc and (c) Alumina powder

The particle sizes of clay, talc and alumina minerals are shown in Fig 5.6 (a), (b) and (c) respectively. It is evident from the Fig.5.6, clay exhibited an average particle size of 1119 nm with unimodal distribution, talc exhibited a bimodal distribution with an average particle size of 1857 nm and alumina has shown an average particle size of 330 nm.

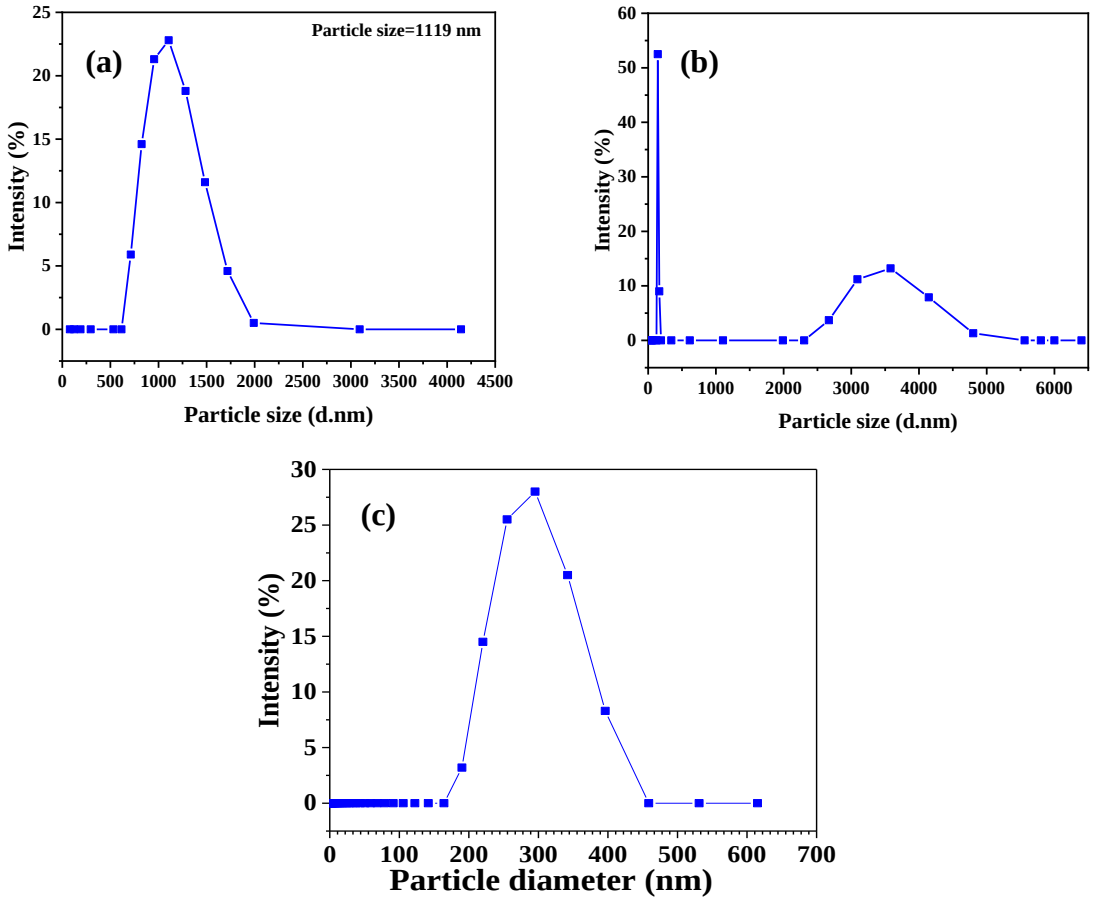

Fig 5.6 Particle size of (a) Clay (b) Talc and (c) Alumina powder

5.3.2.2 Preparation of Cordierite Raw Mix and Paste

Cordierite raw mix was prepared by adding and mixing of precursor oxide such as clay (Aluminum silicate, $Al_2Si_2O_5(OH)_4$), talc (magnesium silicate ($Mg_3Si_4O_{10}(OH)_2$) and α-alumina (Al_2O_3) in an optimized proportions based on the stoichiometry of cordierite ($2MgO:2Al_2O_3:5SiO_2$). Further this mixture was milled for 4 hours in ball mill with alumina balls added in1:2 ratio of the weight of the powder to achieve the homogeneous mixing of all precursor powders. To prepare printable paste with milled cordierite raw mix, an aqueous binder solution was prepared with methylcellulose (MC). MC solution was prepared by dissolving 1wt% of methylcellulose in 40-45 wt.% water with 1wt% polyethylene glycol (PEG) (Mol.wt.380-420) for 30minutes in ball milling. After forming the homogenous MC solution, the cordierite raw mix was added slowly to the MC solution. Further the mixture was kneaded under vacuum for 30 minutes in sigma kneader with a rpm of 30. After ensuring that the prepared feedstock does not contain

any agglomerates and clusters, the paste was subjected to rheological measurements under varying shear rate.

The viscosity of the paste/feedstock was measured using rheometer (MCR 51, Anton Paar, Austria). A small amount of cordierite paste was kept on the parallel plate setup and viscosity of the paste was measured under varying shear rate from 1 to 1000 1/s. The shear rate versus viscosity plot is shown in Fig 5.7(a) and lnγ versus lnŋ is shown in Fig 5.7 (b). It is evident from Fig. 5.7(a) that the viscosity of the paste was decreasing with varying shear rate thus proves the pseudo-plastic behavior and also slope of lnγ versus lnŋ (shear rate exponent(n=0.87<1)) (Fig.7(b)) calculated by the Power law model confirms the pseudo-plastic nature of the prepared paste.

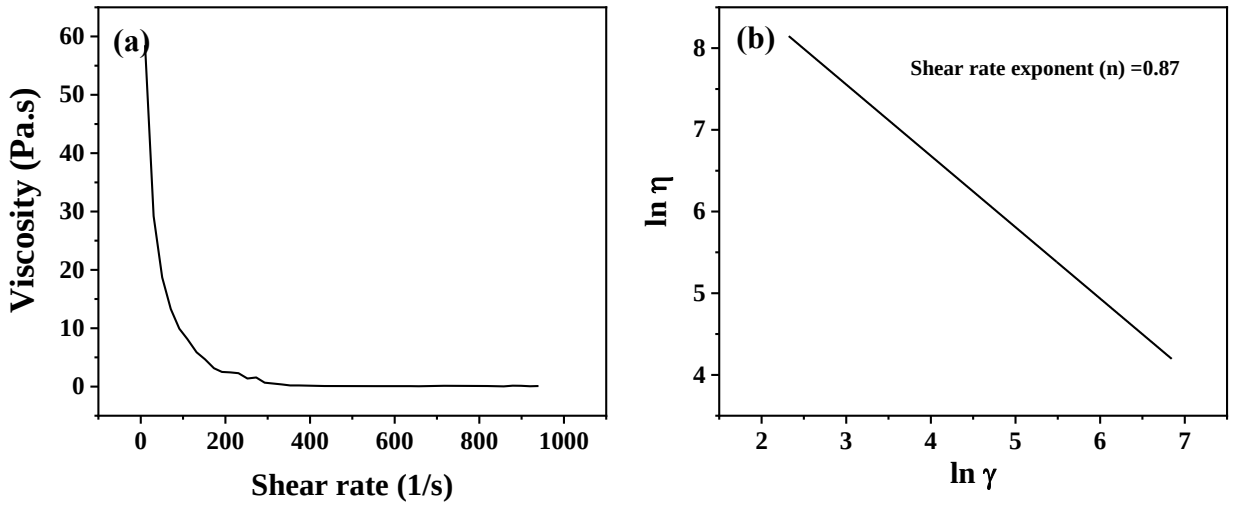

Fig 5.7 Plot of (a) shear rate vs viscosity and (b) lnγ vs lnŋ

5.3.3 3D Printing of Cordierite Honeycombs

To print honeycomb structures with cordierite, a square model was designed by using CAD software and converted into .STL file. Further the STL file was imported into Repetier software and sliced with the printing conditions such as layer thickness of 1 mm, printing speed of 4-5 mm/s, and solid infill density of 15% for square, triangle and hexagonal configured honeycombs to maintain constant relative density for all the honeycomb structures. The term infill density is defined as a percentage of area filled by the material during the printing process. The cellular parameters of honeycomb structure were mentioned in Table. 5.4.

Table. 5.4 Cellular parameters of honeycomb structures

Honeycomb	Thickness (mm)	Edge length (mm)	Surface area (cm^2)	Open frontal area (%)	Relative density
Hexagonal cell	1.00	6.37	24.65	80±5	0.45±5
Square cell	1.00	11.18	23.71	80±5	0.45±5
Triangular cell	1.00	14.38	23.75	80±5	0.45±5

From Table. 5.4 it is clear that the wall thickness of all channels is same due to the uniform layer thickness of printing. The edge length of the hexagonal, square and triangular cells was varied due to the geometry of cells although the infill density percentage is same with in the area. Other cellular parameters such as open frontal area and relative density of the honeycomb structures are calculated using the formulas mentioned in Table. 5.1.

5.3.3.1 Generation of CAD Model

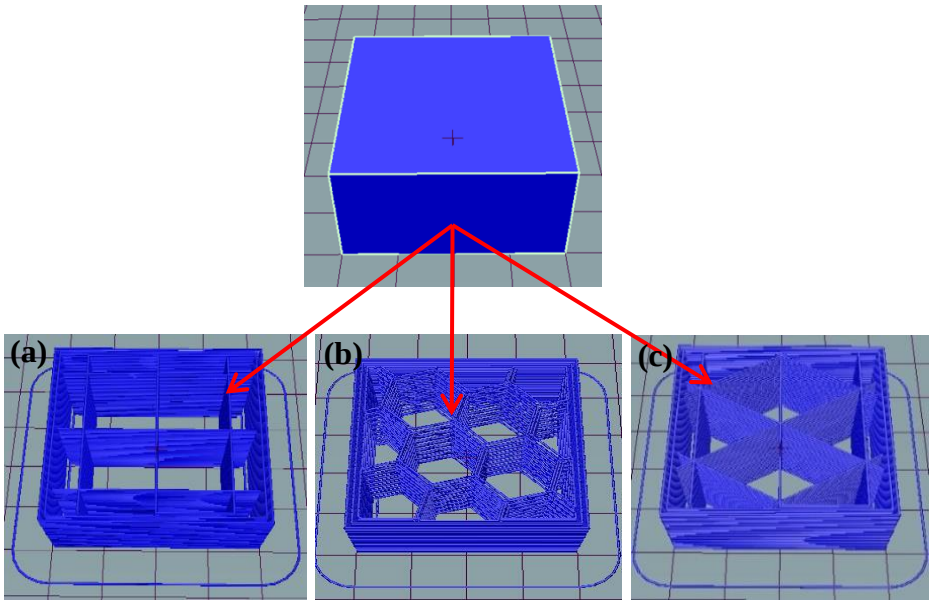

Fig 5.8 3D CAD model with (a) square, (b) hexagonal and (c) triangular configurations sliced with 15% solid infill density

Fig 5.8 (a), (b) and (c) represents the CAD model with sliced honeycomb virtual models with square, hexagonal and triangular channels respectively.

As described in the previous chapter, the thermal gelation behavior of MC was applied during printing process to retain the shape of honeycomb structures [22-25]. The honeycomb structures were printed with square, hexagonal and triangle channel and exposed to the gelation temperature of 45^{o}C to 60^{o}C during the printing process. Later the structure with handleable strength were dried in microwave oven to remove the water present in structure uniformly. 3D Printed dried honeycomb structures with all three configuration is shown in Fig 5.9. A small piece of dried honeycomb structure was characterized for thermogravimetry and Differential thermal analysis (TG-DTA) (STA 449 F3, Netzsch, Germany) to analyze the occurring of various thermal events and reactions during the formation of cordierite phase.

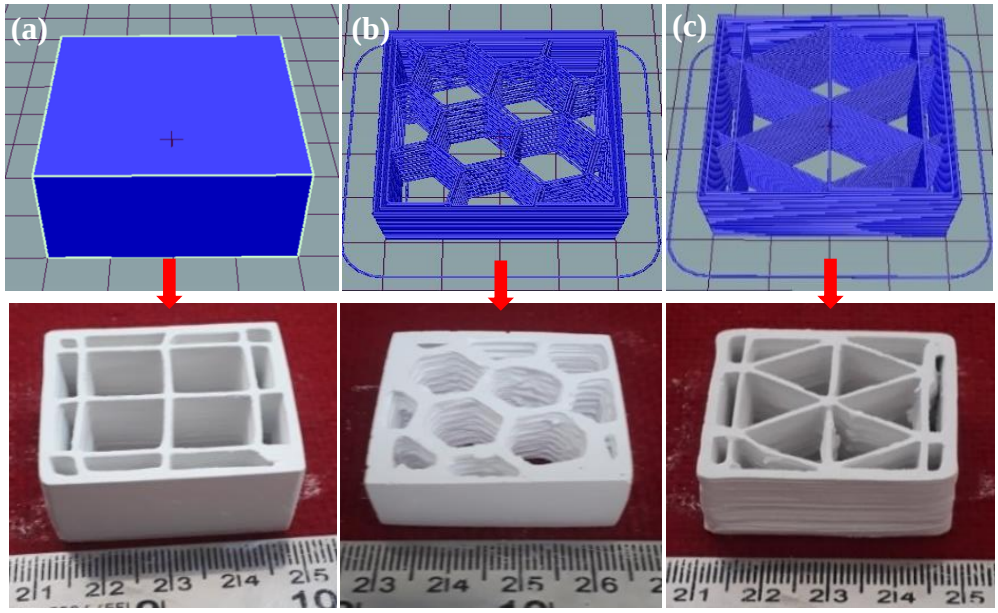

Fig 5.9 3D Printed honeycomb structures with (a) Square, (b) Hexagon and (C) Triangle channel

5.3.4 Characterization of Green Honeycomb Structures

The green density of 3D printed green honeycomb structures were measured using dimensional method. TG-DTA plot for 3D Printed green honeycomb structure is shown in Fig 5.10. It is evident from the TG-DTA plot, various thermal events and reactions occurred during the formation of cordierite from precursor oxides such as clay, talc and alumina. The TG plot represents the total 2.89% of weight loss has been occurred as the temperature rises from room

temperature to 400^{o}C which can be attributed to removal of adsorbed water by surface. Another major weight loss i.e., 2.80% has occurred at 650^{o}C which is because of the degradation of methylcellulose and polyethylene glycol used to make printable paste with cordierite by burning out process. Again, a major weight loss of sample i.e., 0.67 and 1.96% has taken place between 777 to 1082^{o}C with an exothermic peak occurred at 887^{o}C which is due to the removal of structural water accompanied with the talc and clay minerals used as a precursor in the study. Further another two exothermic peaks were found in DTA plot at 1197 and 1252^{o}C with minimum weight loss of 0.83% from 1020 to 1261^{o}C and 0.47% from 1261 to 1363^{o}C which can be related to the formation of cordierite from intermediate compounds. Intermediate compounds such as clay forms metakaolin ($Al_2O_3.2SiO_2$), Mullite ($3Al_2O.2SiO_2$) and crystabolite (SiO2) during heat treatment and talc forms protoenstatite ($2MgO.2SiO_2$) and silica (SiO_2) during heat treatment [26].

$$2(3Al_2O_3.\ 2SiO_2) + 5SiO_2 + 6(MgO.\ SiO_2) \rightarrow 3\ (2MgO.\ 2Al_2O_3.\ 5SiO_2)$$

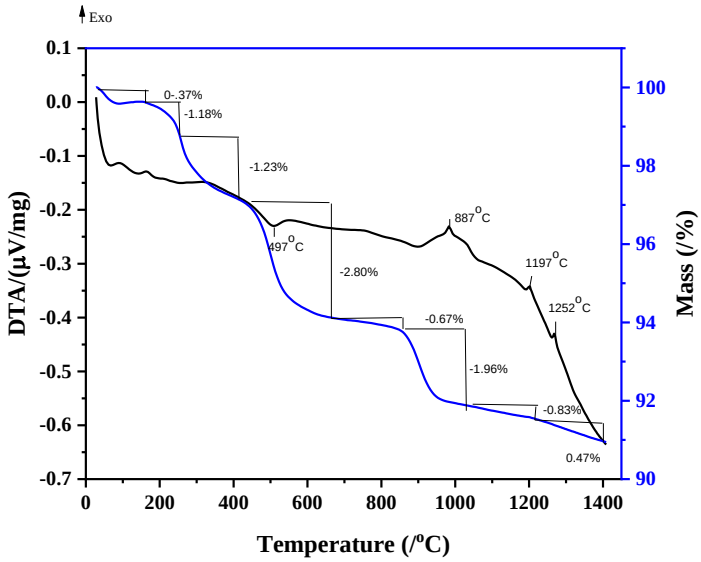

Fig 5.10 TG-DTA of green 3D Printed honeycomb structure

5.3.5 Sintering of 3D Printed Green Honeycombs

According to the TG-DTA plot, the sintering schedule for the honeycomb structures were optimized and represented in Fig 5.11. The sintering of the honeycomb structures was followed till 1200^{o}C with heating rate of 120^{o} C/hour and consequent heating rate of 60^{o}C/ hour was maintained till 1390^{o}C to prevent the softening and melting of cordierite because of very tiny firing range. After reaching the higher temperature (1390^{o}C), the samples were kept for 1 hour soaking

period followed by cooling to the room temperature. The sintered honeycomb structures have shown in Fig 5.12.

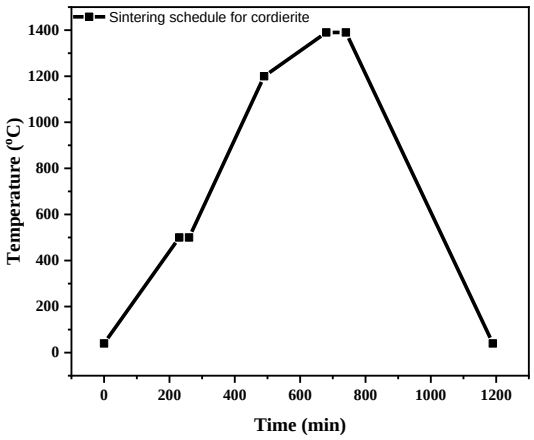

Fig 5.11 Sintering schedule for cordierite 3D Printed honeycomb structures

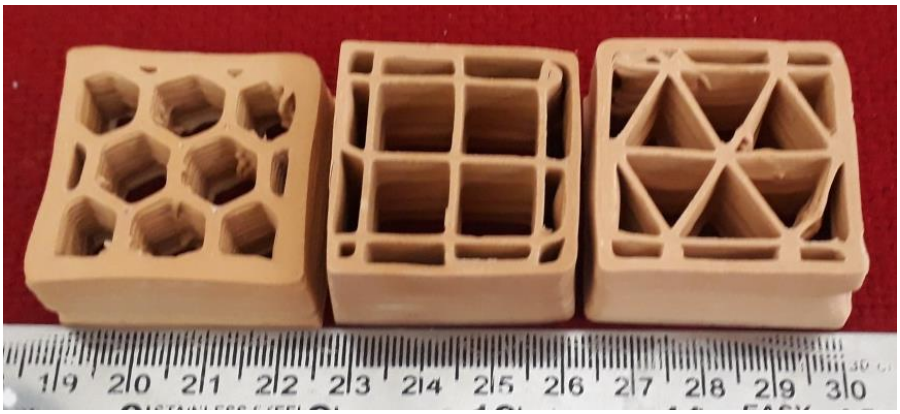

Fig 5.12 Sintered cordierite 3D Printed honeycomb structures

5.3.6 Characterization of Sintered Honeycomb Structures

5.3.6.1 X-Ray Diffraction (XRD)

After sintering a small piece of honeycomb structures were characterized for phase identification using X-ray Diffraction (XRD) technique. The recorded XRD pattern is shown in Fig 5.13 confirms the formation of cordierite as the major phase along with the other crystalline phases as minor phases namely magnesium aluminate spinel ($MgAl_2O_4$), clinoenstatie ($MgSiO_3$) and corundum (Al_2O_3).

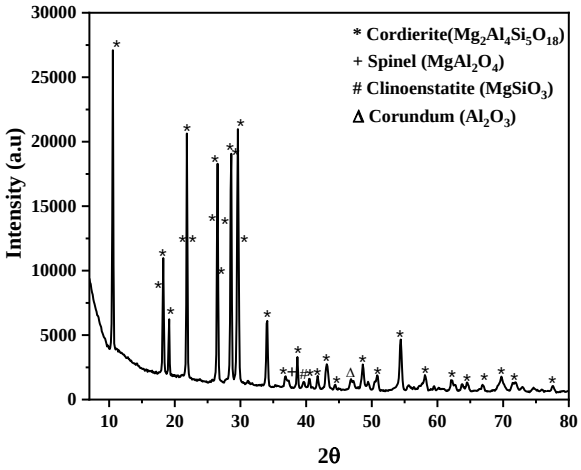

Fig 5.13 XRD pattern of sintered cordierite sample

All honeycomb structures were found defect-free and crack free after firing at 1390^{o}C and the sintered density of a solid cordierite specimen was measured by using Archimedes principle (ASTM 792) and found a density of 2.41-2.48 g/cm^3.

5.3.6.2 Mechanical Characterization

All sintered honeycombs were characterized for their mechanical properties. The compression test was conducted to measure the compressive strength of the honeycomb structures in both axial and perpendicular directions. All printed honeycomb structures were ground and polished to the dimension of 35mm x 35mm x 20mm size to have a uniform surface throughout the sample. Compression test of honeycomb structures were evaluated by Universal Testing Machine (UTM) (5584, Instron, UK). For each configuration of honeycombs, five samples were tested under quasistatic load applied in axial direction of channel represented in Fig 5.14. The load was applied with ram rate of 0.5 mm/min.

The honeycomb structures were placed on fixtures of compression test in UTM and load was applied from the top plate as shown in Fig 5.14 as well as in Fig 5.15(a). The stress-strain curve of honeycomb structures recorded during the experiment is shown in Fig 5.15(b). It is evident from the stress-strain curves of all configured honeycomb structures, the stress attained by the hexagonal configured honeycomb is 20.18 MPa which is 4 times higher than the other configured honeycombs. In Fig.5.15 (b) the honeycomb with hexagon channel represented as A, square channel as B and triangular channel as C as shown in stress-strain curve.

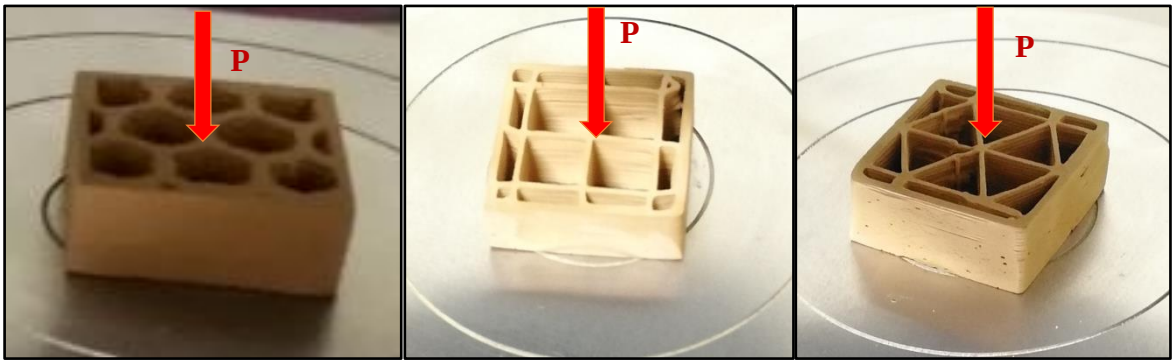

Fig 5.14 Compression strength test of honeycomb structures in axial direction

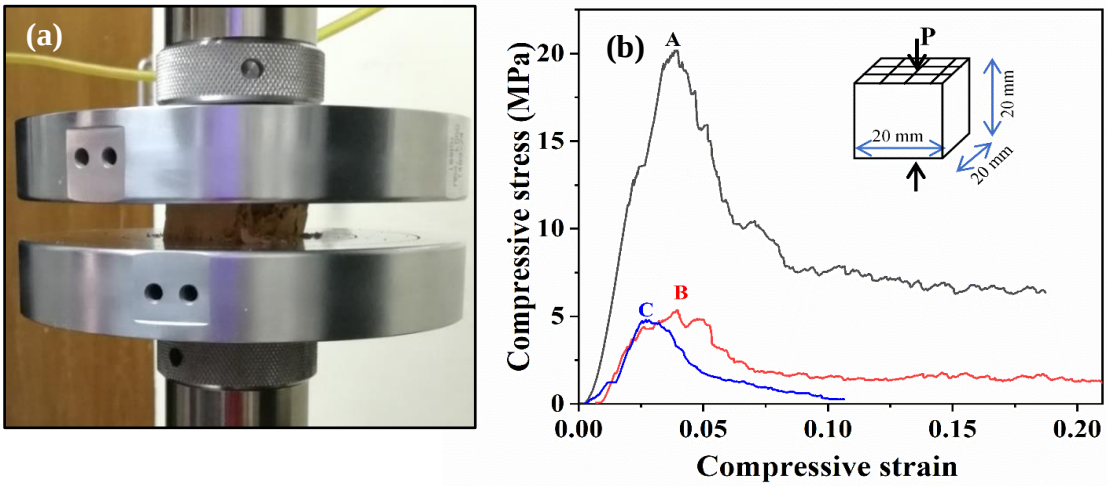

Fig 5.15 (a) Honeycomb structure under axial compression (b) Stress- strain curve of 3D Printed sintered honeycomb structures (A) Hexagonal (B) Square and (C) Triangle

It is evident from Fig. 5.15 (b) that irrespective of their configuration, all the honeycomb structures followed the similar failure trend with maximum compressive strength of 20.18 MPa for hexagonal channel, 5.85 MPa for square channel and 5.29 MPa for triangular channel honeycomb structures.

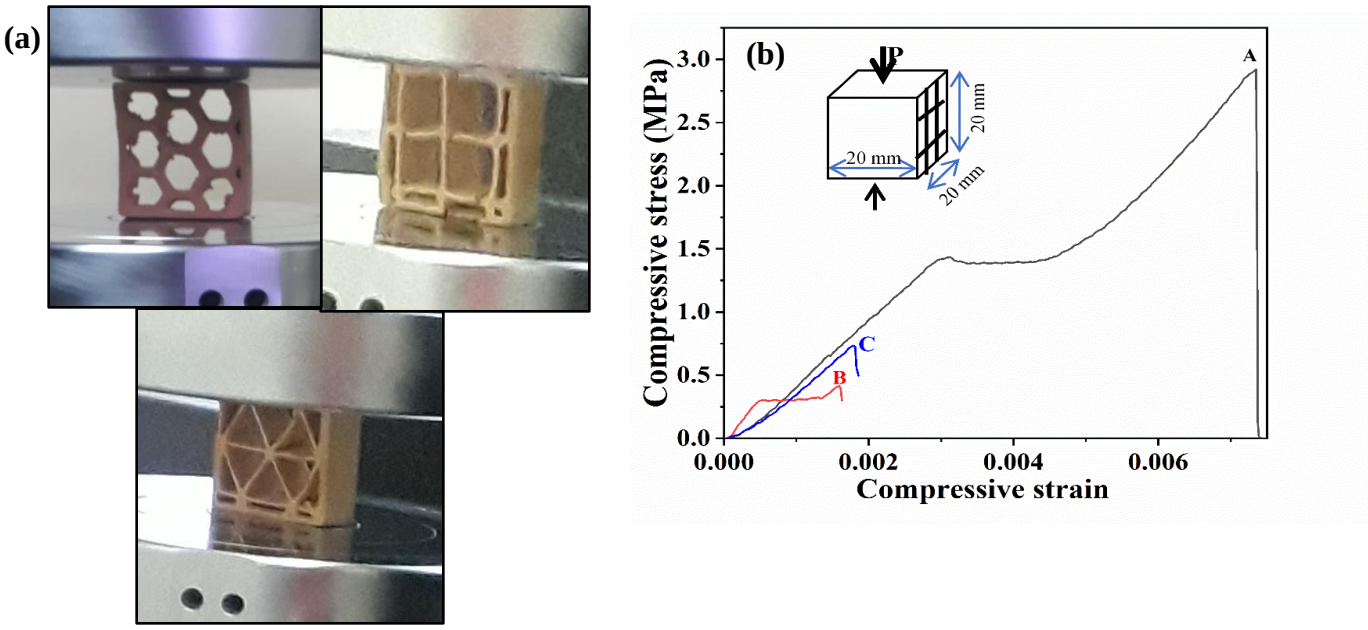

Fig 5.16 (a) Compression test under perpendicular load, (b) Stress-strain curve of 3D Printed sintered honeycomb structures (A) Hexagonal (B) Square and (C) Triangle

Fig 5.16(a) shows the 3D printed sintered honeycomb structure under perpendicular loading condition. The honeycomb structure was place in vertical direction and load was applied across the channels. Same ram rate was applied during the compression test as in the above case. The recorded stress and strain curve have shown in Fig 5.16(b) and it is also proving that irrespective of their honeycomb configuration, all the three types of honeycomb structures were failed catastrophically across the channels. Table. 5.5 indicates, the compression strength of all honeycomb specimens recorded in axial and perpendicular loading conditions. On perpendicular conditions, the hexagonal, square and triangular honeycombs were exhibited the compression strength values as 2.91, 0.41 and 0.72 MPa respectively, which is very less compare to the stress obtained in axial direction.

Table. 5.5 Compressive strength of sintered honeycombs

Properties	Loading direction	Hexagonal (A)	Square (B)	Triangular(C)
Compressive strength (MPa)	Axial	20.18	5.85	5.29
	Perpendicular	2.91	0.41	0.72

The variation of compression strengths values recorded with respect to direction of load in axial and perpendicular of the channel reveals the mechanical anisotropy. This can be attributed to the fact that for perpendicular loading direction, the stress is concentrated along with walls rather than the cross-section. Due to this stress, micro cracks were initiated from the flaws and defects present in honeycomb structure and propagates along the walls and fails catastrophically. But in the case of axial loading direction, the stress is distributed along the channels due to the cross section of cell joints and this allows to propagate the crack in vertical direction rather than the propagation of crack to the neighboring cells. Hence the compressive strengths of honeycomb structures in axial loading were exhibited more stress values than in compression under perpendicular loading direction.

5.4 3D Printing of Aluminum Silicate (Clay) Honeycomb Structures

Aluminum silicate (clay) material is a natural and traditional occurring ceramic material consists of good plasticity with good mechanical properties. This clay material was also used to fabricate complex shapes through the extrusion-based 3D printing process with optimized printing conditions. Several honeycomb structures were printed with various configuration such as hexagonal, square and triangular channel based on predesigned cellular parameters of the honeycomb channel to attain maximum surface area.

5.4.1 Characterization of Clay Material

Clay powder was characterized for the identification of phase and purity through x-ray diffraction technique and the pattern is shown in Fig.5.17 which confirms that clay consists of showing kaolinite phase.

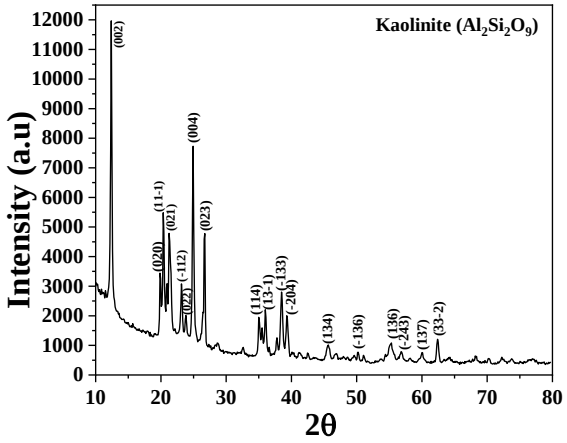

Fig.5.17 X-Ray Diffraction pattern of clay powder

Clay powder in the present study was also characterized for its particle size distribution and analysis by Dynamic Light Scattering (DLS) technique and indicated an average particle size of 620 nm with unimodal distribution which is also evident from the particle size distribution curve shown in Fig.5.18.

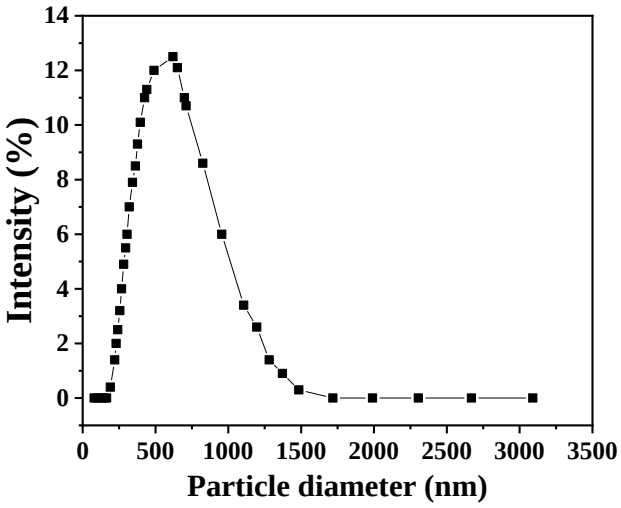

Fig. 5.18 Particle size distribution of clay powder

5.4.2 Preparation of Printable Feedstock with Clay

Fig.5.19 represents process flow chart and the steps involved in the preparation of clay powder into printable paste.

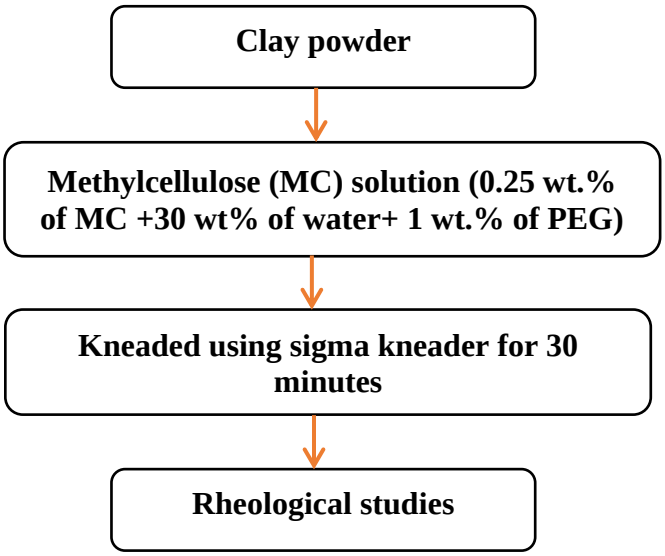

Fig.5.19 Flow chart for preparing the feedstock with clay powder

Methylcellulose (MC) solution was prepared by using of 0.25wt% of MC added to the 30 wt.% deionized water with 1 wt.% polyethylene glycol (PEG). Whole mixture was kneaded in Vacuum sigma kneader for 30 minutes for homogenization and to remove the air bubbles. Prepared homogeneous paste was examined for the rheological behavior through rheometer (Anton paar, MCR 51), by using parallel plate and spindle. Prepared feedstock was placed on parallel plate and 1 to 1000 s^{-1} shear rate was given to spindle. The viscosity behavior with increasing shear rate were recorded which is shown along with and lnγ vs lnŋ in Fig.5.20 (a) and (b) respectively. The viscosity of the paste was decreased with the increasing shear rate i.e., shear thinning behavior. Shear rate exponent (n) is also calculated from the power law model and shear rate exponent value found to be 0.77 which is less than 1 confirming to shear thinning behavior.

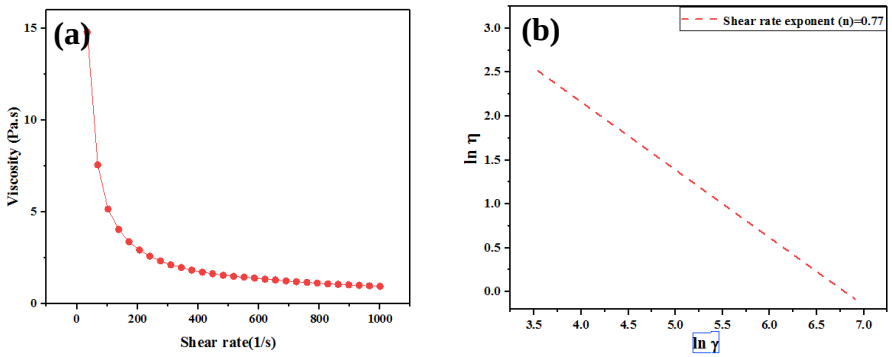

Fig.5.20 Plots of (a) Shear rate vs Viscosity and (b) lnγ vs lnŋ of clay paste

5.4.3 3D Printing Process of Clay Honeycomb Structures

As the paste exhibited pseudoplastic behavior, the paste was used for 3D printing of honeycomb structures as per the procedure detailed below. Predesigned honeycomb models were generated using the CATIA software and saved in .STL format. Further, saved STL files was imported to repetier software (3D printer software) and 35-40% infill density were selected to maintain the solid content in all the configurations of hexagonal, square and triangular patterns. Further, printing of the honeycomb structures was carried out at printing speed of 4-6 mm/s. After incorporating the printing parameters to the CAD design, the STL file was sliced employing slice 3r software to generate G-Code while printing which will control the printing path way. Further the sliced file was saved in micro-processor for printing the honeycomb structures.

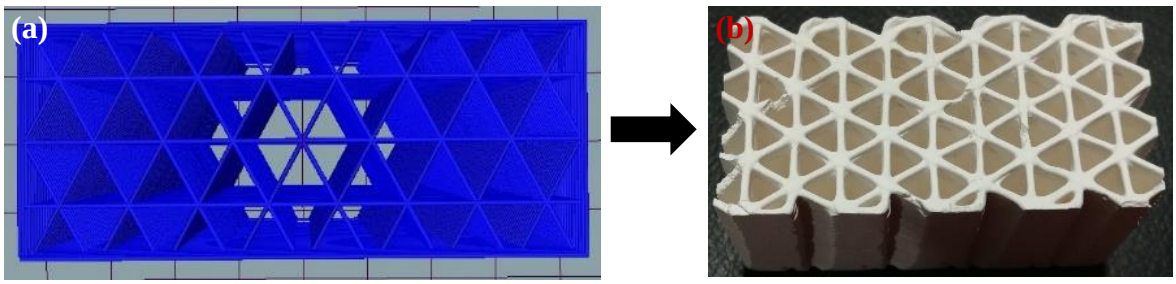

Fig.5.21 (a) A typical CAD model along with (b) printed honeycombs

The prepared feedstock was filled in the barrel without any air gap and printed with the 3D Printer (3D Cerami, Makercity, Trivandrum) along with the designed and sliced CAD model. The infill percentage for the triangular, square and hexagonal was estimated based on the unit cell parameters and the infill density for square and triangular configurations were close to 40%. However, in case of hexagonal channels the shape could not be retained as hexagon and resulted in the formation of circular configuration indicating the parameters were not applicable for printing the hexagons. The problem was identified as the overloading of the paste necessitating the reduction in infill percentage to 20% in order to obtain the hexagonal configuration with the paste and printing parameters under consideration. A sliced honeycomb with triangle pattern is shown in Fig. 5.21 (a) with printed green honeycomb in Fig.5.21(b). All printed samples were dried at atmospheric conditions and sintered according to the sintering schedule shown in Fig.5.22 at 1100^{o}C temperature.

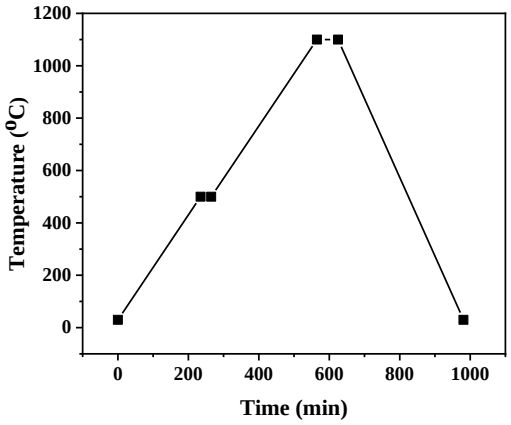

Fig.5.22 Sintering schedule of 3D printed honeycomb structures

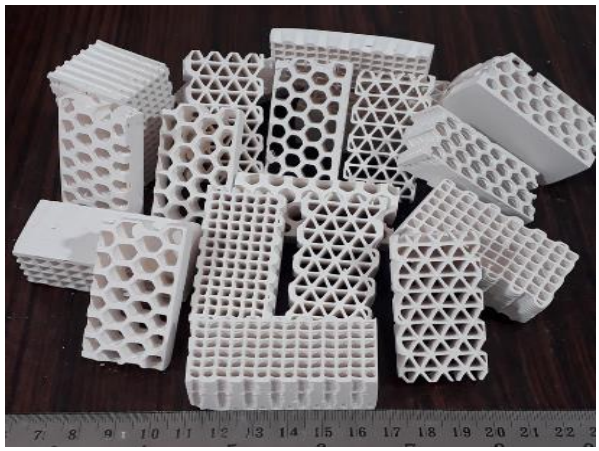

Fig.5.23 Sintered 3D printed honeycomb samples

5.4.4 Characterization of 3D Printed Clay Honeycombs

Sintered samples were subjected to measurement of the density and apparent porosity by using the Archimedes principle (ASTM 792). Table. 5.6 shows density and apparent porosity of the samples.

Table. 5.6 Properties of the 3D printed sintered samples

Property	Density (g/cm^3)	Apparent porosity (%)
	1.68	30-35

An application was conceptualized for the 3D printed honeycombs and were explored as substrates in bioreactor for the immobilization of microorganisms. The various honeycombs printed along with configuration and cellular parameter are shown in Table. 5.7. The purpose of selecting different cellular parameters was to evaluate the effect of surface area on the efficiency of bioreactors which is considered to be a key factor that determines its performance. The evaluation of honeycomb properties with respect to the application is discussed in detail in chapter. 6 of this thesis.

Table. 5.7 Properties of honeycombs

Properties	Ceramic honeycombs		
	Square channel	**Hexagon channel**	**Triangle channel**
Honeycomb cellular parameters (mm) (Edge length (l), Wall thickness (t))	l=3.49 and t=1 l=6.52 and t=1	l=4.06 and t=1 l=5.53 and t=1	l=6.09 and t=1 l=13.40 and t=1
Surface to Volume Ratio	17.29 and 15.16	9.06 and 8.41	13.81 and 4.34
Specific surface area (m^2/g)	53.05	53.05	53.05
Density (g/cc)	1.68	1.68	1.68

Honeycomb structures with square, triangle and hexagon channel were printed into 30x30x25 mm to measure compressive strength (ASTM C1424) using Universal Testing Machine (UTM). Uniaxial load was applied on surface of honeycombs with ramp rate of 0.5mm/min. Recorded compressive stress-strain curves for high and low surface area honeycombs are shown in Fig.5.24. All honeycombs have shown similar compressive stress and strain behavior and compressive stress values found to be 6.95MPa and 3.64MPa for high and low surface area square channel honeycombs, 5.68 and 5.13 MPa for high and low surface area of hexagon channel honeycomb and 8.39 and 3.31 MPa for high and low surface area triangle channel honeycomb.

Table. 5.8 Compressive strength of honeycomb structures

Honeycomb structures						
Configuration	**Square**		**Hexagon**		**Triangle**	
Cellular parameters (mm)	l=3.49 and t=1	l=6.52 and t=1	l=4.06 and t=1	l=5.53 and t=1	l=6.09 and t=1	l=13.40 and t=1
Solid support of honeycomb	40%	20%	20%	15%	40%	20%
Geometrical Surface area (mm^2)	12564	10432	6090	5806	14159	9045
Compressive strength (MPa)	6.95	3.65	5.68	5.13	8.39	3.31

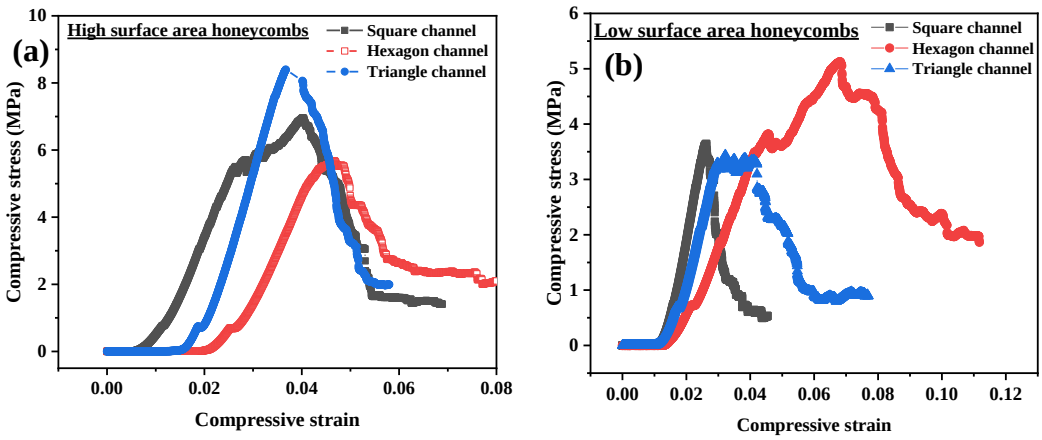

Fig. 5.24 Compressive stress vs compressive strain curve of (a) high and (b) low surface area honeycombs of square, hexagon and triangle channels

It is evident from Table. 5.8 that, the compressive strength of the samples can be well correlated with the solid supporting the load. Further the configuration dependents on the load bearing are also clear from the data. The maximum load bearing is observed with the triangular pattern followed by square and least with the hexagon channel in the case of high surface area honeycomb specimen. A similar trend is also observed with the honeycombs though there are marginal variations with low surface area honeycomb specimens.

5.5 3D Printing of Alumina Honeycomb Structures

The honeycomb structures with corrugated patterns were also printed with alumina which is procured from Rohini Industries, Pune. The basic powder characteristics such as phase purity, particle size, morphology, chemical quantitative analysis and BET surface area were described in chapter.3 at section 3.3.1. Preparation of printable paste and rheological behavior of alumina paste was also discussed in previous chapter at 3.3.2.2.

The cellular parameters of honeycomb structures with corrugated pattern were predesigned and represented in Table. 5.9. A CAD model was designed as per the pre-designed cellular parameters and converted into .STL file. The file was sliced with the optimum printing condition as discussed in chapter 3, and 3D printed green part is shown in Fig. 5.25. Further the sample was dried completely in oven and sintered at 1550^{o}C and sintered samples were shown in Fig. 5.26.

Table. 5.9 Cellular properties of alumina honeycomb

Cellular properties of honeycombs		
Edge length(l), mm	**Thickness(t), mm**	**Geometrical Surface area (mm^2) per one honeycomb**
4	1	42500

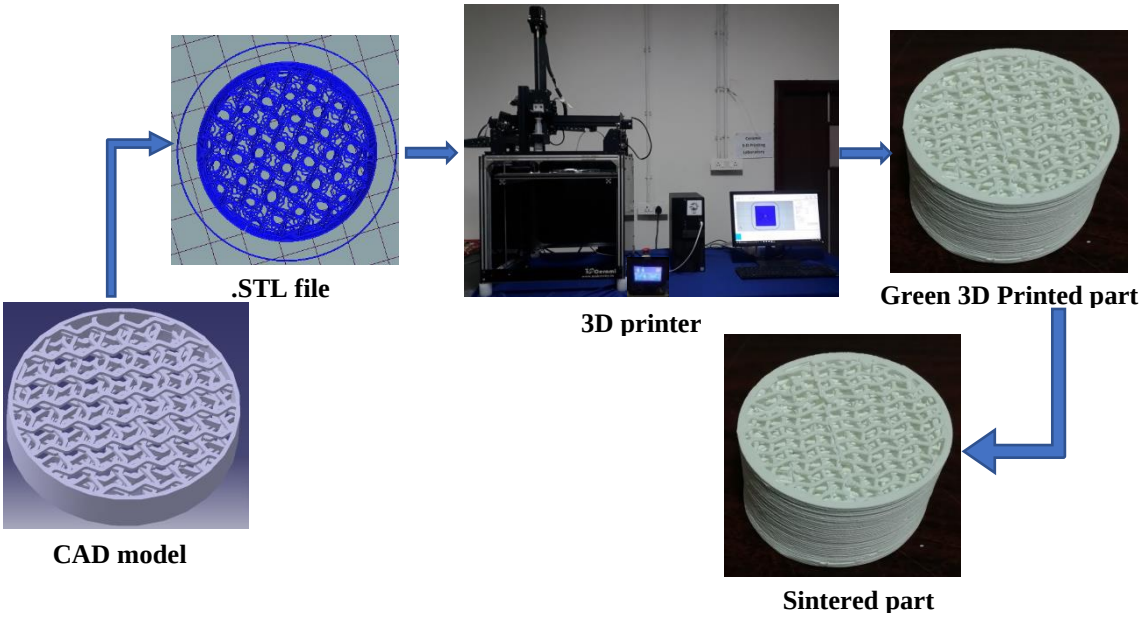

Fig. 5.25 Flowchart of 3D printing of alumina honeycombs

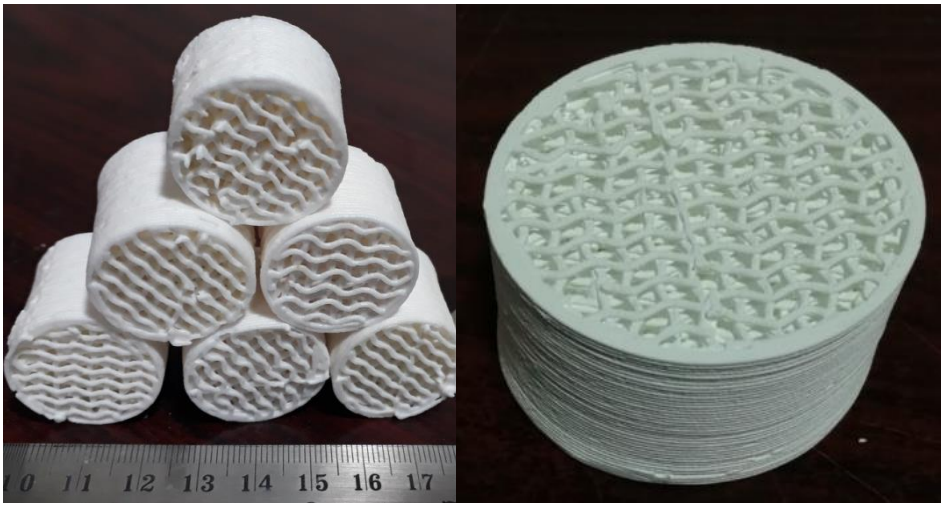

Fig. 5.26 Sintered alumina 3D printed honeycomb structures

The samples were tested for compressive strength measurement using UTM and recorded compressive stress versus strain curve is shown in Fig. 5.27, found the compressive strength of 440 MPa. The surface area was estimated by assumption using an image analysis which is estimated to be 42500 mm^2

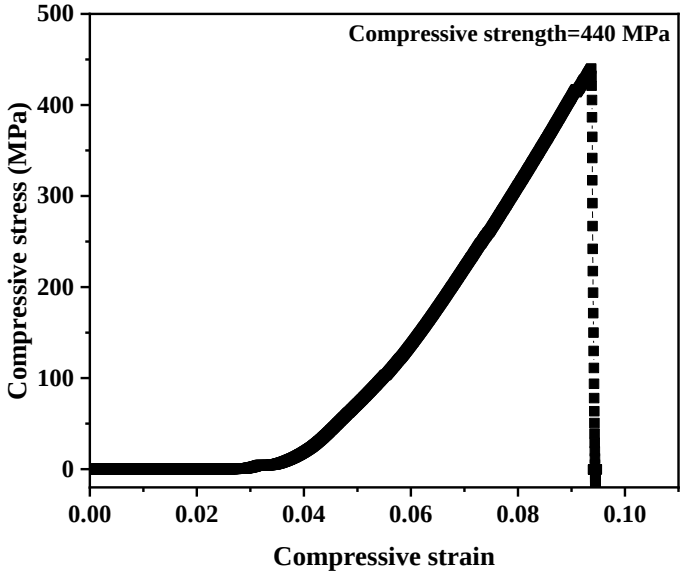

Fig.5.27 Compressive stress versus compressive strain curve of alumina honeycomb structure

Alumina honeycomb samples prepared above were experimented for fluoride removal from the potable water as described in chapter.6.

5.6 Replication of Ceramic Parts from 3D Printed Poly Lactic Acid (PLA) Templates

Another approach that has been applied to fabricate complex structures with micro-features is the replication process using 3D printed poly lactic acid (PLA) templates. The 3D printing process for ceramics is not easy due to its inherent properties of powder such as material chemistry, processing parameters with respect to feedstock and issues related with sintering process [27]. The template replication process is reported by several researchers [28-31], however the replication using 3D printed PLA template is not reported so far. In this investigation, the experimental studies have been conducted on using the 3D printed PLA templates as a sacrificial template for replicating the complex and intricate ceramic structures with engineered porosity.

5.6.1 Experimental Procedure

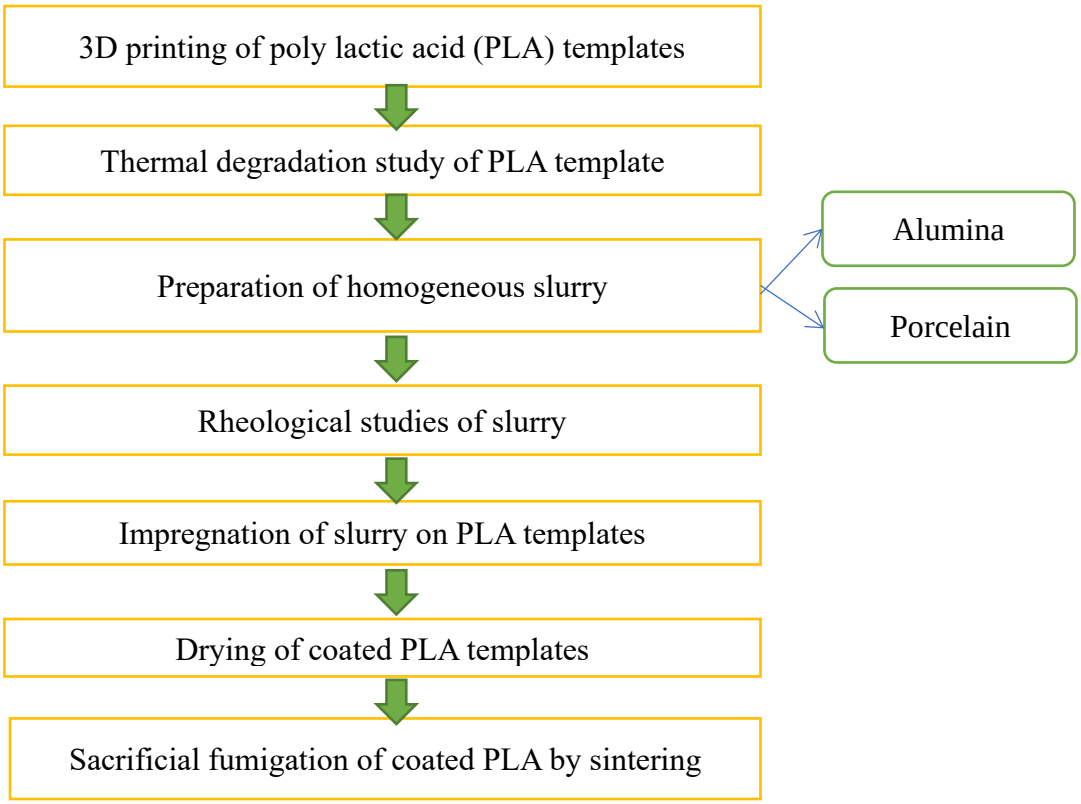

Fig. 5.28 Flow chart of replication process using 3D printed PLA templates

Fig. 5.28 represents the flow chart for fabricating the complex structures through replication process using 3D printed PLA templates.

5.6.1.1 3D Printing of PLA Templates

Poly lactic acid (PLA) is a widely used polymer for fabricating parts through 3D printing. PLA is one of the thermoplastic polymers with the chemical formula of $(C_3H_4O_2)_n$ and it is the highest consumed biopolymer in the world [32]. In this study various complex structures with micro-features were printed using fused deposition modelling (FDM) system (MCHTD, Maker City, India). The printing conditions such as layer thickness of 0.4 mm with nozzle tip temperature of 205^{o}C and printing speed of 60-65 mm/s was used to print these template structures. The printed PLA templates is shown in Fig. 5.29.

After printing a small piece of sample was characterized for its thermal degradation behavior using Thermo-gravimetry (TG) and Differential Thermal analysis (DTA) (STA 449 F3,

Netzsch, Germany). The recorded TG-DTA plot for PLA template is shown in Fig. 5.30. It is evident from the TG-DTA plot that, PLA is completely burnt by showing a steep reduction of weight to 100% loss at temperature of 400-450^{o}C. The weight loss of PLA template with respect to temperature at different heating rates such as 10,15 and 20^{o}C/min were measured using the procedure described elsewhere [33]. The weight loss of the sample was recorded as the removal of binder occurs with temperature. Hence

$$x = (m_o - m_T)/(m_0 - m_f) \quad (1)$$

where, m_o - initial weight, m_T - sample weight at temperature T, m_f - final weight.

Arrhenius parameters, for the thermal decomposition of the samples were determined assuming a first order chemical reaction. This method uses the integral form of rate law. The rate law of any solid phase reaction is given as

$$\frac{dx}{dt} = A\, e^{(-E/RT)} f(x) \quad (2)$$

In non-isothermal TGA experiments, the heating rate is varied as a function of time and hence

$$\frac{dx}{dT} = \frac{dx}{dt} * \frac{dt}{dT} \quad (3)$$

$$\frac{dx}{dT} = \frac{dx}{dt} * \frac{1}{Y} \quad (4)$$

where Y is the heating rate given by dT/dt.

$$\frac{dx}{dT} = (A/Y)\, e^{(-E/RT)} f(x) \quad (5)$$

Plotting the left hand side of Eqn. 5 against 1/T gives E/R as the slope and A as the intercept. The activation energy for 3D printed PLA template found as 392 KJ/mol^{-1}.

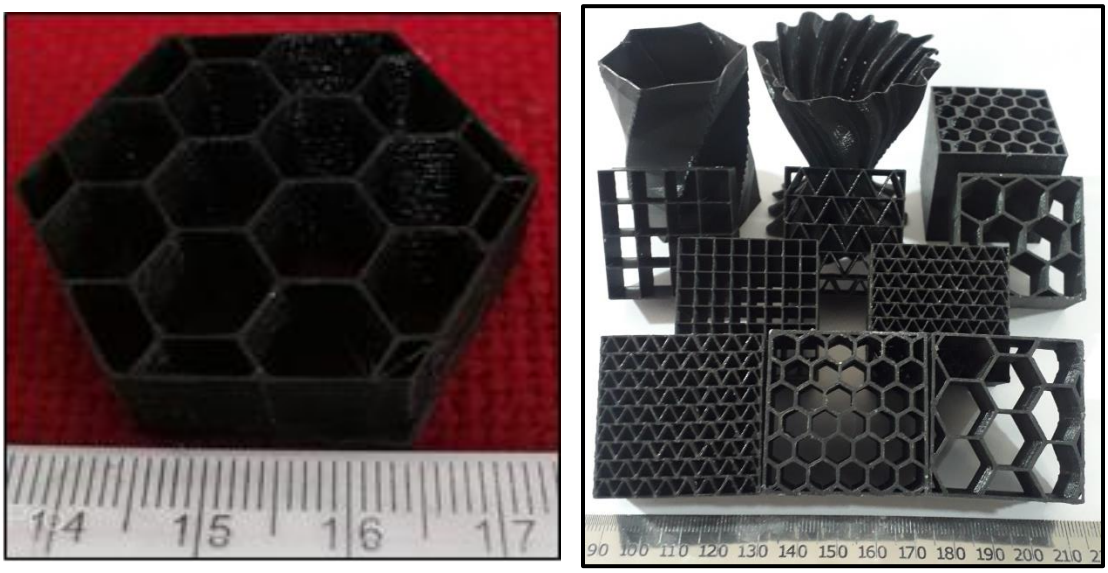

Fig. 5.29 3D printed PLA template

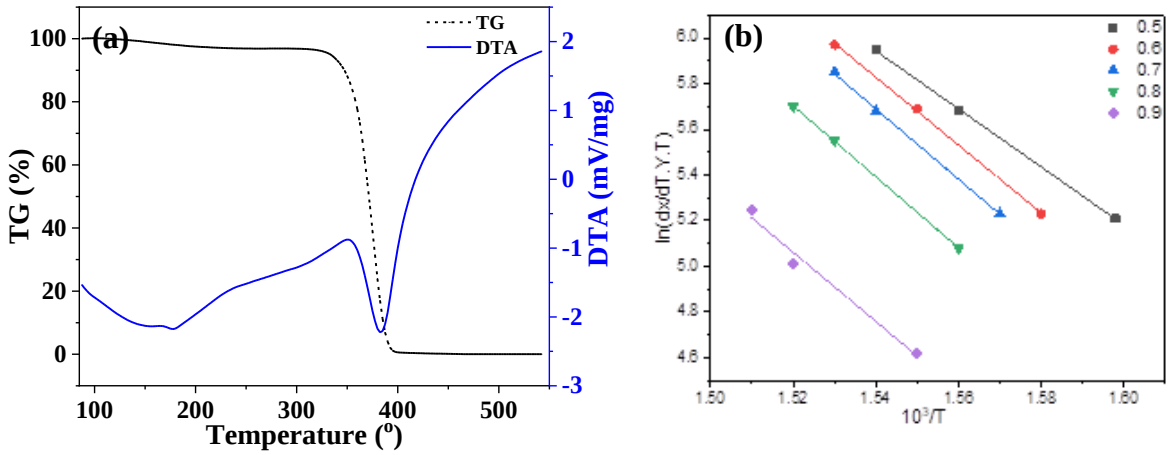

Fig. 5.30 (a) TG-DTA plot of PLA template and (b) Plot of ln[(dx/dT).Y.T] versus 1/*T* for uncoated PLA

5.6.1.2 Preparation of Homogeneous Suspension and Impregnation of the Slurry

In this study, the suspensions were prepared with alumina and porcelain powders to impregnate on the PLA templates. Alumina and porcelain powders were obtained from commercial sources. An aqueous ceramic suspensions were prepared by adding respective ceramic powder to 40-45 wt.% of water and dispersed by adding optimum concentration of Darvan 821 A

(R. T Vanderbilt Co., Inc., Norwalk, CT, USA) as a dispersing agent. Further methylcellulose (MC) was added as a binder to these mixtures along with the alumina balls as a milling media and milled for 4 hours using pot jar mill. The obtained homogeneous slurries were measured for their rheological properties using rheometer (MCR 51, Anton Paar, Austria) and plotted the data as shear rate versus viscosity for alumina and porcelain slurries as represented in Fig. 5.31 (a). It is evident from the figure that both formulations are showing pseudo-plastic behavior and shear rate exponents(n) were also calculated for every formulation using Power law model. The shear rate exponent (n) = 0.43 for alumina and n=0.51 for porcelain slurries were observed and confirms the pseudo-plastic nature of the slurries. The pseudo-plastic behavior of the slurries is an essential property of slurries to coat on PLA templates during the slurry impregnation process.

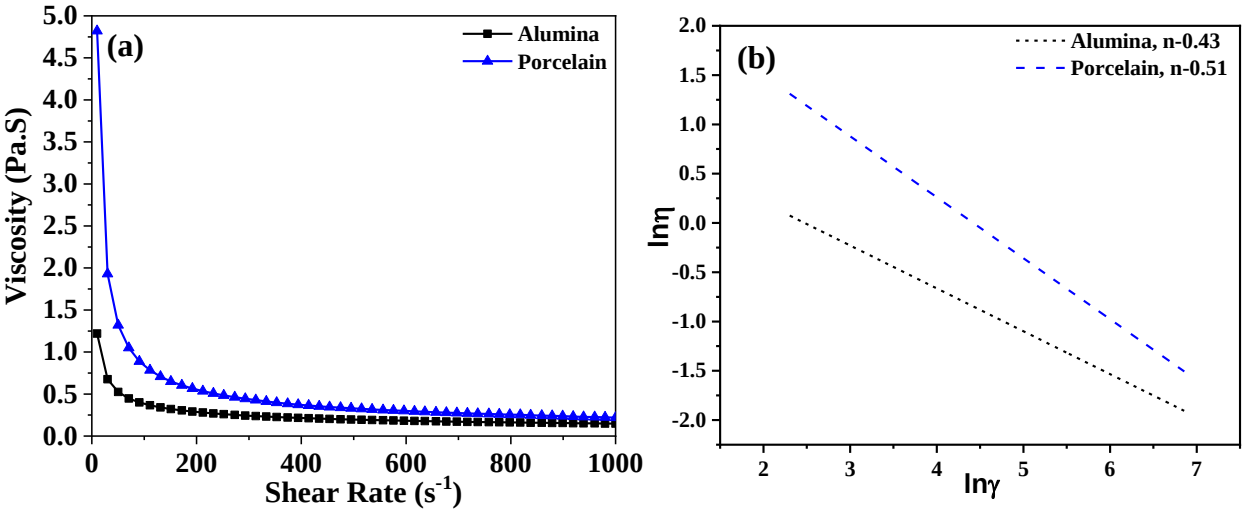

Fig.5.31 Plot of (a) Shear rate vs viscosity and (b) lnγ vs lnη of Alumina and Porcelain slurries

Before impregnate the slurry on PLA templates, templates with various configurations were selected and the surfaces of all templates were etched using acetone which improves the adherence of slurry onto the surface, edges and corners of the PLA templates. All the templates were impregnated with the slurries by dipping method. The templates were dipped in slurry repeatedly to build up the thickness of coating on template. The typical template coated with alumina slurry is shown in Fig.5.32.

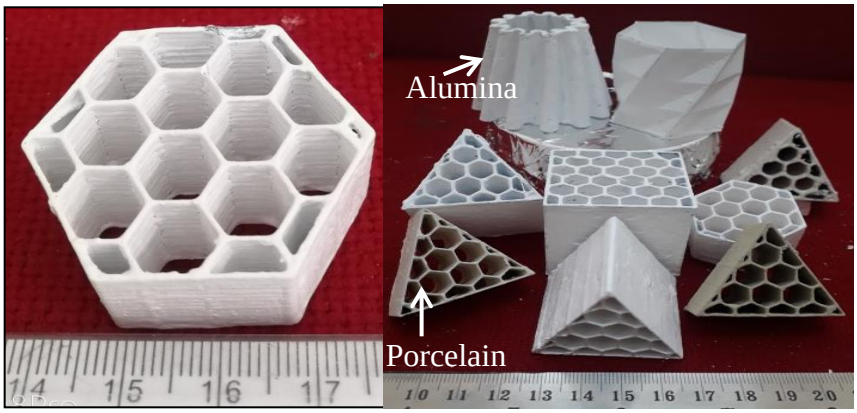

Fig. 5.32 PLA templates coated with alumina and porcelain

Further all the impregnated PLA templates were dried at 110^{o}C in an oven. Templates were attained a slurry loading of 66 wt.% of the weight of the template and the thickness of the coating was found to be 0.2 mm on each side of wall.

5.6.1.3 Sacrificial Fumigation of PLA Templates and Sintering

Based on the TG-DTA studies of the PLA templates, the sintering schedule was optimized for PLA templates coated with alumina and porcelain. Sintering schedule for burning of PLA was common for both formulations. A heating rate of 60^{o}C/min was selected from room temperature to 250^{o}C and heated to 450^{o}C with a heating rate of 30^{o}C/min followed by the soaking time of 15 minutes. Further, all the coated templates were heated to peak temperatures such as 1550 and 1275^{o}C for alumina and porcelain respectively with a heating rate of 120^{o}C/min followed by soaking for 1 hour at the peak temperature. All the sintered samples are shown in Fig.5.33 and cellular properties of replicated honeycomb structures are shown in Table. 5.10. It is evident from the table that, a shrinkage of 5% was observed from the PLA template to sintered replicate structure without any cracks which is indicating that the removal of sacrificial PLA template and structural integrity of the replicated structure without any warpage.

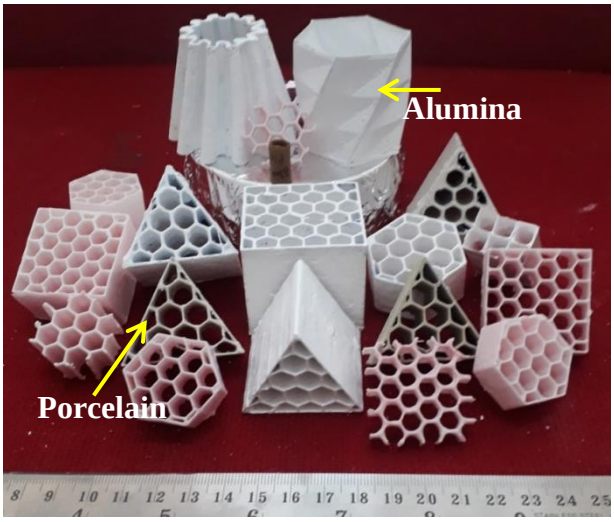

Fig. 5.33 Sintered honeycomb replicated structures

The density and apparent porosity of all the sintered replicated structures were measured using Archimedes principle (ASTM 372). The density of an isolated wall of sintered replicated alumina honeycomb structure was found to be 91% of the theoretical density along with the apparent porosity of 80-85%. Further the alumina replicated structures were sintered to 1650^{o}C and the observed density of the alumina structures was enhanced from 91% to 96% of the theoretical density. Similarly, the apparent porosity of porcelain replicated structures were calculated and found as 80%.

Table. 5.10. Cellular parameters of replicated honeycomb structures

Template type	Dimensions (mm)	Cell parameters				Relative density	
		Unit cell length (mm)		Wall thickness (mm)			
		Before coating	After sintering	Before coating	After sintering	Before coating	After sintering
HC - Square	40 x 40 x 20 40 x 40 x 20	9.5 4.5	9.0 4.0	0.5 0.5	0.65 0.65	0.10 0.20	0.12 0.27
HC- Triangular	40 x 40 x 20	9.5	9.0	0.5	0.65	0.17	0.21
HC-Hexagonal	40 x 40 x 20 40 x 40 x 20	7 3	6.5 2.6	0.5 0.5	0.65 0.65	0.08 0.18	0.10 0.24

The relative density of PLA templates and sintered structures were calculated using the formulae mentioned in Table.5.1. It is evident from Table 5.10 that developed replication process provides to fabricate honeycombs with lower relative density (<0.3) which is the property of cellular nature according to Gibson [4].

All the replicated honeycomb structures were used for compressive strength measurement using Universal Testing Machine (UTM, ASTM C 1424) under compression. All honeycomb structures have exhibited cellular nature by bearing the stress for longer duration under compression. A stress-strain curve recorded for the alumina replicated honeycomb is shown in Fig. 5.34. It is evident from the stress-strain curve that, the capability of energy absorption of the replicated structure is high due to the lower relative density. Being porous structure, the failure of the sample caused by the extension of crack slowly to the other flaws by linking up together and formed crushed zone. Hence alumina replicated honeycomb structure has shown the average compressive strength of 2.27 MPa and 1.5 MPa for the porcelain replicated structures. The lower strength values observed in the case of porcelain is due to their property of lower strength of the materials than alumina.

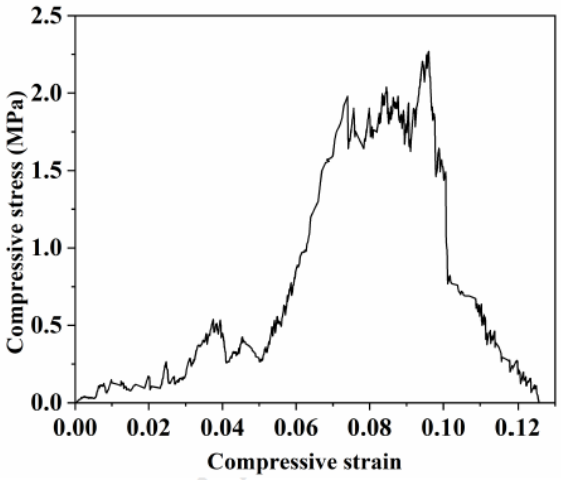

Fig.5.34 Compressive stress versus Compressive strain curve of alumina replicated structure

However, the compressive strength of all the replicated honeycombs can be increased by sintering at higher temperatures, which helps in achieving the higher density with minimum porosity. Also, this replication process allows to fabricate complex ceramic structures with engineered porosity and moderate mechanical strength for catalyst support application.

5.7 Conclusions

Honeycomb structures with various configurations with respect to the relative density, size and shape of the channels were successfully printed using the 3D printing process. A wide range of ceramic formulations such as cordierite, clay and alumina were made into a printable paste with desired rheological properties and employed for printing process. The printing parameters were optimized in order to retain the desired geometry and tolerances within the predesigned honeycomb structures. In addition to the direct 3D printing of the paste, replication has also been experimented using 3D printed PLA honeycomb templates.

The heat treatment schedules for effective binder burnout, insitu formation of desirable stoichiometry and densification were finalized based on the TG-DTA analysis. The samples were characterized for physico-chemical, cellular and mechanical properties as reported in the respective sections. The honeycomb samples in general exhibited a stable fracture behavior, unlike the solid counter parts. Template replicated honeycombs have shown poor compressive strength with more extension of plateau region with several kinks which can be attributed to the typical pore morphologies generated during fumigation process.

Current study demonstrated the 3D printing process and template replication process as an effective process to generate various configuration and formulation of honeycombs and offers wide choices and flexibility unlike the conventional extrusion process. The honeycombs produced as reported in the chapter were explored for various applications such as substrates for the phytorid bioreactor and fluoride removal from potable water etc., as detailed in chapter.6

5.8 References

1. Harry B Dean, Artificial honeycomb, Patent no:US1389294A, US
2. M Elbadawi, M Shbeh, J Mech, High strength yttria-reinforced HA scaffolds fabricated via honeycomb ceramic extrusion Behaviour, Biomedical Materiaals, 2018;77:422-433.
3. A Yamuna, R Johnson, Y R Mahajan, M Lalithambika, Kaolin-based cordierite for pollution control, Journal of European Ceramic Society, 2004;24:65–73.
4. L J Gibson, M F Ashby, Cellular solids-Structure and properties-2nd Edition, ISBN: 9780521499118, 0521499119, 1999.

5. Z Chen, C Liu, J Li, J Zhu, Y Liu, C Lao, J Feng, M Jiang, C Liu, P Wang Li, Mechanical properties and microstructures of 3D printed bulk cordierite parts, Ceramic International, 2019;45:19257-19267.
6. S Couck, J C-S-Remi, S V D Perre, G V Baron, C Minas, P Ruch, J F M Denayer, 3D printed SAPO-34 monoliths for gas separation, Microporous and Mesoporous Materials, 2018;255:185-191.
7. J Maurath, N Willenbacher, 3D printing of open-porous cellular ceramics with high specific strength, Journal of European Ceramic Society, 2017;37:4833-4842.
8. C Minas, D Carnelli, E Tervoort, A.R. Studart, 3D printing of emulsions and foams into hierarchical porous ceramics, Advanced Materials, 2016;28:9993-9999.
9. B.G. Compton, J.A. Lewis, 3D-printing of lightweight cellular composites, Advanced Materials, 2014;26:5930–5935.
10. C Wu, W Fan, Y Zhou, Y Luo, M Gelinsky, J Chang, Y Xiao, 3D printing of highly uniform $CaSiO_3$ ceramic scaffolds: preparation, characterization and in vivo osteogenesis, Journal of Material Chemistry, 2012;22:12288-12295.
11. A Ortona, C D Angelo, S Gianela, D Gaia, Cellular ceramics produced by rapid prototyping and replication, Materials Letters, 2012;80:95-98.
12. R Felzmann, S gruber, G Mitteramskogler, P Tesavibul, A R Boccaccini, R Liska, J Stampfil, Lithography –based additive anufacturing of cellular structures, Advanced Engineering Materials, 2012;14:1052-1058.
13. B Leukers, H Gulkan, S H Irsen, S Milz, C Tille, H Seitz, M Schieker, Biocompatibility of ceramic scaffolds for bone replacement made by 3D Printing, Materials Science and Engineering Technology, 2005;36:781-787.
14. J T Muth, P G Dixon, L Woish, L J Gibson, J A Lewis, Architected cellularceramics with tailored stiffness via direct foam writing, Proceedings of the National Academy of Sciences of the USA, 2017;114:1832-1837.
15. A l Aşkın, I Tatar, S Kilinc, O Tezel, The utilization of waste magnesite in the production of cordierite ceramic, Energy Procedia, 2017;107:137-143.
16. M Nakhara, Y Kondo, K Hamano, Effect of talc grain size on microstructure of cordierite ceramics, Journal of the Ceramic Society of Japan,1995;103:1051-1056.

17. Y M Z Ahmed, E.M.M Ewais, A.M.M Amin, Processing of porous cordierite via the utilization of two waste metal oxides (Al-slag and silica fumes), 12th world congress on Advances in Civil, Environmental and Materials Research, 2012.
18. A A Albhilil, M Palou, J Kozankova, Characterization of cordierite-mullite ceramics prepared from natural raw materials. Acta Chemica Slovaca, 2013.
19. JR González-Velasco, R Ferret, R. López-Fonseca, MA Gutiérrez-Ortiz, Influence of particle size distribution of precursor oxides on the synthesis of cordierite by solid-state reaction. Powder Technol 2005;153:34–42.
20. R Goren, C Ozgur, H Gocmez, The preparation of cordierite from talc, fly ash, fused silica and alumina mixtures. Ceramics International, 2006;32:53-56.
21. Cordierite –Web mineral data, http://webmineral.com/data/Cordierite.shtml.
22. L Li, Thermal gelation of methylcellulose in water: Scaling and theoreversibility, Macromolecules, 2002;35:5990-5998.
23. D K Buslov, N I Sushko, O N Tretinnikov, Study of thermal gelation of methylcelluose in water using FTIR-ATR sopctroscopy, Journal of Applied Spectroscopy, 2008;75:514-518.
24. U N S Hareesh, A Rakesh, P Biswas, K Rajeswari and R Johnson, Collidal shaping of alumina ceramics by thermaly induced gelation of methylcellulose, Journal of American ceramic society, 2011;94:749-753.
25. N Sarkar, Thermal gelation properties of methyl and hydroxypropyl methylcellulose, Journal of Applied Polymer Science, 1979;24:1073-1087.
26. R Johnson, I Ganesh, B P Saha, G V Narasimha Rao,Y R Mahajan, Solid state reactions of cordierite precursor oxides and effect of CaO doping on the thermal expansion behaviour of cordierite honeycomb structures, Journal of Materials Science, 2003;38:2953-2961.
27. A Zocca, P Colombo, C Wirth, J Gunster, Additive manufacturing of ceramics: issues, potentialities, and opportunities, Journal of American Ceramic Society, 2015;98:1983-2001.
28. P Biswas, A Sharma, M Krishnan, R Johnson, M K Mohan, Fabrication of $MgAl_2O_4$ spinel scaffolds and sonochemical synthesis and deposition of hydroxyapatite nanorods, Journal of American Ceramic Society, 2016;99:1544–1549.

29. B Matovic, B Babic, A Egelja, A R-Mihajlovic, V Logar, A Saponjic, S Boskovic, Preparation of porous silica ceramics using the wood template, Material Manufacturing Processing, 2009;24:1109-1113.
30. P Biswas, P Ramavath, C M Nair, M B Suresh, N Ravi, R Johnson, Quasi-static compression behavior of nickel oxide, nickel oxide: zirconia, nickel:zirconia and nickel foams, Ceramics International, 2016;42:10572–10578.
31. M A M Nor, L C Hong, Z A Ahmad, H M Akil, J Mater, Preparation and characterization of ceramic foam produced via polymeric foam replication method, Processing Technology, 2008;207:235-239.
32. Ceresana. "Bioplastics-Study:Market,Analysis,Trends". www.ceresana.com.Archived from the original on 4 November 2017.
33. K Rajeswari, S Chaitanya, P Biswas, M B Suresh, Y S Rao, R Johnson, Binder burnout and sintering kinetic study of alumina ceramics shaped using methylcellulose, Journal of Ceramic Processing Research, 2015;16:24-31.

****

CHAPTER – 6
DEVELOPMENT OF APPLICATION USING 3D PRINTED CELLULAR STRUCTURES

6.1 Introduction:

The 3D printed cellular structures reported in chapter-5 were explored for two applications as a part of the application development envisage in this work. The two applications are namely

- Substrates for the immobilization of the microorganisms in the phytorid sewage treatment system
- Substrates for removal of fluoride from the potable water

6.1.1 Substrates for the Immobilization of the Microorganisms in the Phytorid Sewage Treatment System

Sewage water is waste water consists of solid waste and liquid waste comes from kitchen, washrooms etc., generated by the household and human settlements. Sewage is recognized as the main cause of water pollution in the environment which not only affects the human health but also affect the aquatic life including agricultural field [1].

Sewage system is characterized based on presence of organic matter, suspended solids, dissolved solids, nitrogen, carbon, phosphorous and fecal coliform bacteria. Organic matter usually consists of fats, proteins and carbohydrates. Discharging of these organic wastes into the land or water, without treatment causes water, air and soil pollution. Suspended solids will present in sewage is fractions of total solids and that can be settled due to gravity. Dissolved solids are non-settle able matter and forms sludge.

As the population of the country increasing every year and there is scarcity of water, minerals in the ground. Hence there is a necessity to prevent the pollution causes by the sewage mix and it is to be treated for reusing for agricultural land or gardening purposes [2-3].

6.1.1.1 Treatment Processes for Waste Water:

Four treatment processes for the wastewater are described below [4-7].

1. **Pre-treatment**: It is a first step of treatment before using it in the actual treatment. In this step coarse suspended particle or solid waste will get filtered. Then it passed

through the 2nd tank i.e., comminatory consists of small blades which breaks remaining coarse solid wastes into small particle. Later the broken small particles will pass through the grits of chamber filled with grits of stone which removes small and coarse solid matter present in the waste water and prevent the pipes from blockage. This is an essential step to prevent the entry of large waste to next treatment level.

2. **Primary treatment**: Primary treatment takes place in sedimentation tank, where the entered organic and inorganic waste will degrade by settling of solid waste due to gravity and all the settled solid waste called as sludge.
3. **Secondary treatment**: This step includes the passage of water through the chamber consists of various grades of stones and growth of microorganisms occurs on the surfaces of stones. Microorganisms will consume the organic matter present in the sewage and converts it into water, ammonia, carbon dioxide during their growth and multiplication. Most of the minute suspended particles will be removed by the secondary treatment.
4. **Tertiary treatment:** This stage is used to remove the nitrogen, carbon and phosphorous.

There are 3 methods to treat the sewage sludge namely thickening, digestion and dewatering process [8]

1. **Thickening:** It is the basic method of sewage sludge treatment. Thickening of settled suspended and dissolved matter present in sewage will do by gravity in a tank. Thickening of sewage leads to reduction of total volume of sewage matter to the less than half volume.
2. **Digestion:** Digestion is a biological treatment method in which total thickened organic content will be decomposed to stable solids. This method enables to remove all the micro-organisms, pathogens, hence it reduces the total mass of solid matter and leads it to dry. Digested sludge appears in rich potting soil. Large sewage treatment plants use two-stage digestion method in which organic matter decomposes at anaerobic condition. Generally, in the first step the sludge will get thickened and get dried in closed tank for several days. Anaerobic conditions result the bacteria to hydrolyze the enzymes and break the proteins, lipids into small particle by producing heat and bio-gas (carbon dioxide and methane.

3. **Dewatering:** Sludge will be disposed after removing the water from the digested sludge. However, concentrations of water present in the sludge as moisture and it will be removed by dewatering method. Sludge slurry spread on the open bed consists of sand on its surface and allows the sludge to dry at atmospheric condition about 6 weeks by evaporating the water and settle the dried sludge by gravity through the sand. Separated water will be collected through pipe and retreated in the head of the tank. After drying dried sludge will be removed from the sand. But this requires sufficient land which is very difficult in urban regions. Hence this method is a common treatment method applicable to rural and sub-urban regions. Mechanical pumps such as centrifuge, rotary drum vacuum filter press was useful to dry the sludge. Sludge contains chemicals which are toxic to aquatic life and agricultural lands. Incinerators were developed for the disposal of sludge with proper control without causing any pollution to the environment.

There are certain methods and technologies were developed to meet the environmental guidelines for water quality, purity and human health protection by considering the climate changes, population and land. Those are membrane bioreactor process, integrated fixed film activated sludge (IFAS) and ballasted floc reactor processes [9-10]. Membrane bioreactor process involves the submerging of hollow micro-fiber filter membranes in single tank and allows the primary, secondary, tertiary treatment in one tank (small area). Considering the environmental issues such as pollution, electricity, land challenges, use of technologies with help of renewable energy sources like wind and solar energy, minimizes the environmental impact of human activities [11-12].

6.1.1.2 Literature Survey

Scientifically so many researchers [13-20] have explored many methods by using of wetland systems for the treatment of wastewater by enhancing the sub surface horizontal flow. It is an effective method which uses plants, microorganisms, gravity and sun light for treating waste water to reusable for gardening and agricultural purposes. Using treatment mechanisms such as physical treatment which involves filtration and sedimentation of sewage, chemical treatment involves absorption, precipitation and decomposition of sewage and biological treatment includes

biological uptake, plant roots and metabolism, transformation of nutrients by bacteria at anaerobic and aerobic conditions to treat the sewage.

The wetland system involves the treatment of waste water in reactor consists of two or more chambers filled with soil, different grades of granite stones and allows the effluent to pass through it. Natural plants such as Typha species, Scirpus species and Phragmites were used as a cap for substrate and the roots of this plants will spread towards down to sand and stone matrix. As a pre-treatment the pre nutrients will be added to the waste water and allows the microbial growth results in good efficiency in treating the waste water. Plant roots helps in absorbing the undesirable matter and filter the waste water. Canny lily (Canna species), arrow arum and combination of any these plants can be used for treating the waste water [21-22].

J Vymazal [23] have discussed various constructed wetland systems and their performances in terms of BOD and COD for wastewater treatment namely vegetation type (free-floating, submerged, floating leaves), surface and subsurface flow constructed wetlands according to the flow direction (vertical and horizontal). The author observed that all the types of constructed wetlands were able to remove the suspended solids and organics but these are less effective in terms of nitrogen removal. The study reveals that the efficiency in removing the nitrogen could be increased by using of combination of different constructed wetland systems. Using of special media with good adsorption capacity could results in high efficiency in removing the phosphorus.

U Stottmeister et al, [24] have investigated the effect of microorganisms and plants in constructed wetland system for treating the wastewater. The authors examined the mechanisms of microorganisms and plant roots in constructed wetlands such as the supply of oxygen plays an important role in deciding the activity and metabolism by microorganisms at plant roots. Plants supplies the oxygen to the root zone and uptake the nutrients by direct degradation of pollutants. The author also studied the effect of plants on removing the pathogenic germs. It was noted that the combination of various species of ten plants were able to remove the 99% Esherichia coli in 48 hours.

H Wu et al, [25] were investigated on the processes to provide sustainable solutions for the performance of constructed wetland systems and discussed the developments on sustainable design and operation of the wastewater treatment. The author reported the designing parameters of free water surface (FWS) and subsurface flow (SSF) constructed wetlands such as larger bed size of $<2500\ m^2$, length to breadth ratio of 3:1-5:1 for FWS and <3:1 for SSF, water depth of 0.3-0.5 m

for FWS and 0.4-1.6 for SSF, hydraulic loading rate of <0.1 for FWS and <0.5 for SSF, retention time of 5-30 days for FWS and 2-5 days for SSF and media with porosity of 0.3 to 0.5 were found optimum.

H Wang et al, [26] investigated the performance of the constructed wetland systems using zeolite materials with good denitrification as substrates. The author investigated the zeolite for its material properties, adsorption kinetic simulation at isothermal condition and purification effect of pollutants. The study reports that, zeolite has exhibited high static adsorption capacity of NH_4^+-N than the total phosphorus. These adsorption capacities were plotted using Langmuir and Freundlich equations and adsorption kinetic simulation exhibited the highest correlation coefficient (R^2) for both equations. Constructed wetlands with zeolites as substrates have shown highest purification on NH_4^+-N in treating the sewage and the combination of zeolites and ceramsite was improved the purification effect of wetlands. Author also reported that by modifying the zeolites, the adsorption capacity of pollutants was improved.

A A Beni and A Esmaeili [27] investigated on design and optimization of parameters of biofilm reactor with flat ceramic substrates to remove the Co (II), Ni (II and Zn (II) from industrial wastewater. Authors have used clay ceramics prepared with nano-rubber which have high mechanical resistance. Hydroxyapatite and neutral fiber were used to modify the surface of ceramic substrates and produced a stable biofilm mass of 320 g with 2mm thickness on the surface after completion of 3 days. Polymerase chain reaction method was used to identify the microorganism on the biofilm and FTIR was used to identify functional groups of biofilms. Experiments were designed using central composite design (CCD) through responsive surface method (RSM) and biosorption process was found optimum at conditions namely pH of 5.8, temperature of 22^{o}C, metal wastewater feed flux of 225 ml, substrate flow of 30 ml and retention time of 7.825 hours. Pseudo first and second-order kinetic models were used to analyze the kinetic data and isotherms models were applied to analyze the biosorption capacity of the biofilm reactor. Authors found that the maximum biosorption capacity of 72% and heavy metal ions of 57.21 mg was achieved.

Similarly, another scientific wetland system was developed by the Council of Scientific and Industrial Research-National Environmental Engineering Research Institute (CSIR-NEERI) named as Phytorid [28]. This involves subsurface flow wetland system using microorganisms and selected species of plants. Phytorid is an effective system for treating the waste water without

adding any chemicals to the domestic waste and providing many advantages such as no electricity requirement, low cost and least man power for maintaining. This system does not require large facilities and system is adaptable to temperature ranges between 5- 50^0C. This technology uses aquatic, semi aquatic and mixed type of plants to remove the pollutants, pathogens and other micro-organisms present in the waste water with attached bacteria to the root profile. Phytorid system consists of bed with odd numbers of baffles to provide sinusoidal flow and every chamber of the reactor bed filled with sand, crushed stones and bricks as filter media along with aquatic and semi aquatic plants (canny lily (Canna sps), elephant grasses (Pennisetum purpurem), cattalis (Typha sps), dwarf palm (Cyperus alternifolious), arrow arum (Peltandra Virginia), sweet flag (Acorus calamus) etc.). Phytorid system consists of three zones namely inlet, treatment and outlet where the sewage mix filled in inlet tank and enters to the treatment zone. This treatment tank consists of aquatic or semi aquatic plants which are grown on the top of the substrate by spreading the roots down to the substrate and the bacteria attached to the roots of the plants treats the sewage water. This treatment zone helps in removing the suspended solids present in sewage through the substrates (sand, gravel stones and crushed bricks) and the bacteria. Further, treated water can be used for irrigation and gardening or discharged into lakes. A typical phytorid system of 15 KL/D installed at ARCI by CSIR-NEERI is shown in Fig.6.1.

Fig. 6.1 Phytorid sewage treatment plant of 15 KLD established at ARCI by CSIR-NEERI

Major drawback of the subsurface flow constructed wetland system that it requires more land for installation where the availability of the land and cost of land in urban regions are high. A better option to address the above problem is to use the substrates with high geometrical surface

area and also high specific surface area to make the system more compact minimizing the land utilization. In view of this, laboratory scale reactors are designed in collaboration with CSIR-NEERI to explore the possibility of employing the 3D printed honeycomb structures with square, hexagonal and triangular configurations and to evaluate the advantages over conventional substrates currently used. Since 3D printing permits use of naturally occurring clay along with flexibility in designing various configurations it is expected to tailor material and configuration to achieve optimum results. In addition to honeycombs, gravel stones (currently used substrates) and a combination of gravel stones with honeycombs were also experimented for the sake of comparison of results. In order to evaluate the performance inlet and treated water of all reactors evaluated for pH, Total Suspended Solids (TSS), Chemical Oxygen demand (COD) and Biological Oxygen Demand (BOD). An attempt has also been made to characterize the surface area, surface morphology, density, porosity and compressive strength of the substrates and to correlate with the above parameters.

6.1.1.3 Experimental Procedures

6.1.1.3.1 3D Printing of Honeycomb Structures

Clay based honeycombs structures with various configuration such as hexagonal, square and triangle channel were prepared by ram extrusion-based 3D printing process and the process detailed in the chapter 5 at section 5.2.1.3. Printed clay honeycomb structures are shown in Fig. 6.2 and cellular parameters of all honeycomb configurations were measured and tabulated in Table 6.1.

Fig. 6.2 3D printed clay honeycomb structures

Table 6.1 Properties of 3D printed clay honeycomb

Properties	**Ceramic honeycombs**			**Gravel stones**
	Square channel 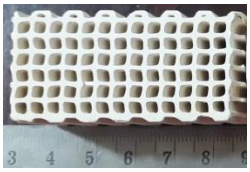	**Hexagon channel** 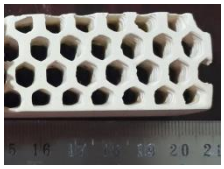	**Triangle channel** 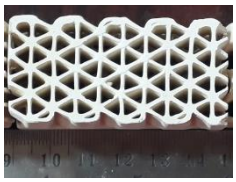	-
Honeycomb cellular parameters (mm) (Edge length (l), Wall thickness (t))	l=6.52 and t=1	l=5.53 and t=2	l=13.40 and t=1	-
Surface to Volume Ratio	15.16	8.41	4.34	3.78
Specific surface area (m^2/g)	53.05	53.05	53.05	1.4[29]
Density (g/cc)	1.68	1.68	1.68	2.59
Compressive strength (MPa)	3.64	5.13	3.31	-

6.1.1.3.2 Design of the Reactor

In the present study, a laboratory scale reactor which is similar to the actual phytorid system installed at ARCI was fabricated at our laboratory with the guidance obtained from NEERI, Nagpur. Engineering drawing of the reactor is shown in Fig.6.3 and fabricated reactor is shown in Fig.6.4

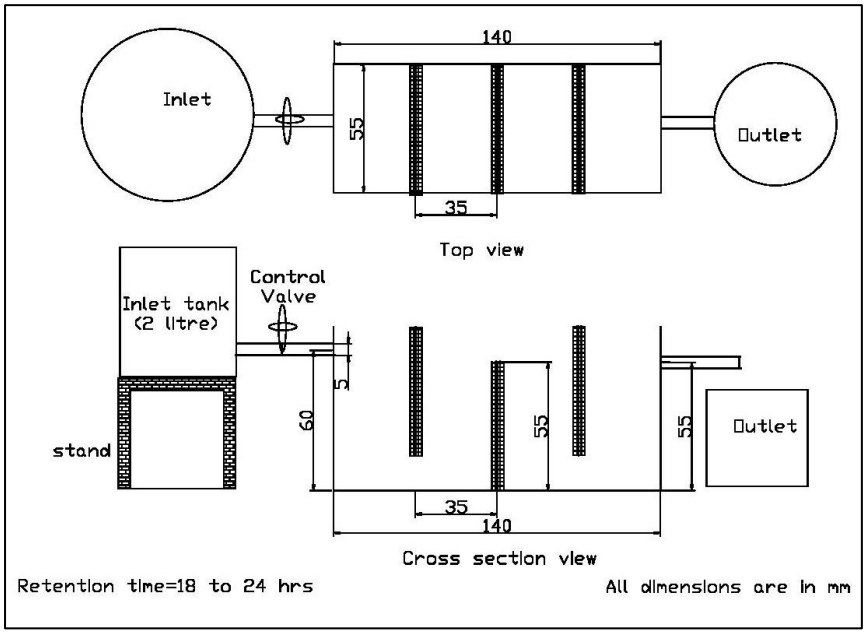

Fig.6.3 Engineering drawing of the laboratory scale bio-reactor

Engineering drawing of the laboratory scale bio reactor shows three compartments namely inlet tank, reactor bed and outlet. In order to acclimatize the microorganism, the enriched water was stored for 15 days before in letting the sewage water. Inlet tank is used to collect all the sewage waste water and reactor bed act as the treatment tank in which inlet wastewater flows through the reactor bed and undergo the treatment process. Outlet tank will be used to collect the treated water. Considering the quantity of water need to be treated in the treated tank, the inlet and outlet tanks were designed. Inlet tank works as a sedimentation chamber and provides pre-primary treatment to the wastewater before entering into the reactor bed. Design of reactor bed depends on the ratio of length and breadth (3:1) and bed contains odd number of baffles placed up and down to the wall in the reactor bed, which results the sinusoidal flow of the wastewater. Further the arrangement of baffles also results in effective treatment of entered wastewater and prevents the short circuiting

of wastewater. In conventional reactors, the different grades of stones/gravels are used as substrate for the subsurface flow of wastewater.

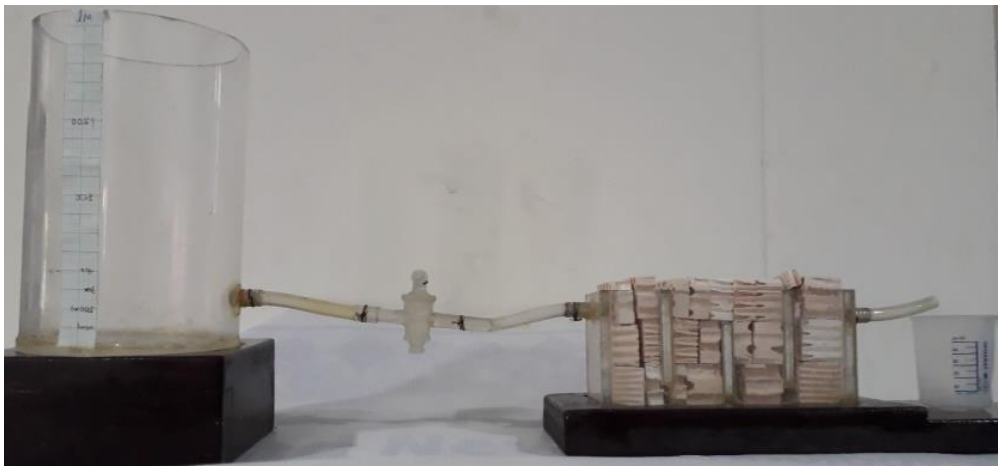

Fig 6.4 Fabricated laboratory scale bio-reactor

6.1.1.3.3 Configuration of Phytorid Bio-Reactors

Three reactors were fabricated with same volume to investigate the substrate properties on the performance of the reactor and named the reactors as Reactor-1, Reactor-2 and Reactor-3. Reactor beds shown in Fig.6.5 (a), (b) and (c) filled with 3D printed clay honeycombs, combination of gravel stones and honeycombs and only with gravel stones respectively. All the chambers of the Reactor-1 were filled with 3D printed clay honeycombs of square, hexagon and triangle channel. In Reactor-2, the first chamber was filled with gravel stones and other three chambers filled with 3D printed clay honeycombs. For sake of comparison, treatment bed of Reactor-3 was filled with gravel stones. Flow conditions such as space velocity, flow rate and retention time of all the reactors were maintained constant. A space velocity of 0.041 hr^{-1}, flow rate of 7.9 ml/hr and retention time of 24.3 hr were used for all three reactors. The properties of phytorid reactors bed have been tabulated below in Table 6.2. It is evident from the Table.2 that, geometrical surface area of substrates of the reactor bed was varied as 0.185, 0.1623 and 0.0945 m^2 to evaluate effect of substrate on the efficiency of the reactor.

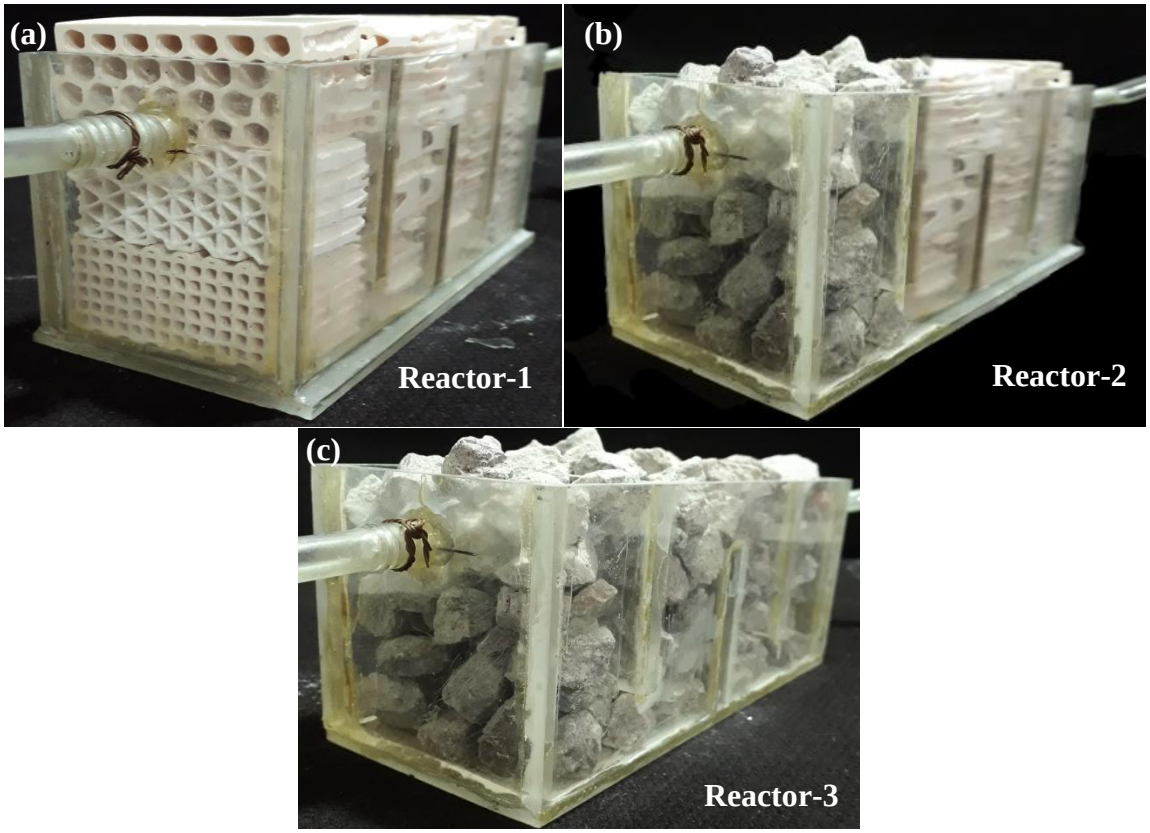

Fig.6.5 Phytorid reactor bed filled with (a) 3D printed clay honeycombs, (b) Combination of honeycombs and gravel stones and (c) gravel stones

Table 6.2 Properties of phytorid reactors

	Reactor-1	**Reactor-2**	**Reactor-3**
Geometrical surface area: Reacting bed (m^2)	0.1850	0.1623	0.0945
Specific surface area: Reacting bed (m^2)	10494	8104	934
Space velocity (Flow/Reactor volume) (hr^{-1})	0.041	0.041	0.041
Retention time (hr)	24.3	24.3	24.3
Weight of reactor (g)	478	595	947

Further, sewage water passed through the reactor at identical flow conditions and treated water was collected after every 15 days to analyze the outlet samples for pH, total suspended solids (TSS), biological oxygen demand (BOD) and chemical oxygen demand (COD) which are key and important parameters to decide the quality of treated water as per the Indian guidelines at NEERI

zonal laboratory- Hyderabad. Test samples were collected at after 15th, 30th and 45th days of bacteria acclimatization and analyzed using the standard procedure of American Public Health Association (APHA) [30]. The acidic or basic nature of the waste water was measured by instrumental method and also it affects the rate of growth of the microorganisms. The water with pH ranges from 6.5 to 8.5 is suitable to microorganisms to perform well. Standard procedure for measuring TSS, BOD and COD are described below.

Total Suspended Solids (TSS):

It is one of the quality control parameters of waste water and it is defined as the fine solid particles which are remain suspended in water. Standard procedure was described in a book "Standard Methods (2005), 2540D & EPA (1983)" used to measure TSS present in the water. To determine TSS present in the water, a known volume of well mixed water which contains suspended solids were taken and filtered through glass fiber filter paper whose pore size is known and weight of the filter paper was taken using analytical balance. Vacuum was applied to the filtration apparatus to fast filtration of water and after filtration, the filter paper was heated to 104±1^{o} C and cooled till it attains the room temperature and weighed. The gain of weight of the filter paper is dry weight of the suspended matter present in that particular volume of water and expressed in mg/L.

TSS in mg/L calculated using formula

$$TSS = \left(\frac{A - B}{V}\right) * 10^{6}$$

Where A is Dry weight of residue and filter in grams

B is the dry weight of filter alone in grams

V is the volume of sample in mL

This method is suitable to measure water with TSS of up to 20,000 mg/L.

Biological Oxygen Demand (BOD):

It is defined as the consumption of oxygen by microorganisms and bacteria during the decomposition of organic matter under aerobic atmosphere at specified temperature. Standard method (5210B) was used to measure BOD and this method allows the estimation of BOD at pH of 6.5 to 7.5 and incubation time of 5 days. To measure BOD of the waste water, pH was measured

and adjusted it to 7.0-7.2 by adding sulphuric acid or sodium hydroxide at sample temperature of 20 ± 3°C. These reagents and quantity do not dilute the sample more than 0.5%. Further, adding of Na_2SO_3 remove the residual of chlorine compounds. Determined the required volume of Na_2SO_3 solution on 100-1000 ml of neutralized sample by adding 10 ml of acetic acid reagent and 10 ml of potassium iodide (KI) solution per 1000 ml to the sample by titrating with the Na_2SO_3 solution to the starch-iodine end point for residual. Later the sample diluted with DI water and prepare a seed suspension in BOD bottle (300ml) by adding sufficient microorganisms.

During the test, the suitable volume of source water transferred to BOD bottle and check the dissolved oxygen concentrations which should be at least 7.5 mg/L before conducting the test. Later, 1 mL of phosphate buffer, $MgSO_4$, $CaCl_2$, $FeCl_3$ solution added to the source water and adjusted the temperature to 20±3°C. After 5 days of incubation, three dilutions of prepared samples estimated to produce DO of at least 1.0 mg/L. These dilutions prepared in BOD bottles and added the seed suspension. Further these bottles were subjected to nitrification inhibitor followed by the sealing. Initial DO of the sample estimated by membrane electrode method and incubated at 20 ± 1°C followed by the measuring of final DO after incubation period of 5 days± 6 hrs.

BOD of the wastewater was calculated by using formula,

$$BOD_5 = ((D1 - D2) - (S)Vs)/P$$

Where D1 is DO of the diluted sample immediately after preparation, mg/L

D2 is DO of the diluted sample after 5 days incubation at 20°C, mg/L

S is Oxygen uptake of seed,

Vs is Volume of seed in respective test bottle in mL and

P is decimal volumetric fraction of sample used; 1/P is dilution factor.

Chemical Oxygen Demand (COD):

It is defined as an indicative measure of quantity of oxygen that is consumed by the chemical reactions in the measured solution and represents as mg/L. All the organic compounds present in the sample oxidized to carbon dioxide with strong oxidizing reagent. Dichromate is used as oxidizing agent for determining the COD and used potassium dichromate which is a strong oxidizing agent under acidic conditions (achieved by adding sulphuric acid). Potassium dichromate solution of 0.25 N used for determining the COD. During the process oxidizing the organic substances in water sample, potassium dichromate reduces and forms Cr^{3+}. High mount of

potassium dichromate has to be added to the solution to oxidize all the organic matter present in the sample. For this high amount of potassium dichromate is subjected to titration while adding ferrous ammonium sulphate until excess oxidizing agent reduces to Cr^{3+} and added the ferroin (oxidation-reduction indicator) which is prepare by adding 1.485 g, 1,10-phenanthroline monohydrate to 695 mg $FeSO_4.7H_2O$ in DI water followed by dilution of resulted red solution to 100 ml. As the excess dichromate reduced, the ferroin indicator changes its color from blue-green to reddish brown. The quantity of ferrous ammonium sulphate (FAS) added is equivalent to excess amount of potassium dichromate added to the original sample.

COD of the sample calculated using formula

$$COD = \frac{8000(b-s)n}{sample\ volume}$$

Where b is the volume of ferrous ammonium sulphate (FAS) in blank sample

s is the volume of FAS in original sample

n is the normality of FAS.

6.1.1.3.4 Performance of the Reactors

Outlet water was collected from the three reactors and analyzed for the pH, TSS, BOD and COD along with the inlet water at laboratory of CSIR-NEERI, Hyderabad. Five measurements were recorded for every parameter and average value of the parameter is tabulated in Table 6.3. It was observed that, the reactors have shown better performance in terms of pH, TSS, BOD and COD as the day of bacterial acclimatization increasing and forming the bio-films on the substrates leads to efficient sewage treatment. The pH of the collected outlet water was approximately same in all three reactors. Reactor-2 and Reactor-3 have shown relatively lower performance than the Reactor-1. The efficiency in terms of TSS, BOD and COD was high for Reactor-2 and it was due to the combined effect of tortuous path offered by gravel stones in first chamber of the reactor along with the laminar flow offered by the regular array of channels of honeycomb structures. Higher efficiency was observed in the case of Reactor-1 against the Reactor-3 which was resulted due to the layer structure in combination with optimum sintering temperatures to obtain high porosity and surface morphology. Performance markers of all three reactors were plotted as a bar graph and shown in Fig.6.6 (a)-(c). The layered structure of 3D printed honeycomb is shown in

Fig. 6.7 (a) and morphology of honeycomb structure were recorded using Scanning Electron Microscope (SEM) and is shown in Fig.6.7 (b).

Table 6.3 Performance markers of the phytorid bioreactors

		After 15 days				After 30 days				After 45 days			
		pH	TSS	BOD	COD	pH	TSS	BOD	COD	pH	TSS	BOD	COD
Inlet		5.39	255	150	480	6.88	250	145	450	6.55	258	140	440
Outlet	Reactor -1	7.83	57	86	224	8.02	56	81	224	7.36	54	77	156
	Reactor -2	7.54	53	73	215	7.86	51	72	220	7.25	50	65	156
	Reactor -3	7.73	111	110	252	8.08	61	85	244	7.48	50	79	212
Standard		5.5-9.0	200	100	250	5.5-9.0	200	100	250	5.5-9.0	200	100	250

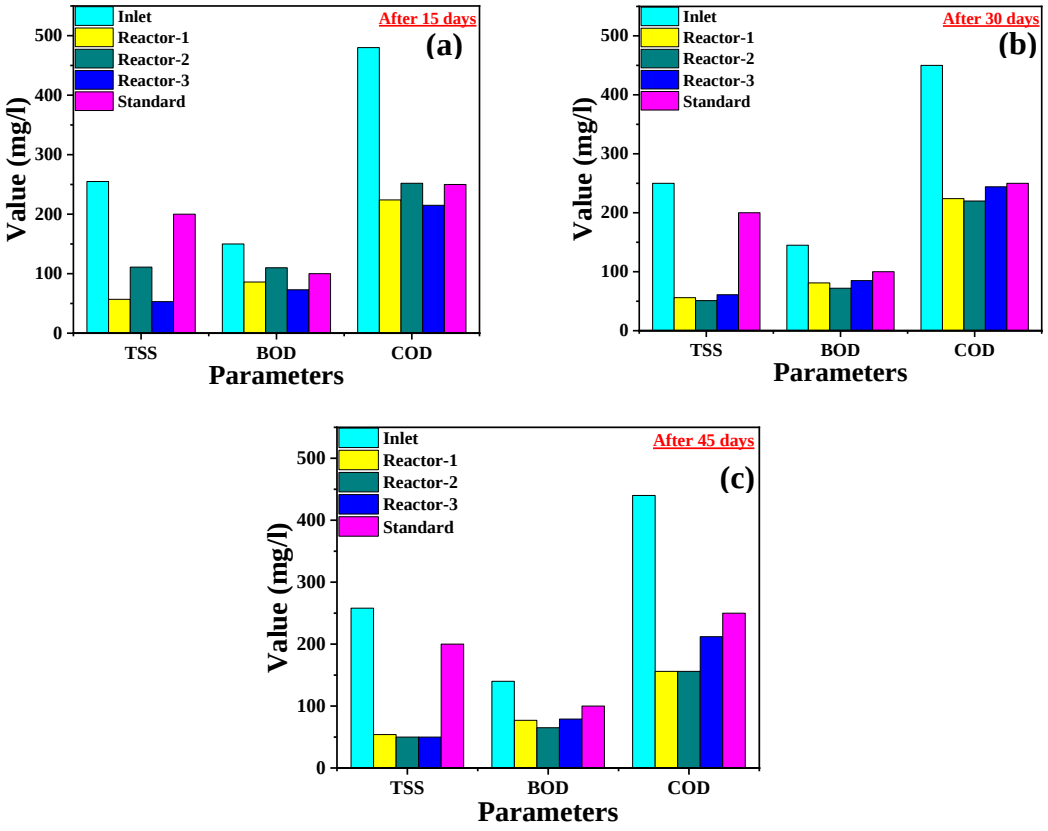

Fig.6.6 Efficiency of parameters for reactors (a) 15 days (b) 30 days and (c) 45 days of micro-organism acclimatization on substrates

It is evident from the Fig. 6.7 that the porous microstructure and layered structure results in the boundary layer formation which works as a filter medium. Also, the both biological and chemical decomposition of sewage was better compared to the conventional reactor (Reactor-3) filled with gravel stones. The SEM image of gravel stone is shown in Fig. 6.8 and it is clear that the surface of gravel stones is irregular and not porous. Due to these surface features of gravel stones, the conventional reactor has shown effective filtration in the case of TSS but lower efficiencies in BOD and COD.

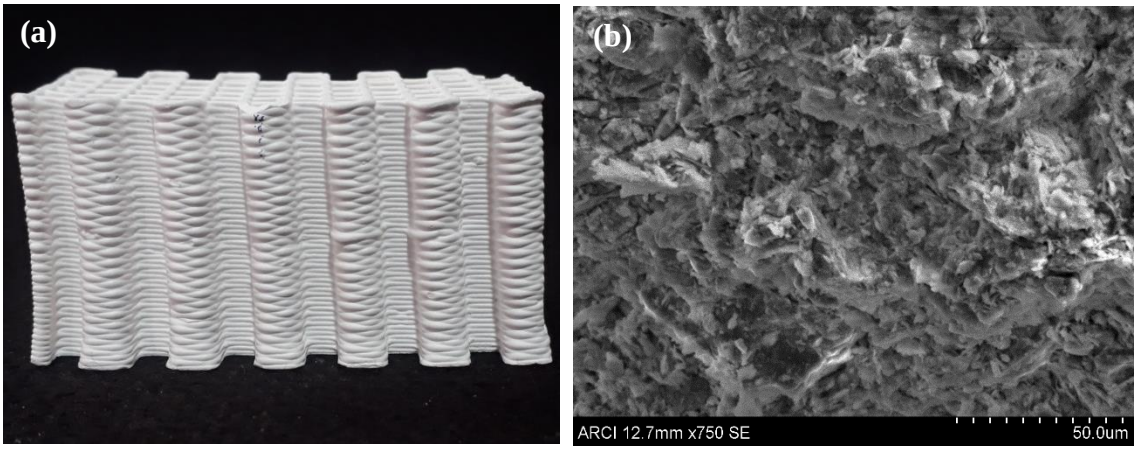

Fig. 6.7 (a) Layered structure of 3D printed honeycomb sample and (b) Microstructure of honeycomb

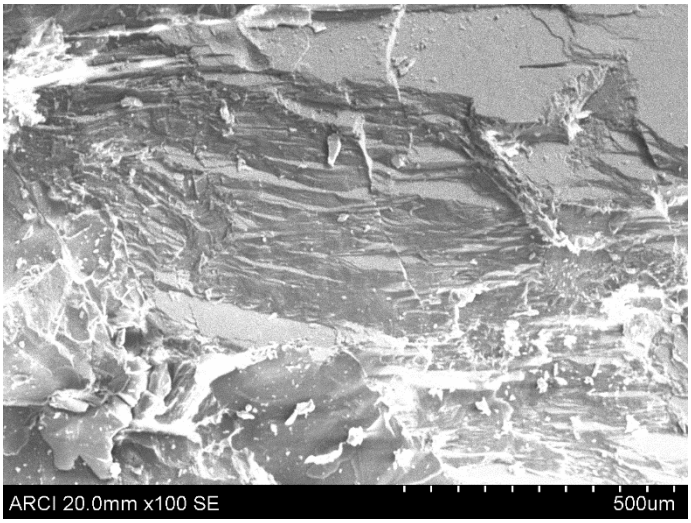

Fig.6.8 Microstructure of gravel stones used in Reactor-3

The investigation carried out of using clay-based honeycomb structures as substrates for phytorid bioreactor sewage treatment system reveals that, phytorid bioreactor system filled with combination of gravel stones and honeycombs could improve the performance of the reactors in case of BOD and COD. Weight of the reactors was also reduced by using the 3D printed honeycombs structures as substrates and offers the flexibility of using 3D printed honeycomb structures instead of gravel stones. Additionally, use of 3D printed honeycomb substrates with optimum surface to volume ratio and scaling up the flow parameters results in sub-scaling the phytorid sewage bioreactor on economy scale.

6.1.1.3.5 Summary of the Work

Clay honeycombs with square, hexagonal and triangle configurations were 3D printed using predesigned cellular parameters and sintered to achieve the desired porosity and microstructural properties. A comparative study and investigations were carried out to evaluate the performance of the phytorid bioreactors filled with 3D printed clay honeycombs, combination of honeycombs and gravel stones and gravels. Inlet and outlet water were measured for performance markers such as pH, TSS, BOD and COD which have shown substantial reduction in the outlet water and meeting with the standards. It is also confirmed that, reactor with the combination of stones and honeycombs resulted in highest efficiency due to the tortuous path and laminar flow offered by the gravel stones and honeycombs respectively. It reveals that, exploring the use of 3D printed honeycomb substrate with weight reduction, high mass transfer and optimum surface to volume ratio offers the miniaturization of phytorid bio-reactors economically.

---

* This work has been published in Journal of Water Process Engineering 37(2020), 101503, Impact factor: 5.48

6.1.2 3D Printed Substrates for Removal of Fluoride from the Drinking Water

Another application was explored using 3D printed cellular structures to remove the fluoride from drinking water. The aim of this study is to use high surface area 3D printed cellular structures as substrates to remove the fluoride contaminated water where it is major problem in some of the semi-arid regions of India such as Gujarat, Southern Punjab, Rajasthan, Tamilnadu, Karnataka, Andhra Pradesh, Madya Pradesh and southern Haryana [31]. The consumption of water with high

amount of fluoride content (1.5-2.0 ppm) results in dental fluorosis and at higher concentrations of fluoride of 3-6 ppm causes skeletal fluorosis.

6.1.2.1 Literature Survey

J He et al, [32] have investigated on removal of fluoride from drinking water by using novelty-defined adsorption membrane. Authors have prepared zirconium metal-organic frameworks (Zr-MOFs) and studied the adsorption characteristics in batch mode. Using as prepared Zr-MOFs as adsorbent resulted in maximum adsorption capacity of 102.4 mg/g at pH 7.0 for inlet concentration of 200 mg/L. For membrane experiments prepared Zr-MOFs was supported on alumina substrate and used as substrates for the removal of fluoride through dynamic filtration. Both Zr-MOFs adsorbent and membrane with high specific surface area (740.28 m^2/g) were used for the first time for defluoridation experiments. The author reported that efficiency of the Zr-MOFs membrane is depends on the initial concentration of fluoride and flow rate.

J He et al, [33] prepared biocompatible adsorption membrane for quick removal of fluoride from drinking water. Al-HAP membranes were prepared using $Al(OH)_3$ nanoparticles and modified nanowires of hydroxyapatite (Al-HAP). The adsorption occurred due to the AL-HAP adsorbent was analyzed by Freundlich isotherm model and the kinetics of adsorption has followed the pseudo-second order model. The study reported that maximum adsorption of 93.84 mg/g occurred for the inlet fluoride concentrations of 200 mg/L. The study also reported that HAP nanowires contributed 36.7% and $Al(OH)_3$ nanoparticles contributed 63.3% in removing the fluoride from the drinking water. It is also stated that Al-HAP membrane with 0.3 mm thickness could achieve 1668 L/m^2 for the inlet concentrations of 5 mg/L.

J Saikia and R L Goswamee [34] have used flat and porous ceramic substrates made with clay and coated with aluminum oxyhydroxide deposited carbon using vacuum driven filtration process. Further these carbon substrates were used to remove the fluoride from the contaminated water. The authors were also focused on to immobilization of the adsorbed fluoride ions to prevent leaching from the substrates. Authors used cement clinkers for permanent immobilization of the adsorbed fluoride from the membrane by reacting with lime and clay. The studies have shown a decrement in firing temperature for clinker formation from 1450^oC to 1350^oC due to the addition of adsorbed fluoride ceramic waste.

A Nijhawan et al. [35] conducted continuous-flow column experiments to evaluate the fluoride removal using porous hydroxyapatite ceramics. It is found that the uptake of fluoride is high for smaller adsorbent particles. Adsorption kinetics were investigated at different flow rates and found that at lower flow rates, the adsorption of fluoride by the adsorbent at point of exhaustion is increased at constant mass loading. The authors reported that decrement in effluent fluoride concentrations was due to the flow interruptions and non-equilibrium condition of the column. The study used the concept of Rapid Small-Scale Column Test (RSSCT) for scaling up the process.

J Saikia et al. [36] investigated the removal of fluoride from the ground water using low cost ceramic raw materials naturally available at Assam, India. The author have prepared the ceramic nodules and evaluated for its porosity, mechanical strength, density and water absorption. Defluoridation experiments were conducted for real life ground water and fluoride spiked water in batch mode and studied the effect of pH, retention time, temperature, adsorbate dose on the efficiency. The results were analyzed and isotherms were plotted using Freundlich model which have shown best fitting based on the regression coefficient (R^2) and pseudo-second-order kinetics.

In the current study, due to the unique configurations that can be achieved through the 3D printing process which can offer several advantages an exploratory study was initiated for the first time as reported below.

6.1.2.2 3D Printing of Alumina Cellular Structures

The alumina honeycombs with corrugated designed pattern were printed using 3D CAD model through ram type extrusion-based 3D printing process at optimum printing conditions described in chapter.5 at section 5.4 and shown the 3D printed alumina structure in Fig.6.9. For application purpose, dried honeycombs were sintered at 1200^{o}C to obtain required porosity and surface morphology. The sintered alumina corrugated structures were measured for its physical properties such as density and apparent porosity by Archimedes principle and found that the samples have shown 65% of theoretical density along with the apparent porosity of 30-35%. Cellular properties of these corrugated structures are shown in Table 6.4.

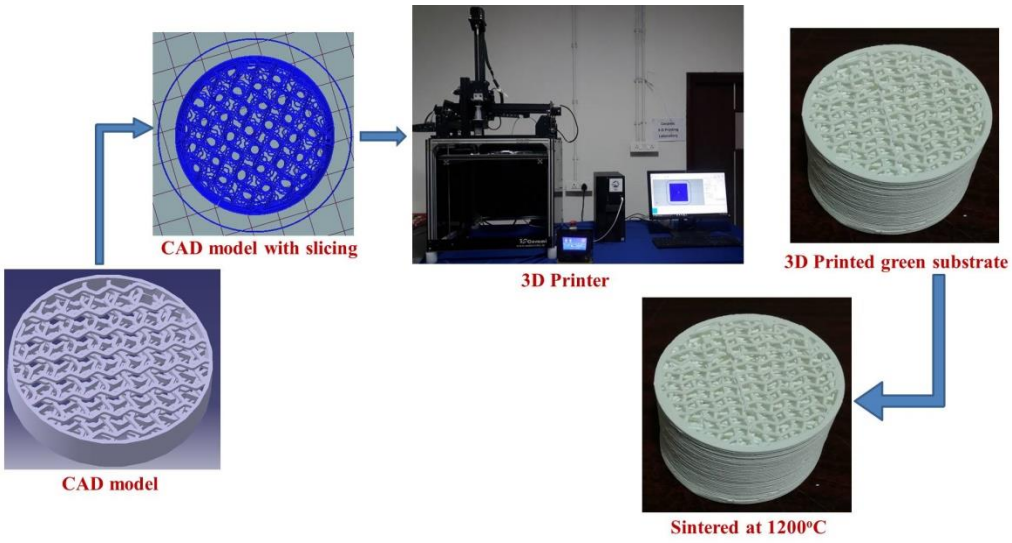

Fig. 6.9 3D printing process of alumina substrate with corrugated pattern

Table 6.4 Cellular properties of 3D printed alumina substrate with corrugated pattern

Cellular properties of 3D printed alumina substrate with corrugated pattern		
Edge length(l), cm	**Thickness(t), cm**	**Geometrical Surface area (cm^2) per one 3D printed alumina substrate**
0.4	**0.1**	**425**
Physico-chemical properties of sintered alumina substrate		
Density by Archimedes principle (ASTM B962) (g/cc)		**2.54**
Apparent porosity (%)		**30-35**

6.1.2.3 Wash Coating of 3D Printed Alumina Substrates with γ-Alumina

The flow chart in Fig.6.10 indicates steps involved in the coating of gamma alumina on 3D printed alumina substrates of corrugated pattern with high geometrical surface area. As **γ**-alumina is one of the materials that possess high specific surface area and it is not commercially available.

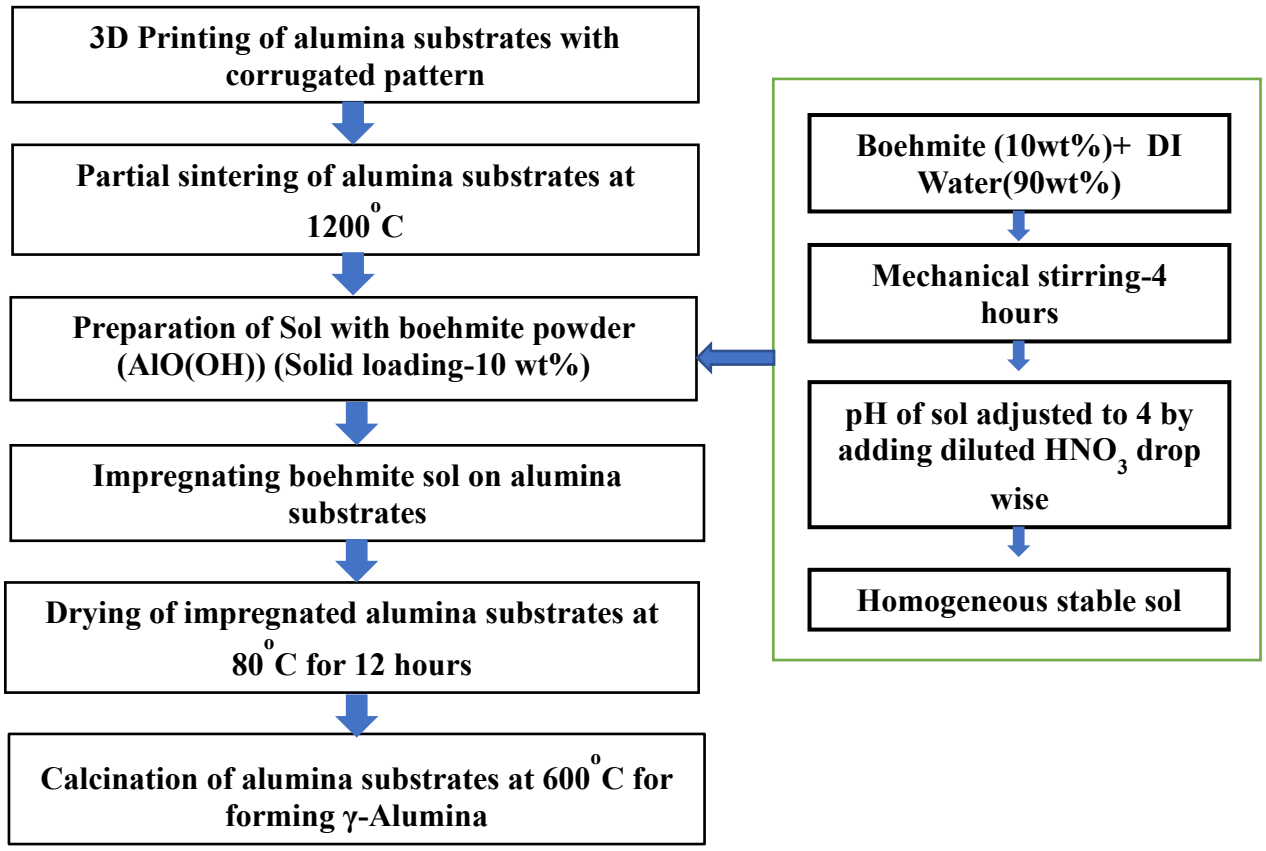

Fig.6.10 Flow chart of coating process of γ-alumina on 3D printed alumina substrates

In the current study, a commercially available boehmite powder was used to coat on 3D printed alumina substrates. For this, an aqueous boehmite sol was prepared with 10 wt.% solid loading under mechanical stirring condition for 4 hours. During stirring the pH of the sol was adjusted to 4 by adding diluted nitric acid drop wise. Further the obtained stable sol was used to coat on 3D printed alumina substrates through dipping method. Five alumina substrates with corrugated patterns were coated with the sol for 2 times and dried at 80^{o}C for 12 hours. Further all these coated samples were calcined at 600^{o}C to form **γ** -alumina and confirmed by the XRD technique and recorded diffraction pattern is shown in Fig.6.11.

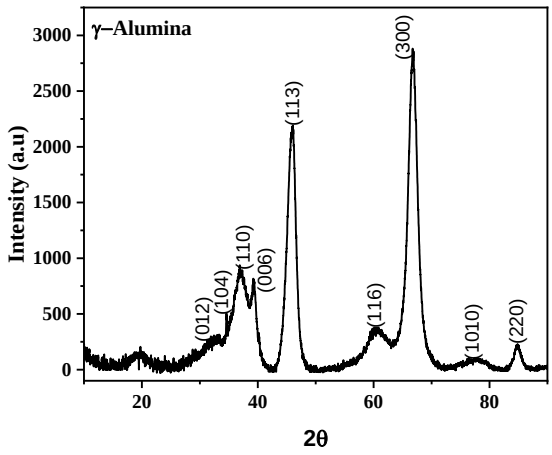

Fig.6.11 XRD pattern of γ-alumina coated on alumina substrate

6.1.2.4 Design of the Defluoridation reactor

A laboratory scale defluoridation system was designed with a volume of 380 cc and the schematic is shown in Fig. 6.12. It represents that the defluoridation reactor was placed with γ-alumina coated 3D printed alumina substrates channelized in a vertical direction. The inlet water will flow through the reactor as opposed to the gravity and collected through outlet. The design parameters of the reactor are shown in Table 6.5.

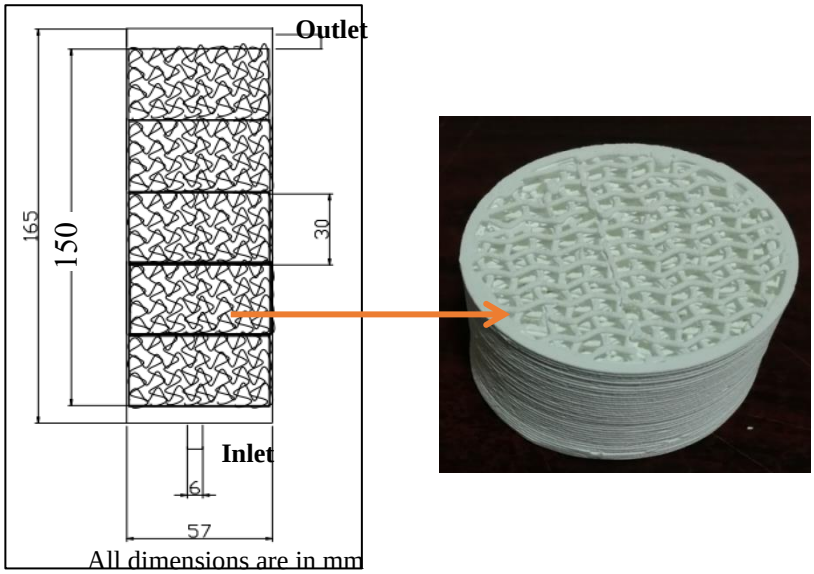

Fig.6.12 Cross-section view of defluoridation system with γ-alumina coated 3D printed alumina corrugated structures as the substrate

Table 6.5 Design parameters of the defluoridation reactor

Reactor Design Parameters	
Retention time	1.76 hr
Volume of reactor bed	380 cm^3
Flow rate	240 ml/ hr

As mentioned in Fig. 6.12, a reactor was assembled and shown in the Fig.6.13. Five coated alumina substrates were channelized in a vertical direction in the chamber. The reactor was filled with deionized water (DI) and left for 24 hours and drained. Further the inlet water was spiked with 3-7 ppm of fluoride concentration was prepared by dissolving Sodium fluoride (NaF) (AR RANKEM, Avantor Performance Material India Limited, Maharashtra, India) in DI water and passed through the reactor at a flow rate of 4 ml/min. The water was reacting with the **γ-**alumina coated on the walls of the alumina substrate and adsorbed by the adsorption sites. The treated water collected from the outlet after every 2.5 hours and measured for fluoride concentration through Inductively Coupled Plasma-Atomic Emission Spectroscopy (ICP-AES) at National Centre for Compositional Characterization of Materials (CCCM), Hyderabad and the results have been tabulated in Table 6.6. It is evident from Table 6.6 that the inlet water with 3 ppm fluoride concentrations were meeting with standard (desirable limit of fluoride=0.5 to 1.5 ppm) of World Health Organization (WHO). The water consisting higher amount of fluoride i.e., 5 and 7 ppm were not meeting with the stipulated standards, though it has shown 50% reduction of fluoride in the outlet water compare to the inlet water.

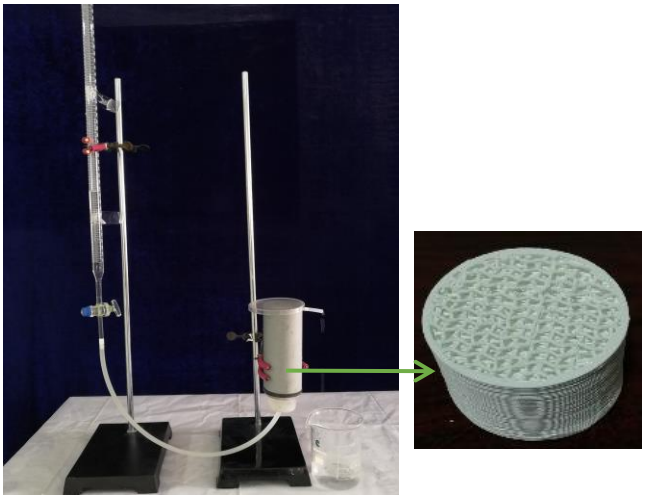

Fig. 6.13 Defluoridation reactor

Table 6.6 Defluoridation results

Inlet (mg/L)	Outlet (mg/L)	Adsorption with respective to γ-Al_2O_3 coated on substrate (mg/g)
3.17	1.22	2.96
3.17	1.23	2.98
3.17	1.20	2.99
5.12	2.13	4.55
5.12	2.17	4.48
5.12	2.63	3.78
5.12	3.39	2.63
7.59	5.18	3.66
7.59	5.35	3.40
7.59	5.35	3.40
7.59	5.56	3.08

The performance of the reactor can be enhanced by increasing the surface area of cellular structures as well as the percentage loading of γ-alumina on cellular structures. Recirculation of the outlet water with higher fluoride concentrations through the reactor is also an option to meet the standards of WHO.

6.1.2.5 Summary of the Work

Alumina substrates with corrugate pattern were 3D printed using predesigned cellular parameters successfully. 3D printed alumina substrates with corrugated patterns were sintered at optimum conditions to achieve required porosity, surface morphology and coated with high surface area gamma alumina through sol-gel process, found an adsorbent dose of 0.4% by wt. on the alumina substrates. A laboratory reactor was fabricated with a reactor bed volume of 380 cm^3 and a flow rate of 250 ml/hour was maintained identically for water containing 3, 5 and 7 PPM. Water containing 3 PPM of fluoride has met the stipulated standard for potable

water, the water with higher concentrations of 5 and 7 PPM required to be treated through recirculation or higher loading of gamma alumina to achieve the standards.

---

*This work presented at 84th Annual session of Indian Ceramic Society and National seminar on "Propelling Innovations in Glass and Ceramics for Atmanirbhar Bharath" on 10-12th of December, 2020

6.2 References

1. F L Burton, G Tchobanoglous, R Tsuchihashi, H D Stensel, Metcalf and Eddy, Inc. Wastewater Engineering: Treatment and Resource Recovery, McGraw-Hill Education, 2013, ISBN:0073401188.
2. K Andersson, A Rosemarin, B Lamizana, E Kvarnström, J McConville, R Seidu, S Dickin, C Trimmer, Sanitation, Wastewater Management and Sustainability: from Waste Disposal to Resource Recovery. Nairobi and Stockholm: United Nations Environment Program and Stockholm Environment Institute. ISBN:978-92-807-3488-1, p. 56, 2016.
3. S M Khopkar, Environmental Pollution Monitoring And Control, New Delhi: New Age International., ISBN:978-81-224-1507-0, p. 299, 2004.
4. How Wastewater Treatment Works...The Basics (PDF). EPA. 1998. Retrieved 27 March 2021.
5. Huber Company, Berching, Germany (2012). "Sedimentation Tanks."
6. Stage 3 - Tertiary treatment, Sydney Water. 2010.
7. Hopcroft, Francis (2014). Wastewater Treatment Concepts and Practices. Momentum Press.
8. J Patel, 4-step waste water sludge treatment process, Water Online, 2018
9. Barwal, Anjali, Chaudhary, Rubina, To study the performance of biocarriers in moving bed biofilm reactor (MBBR) technology and kinetics of biofilm for retrofitting the existing aerobic treatment systems: a review. Reviews in Environmental Science and Bio/Technology. 2014;13: 285–299.

10. Randall, W Clifford, Sen, Dipankar, Full-scale evaluation of an integrated fixed-film activated sludge (IFAS) process for enhanced nitrogen removal. Water Science and Technology. 1996;33: 155–162.
11. N L Panwar, S C Kaushik, S Kothari, Role of renewable energy sources in environmental protection: A review, Renewable and Sustainable Energy Reviews, 2011;15:1513-1524.
12. Reports & multimedia/Explainer, Environmental impacts of renewable energy technologies, 2013.
13. N A Akhade, A R Mhaske, B Punde, Modeling of COD using phytorid sewage treatment plant, International Journal Innovative Research Science Engineering and Technology, 2019;4:35-45.
14. S S Patil, V P Dhulap, G Kaushik, Application of constructed wetland using eichhornia crassipes for sewage treatment, Journal of Materials and Environmental Science, 2019;7:3256-3263.
15. D M Koranne, D G Patil, K P Barne, A S Pasalkar, D A Narayankar, Urban wastewater treatment using phytorid, International Journal of Scientific Research and Development, 2018;6:1100-1102.
16. A M Patil, S Gawande, Implementation of sewage treatment plant by using phytorid technology, International Journal of Innovative Research Technology, 2016;3:121-123.
17. A R Mhaske, G R Atal, S P Gawande, Optimization of potassium from domestic sewage water phytorid sewage treatment plant: a study using Box-Behenken design, Journal of Soils and Crops, 2017;27:169-177.
18. J Teng, L Shen, Y Xu, Y Chen, X-L Wu, Y He, J Chen, H Lin, Effects of molecular weight distribution of soluble microbial products (SMPs) on membrane fouling in a membrane bioreactor (MBR): Novel mechanistic insights, Chemosphere, 2020;248:126013-126023
19. M Wu, Y Chen, H Lin, L Zhao, L Shen, R Li, Y Xu, H Hong, Y He, Membrane fouling caused by biological foams in a submerged membrane bioreactor: Mechanism insights, Water Research, 2020;181:115932-115942.
20. W Yu, Y Liu, L Shen, Y Xu, R Li, T Sun, H Lin, Magnetic field assisted preparation of PES-Ni@MWCNTs membrane with enhanced permeability and anti-fouling performance, Chemosphere, 2020;243:125446-125455.

21. R Kaalipushpa, S Karthika, S Revathi, Domestic wastewater treatment using Phytorid technology, International Journal of Engineering Research and Technology, 2017;5:1-4.
22. M Kejariwal, Effect on growth of plants under “Phytorid technology based” treated water at Education Institute: A Case Study at RD National College, Technologies for Renewable Energy and Water, Harshvardhan Publication Pvt. Ltd., 2016;207-216, ISBN 978-93-85882-53-1.
23. J Vymazal, Constructed wetlands for wastewater treatment, Water, 2010;2:530-549.
24. U Stottmeister, A Wiebner, P Kuschk, U Kappelmeyer, M Kastner, O Bederski, R A Muller, H Moormann, Effects of plants and microorganisms in constructed wetlands for wastewater treatment, Biotechnology Advances, 2003;22:93-117.
25. H Wu, J Zhang, H H Ngo, W Guo, Z Hu, S Liang, J Fan, H Liu, A review on the sustainability of constructed wetlandsfor wastewater treatment: Design an operation, Bioresource Technology, 2015;175:594-601.
26. H Wang, J Xu, L Sheng, Purification mechanism of sewage from constructed wetlands with zeolite substrates: A review, Journal of Cleaner Production, 2020;258:120760-120773.
27. A A Beni, A Esmaeili, Design and optimization of a new reactor based on biofilm-ceramic for industrial wastewater treatment, Environmental Pollution, 2019;255:113298.
28. R Kumar, S Tayade, R N Singh, System and method for the treatment of wastewater using plants, WO 2004/087584A1, 2004.
29. S O Alayande, M P Mubiayi, R Derek, Experimental characterization of physicochemical and geological properties of granite from Olowu, Ibadan, Oyo State, Nigeria, Proceedings of the World Congress on Mechanical, Chemical and Materials Engineering, 2015; 337:1-9.
30. American Public Health Association, https://www.apha.org/
31. Fluorosis, National Health Portal of India, http://nhp.gov.in
32. J He, X Cai, K Chen. Y Li, K Zhng, Z Jin, F Meng, N Liu, X Wang, L Kong, X Huang, J Liu, Performance of a novelly-defined zirconium metal-organics frameworks adsorption membrane in fluoride removal, Journal of Colloid and Interface Science, 2016;484:162-172.

33. J He, K Chen, X Cai, Y Li, C Wang, K Zhang, Z Jin, F Meng, X Wang, L Kong, J Liu, A biocompatible and novelly-defined Al-HAP adsorption membrane for highly effective removal of fluoride from drinking water, 2017;490:97-107.
34. J Saikia, R L Goswamee, Use of carbon coated ceramic barriers for adsorptive removal of fluoride and permanent immobilization of the spent adsorbent barriers, SN Applied Sciences, 2019, Article number: 634.
35. A Nijhawan, E C Buttler, D A Sabatini, Fluoride adsorption on porous hydroxyapatite ceramic filters: A study of kinetics, Environmental Engineering Science,2020;37.
36. J Saikia, S Sarmah, T H Ahmed, P J Kalita, R L Goswamee, Removal of toxic fluoride ion from water using low cost ceramic nodules prepared from some locally available raw materials of Assam, India, Journal of Environmental Chemical Engineering, 2017;5:2488-2497.

****

A. Scope of Future Work:

1. There is a good scope to extend the work to various oxide ceramic formulation as well as non-oxide ceramics as the feasibility with respect to additives, rheology and printing parameters to fabricate various simple and complex ceramic parts are demonstrated.

2. The study conceptualized, designed and fabricated screw type extruder, however the printing could not be carried out in the current study. The future study can undertake printing based on the screw type extruder which provide opportunity for the continuous printing and parts with bigger dimensions.

3. Two applications are identified for 3D printed structures such as bioreactor substrates for sewage treatment as well as defluoridation of potable water. As the study is limited to the laboratory demonstration, further studies with respect to the durability and scale-up will be interesting.

4. The biomedical implants have a potential area where the 3D printing can produce patient specific implants and a magnesium aluminate spinel mesh is printed in the study in collaboration with Baylor College of Medicine, USA for possible application in cranioplasty. Future studies for biocompatibility (invitro and invivo) will be a potential sector to be explored.

B. List of Publications from the Current Research Work:

1. **S. Mamatha**, P Biswas, P Ramavath, D Das, R Johnson, 3D-Printing of complex shaped alumina parts, Ceramic International, 2018;44:19278–19281, Impact Factor: 4.52

2. **S. Mamatha**, P Biswas, D Das, R Johnson**,** Complex Shaped Ceramic Fabrication From 3D Printed Poly Lactic Acid Templates Through Replication Process, Ceramic International, 2019; 45: 19577-19580, Impact Factor: 4.52

3. **S Mamatha**, P Biswas, D Das, R Johnson**,** 3D Printing of Cordierite Honeycomb Structures and Evaluation of Compressive Strength under Quasi-static Condition, International Journal of Applied Ceramic Technology, 2020;17:211-216, Impact Factor: 1.96

4. **S Mamatha,** P Biswas, P Ramavath, D Das, R Johnson**,** Effect of parameters on 3D printing of alumina ceramics and evaluation of properties of sintered parts, Journal of Asian Ceramic Societies, 2021, Impact factor: 3.12

5. P Biswas, **S Mamatha**, S Naskar, Y S Rao, R Johnson, G Padmanabham, 3D Extrusion Printing of Magnesium Aluminate Spinel Ceramic Parts Using Thermally Induced Gelation of Methyl Cellulose, Journal of Alloys and Compounds 2019;770:419-423, Impact Factor: 5.31

6. P Biswas, **S Mamatha**, K Varghese, R Johnson, R Vijay, R Kumar, 3D printing of high surface area ceramic honeycombs substrates and comparative evaluation for treatment of sewage in Phytorid application, Journal of Water Process Engineering Technology, 2020;37:101503-101508**,** Impact factor: 5.48

7. A Adumbumkulath, C Shin, G Acharya, P Biswas, **S Mamatha**, R Johnson, G Padmanabham**,** 3D printing of $MgAl_2O_4$ spinel mesh and densification through Pressure-less sintering and hot-isostatic pressing, 3D Printing and Additive Manufacturing, 2021, Impact factor: 5.44

C. Conference presentations/Talks:

1. Poster presentation on "**Mechanical behaviour of 3D extrusion printed alumina specimens**", S Mamatha, Papiya Biswas, Dibakar Das, Roy Johnson, 83rd Annual Session of Indian Ceramic Society (ICS) and National conference on Innovation and Technologies for Ceramics (InTec-2019), on December 11-12, 2019, Trivandrum, Kerala, India.

2. Oral presentation on "**Fluoride Removal Studies in Potable Water using gamma-Alumina Coated 3D Printed Ceramic Honeycomb Substrates**". S Mamatha, Shiv Prakash Singh, Papiya Biswas, Y. Srinivasa Rao, Dibakar Das, Roy Johnson, at 84th Annual Session of Indian Ceramic Society (ICS) and National seminar on "Propelling Innovations in Glass and Ceramics for Atma Nirbhar Bharat" held on 10-12th December, 2020, organised by CSIR-CGCRI, Kolkata, India.

3. Flash Talk on "**3D printing of ceramics-An emerging technology**" at National Science Day celebrations at ARCI on 28th February 2020, Hyderabad.

4. Talk on "**3D printing of Ceramics-An Emerging Technology**", S Mamatha, Papiya Biswas, Dibakar Das, Y Srinivasa Rao, Roy Johnson at Science Technology and Innovation Talks (STIN-2021) conducted national level as a part of National Science Day celebrations organized by International Advanced Research Centre for Powder Metallurgy and New Materials (ARCI), 26th February-2021, Hyderabad.

5. Poster presentation on "**Investigations on 3D printing of complex shaped alumina parts**", S Mamatha, S Naskar, P Biswas, Y S Rao, Roy Johnson at 81st Annual Session of Indian Ceramic Society (ICS) and International Conference on "Expanding Horizons of Technological Applications of Ceramics and Glasses (EH-TACAG'17), 14-16th December, 2017, Pune.

Honours/Awards:

1. Third prize in Science Technology and Innovation Talks (STIN-2021), National Science Day celebrations organized by ARCI, Hyderabad on 26th February for the talk titled "3D Printing of Ceramics- An Emerging Technology".

Ceramics International 44 (2018) 19278–19281

Contents lists available at ScienceDirect

Ceramics International

journal homepage: www.elsevier.com/locate/ceramint

3D printing of complex shaped alumina parts

Sirisala Mamatha[a], Papiya Biswas[a], Pandu Ramavath[a], Dibakar Das[b], Roy Johnson[a,*]

[a] International Advanced Research Centre for Powder Metallurgy and New Materials, Balapur, Hyderabad 500005, India
[b] School of Engineering Sciences and Technology, University of Hyderabad, Hyderabad 500046, India

ARTICLE INFO

Keywords:
3D printing
Alumina
Rheology
Densification
Mechanical properties

ABSTRACT

Alpha-alumina powder was mixed with methyl cellulose as a binder with concentration as low as 0.25% by weight in an aquoes medium and kneaded in a high shear mixer to obtain a printable paste. The paste was subjected to rheological measurements and exhibited a shear rate exponent of 0.54 signifying the shear thinning behavior. The paste was used for printing parts with various shapes according to CAD model by employing a ram type 3D printer. Printed parts were dried and the green density was determined. Further, the parts were also subjected to X-ray radiography in order to evaluate the possible occurrence of printing defects. The samples were sintered under pressureless condition at 1650 °C in a muffle furnace and Hot Isostsically Pressed (HIP) at 1350 °C and a pressure of 1650 bar using a vacuum encapsulated SS CAN. Hot Isostatic pressing resulted in a higher density of 3.94 g/cc in comparison to 3.88 g/cc obtained under pressureless conditions and also shown superior mechanical properties. HIPing of 3D printed samples not only resulted in possible healing of printing defects as reavealed by X-ray radiography but also enhanced the diffusion at low temperature of 1350 °C leading to finer grain sizes as complemented by the microstructure.

1. Introduction

3D printing technique is an emerging area in the ceramic fabrication due to the unlimited flexibility and offers advantages for complex shaping of components with micro-features. Though the process is practiced for a long time in case of polymers and later for metals, recently the process is also being explored in the area of ceramics [1–5]. Generally complex shaped prototyping of ceramic parts for design optimization for a given service condition proceed through several steps. Some of these steps include selection of powder with optimum properties, fabrication of number of expensive molds, dies and fixtures for iterations. Generally, this is followed by cumbersome machining processes before or after sintering. Inherent advantages of the 3D printing process are prototyping of complex shapes using the same infrastructure facility leading to significant savings in process time and cost [6–10]. Stereolithography (SLA) [11,12], extrusion of ceramic pastes [13] and binder jetting [14,15] are the 3D printing processes currently explored for ceramic shaping. Ceramic 3D printing generally employs clay-based formulations due to the inherent plasticity offered by the silicate structure when mixed with organic or aqueous medium for easy shaping. Additionally, these formulations are also mixed with ultraviolet (UV) curable monomer resins as an essential component for effective polymerization which in turn provides sufficient green strength for retention of shape after printing and further processing.

In the present study, alpha alumina was blended with varying concentrations of methyl cellulose as a binder in water medium. Viscosity of the paste was modified using poly ethylene glycol (PEG) as a plasticizer to increase the cohesivity for smooth printing. The paste was printed using a ram type 3D printer fitted with nozzle and characterized the printed parts for the green density after drying. The parts were also subjected to X-ray radiography to identify any possible processing defects. The printed parts were subjected to sintering under pressureless and HIP conditions at temperature and pressure optimized through several trials at our laboratory. The samples were evaluated for sintered density, microstructure and mechanical properties. HIPed samples were exhibited higher sintered density with superior mechanical properties. This can be attributed to the HIPing conditions resulting in healing of laminations in combination with finer grains obtained due to enhanced diffusion leading to low temperature sintering.

2. Experimental procedures

Alumina powder procured from M/s Rohini Industries, India was characterized for phase purity using X-ray Diffraction Technique (XRD) (D8-Bruker, Germany) and particle size by Dynamic Light Scattering (DLS) (Malvern Instruments, UK). The powder was blended with 35 wt

* Corresponding author.
E-mail address: royjohnson@arci.res.in (R. Johnson).

https://doi.org/10.1016/j.ceramint.2018.07.153
Received 8 June 2018; Received in revised form 17 July 2018; Accepted 17 July 2018
Available online 19 July 2018

% water along with 0.25 wt% of methyl cellulose and PEG in a vacuum sigma kneader for a duration of 30 min. Resulted homogeneous alumina paste was subjected to rheological studies under varying shear rates (MCR 51, Anton Paar, Austria). 3D printing was carried out with optimized alumina paste with shear thinning behavior, using a ram type extruder. Printed parts were dried and green density measurements were carried out using dimensional method followed by X-ray radiographic analysis. Binder removal was carried out at 550 °C based on the TG/DTA curves recorded on the green samples. A slow heating rate of 1.5 °C/min was employed till 550 °C and retained at 550 °C for a period of one hour to ensure the complete removal of the binder. The binder removed samples were subjected to a heating rate of 3 °C/min till the peak temperature of 1650 °C and soaking period of one hour in a muffle furnace in air under pressureless conditions. In order to evaluate the effect of simultaneous application of temperature and pressure, the green parts were vacuum encapsulated in a specially designed SS CAN and subjected to HIPing at 1350 °C and 1650 bar pressure for densification. Sintered samples under pressureless and HIPed conditions were characterized for their physico-chemical, microstructural and mechanical properties. Density of the sintered samples was evaluated by Archimedes principle (ASTM 792) and the samples were subjected to X-ray radiography. Samples were polished and subjected to Vickers hardness testing by using hardness tester (Leco, St. Joseph, MI) at 300 g load. Further, the pressureless sintered samples were machined to rectangular specimens of 45 (l) × 4 (w) × 3 (h) mm sizes and then ground and polished for the evaluation of flexural strength using 3-point bend loading (ASTM C-1161-02C). The fractographic analysis of both the samples were also evaluated and compared for the microstructural features.

3. Results and discussion

Fig. 1 shows the XRD pattern recorded for alumina powder and it is evident from the XRD pattern that the powder is having pure α- phase of alumina with average particle size of 331 nm as shown in Fig. 2. The viscosity (η) vs. shear rate (γ) plot of the paste is shown in Fig. 3(a) and ln η vs. ln γ for the paste is shown in Fig. 3(b). The paste has shown shear thinning behavior at lower shear rate; however, a Newtonian behavior is observed at shear rate beyond 200 s^{-1}. Shear rate exponent value is estimated as 0.54 indicating shear thinning behavior ($n < 1$) which can be attributed to the optimum concentration of methyl cellulose binder and PEG dispersed in water medium optimized through several experiments at our laboratory.

The paste with shear thinning behavior was 3D printed using a ram type 3D printer (3D Cerami, Maker City, India) as shown in Fig. 4(a). 3D printed components shown in Fig. 4(b) were designed using CAD software which is converted into STL file with the printing parameters

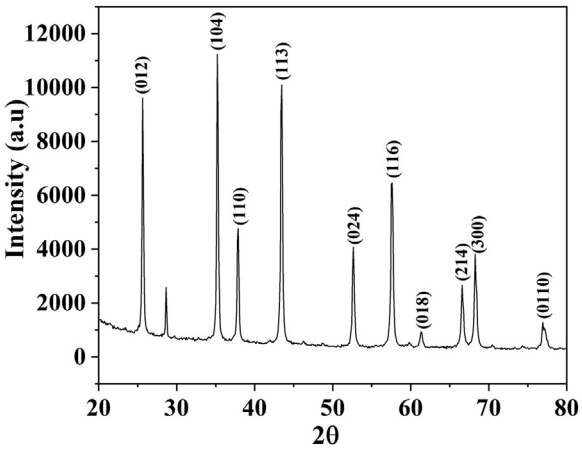

Fig. 1. X-ray diffraction pattern of alumina powder.

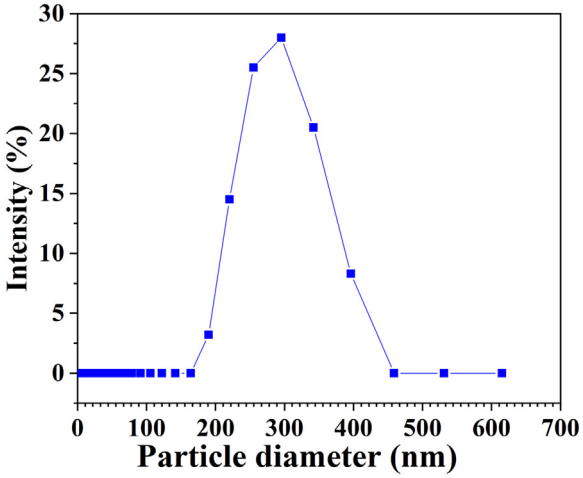

Fig. 2. Particle size distribution of alumina powder.

followed by transferring the data into a microprocessor which in turn control the nozzle movement while printing. It was observed that a ram rate > 6 mm/min results in overflow of the paste leading to the formation of the component beyond the pre-designed layer tolerance. A rate < 6 mm/min though it is desirable results in extended duration of printing and accordingly loss of moisture and hence, layer to layer inhomogeneities.

Green components printed and dried are shown in Fig. 4(b). The samples were subjected to green density measurement by dimensional method and also visual inspection followed by X-ray radiography. The samples have shown a green density of 1.93 g/cc. Though there are no visual inspection defects due to the inherent layer by layer build up of the structure, there are laminations observed mostly on the surface on radiographic examination. Typical radiograph obtained for the green sample is shown in Fig. 5(a).

Printed samples were sintered in the muffle furnace at 1650 °C for 1 h soaking time based on the dilatometric sintering studies at our laboratory. Sintered specimens are shown in Fig. 4(c) demonstrating the complex shaping capability of 3D printing process. It is evident that these parts can not be prepared by any conventional shaping technique without post machining. Printing of the shapes with close tolerance according to the conceptualized design with the retention of the shape can be attributed to the optimum rheological properties. The samples are exhibited the sintered density of 3.88 g/cc. Though lamination defects (Fig. 5(b)) reduced significantly in radiographic analysis of the pressureless sintered samples, radiography has shown randomly distributed finer flaws originating from lamination.

As the green samples are not suitable for HIPing due to the inherent porosity, an SS CAN was designed and fabricated for vacuum encapsulating the green samples as shown in Fig. 6(a). Samples were encapsulated by TIG welding and the CAN was helium leak tested. The CAN is shown in Fig. 6(b) which was further encapsulated and degassed followed by crimping under the vacuum of 10^{-3} Torr and welding. Simultaneous application of temperature of 1350 °C and pressure of 1650 bar resulted in the deformation of the SS CAN as depicted in Fig. 6(c) leading to densification of the printed parts. The sample has shown a density of 3.94 g/cc close to theoretical value even at low temperature of 1350 °C. This can be attributed to the effect of pressure assisted sintering due to enhanced diffusion. Application of pressure also fecilitate the elimination of finer defects resulting in enhanced densification.

Vickers hardness of pressureless sintered and HIPed samples were found to be 15 and 18 GPa respectively. Finer grain size resulting from the enhanced diffusion under pressure during HIPing in combination with healing of defects are responsible for higher hardness values. Flexural strength of the pressureless sintered samples are found to be

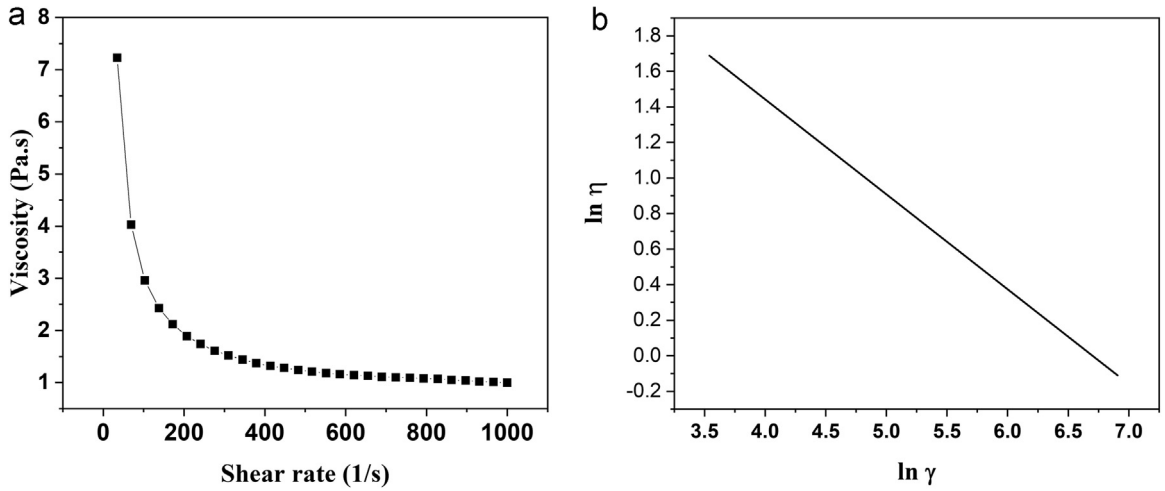

Fig. 3. Plot of (a) viscosity vs. shear rate and (b) ln η vs ln γ.

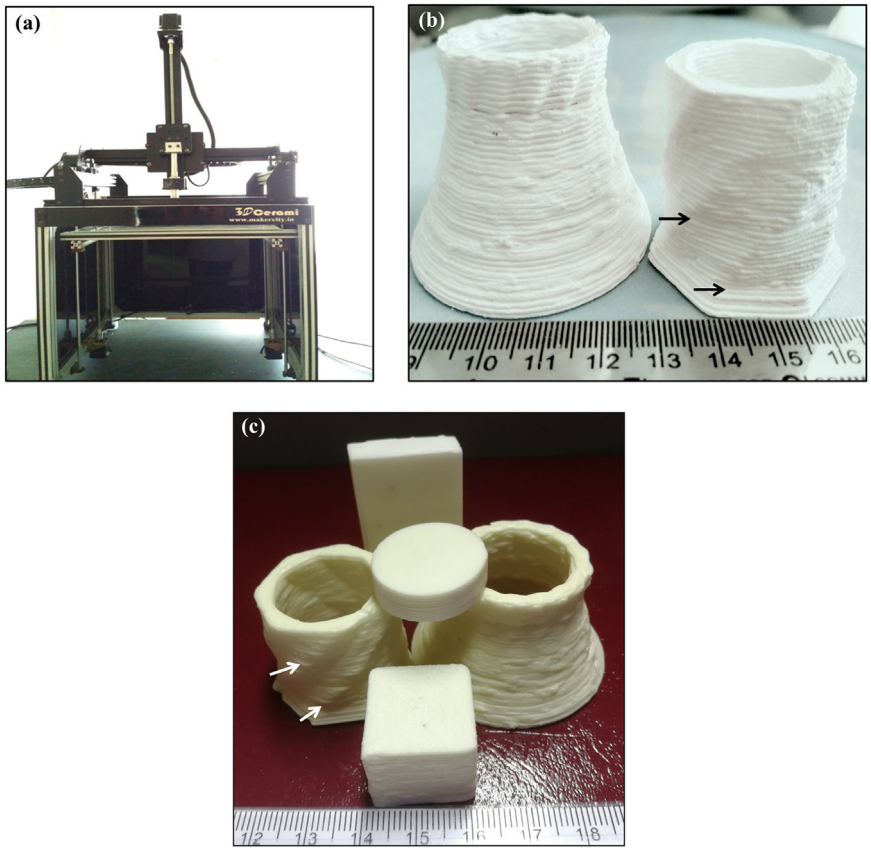

Fig. 4. Image of (a) 3D printing machine, (b) green 3D printed samples and (c) sintered 3D printed samples.

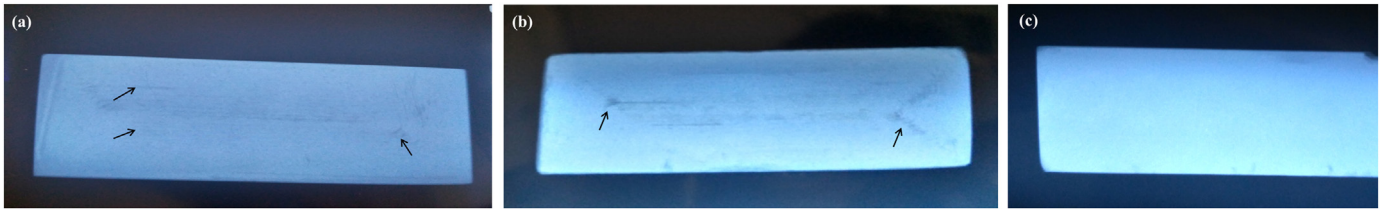

Fig. 5. Radiographs of 3D printed (a) green sample, (b) pressureless sintered sample and (c) HIPed sample.

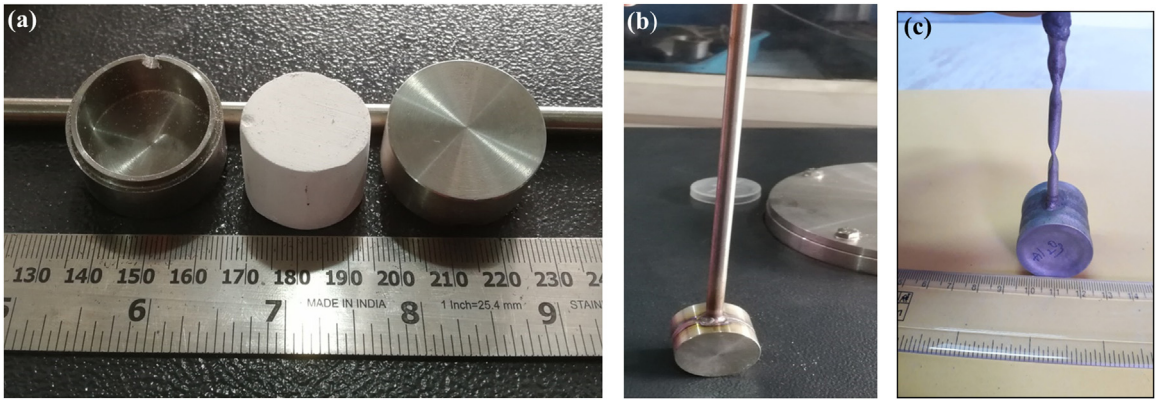

Fig. 6. Image of (a) 3D printed green sample along with SS CAN, (b) encapsulated CAN after TIG welding and (c) deformed CAN.

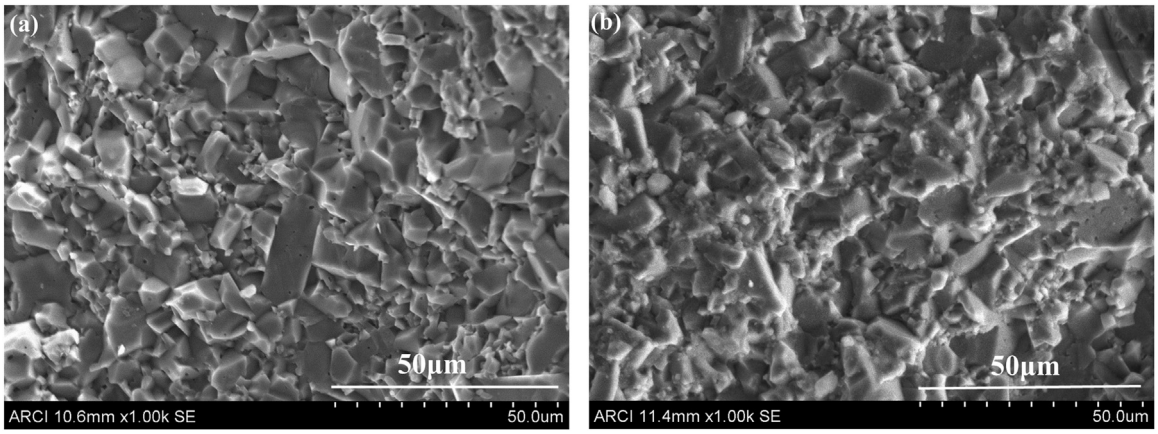

Fig. 7. Fractographs of (a) pressureless sintered and (b) HIPed sample.

252 MPa probably due to the presence of flaws. It is evident from the fractographs in Fig. 7(a) and (b) that the samples failed through a mixed type of intragranular and intergranular fractures following linear elastic fracture mechanism and the cleavage facet size of the pressureless sintered sample is found to be larger complementing the strength values.

4. Conclusions

Extrusion based 3D printing has been successfully carried out to print the simple and complex shaped alumina ceramics. The surface properties of the powder was modified with additives to reach the printable rheological regime as demonstrated in the current study.

3D printed green samples were subjected to X-ray radiography and the observed lamination defects can be attributed to inherent layer by layer formation of the parts while printing. Though the sintering under pressureless conditions results in the eliminations of most of the printing defects, randomly oriented flaws are evident from the radiographic studies which resulted in the deteriotion of the mechanical properties.

HIPing of 3D printed green samples results in elimination of flaws and also finer grained microstructure due to the low temperature sintering leading to the higher density and superior mechanical properties. Pressureless sintered samples have shown a maximum density of 3.88 g/cc at 1650 °C against the HIPed samples exhibiting density of 3.94 g/cc even at low temperature of 1350 °C revealing the effect of pressure assisted sintering. HIPed sample has shown a higher hardness of 18 GPa against 15 GPa observed for pressureless sintering.

References

[1] A.C. de Leon, Q. Chen, N.B. Palaganas, J.O. Palaganas, J. Manapat, R.C. Advincula, High performance polymer nanocomposites for additive manufacturing applications, React. Funct. Polym. 103 (2016) 141–155.
[2] P. Parandoush, D. Lin, A review on additive manufacturing of polymer-fiber composites, Compos. Struct. 182 (2017) 36–53.
[3] J. Raasch, M. Ivey, D. Aldrich, D.S. Nobes, C. Ayranci, Characterization of polyurethane shape memory polymer processed by material extrusion additive manufacturing, Addit. Manuf. 8 (2015) 132–141.
[4] J. de Ciuranaa, L. Serenóa, È. Vallès, Selecting process parameters in RepRap additive manufacturing system for PLA scaffolds manufacture, Procedia CIRP 5 (2013) 152–157.
[5] S. Fathi, P. Dickens, Jettability of reactive nylon materials for additive manufacturing applications, J. Manuf. Process. 14 (2012) 403–413.
[6] D. Herzog, V. Seyda, E. Wycisk, C. Emmelmann, Additive manufacturing of metals, Acta Mater. 117 (2016) 371–392.
[7] M.M. Kirka, P. Nandwana, Y. Lee, R.R. Dehoff, Solidification and solid-state transformation sciences in metals additive manufacturing, Scr. Mater. 135 (2017) 130–134.
[8] A. Townsend, N. Senin, L. Blunt, R.K. Leach, J.S. Taylor, Surface texture metrology for metal additive manufacturing: a review, Precis. Eng. 46 (2016) 34–47.
[9] W. Harrer, M. Schwentenwein, T. Lube, R. Danzer, Fractography of zirconia-specimens made using additive manufacturing (LCM) technology, J. Eur. Ceram. Soc. 37 (2017) 4331–4338.
[10] S. Bose, D. Ke, H. Sahasrabudhe, A. Bandyopadhyay, Additive manufacturing of biomaterials, Prog. Mater. Sci. 93 (2018) 45–111.
[11] M. Dehurtevent, L. Robberecht, J.–C. Hornez, A. Thuault, E. Deveaux, P. Béhin, Stereolithography: a new method for processing dental ceramics by additive computer-aided manufacturing, Dent. Mater. 33 (2017) 477–485.
[12] H. Wu, W. Liu, R. He, Z. Wu, Q. Jiang, X. Song, Y. Chen, L. Cheng, S. Wu, Fabrication of dense zirconia-toughened alumina ceramics through a stereolithography-based additive manufacturing, Ceram. Int. 43 (2017) 968–972.
[13] M. Faes, J. Vleugels, F. Vogeler, E. Ferraris, Extrusion-based additive manufacturing of ZrO_2 using photoinitiated polymerization, CIRP J. Manuf. Sci. Technol. 14 (2016) 28–34.
[14] J. Gonzalez, J. Mireles, Y. Lin, R.B. Wicker, Characterization of ceramic components fabricated using binder jetting additive manufacturing technology, Ceram. Int. 42 (2016) 10559–10564.
[15] S.M. Gaytan, M.A. Cadena, H. Karim, D. Delfin, Y. Lin, D. Espalin, E. MacDonald, R.B. Wicker, Fabrication of barium titanate by binder jetting additive manufacturing technology, Ceram. Int. 41 (2015) 6610–6619.

Ceramics International 45 (2019) 19577–19580

Contents lists available at ScienceDirect

Ceramics International

journal homepage: www.elsevier.com/locate/ceramint

Short communication

Fabrication of complex shaped ceramic articles from 3D printed polylactic acid templates by replication process

Sirisala Mamatha[a], Papiya Biswas[a], Dibakar Das[b], Roy Johnson[a,*]

[a] International Advanced Research Centre for Powder Metallurgy and New Materials (ARCI), Hyderabad, 500 005, India
[b] School of Engineering Science and Technology, University of Hyderabad, Hyderabad, 500 046, India

ARTICLE INFO

Keywords:
3D printed polylactic acid templates
Replication
Rheology
Ceramic complex shapes

ABSTRACT

Porous honeycombs of three ceramic formulations and configurations were replicated from 3D printed polylactic acid (PLA) templates. Sacrificial PLA templates were coated with ceramic slurries of optimum rheology and were subjected to fugitive thermal degradation based on the TG-DTA patterns recorded followed by sintering. Though the polymer replication process is known, 3D printed PLA templates are not explored for fabrication of ceramic complex shapes. 3D printed PLA offers flexibility to produce complex ceramic parts with structural integrity and engineered porosity. In the present study, 3D printed template replication technique has been used to demonstrate fabrication of honeycombs with relative density as low as 0.1 with porosity of 75–85% which is alo complemented by microstructural studies. Further, the samples exhibited cellular behavior under quasistatic compression with high energy absorption capabilities and moderate compressive strength of 1.5–2.2 MPa depending upon the ceramic formulations.

1. Introduction

Ceramic honeycombs due to the flexibility in tailoring the unit cell parameters in combination with engineered porosity are useful for various potential structural and functional applications [1–3]. Honeycombs are used as catalyst supports for environmental control as well as energy generation and conservation related applications [4–7]. Honeycombs are generally produced through extrusion process using honeycomb dies for each configuration, which are fabricated through complex process [8]. Based on virtual images, recently 3D printing of honeycombs using extrusion paste has also been reported [9,10]. 3D forming of ceramic parts are not easy due to their inherent powder properties and material chemistry in addition to the processing requirements in terms of printable feedstock and sintering related issues [11]. Further, extrusion through the nozzle generally exhibits the disadvantage of erosion of the nozzle due to the abrasive nature of ceramics. It is well known that plastics can be 3D printed due to its inherent flexibility to form intricate and complex shapes using the CAD models employing relatively simple machines. In the present study, authors explored the possibility of using the 3D printed PLA as sacrificial templates for replicating ceramic honeycombs with various configurations and other complex parts. The template replication process is well reported by several researchers [12–15], however, 3D printed PLA template ceramic replication has not been reported so far. This process due to its inherent flexibility and capability to form intricate and complicated structures like honeycombs offers significant potential to produce complex ceramic shapes with structural integrity either with dense or with engineered porosity.

Three ceramic formulations such as alumina, porcelain and fly ash have been used in this study to replicate honeycombs and other complex parts using 3D printed PLA templates. Since, PLA replication process is flexible with respect to its configuration, porous alumina honeycombs produced in this study find application as catalyst substrate with or without wash coats depending on the surface area requirement. Porcelain and fly ash honeycombs can be a choice as low cost substrates for bio reators in sewage and waste water treatment. The samples were also characterized for their density, porosity and mechanical properties.

2. Experimental procedure

2.1. Processing of honeycombs and complex parts

2.1.1. 3D printing of polylactic acid templates

Polylactic acid (industrial grade) an important biodegradable plastic of plant origin, is 3D printed into templates using a Fused Deposition Machine (FDM) system (MCHTD, Maker City, India). A nozzle diameter of 0.4 mm and a nozzle tip temperature of 205 °C was employed while

* Corresponding author.
E-mail address: royjohnson@arci.res.in (R. Johnson).

https://doi.org/10.1016/j.ceramint.2019.06.203
Received 14 May 2019; Received in revised form 18 June 2019; Accepted 19 June 2019
Available online 21 June 2019

printing using average printing speed of 60–65 mm/s.

2.1.2. Preparation of homogeneous suspensions and impregnation of the slurry

Alumina and porcelain procured from the commercial sources and fly ash obtained from a thermal power plant were used as the raw materials for the fabrication of ceramic honeycombs. Desired ceramic powders and water proportion in the range of 40–45 percentages by weight were made into an aqueous slurry using Darvan 821A (R. T. Vanderbilt Co., Inc., Norwalk, CT, USA) as a dispersant and methyl cellulose (MC) as binder. The formulations were milled for 4 h in a pot jar mill using alumina balls as the milling media to achieve homogenous slurry. The concentration of the dispersant and the milling time were optimized based on the rheology of the slurry for each formulation. Viscosities of all the three slurries were measured using rheometer (MCR 51, Anton Paar, Austria) and shear rate exponent (n) was calculated. PLA samples with different configuration were used as the template for the fabrication of alumina, porcelain and fly ash samples and honeycombs. All PLA templates were impregnated with homogeneous slurries with optimum rheology, to ensure uniform coating.

2.1.3. Sacrificial fumigation of PLA templates and sintering

PLA samples were subjected to TG-DTA (STA 449 F3, Netzsch, Germany) analysis to study the degradation pattern and the activation energy was calculated using kinetic analysis. The PLA templates impregnated with three different slurries were dried in an oven at 110 °C. Heating schedule for PLA burnout for coated samples were common for all the samples with a heating rate of 60 °C/h from room temperature to 250°C followed by a heating rate of 30 °C/h till 450 °C with a soak of 15 min. Alumina, porcelain and fly ash samples were finally sintered at 1550, 1100 and 1275 °C respectively with heating rate of 120 °C/hour till reaching the peak temperature with a soaking period of 1 h at the peak temperature.

2.2. Characterization of the PLA replicated sintered samples

Sintered samples were subjected to XRD phase analysis to confirm the desired phase formation and the bulk density was determined by Archimedes principle (ASTM). Relative density of the samples was calculated using standard equations described elsewhere [15]. SEM (S-4300SE/N, Hitachi, Tokyo, Japan) microstructure was also recorded for alumina, porcelain and fly ash honeycombs. The honeycomb samples (five in each case) were further subjected to compression tests using the universal testing machine (INSTRON - 8801, UK) at room temperature keeping the direction of compressive stress along the channels at a strain rate of 0.00023 s^{-1}. Compressive strength was evaluated based on load/area.

3. Results and discussions

Typical PLA sample 3D printed using the virtual CAD model and alumina coated template are shown in Fig. 1(a) and (b) respectively along with the dimensions depicted in Table 1 (typically for alumina). TG-DTA plot of PLA template is shown in Fig. 2(a). TG-DTA studies have demonstrated several thermal events with a steep decrease in weight reaching almost 100% loss at 400–450 °C. Based on the corresponding weight loss with respect to temperature the activation energy is estimated as 512 kJ/mol using the procedure described elsewhere [16].

Plots of viscosity with respect to shear rate of alumina, porcelain and fly ash slurries are shown in Fig. 2(b). All the slurries have shown a pseudo-plastic behavior due to the concentration of dispersants optimized in each case. Shear rate exponent (n) of the alumina, porcelain and fly ash slurries are 0.43, 0.46 and 0.51 respectively. A pseudo-plastic behavior is essential to retain the thin layer coating on PLA after the coating procedure is completed. It was observed that surface etching using acetone enhances the adherence of the slurry to the PLA surfaces especially at the edges and corners. The dipping procedure and repeated dipping is found to have a clear effect on thickness build-up. The maximum slurry loading was 66 wt% of the template weight and thickness of the coating was 0.2 mm on each side. All the sintered samples of alumina, porcelain and fly ash are shown in Fig. 1(c). The samples after sintering have shown no cracks indicating stress free PLA removal and warpage free sintering of the samples with good structural integrity.

XRD pattern of the samples have shown α-alumina in case of alumina and aluminum silicate as a major phase in case of fly ash and porcelain. Sintered alumina honeycombs samples have shown 80–85% porosity based on the Archimedes principle with isolated wall showing 91% of the theoretical density. For the sake of comparison, alumina samples were also sintered in the peak temperature of 1650°C and correspondingly the density of the isolated wall has enhanced to 96% of the theoretical density. In case of fly ash and porcelain porosity values were 75 and 80% respectively at the peak temperature of sintering. Microstructure of all the three formulation were mostly similar and complementing with porosity value recorded.

Further, it is evident from the table that, the currently developed replication process permits the fabrication of honeycombs with relative densities as low as 0.1. According to Gibson et al. the formed material can be regarded as cellular only if the relative density is less than 0.3 [17].

In the current study, honeycomb samples have exhibited cellular behavior extending the stress for longer duration under quasi-static compression for all the three formulations. A typical stress-strain curve for alumina honeycomb is shown in Fig. 3. This signifies high energy absorption capability of the honeycomb samples due to its inherent low relative density. Being porous structures the fracture under compression is caused not by unstable propagation of a single flaw, but by the slow extension and linking up of many flaws to form the crushed zone. Thus, progressive micro cracking and the coalescence of these micro cracks have resulted in a typical stress – strain curve that shows gradual fall in the stress with strain. However, the average compressive strength was 2.2 MPa which is moderate for alumina honeycombs with 0.1 relative density value. Strength values were 1.5 and 1.7 MPa for porcelain and fly ash samples respectively. Low compressive strength observed in case of fly ash and porcelain can be attributed to the inherently low strength of the materials in comparison to alumina.

However, the compressive strength can be enhanced with high sintering temperatures which will significantly affect the porosity and may also result in warpage due to thin walls. Thus, 3D printed template replication procedure described in this study provides a technique to produce simple and especially complex ceramic structures. These structures with moderate strength and engineered porosity can be explored for application as catalyst supports for various chemical synthesis especially for bio reactors used in environmental control.

4. Conclusions

- Template replication of 3D printed PLA samples successfully demonstrated for fabrication of honeycombs and other complex shaped ceramic parts. Additives for alumina, porcelain and fly ash based slurries are optimized and the shear rate exponent of alumina, porcelain and fly ash slurries are found to be 0.43, 0.46 and 0.51 respectively, which have resulted in uniform coating on PLA templates.
- Alumina, porcelain and fly ash PLA replicated sintered samples have shown a maximum porosity of 85, 75 and 80% respectively as complemented by the microstructural studies.
- Honeycomb exhibited cellular behavior under quasistatic compression showing high energy absorption and the moderate compressive strength of 2.2, 1.5 and 1.7 MPa respectively for alumina, porcelain and fly ash.

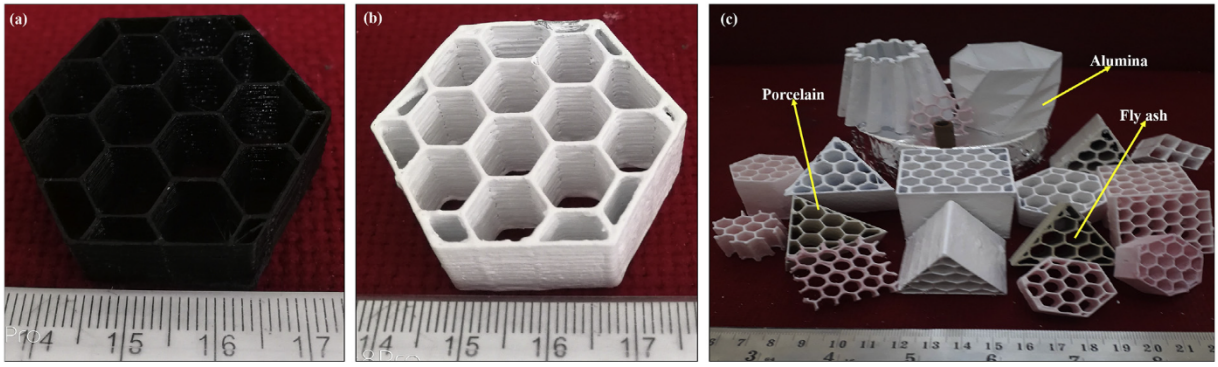

Fig. 1. (a) 3D printed PLA template, (b) Alumina slurry coated PLA honeycomb template and (c) Sintered ceramic (alumina, porcelain and fly ash) samples and honeycombs.

Table 1
Dimensions of templates and sintered samples.

S. No	Template type	Dimensions (mm)	Cell parameters				Relative density	
			Unit cell length (mm)		Wall thickness (mm)			
			Before coating	After sintering	Before coating	After sintering	Before coating	After sintering
1	HC - Square	40 × 40 x 20	9.5	9.0	0.5	0.65	0.10	0.12
			4.5	4.0	0.5	0.65	0.20	0.27
2	HC- Triangular	40 × 40 x 20	9.5	9.0	0.5	0.65	0.17	0.21
3	HC-Hexagonal	40 × 40 x 20	7	6.5	0.5	0.65	0.08	0.10
		40 × 40 x 20	3	2.6	0.5	0.65	0.18	0.24

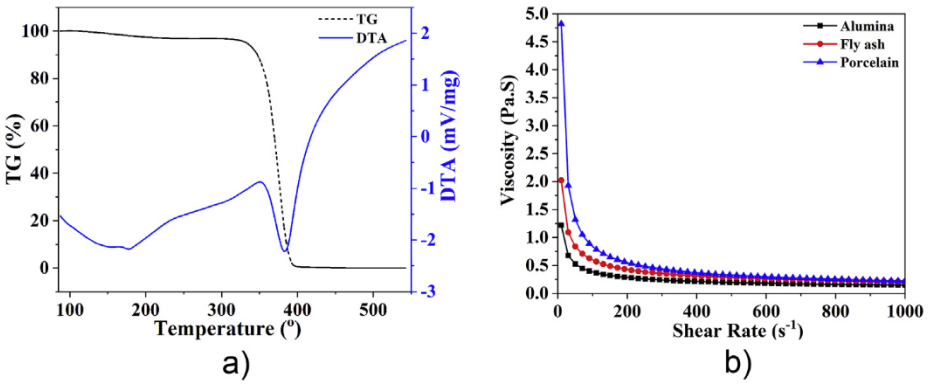

Fig. 2. (a) TG-DTA plot of PLA sample and (b) Shear rate depended viscosities of alumina, porcelain and fly ash slurries.

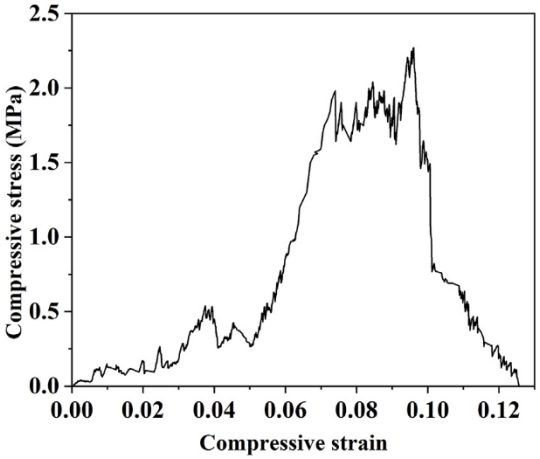

Fig. 3. A typical stress-strain curve of alumina honeycomb.

- 3D printed template replicated honeycombs with engineered porosity can be explored for application as catalyst supports for various chemical synthesis and environmental related applications.

References

[1] P.M. Then, P. Day, The catalytic converter ceramic substrate-an astonishing and enduring invention, Int. Ceram. 49 (2000) 20–23.
[2] P. Biswas, K. Rajeswari, V. Mahendar, R. Johnson, Extrusion processing of dense $MgAl_2O_4$ spinel honeycombs with low relative density, Ceram. Int. 39 (2013) 9819–9821.
[3] M. Elbadawi, M. Shbeh, J. Mech, High strength yttria-reinforced HA scaffolds fabricated via honeycomb ceramic extrusion, Behav. Biomed. Mater. 77 (2018) 422–433.
[4] A. Yamuna, R. Johnson, Y.R. Mahajan, M. Lalithambika, Kaolin-based cordierite for pollution control, J. Eur. Ceram. Soc. 24 (2004) 65–73.
[5] P. Bardhan, Ceramic honeycomb filters and catalysts, Curr. Opin. Solid State Mater. Sci. 2 (1997) 577–583.
[6] T. Yamaguchi, S. Shimizu, T. Suzuki, Y. Fujishiro, M. Awano, Development and evaluation of a cathode-supported SOFC having a honeycomb structure, Electrochem. Solid State Lett. 11B (2008) 117–121.
[7] C.C. Agrafiotis, I. Mavroidis, A.G. Konstandopoulos, B. Hoffschmidt, P. Stobbe, M. Romero, V. Fernandez-Quero, Evaluation of porous silicon carbide monolithic

honeycombs as volumetric receivers/collectors of concentrated solar radiation, Sol. Energy Mater. Sol. Cell. 91 (2007) 474–488.
[8] R.L. Seely, Process for forming honeycomb extrusion die, (1999) US5865983A.
[9] A. Ortona, C. D'Angelo, S. Gianella, D. Gaia, Cellular ceramics produced by rapid prototyping and replication, Mater. Lett. 80 (2012) 95–98.
[10] S.R.G. Bates, I.R. Farrow, R.S. Trask, Compressive behaviour of 3D printed thermoplastic polyurethane honeycombs with graded density, Mater. Des. 162 (2019) 130–142.
[11] A. Zocca, P. Colombo, C. Wirth, J. Gunster, Additive manufacturing of ceramics: issues, potentialities, and opportunities, J. Am. Ceram. Soc. 98 (2015) 1983–2001.
[12] P. Biswas, A. Sharma, M. Krishnan, R. Johnson, M.K. Mohan, Fabrication of $MgAl_2O_4$ spinel scaffolds and sonochemical synthesis and deposition of hydroxyapatite nanorods, J. Am. Ceram. Soc. 99 (2016) 1544–1549.
[13] B. Matovic, B. Babic, A. Egelja, A. Radosavljevic-Mihajlovic, V. Logar, A. Saponjic, S. Boskovic, Preparation of porous silica ceramics using the wood template, Mater. Manuf. Process. 24 (2009) 1109–1113.
[14] P. Biswas, P. Ramavath, C.M. Nair, M.B. Suresh, N. Ravi, R. Johnson, Quasi-static compression behavior of nickel oxide, nickel oxide: zirconia, nickel:zirconia and nickel foams, Ceram. Int. 42 (2016) 10572–10578.
[15] M.A.M. Nor, L.C. Hong, Z.A. Ahmad, H.M. Akil, Preparation and characterization of ceramic foam produced via polymeric foam replication method, J. Mater. Process. Techmol. 207 (2008) 235–239.
[16] K. Rajeswari, S. Chaitanya, P. Biswas, M. Buchi Suresh, Y.S. Rao, R. Johnson, Binder burnout and sintering kinetic study of alumina ceramics shaped using methylcellulose, J. Ceram. Process. Res. 16 (2015) 24–31.
[17] L.J. Gibson, M.F. Ashby, Celullar Solids, second ed., Cambridge University Press, Cambridge, 1997.

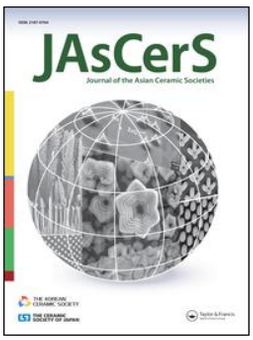

Journal of Asian Ceramic Societies

ISSN: (Print) (Online) Journal homepage: https://www.tandfonline.com/loi/tace20

Effect of parameters on 3D printing of alumina ceramics and evaluation of properties of sintered parts

Sirisala Mamatha, Papiya Biswas, Pandu Ramavath, Dibakar Das & Roy Johnson

To cite this article: Sirisala Mamatha, Papiya Biswas, Pandu Ramavath, Dibakar Das & Roy Johnson (2021): Effect of parameters on 3D printing of alumina ceramics and evaluation of properties of sintered parts, Journal of Asian Ceramic Societies, DOI: 10.1080/21870764.2021.1920159

To link to this article: https://doi.org/10.1080/21870764.2021.1920159

Published online: 16 May 2021.

JOURNAL OF ASIAN CERAMIC SOCIETIES
https://doi.org/10.1080/21870764.2021.1920159

Effect of parameters on 3D printing of alumina ceramics and evaluation of properties of sintered parts

Sirisala Mamatha[a], Papiya Biswas[a], Pandu Ramavath[a], Dibakar Das[b] and Roy Johnson[a]

[a]Centre for Ceramic Processing, International Advanced Research Centre for Powder Metallurgy and New Materials, Balapur, Hyderabad, Telangana, India; [b]School of Engineering Science and Technology, University of Hyderabad, Hyderabad, Telangana, India

ABSTRACT

Paste rheology and printing parameters contribute to a great extent to engineer the properties of ceramic parts produced through 3D printing process. Alumina paste, which showed shear thinning behavior, was prepared using optimum concentration of additives. Paste was 3D printed and effect of printing parameters such as printing speed, length to diameter (L/D) ratio of nozzle, self-standing distance of extrudate, filling pattern and filling angle have been studied. Additionally, effect of the substrate material on which the extrudate is printed was also elucidated. A printing speed of 5–6 mm/s, an L/D ratio of 25 mm and self-standing distance of 1.25 ± 0.25 mm are found to be optimum. Further, a filling pattern of rectilinear geometry along with filling angle of 90° is found to be desirable. Out of the substrates evaluated, polished metal surface is found to be relatively better to achieve close tolerances. The alumina samples printed under optimized conditions are found to possess integrity with respect to the structure and close to pre-designed dimensions. Sintered samples were found to be free of crack and exhibited a density of 3.88 g/cc (97.5% of theoretical density). Density and hardness (16.5 GPa) of printed part correlates well with the microstructure consisting of grains of average size of 9.68 µm.

ARTICLE HISTORY
Received 5 January 2021
Accepted 18 April 2021

KEYWORDS
3D printing; alumina; paste rheology; length to diameter ratio; filling pattern; filling angle

1. Introduction

Additive manufacturing (AM) is extensively used in polymers for prototyping due to the flexibility in shaping [1–5]. Recently, interest has also been seen for 3D printing of ceramic and metals [6–10]. Conventional shaping of traditional and advanced ceramics proceeds through a series of operations from powder processing to shaping using expensive die or molds followed by sintering. These components are generally machined to achieve the final dimensions. Stereolithography (SLA) [11–13], binder jetting [14–17] and extrusion of ceramic pastes [18–20] are the 3D printing processes presently explored for ceramic shaping. As the current study is based on extrusion of alumina paste similar to fused deposition modeling shear thinning or pseudo-plastic behavior of the paste through proper selection of binder and plasticizing agents is critical [21–23]. Further, nozzle dimensions, self-standing distance of the extrudate, printing speed and interaction of the surface with the extrudate are found to have an effect on the process or printed parts. Filling patterns such as rectilinear, aligned rectilinear, concentric and filling angle is found to have minimal effect on the density and mechanical properties of the printed part.

In the present study, alumina powder was subjected to XRD analysis to assess the phase purity and Dynamic Light Scattering (DLS) for particle size analysis. Varying concentrations of binder and water were added to the mix which was subsequently kneaded for 30 minutes under vacuum in a high shear blender. The homogeneous paste thus made was characterized by rheological properties with respect to shear rates and extrusions were carried out with the paste having the shear rate exponent, n = 0.67. A ram type 3D printer was used to print the paste through a nozzle with 1.0 mm diameter and varying L/D ratio of 10–25 with L/D of 25 found to be the optimum. Desirable self-standing distance was found to be 1.25 ± 0.25 mm and is optimum for the current nozzle dimensions. The effect of filling pattern and filling angle are found to be negligible for printed parts. Green density of the dried samples was determined and was subjected to binder removal followed by sintering at 1650°C. The samples were subjected to microstructural characterization which correlates well with the density and hardness of the samples.

2. Experimental procedures

Alumina powder procured from commercial source (Rohini Industries, Pune, India) was characterized by X-Ray Diffraction (D8-Bruker, Germany) for phase identification and Dynamic Light Scattering (DLS) (Nanosizer, Malvern Instruments Limited, UK) for particle size and distribution analysis. Alumina powder was

CONTACT Roy Johnson royjohnson@arci.res.in

blended with 0.25–0.75 wt% of methyl cellulose (MC) (Loba Chemie, Mumbai, India) as binder and 35–39% of water by weight of the powder and the mixture was kneaded in a high shear blender for 30 minutes to form cohesive dough. The rheological behavior of all the pastes was determined with respect to shear rate to assess the flow properties of the paste using rheometer (MCR 51, Anton Paar, Austria).

A ram 3D printer was used for the printing of the specimens. SS 316 nozzles with 1 mm diameter with varying length of 10, 15 and 25 mm were fabricated and specimens were printed at printing speed of 5–6 mm/s. Optimum self-standing distance was obtained by varying the distances from 0.5 to 2 mm. Glass plate, aluminum foil and plaster of paris were used as substrates for printing of extrudate. Additionally, three filling patterns such as rectilinear, aligned rectilinear, concentric pattern and filling angles of 30, 45, 60, 90° are also investigated. All the parameters are correlated with green density after drying. All the printed and dried samples were subjected to binder removal followed by sintering at 1650° C for a dwell time of 1 hour in high-temperature furnace (Deltech, USA). The alumina powder used in the current study is of 99.9% purity with no sintering or grain refining agent present in it. As reported in our earlier studies [24], the sintering temperature of 1650° C is found to yield sintered density (~98-99%) close to theoretical density.

The samples were also characterized for density by Archimedes principle (ASTM B962), microstructure of the etched ceramo-graphically polished surface by FESEM (Gemini 500, Carl Zeiss, Germany) and hardness by Vickers indentation method (ASTM C1327) followed by grain size measurement by linear intercept method.

3. Results and discussion

Figure 1(a) and (b) shows the powder XRD pattern and the particle size distribution of the alumina powder, respectively. XRD pattern of alumina powder clearly exhibits α-alumina phase and the particle size distribution of the powder is indicating the average particle size of 330 nm.

3.1. Rheological properties of the paste

Alumina with a mixture of 0.25 wt% of MC and 35 wt% of water formed homogeneous cohesive dough after kneading for 30 minutes, however, mix with 0.50 and 0.75 wt% of MC have resulted in visible segregation. On gradual addition of water to 37 wt% and 39 wt%, to the mix with 0.50 and 0.75 wt% of MC respectively have resulted in the gradual disappearance of the agglomerates forming cohesive dough. Plot of apparent viscosity vs shear rate data is shown in Figure 2(a). It is evident from the plot that, the viscosity decreases with shear rate suggesting a non-Newtonian behavior. A Power Law Model, $\eta = m * \gamma^{n-1}$ can be applied for analyzing such behavior, where η is the viscosity, m is the consistency constant, γ is the shear rate and n is the shear rate exponent or power law index, proposed by Ostwald de Wale [25] for the pseudo-plastic polymeric materials. A plot of lnη vs. lnγ, shown in Figure 2 (b), shows a linear relation with acceptable fit. Though all mix have formed homogeneous cohesive dough the shear rate exponent (n) was 0.67, 0.88 and 0.93 respectively with increasing concentration of MC.

Pseudo-plastic or shear thinning behavior of alumina paste used for the 3D printing process dictates the properties of 3D printed parts within the predesigned tolerances of the parts after shaping. In order to have easy flow of the paste, under the application of the shear while printing a lower the viscosity of the paste is desirable. However, for the retention of the shape after printing a higher viscosity is advantageous [26]. The parts also must have adequate handling strength to maintain the shape until drying and subsequent also further post-heat treatment process. In view of this, paste with the shear rate exponent (n) of 0.67 and minimum additives with respect to binder (0.25 wt%) and water (35 wt%) is desirable.

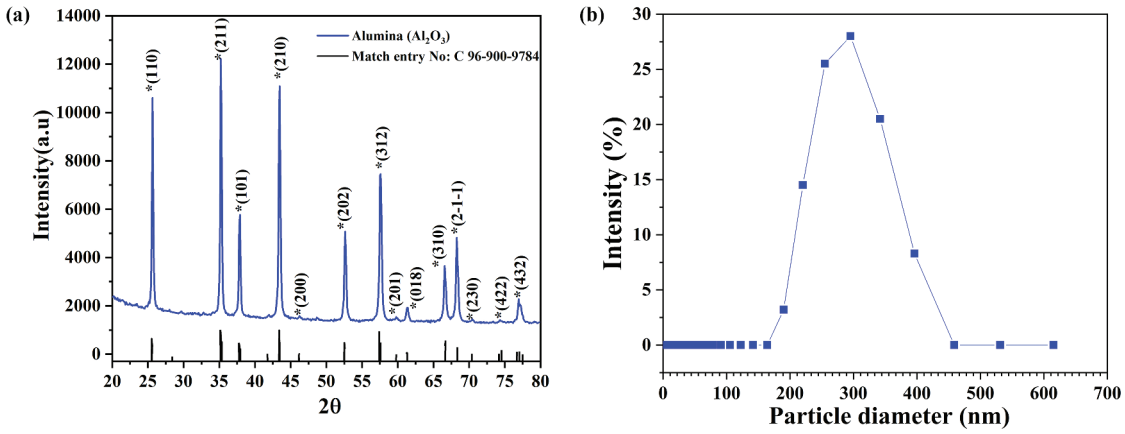

Figure 1. (a) X-Ray Diffraction pattern and (b) Particle size distribution of alumina powder.

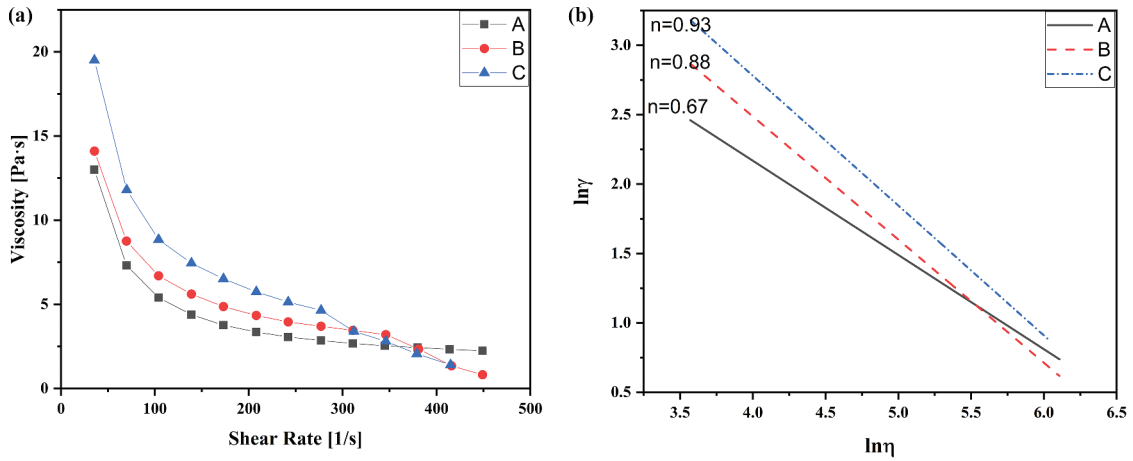

Figure 2. Plot of (a) Viscosity with respect to shear rate and (b) ln γ vs ln η of (A) 0.25 wt.% and 35 wt.%, (B) 0.50 wt.% and 37 wt. % (C) 0.75 wt.% and 38 wt.% of MC and water.

3.2. 3D printing of alumina parts

The block diagram of 3D printer used in the present study is shown in Figure 3. The printer is equipped with a ram type extruder with a cylinder and piston fitted with an interchangeable nozzle. 3D printing process involves the flow of the paste through a barrel which stores the mix, a cone at the end channelizes the flow of paste into a nozzle of the diameter typically 22 times smaller than the diameter of the barrel and the details of the actual system assembly is shown as an inset image in Figure 3. During this process the paste is compressed within the barrel which peaks up a load to overcome the initial resistance and starts flowing as extrudate through the nozzle and printing occur at the preset control printing parameters.

3.3. Printing speed

Alumina parts are 3D printed at various printing speeds. It was observed that a printing speed of > 6 mm/s leads to overflow of the paste and results in the formation of the component beyond the pre-designed layer tolerance. Further the extended duration of printing and loss of moisture are the undesirable results when the speed is <5 mm/s as it causes layer to layer inhomogeneity. An optimum printing

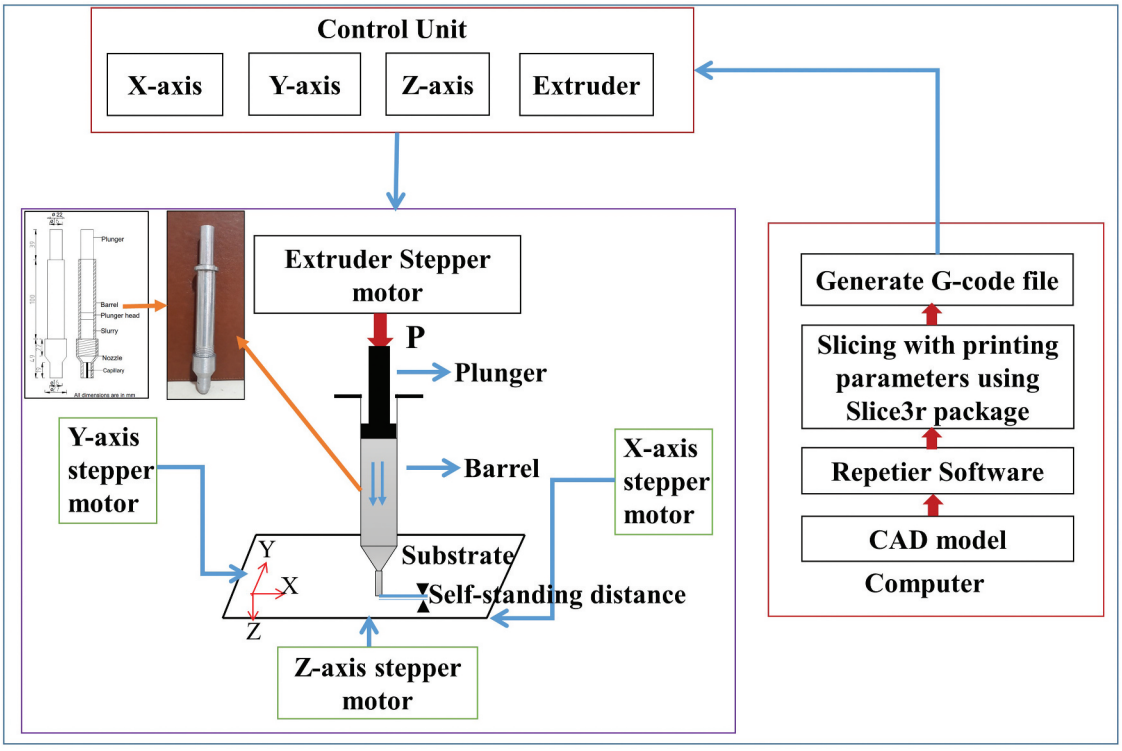

Figure 3. Block diagram of the ram extrusion-based 3D Printing process.

speed of 5–6 mm/s is identified to provide desirable results with respect to pre-designed layer tolerance.

3.4. Effect of L/D ratio of the nozzle on printed samples

Nozzle with L/D ratios of 10, 15 and 25 and the green densities of 3D printed samples are shown in Figure 4. Length-to-diameter ratio (L/D ratio) of 10 and 15 has shown an identical green density of 2.10 g/cc; however, the green density has shown a marginal increase to 2.14 g/cc at an L/D ratio of 25. The relatively high-density values can be attributed to the additional wall shear and intermixing of the paste due to the increased length of the nozzle leading to a better homogeneity of the paste.

3.5. Effect of self-standing distance of extrudate

Self-standing distance of the extrudate is illustrated in Figure 3 and is found to have a significant influence on the retention of the shape of the part.

The effect of self-standing distance on the dimensional tolerance is represented in Figure 5. At a distance of 0.5 and 0.75 mm the surface of the extrudate layer was smeared and part was printed

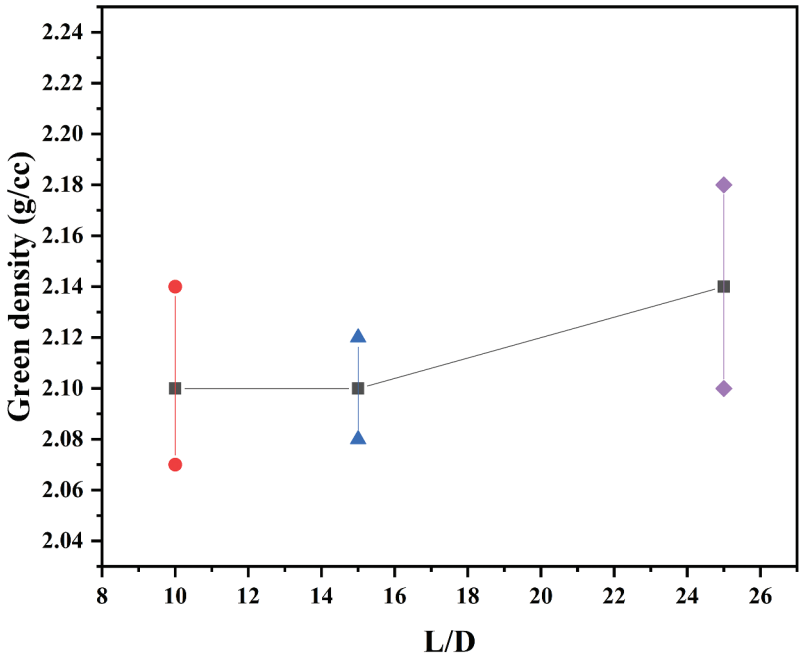

Figure 4. Plot of green density versus L/D ratio of alumina samples.

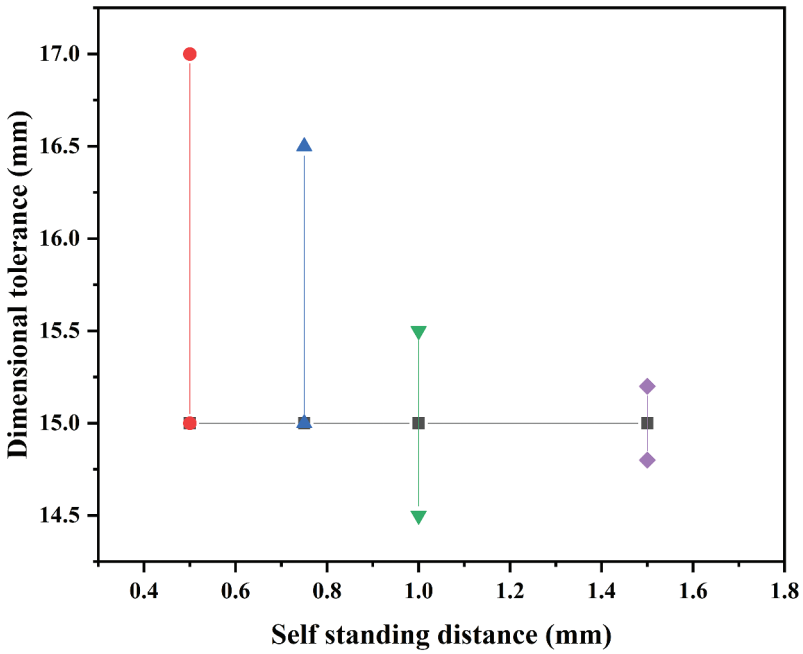

Figure 5. Self-standing distance versus dimensional tolerances.

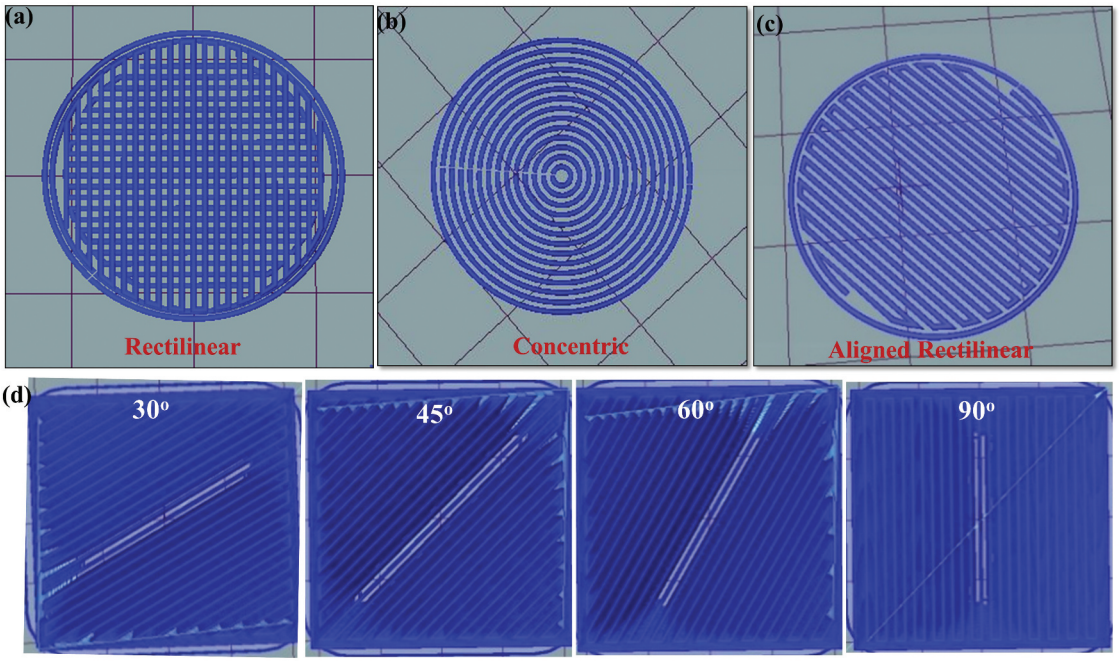

Figure 6. Schematic of fill patterns (a) Rectilinear, (b) Concentric and (c) Aligned rectilinear with (d) fill angles of 30, 45, 60 and 90°.

out of the tolerance limits. When the self-standing distance is increased to 1 mm and 1.5 mm printed, extrudate is found to maintain the designed layer thickness and the printed parts were well within the tolerance limit. Further, the self-standing distance beyond 1.5 mm, the extrudate was overhanging and deviated from the designed print path with discontinuities throughout the printed parts.

3.6. Effect of type of substrates

Substrate surface on which the parts are printed is also found to have an influence on the properties of the printed parts. Among various substrates experimented in the current study, the plaster of paris (POP) holds the first layer of the extrudate by providing better adherence due to its inherent porosity related capillary action which absorbs the water from the extrudate leading to non-uniform drying and intermittent cracking of samples while drying. Glass plate as substrate for printing of extrudate, the first layer does not adhere properly leading to occasionally minor displacement of the subsequent layers. In the case of the metallic surface or an aluminum foil placed on glass plate, MC binder interacts chemically with the metal surface and holds the first layer [27] of extrudate without deformation. This helps in building the subsequent layers according to the predesigned model. Further, on exposure of MC to drying temperatures gradually releases the extrudate due to polymerization and gelling.

3.7. Effect of filling pattern and filling angle

The filling patterns namely rectilinear, concentric and aligned rectilinear are experimented in the current study and the typical filling patterns are shown in Figure 6(a–c). It is evident from Table 1 that the duration of printing as well as the average green density of the printed samples are similar and no significant effect on filling pattern is observed. Experiments were also conducted to study the effect of filling angle on the rectilinear filling pattern and the angle was varied from 30° to 90°. A schematic of the filling angles used for printing of specimens is shown in Figure 6(d). Green density of the alumina samples is shown in Table 1 signifies the minimum effect on density values.

3.8. Properties of sintered alumina parts

Table 2 depicts the optimum conditions desirable for printing. Sintered density, grain size and hardness of the alumina parts printed at optimum condition are shown in Table 3. The 3D printed samples at optimum conditions in green and sintered stage are shown in Figure 7(a) and (b) respectively. Further, the microstructure of the sintered sample

Table 1. Properties of printed samples with rectilinear pattern with different filling angles.

	Filling pattern			Filling angle (Rectilinear)			
Properties	Rectilinear	Concentric	Aligned rectilinear	30°	45°	60°	90°
Green density (g/cc)	2.03 ± 0.04	2.04 ± 0.06	2.08 ± 0.06	2.03 ± 0.07	2.02 ± 0.08	2.03 ± 0.06	2.00 ± 0.06

Table 2. Optimum parameters for 3D printing alumina parts.

S. No	Parameters	Optimum values
1	Printing Speed (mm/s)	5–6
2	L/D ratio	25
3	Self-standing distance (mm)	1.25±0.25
4	Filling angle (°)	90
5	Filling pattern	Rectilinear
6	Substrate	Aluminum foil

Table 3. Properties of sintered alumina specimens.

Properties of sintered alumina specimens	
Sintered density (g/cc)	3.88
Average grain size (μm)	9.68
Hardness (GPa)	16.5

recorded on the ceramographically polished surface is shown in Figure 8.

4. Conclusions

Out of the various printing parameters studied, printing speed and self-standing distance have been found to be most critical. Substrate surface and chemistry are found to have a prominent effect on dimensional tolerance. Filling angle and filling patterns have shown only negligible effect. Optimum parameters used for printing are summarized in Table 2.

3D printed and sintered samples are found to exhibit a density of 3.88 g/cc (97% of theoretical density). Samples have shown a hardness of 16.5 GPa. Microstructure of the sample has shown average grain

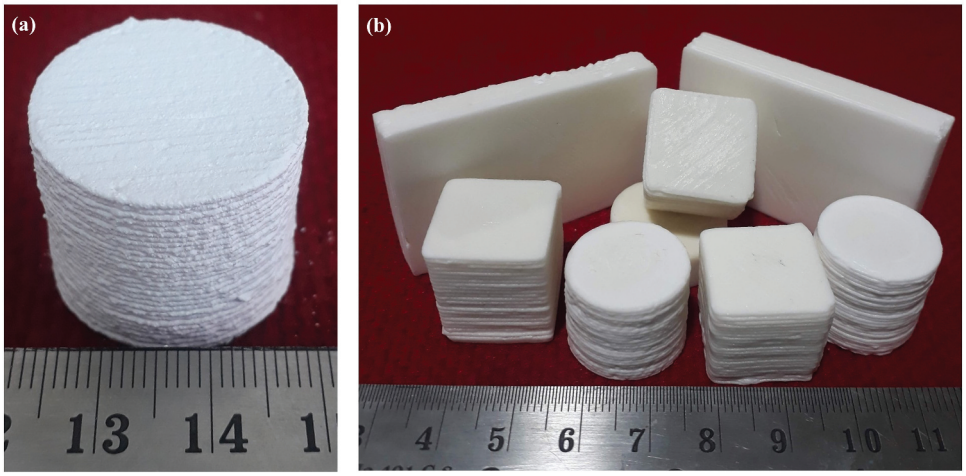

Figure 7. 3D Printed alumina samples at optimum conditions (a) Green and (b) Sintered samples.

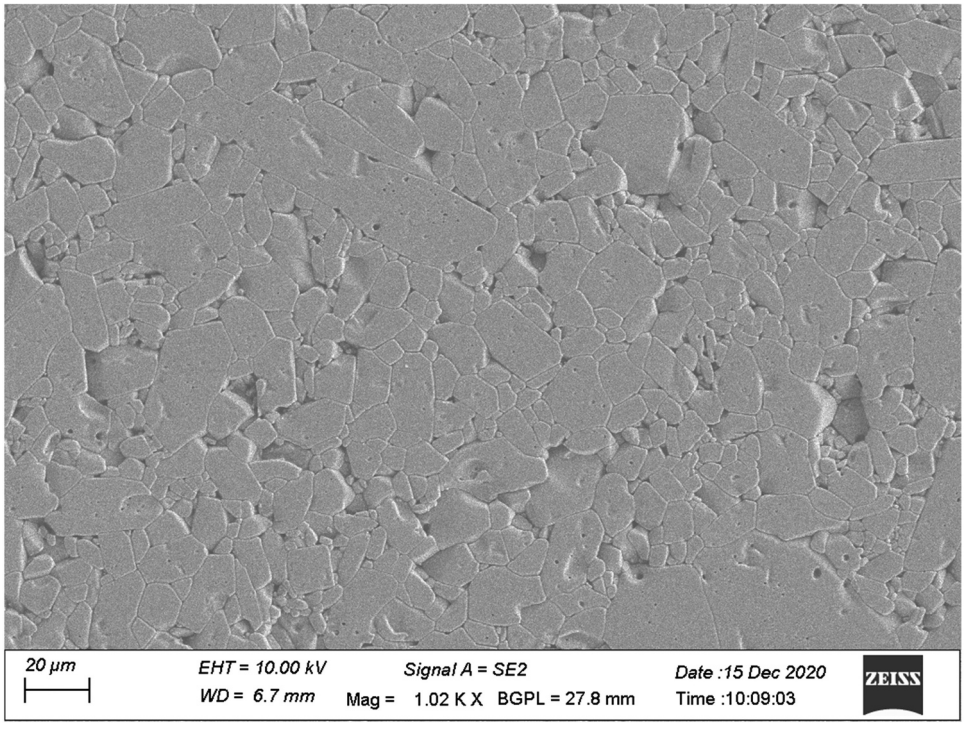

Figure 8. Microstructure of the alumina sample.

size of ~9.68 μm correlating well with the density and hardness values.

Disclosure statement

No potential conflict of interest was reported by the author(s).

References

[1] Kukla C, Gonzalez-Gutierrez J, Duretek I, et al. Effect of particle size on the properties on highly filled polymer for fused filament fabrication. AIP Conf Proc. 2017;1914:190006-1 - 190006-4.

[2] Kucherov FA, Gordeev EG, Kashin AS, et al. Three-dimensional printing with biomass-derived PEF for carbon-neutral manufacturing. Angew Chem Int Ed. 2017;56:15931–15935.

[3] Ramezani DH, Barbe F, Delbreilh L, et al. Polymer additive manufacturing of ABS structure: influence of printing direction on mechanical properties. J Manuf Proc. 2019;44:288–298.

[4] Prajapati H, Chalise D, Ravoori D, et al. Improvement in build-direction thermal conductivity in extrusion-based polymer additive manufacturing through thermal annealing. Addit Manuf. 2019;26:242–249.

[5] Jasiuk I, Abueidda DW, Kozuch C, et al. An overview on additive manufacturing of polymers. J Minerals Met Mater Soc. 2018;70:275–283.

[6] Mansfield B, Torres S, Yu T, et al. A review on additive manufacturing of ceramics. ASME 2019 14th Int Manuf Sci Eng Conf. 2019 June 10-14; Erie, Pennsylvania, USA: ASME; 2019.

[7] Dobrzański LA, Dobrzański LB, Dobrzańska-Danikiewicz AD. Additive and hybrid technologies for products manufacturing using powders of metals, their alloys and ceramics. Arch Mater Sci Eng. 2020;2 (102):59–85.

[8] Datsiou KC, Saleh E, Spirrett F, et al. Additive manufacturing of glass with laser powder bed fusion. J Am Ceram Soc. 2019;102:4410–4414.

[9] Kennedy SK, Dalley AM, Kotyk GJ. Additive manufacturing: assessing metal powder quality through characterizing feedstock and contaminants. J Mater Eng Perf. 2019;28:728–740.

[10] Thakur AR, Pappas JM, Dong X. Fabrication and characterization of high-purity alumina ceramics doped with zirconia via laser direct deposition. J Minerals Met Mater Soc. 2020;72:1299–1306.

[11] Yuelong F, Zhangwei C, Gang X, et al. Preparation and stereolithography 3D printing of ultralight and ultrastrong ZrO_2 porous ceramics. J Alloys Compds. 2019;789:867–873.

[12] He R, Liu W, Wu Z, et al. Fabrication of complex-shaped zirconia ceramic parts via a DLP-stereolithography-based 3D printing method. Ceram Int. 2018;44(3):3412–3416.

[13] Hongyu X, Bin Z, Xiaoyan L, et al. Effect of particle size distribution on the preparation of ZTA ceramic paste applying for stereolithography 3D printing. Pow Technol. 2020;359:314–322.

[14] Xinyuan L, Fang Y, Laifei C, et al. Binder jetting of ceramics: powders, binders, printing parameters, equipment, and post-treatment. Ceram Int. 2019;45:12609–12624.

[15] Pragnya K, Keerti K. 3D printing high density ceramics using binder jetting with nanoparticle densifiers. Mater Des. 2018;155:443–450.

[16] Shuangjun H, Chunsheng Y, Huoping Z, et al. Additive manufacturing of thin alumina ceramic cores using binder-jetting. Addit Manuf. 2019;29:100802 1–7.

[17] Wenchao D, Xiaorui R, Chao M, et al. Ceramic binder jetting additive manufacturing: particle coating for increasing powder sinterability and part strength. Mater Lett. 2019;234:327–330.

[18] Shiyan T, Li Y, Guanjin L, et al. 3D printing of highly-loaded slurries via layered extrusion forming: parameters optimization and control. Addit Manuf. 2019;28:546–553.

[19] Papiya B, Sirisala M, Subhendu N, et al. 3D extrusion printing of magnesium aluminate spinel ceramic parts using thermally induced gelation of methyl cellulose. J Alloys Compds. 2019;770:419–423.

[20] Mamatha S, Biswas P, Das D, et al. 3D printing of cordierite honeycomb structures and evaluation of compressive strength under quasi-static condition. Int J Appl Ceram Technol. 2019;17:211–216.

[21] Swathi M, Papitha R, Hareesh US, et al. Rheological studies on aqueous alumina extrusion mixes. Trans Indian Inst Met. 2011;64:541–547.

[22] Gorjan L, Galusca C, Sami M, et al. Effect of stearic acid on rheological properties and printability of ethylene vinyl acetate based feedstocks for fused filament fabrication of alumina. Addit Manuf. 2020;36:101391–101399.

[23] Reed JS. Principles of ceramic processing. 2nd ed. New York: John Wiley and Sons Inc.; 1995. ISBN: 978-0-471-59721-6.

[24] Mamatha S, Papiya B, Pandu R, et al. 3D printing of complex shaped alumina parts. Ceram Int. 2018;44:19278–19281.

[25] Deshpande AP, Krishnan JM, Kumar PBS, Eds. Rheology of complex fluids. New York: Springer; 2010. (ISBN 978-1-4419-6494-6).

[26] Weiwei L, Maoshan L, Jianbin N, et al. Synergy of solid loading and printability of ceramic pastes for optimized properties of alumina via stereolithography based 3D printing. J Mater Res Technol. 2020;9:11476–11483.

[27] Innocent OK, Innocent CM, Okoro O. Hydroxypropyl methylcellulose as a polymeric corrosion inhibitor for aluminium. Pigment Resin Technol. 2014;43:151–158.

Received: 20 August 2019 | Revised: 20 August 2019 | Accepted: 25 September 2019

DOI: 10.1111/ijac.13399

ORIGINAL ARTICLE

International Journal of Applied Ceramic TECHNOLOGY

3D printing of cordierite honeycomb structures and evaluation of compressive strength under quasi-static condition

Sirisala Mamatha[1] | **Papiya Biswas**[1] | **Dibakar Das**[2] | **Roy Johnson**[1]

[1]International Advanced Research Centre for Powder Metallurgy and New Materials, Balapur, Hyderabad, India

[2]School of Engineering Science and Technology, University of Hyderabad, Hyderabad, India

Correspondence
Roy Johnson, International Advanced Research Centre for Powder Metallurgy and New Materials, Balapur, Hyderabad-500005, India.
Email: royjohnson@arci.res.in

Abstract

Ceramic honeycombs exhibit unique mechanical properties based on engineered formulations and geometry of cells. Extrusion of formable paste through a complex honeycomb die is the commonly practiced technique for the manufacturing of honeycombs globally. Extrusion die fabrication is a complex process which necessitates sophisticated infrastructure facilities that provide high geometrical accuracy and finish to produce defect free honeycombs. Furthermore, every configuration of honeycomb requires a specific tool. Additive manufacturing (AM)/ 3D printing is a rapid prototyping technique which offers flexibility in fabrication of honeycombs with desired geometries from a virtual model directly. Further, this does not require complicated dies. In this study, viscoplastic printable cordierite raw mix paste with a shear rate exponent of 0.87 was printed into honeycombs with hexagonal, square, and triangular cells using a ram type 3D printer. The printed honeycomb samples are found to possess good integrity and near net shape after drying. Sintered 3D-printed honeycomb samples of all configurations have exhibited cordierite as a major phase along with minor phases of magnesium aluminate ($MgAl_2O_4$) spinel, clinoenstatite ($MgSiO_3$), and corundum (Al_2O_3) with sintered density of 2.41-2.48 g/cc. The samples are also subjected to compression testing under quasi-static condition. The study demonstrates 3D printing as a viable and flexible technique for rapid prototyping of honeycombs with desired configurations and engineered properties.

KEYWORDS

3D printing, cordierite, honeycomb, quasi-static compression

1 | INTRODUCTION

Honeycomb structures are a novel class of advanced ceramics with unique thermomechanical properties by the virtue of its engineered configurations caters to diverse applications.[1–3] Current applications of ceramic honeycombs include catalyst supports for environmental control, biotechnological applications, filtration of molten metal and gas particulates, energy conservation etc.[4–15] Variables that determine the thermomechanical properties of honeycombs are relative density (r/r_s where r is the density of the cellular material and r_s that of the solid of which it is made), material of cell wall fabrication, and cell geometry.

Ceramic honeycombs are generally processed by the extrusion process and extrusion processing is carried out by the shaping of a viscoplastic formable paste through a sophisticated die which consists of large number of feed holes on one side and thin slits on the other side.[16] Extrusion die fabrication is complex process which requires high geometrical and surface finish to allow lateral flow of the dough followed by the knitting with adjacent cross section within the

[†]Member, The American Ceramic Society.

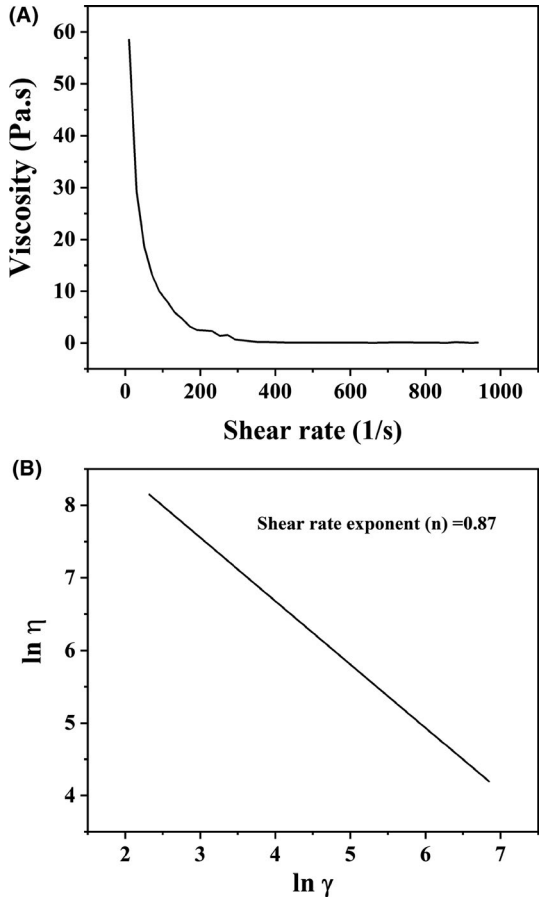

FIGURE 1 Plot of (A) viscosity vs shear rate and (B) ln γ vs ln η

die to form defect-free honeycombs.[17] 3D printing is a type of AM-based rapid prototyping technique which is a flexible process and complex parts are generated from a virtual model directly.[18–20] Hence, irrespective of the configurations honeycombs can be printed from virtual images using the same infrastructural facility without employing complicated dies with specific configurations.[21]

In the present study, cordierite raw mix consisting of clay, talc, and alumina were blended with binder, plasticizer, and water which is subsequently kneaded in a vacuum sigma kneader into a paste. Paste was characterized for its rheological properties and exhibited a shear rate exponent of 0.87 showing a shear thinning behavior. Pastes were printed into honeycombs with hexagonal, square, and triangular cells using a ram type 3D printer. The printed cordierite honeycomb samples are found to possess good integrity and close to near net shape. Honeycomb samples after drying were sintered at 1390°C based on thermogravimetric studies. Honeycomb samples are found to be crack-free with density in the range of 2.41-2.48 g/cc. All honeycomb samples have shown cordierite as a major phase along with minor phases of magnesium aluminate ($MgAl_2O_4$) spinel, clinoenstatite ($MgSiO_3$), and corundum (Al_2O_3). Compressive strength for hexagonal, square, and triangular cells geometries was found to be 20.18, 5.85, and 5.27 MPa, respectively. Attempts were also made to correlate the properties with the processing parameters as reported in the study.

2 | EXPERIMENTAL PROCEDURE

Precursor oxides such as clay (aluminum silicate, $Al_2Si_2O_5(OH)_4$), talc (magnesium silicate, $Mg_3Si_4O_{10}(OH)_2$), and alpha alumina (Al_2O_3) according to the cordierite ($Mg_2Al_4Si_5O_{18}$) stoichiometry is blended in a ball mill to achieve a homogeneous mix. Further, 1 wt% of methylcellulose (MC) dissolved in water as a binder along with 1 wt% of polyethylene glycol (Mol. wt. 380-420) and 45 to 50 wt% of water were added and further homogenized in a sigma kneader under vacuum for 30 minutes. The homogeneity of the paste thus prepared was tested by thermogravimetry (STA 449 F3, Netzsch, Germany) of the specimens collected from multiple points and rheological behavior of the paste was measured at varying shear rates using Anton Paar rheometer (MCR 51, Anton Paar, Austria) to determine the flow properties.

Printable paste with optimum rheology was printed into honeycomb structures with hexagonal, square, and triangular cells using a ram type 3D printer fitted with 1.0 mm nozzle based on a virtual CAD design and converted into a STL file. STL file with printing parameters such as thickness of the layer as 1mm and 4-5mm/s printing speed and a constant paste infill density of 15% was used for printing of honeycombs irrespective of the cell geometry to achieve identical solid content and hence, the same relative density. After incorporating these input parameters to the STL file, image was sliced and saved as G-code file and further fed to a microprocessor which will control the nozzle path for printing the honeycombs with desired configurations.

3D printing of the honeycombs was carried out with simultaneous exposure to the MC gelation temperature of 45°C-60°C as described elsewhere.[22] The honeycombs with handleable strength was subjected to microwave for the uniform removal of water and sintered at 1390°C in an air sintering furnace (Deltech) at a ramp rate of 100°C/hr with a soaking period of 1 hour to ensure the simultaneous formation of cordierite phase and densification. These heating conditions were optimized based on the TG-DTA experiments at our laboratory. Relative density of the sintered samples was calculated based on the cell geometry and density of the samples evaluated by Archimedes principle (ASTM-792) and the samples were also subjected to XRD for phase analysis. Samples were machined to the specimens of 20 mm^3 sizes and then ground to parallel for the evaluation of compressive strength using a Universal testing machine (5584, Instron, UK).

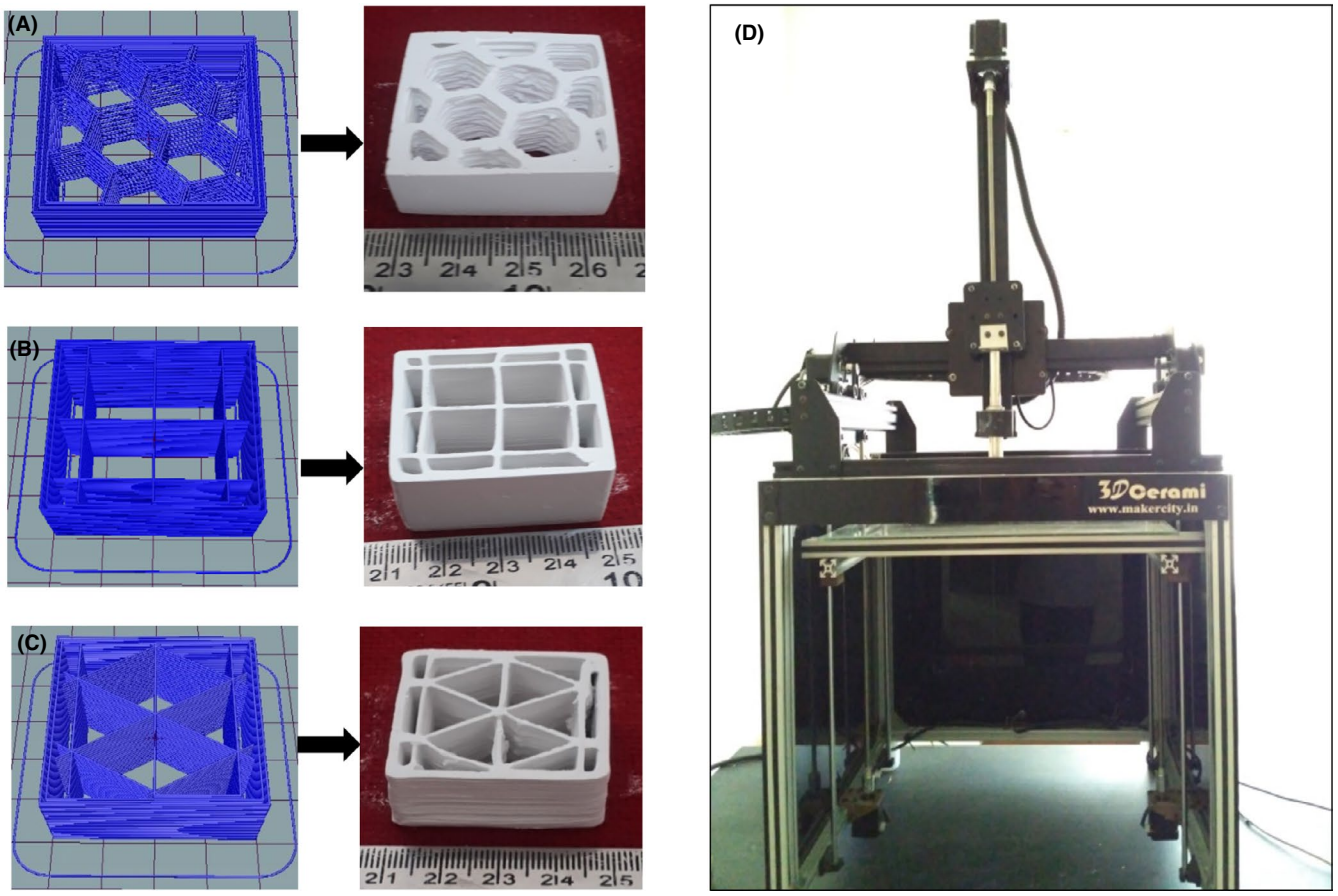

FIGURE 2 Virtual and printed honeycombs with (A) Hexagonal, (B) Square, (C) Triangular channels along with (D) 3D printer [Color figure can be viewed at wileyonlinelibrary.com]

3 | RESULTS AND DISCUSSION

The viscosity vs shear rate and ln η vs ln γ for the cordierite raw mix are shown in Figure 1A,B respectively. The shear rate exponent (n) of 0.87 clearly indicated a non-Newtonian shear thinning (shear rate exponent $n < 1$) behavior. 3D printing of honeycombs through extrusion process of the paste should have desirable flow characteristics that are good enough to provide defect-free formation of honeycomb structures. Further, the paste must have sufficient mechanical strength to maintain the shape integrity until thermal gelation of methylcellulose occurs through in situ heating. Thermal gelation results in dehydration of hydrated methoxyl groups, which then undergo hydrophobic association giving rise to the formation of the gel network providing high green strength values as reported in our earlier studies.[23,24]

Figures 2A-C shows the honeycombs with hexagonal, square, and triangular channels, respectively (virtual model and printed) along with the 3D printer (Figure 2D) used in the current study. A printing speed of 4 mm/s for initial layer formation followed by 5 mm/s to print rest of the layers is found to be optimum for printing all honeycomb samples with different configurations. Initial slower printing speed of 4 mm/s provides sufficient adhesion to aluminum foil (substrate) and the extrudate not only because of the optimum printing speed but also because of the interaction between methyl cellulose and the aluminum metal surface.[25] It was

TABLE 1 Cellular parameters of honeycomb samples with hexagonal, square, and triangular channels

Honeycomb	Thickness (mm)	Edge length (mm)	Surface area (cm^2)	Open frontal area (%)	Relative density
Hexagonal cell	1.02	6.37	24.65	80±5	0.45±5
Square cell	1.00	11.18	23.71	80±5	0.45±5
Triangular cell	.95	14.38	23.75	80±5	0.45±5

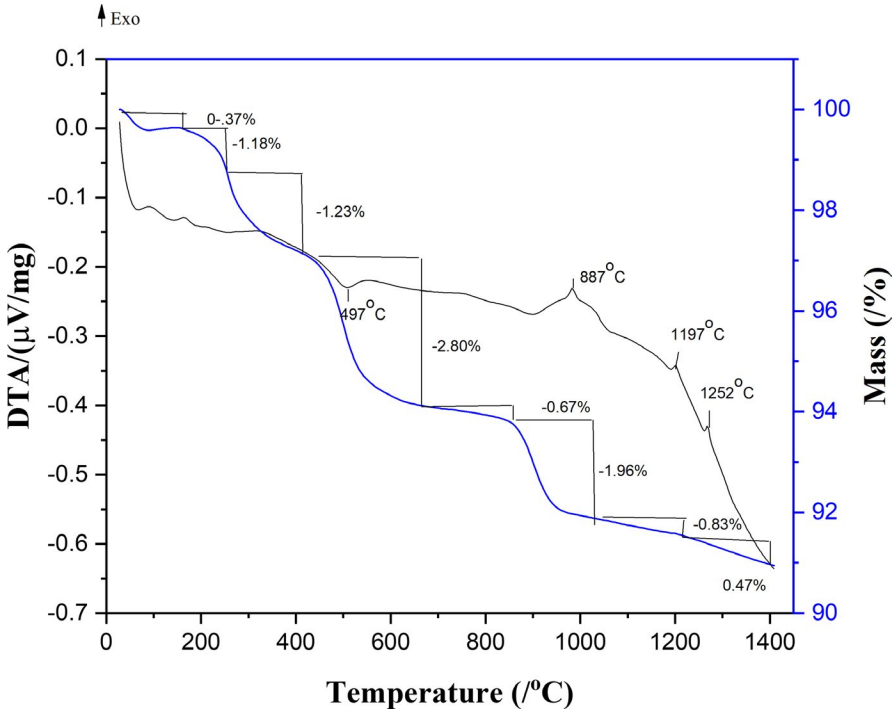

FIGURE 3 TG-DTA plot of the cordierite 3D-printed green sample [Color figure can be viewed at wileyonlinelibrary.com]

also observed that a printing speed of beyond 5 mm/s results in occasional discontinuity due to the inconsistent flow of paste which is not desirable. Printing speed below this parameter will further increase the formation time resulting in delayed drying time of printed layers which further may not merge as a single monolith. In order to maintain the relative density of green honeycombs approximately same, a paste infill density of 15% was selected and also confirmed by printed honeycombs. Cellular parameters of the honeycomb samples before and after sintering along with density values are shown in Table 1.

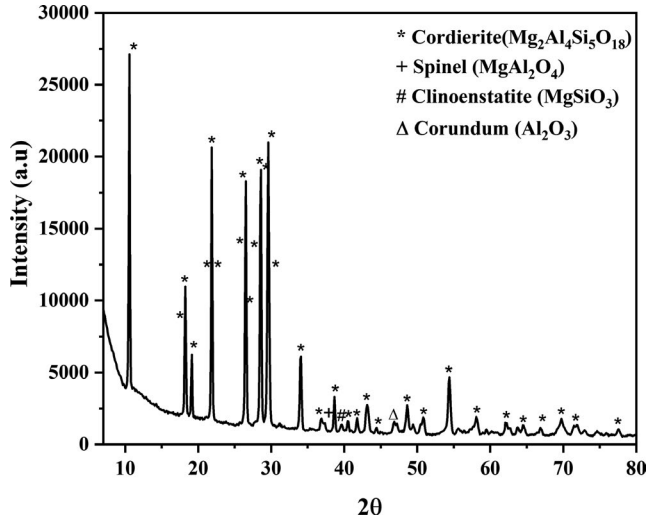

FIGURE 4 X-ray diffraction pattern of sintered cordierite honeycomb sample

Figure 3 shows the thermogravimetric (TG) and differential thermal analysis (DTA) plot of 3D-printed green honeycomb sample. Various thermal events occur during the formation of cordierite ($Mg_2Al_4Si_5O_{18}$) from precursor oxides such as clay (aluminum silicate, $Al_2Si_2O_5(OH)_4$), talc (magnesium silicate, $Mg_3Si_4O_{10}(OH)_2$), and alpha alumina (Al_2O_3). TG curve shows an initial major weight loss till 650°C due to the degradation of methylcellulose and polyethylene glycol used in this study as the binder and plasticizer, respectively. Another weight loss of ~1.96% has occurred between 777°C and 982°C along with an exothermic peak at 887°C because of the removal of structural water associated with the silicate mineral-based raw materials especially with talc formulation. Further, there are two exothermic peaks observed in DTA plot at 1197°C and 1252°C and negligible weight loss of 0.83% from 982°C to 1261°C and 0.47% from 1261°C to 1363°C, which can be attributed to the formation of cordierite from intermediate compounds. It is well known that during heat treatment metakaolin ($Al_2O_3{\cdot}2SiO_2$) is formed from clay and further forms mullite ($3Al_2O{\cdot}2SiO_2$) and cristobalite (SiO_2). Protoenstatite $2(MgO{\cdot}SiO_2)$ and silica (SiO_2) formed from the talc are also the intermediate phases during cordierite formation. The chemical reaction of intermediate phases resulting in the formation of cordierite ($2MgO{:}2Al_2O_3{:}5SiO_2$) is according to the chemical reaction

$$2\left(3Al_2O_3\cdot 2SiO_2\right)+5SiO_2+6\left(MgO\cdot SiO_2\right)\rightarrow 3\left(2MgO{:}2Al_2O_3{:}5SiO_2\right)$$

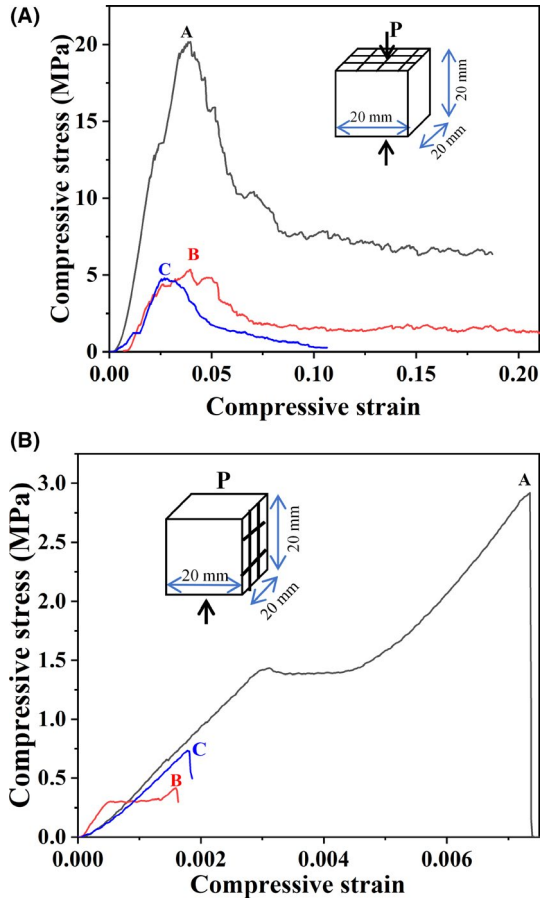

FIGURE 5 Stress-strain curve of 3D-printed sintered honeycombs (A) axial and (B) perpendicular to the channels [Color figure can be viewed at wileyonlinelibrary.com]

Based on the TG/DTA curve, a sintering schedule of cordierite was followed till 1200°C with heating rate of 2°C/min and subsequent heating rate of 1°C/min was followed till 1390°C to avoid the softening and melting of cordierite due to its very short firing range. Samples were kept for 1 hour soaking at 1390°C. XRD pattern recorded for sintered honeycomb is shown in Figure 4 which confirmed the in situ formation of cordierite as a major phase along with minor phases such as magnesium aluminate ($MgAl_2O_4$) spinel, clinoenstatite ($MgSiO_3$), and corundum (Al_2O_3).

Figure 5A,B shows the stress vs strain curve for honeycombs with hexagonal represented as A, square represented as B, and triangular represented as C channel configuration, recorded while quasi-static compression along and across the channels and the corresponding compressive strength is shown in Table 2. It is evident from Figure 5A,B that 3D-printed cordierite honeycombs have shown a similar trend in the compressive deformation behavior irrespective of their configuration under axial and perpendicular loading conditions. For the stress vs strain curves of 3D-printed honeycombs on axial loading irrespective of their configuration, stress increases to a highest peak value. A peak compressive value of 20.18 MPa in case of hexagonal configuration followed by 5.85 MPa for square and 5.29 MPa for triangular configurations is observed. On perpendicular compression hexagonal, square, and triangular compression stress were found to be 2.91, 0.41, and 0.72 MPa, respectively which are substantially lower than the axial values exhibiting strong mechanical anisotropy. This can be attributed to the fact that under perpendicular compression stress is concentered in-line with the walls rather than the cross section as in the case of axial loading. Under this condition micro cracks are initiated and due to the stress concentration at the inherent processing flaws or defects present in the ceramics, it propagates rapidly and fails catastrophically. However, on axial loading, it exhibit more stress tolerance by distributing the load of compression for longer period of time through buckling at the cross section of cell joints. This restricts cracks to grow preferentially vertical rather than spreading in to the neighboring cells. It was observed during compression under axial loading, unlike in the case of perpendicular, splitting of columns individually and partial load bearing behavior even after the collapse of the few cells which is the reason for graceful failure.

4 | CONCLUSIONS

Viscoplastic printable paste of cordierite precursors was prepared and honeycombs with square, hexagonal, and triangular cells were 3D printed successfully as per pre-set design.

Printing speed of 4 mm/s for initial layer formation followed by 5 mm/s to print rest of the layers are found to be optimum and a paste infill density of 15% is selected for printing all honeycomb samples of different configurations with identical relative density.

XRD pattern confirmed the in situ formation of cordierite as a major phase along with minor phases such as magnesium aluminate ($MgAl_2O_4$) spinel, clinoenstatite ($MgSiO_3$), and corundum (Al_2O_3) from precursors and major thermal events. Furthermore, the intermediate compounds and corresponding pathways for the reaction to the formation of cordierite phase is identified through thermogravimetric analysis

From the stress vs strain curves of 3D-printed honeycombs recorded under quasi-static compression on axial direction, it

TABLE 2 Compressive strength of 3D-printed sintered honeycombs

Properties	Loading direction	Hexagonal	Square	Triangular
Compressive strength (MPa)	Axial	20.18	5.85	5.29
	Perpendicular	2.91	0.41	0.72

is seen that irrespective of the configuration of honeycombs exhibited graceful failure with the highest peak load value for hexagonal configuration followed by square and triangular configurations. On perpendicular compression, the honeycomb samples failed catastrophically with substantially lower values following a similar trend in the configurations and further exhibiting strong mechanical anisotropy.

ORCID

Roy Johnson https://orcid.org/0000-0001-6478-7824

REFERENCES

1. Then PM, Day P. The catalytic converter ceramic substrate-an astonishing and enduring invention. InterCeram-Int Ceram Rev. 2000;49:20–3.
2. Tiwari G, Thomas T, Khandelwal RP. Influence of reinforcement in the honeycomb structures under axial compressive load. Thin-Walled Struc. 2019;126:238–45.
3. Biswas P, Rajeswari K, Mahendar V, Johnson R. Extrusion processing of dense $MgAl_2O_4$ spinel honeycombs with low relative density. Ceram Inter. 2013;39:9819–21.
4. Kang WS, Lee DH, Lee J-O, Hur M, Song Y-H. Combination of plasma with a honeycomb-structured catalyst for automobile exhaust treatment. Environ Sci Technol. 2013;19:11358–62.
5. Yamuna A, Johnson R, Mahajan YR, Lalithambika M. Kaolin based cordierite for pollution control. J Eur Ceram Soc. 2004;24:65–73.
6. Gatica JM, Gómez DM, Harti S, Vidal H. Clay honeycomb monoliths for water purification: modulating methylene blue adsorption through controlled activation via natural coal templating. Appl Surface Sci. 2013;277:242–8.
7. Saha BP, Johnson R, Ganesh I, Rao G, Bhattacharjee S, Mahajan YR. Thermal anisotropy in sintered cordierite monoliths. Mater Chem Phys. 2001;67:140–5.
8. Sundararajan G, Hareesh US, Johnson R, Mahajan YR. Hidden ceramics in energy and transport sectors—current status and road map for the future. Proc. 1st Inter. Congress on 'Ceramics', Toronto, Canada, June 2006, The American Ceramic Society; 2007: 553–594.
9. Agrafiotis C, Mavroidis I, Konstandopoulos A, Hoffschmidt B, Stobbe P, Romero M, et al. Evaluation of porous silicon carbide monolithic honeycombs as volumetric receivers/collectors of concentrated solar radiation. Sol Energy Mater Sol Cells. 2007;91:474–88.
10. Johnson R, Mahajan YRChidambram R editor Material research: current scenario and future projections. India: Material Research Society of India; 2002.
11. Yamaguchi T, Shimizu S, Suzuki T, Fujishiro Y, Awano M. Development and evaluation of a cathode-supported SOFC having a honeycomb structure. Electrochem Solid-State Lett. 2008;11:117–21.
12. Badding ME, Wight JF Jr. Honeycomb electrode fuel cell, US patent 6551735B2; 2000.
13. Wittenauer J, Norris B. Structural honeycomb materials for advanced aerospace designs. J Miner Metal Mater Soc. 1990;42:36–41.
14. Boger TR, He S, Shen M. Honeycomb filters for reducing NOx and particulate matter in diesel engine exhaust. US patent 20120230881A1; 2011.
15. Kaushika ND, Sharma PP. Transparent honeycomb insulated solar thermal systems for energy conservation. Heat Recovery System CHP. 1994;14:37–44.
16. Bagley RD Extrusion method for forming thin-walled honeycomb structures. US Patent 3790654;1974.
17. Miwa M, Shiji Y. Process for producing ceramic honeycomb structure extrusion dies. US patent 5070588A;1989.
18. Deckers J, Vleugels J, Kruth J-P. Additive manufacturing of ceramics: a review. J Ceram Sci Technol. 2014;5:245–60.
19. Ren X, Shao H, Lin T, Zheng H. 3D gel-printing—an additive manufacturing method for producing complex shape parts. Mate Des. 2016;101:80–7.
20. Brunello G, Sivolella S, Meneghello R, Ferroni L, Gardin C, Piattelli A, et al. Powder-based 3D printing for bone tissue engineering. Biotechnol Adv. 2016;34:740–53.
21. Jared BH, Aguilo MA, Beghini LL, Boyce BL, Clark BW, Cook A, et al. Additive manufacturing: toward holistic design. Scripta Mater. 2017;135:141–7.
22. Biswas P, Mamatha S, Naskar S, Rao YS, Johnson R, Padmanabham G. 3D extrusion printing of magnesium aluminate spinel ceramic parts using thermally induced gelation of methyl cellulose. J Alloys Compds. 2019;770:419–23.
23. Biswas P, Rajeswari K, Ramavath P, Johnson R, Maiti HS. Fabrication of transparent spinel honeycomb structures by methyl cellulose based thermal gelation processing. J Am Ceram Soc. 2013;96:3042–5.
24. Hareesh US, Anantharaju R, Biswas P, Rajeswari K, Johnson R. Colloidal shaping of alumina ceramics by thermally induced gelation of methylcellulose. J Am Ceram Soc. 2011;94:749–53.s
25. Arukalam IO, Madufor IC, Ogbobe O, Oguzie EE. Cellulosic polymers for corrosion protection of aluminium. Int J Eng Tech Res. 2015;3:163–9.

How to cite this article: Mamatha S, Biswas P, Das D, Johnson R. 3D printing of cordierite honeycomb structures and evaluation of compressive strength under quasi-static condition. *Int J Appl Ceram Technol*. 2020;17:211–216. https://doi.org/10.1111/ijac.13399

Journal of Alloys and Compounds 770 (2019) 419–423

Contents lists available at ScienceDirect

Journal of Alloys and Compounds

journal homepage: http://www.elsevier.com/locate/jalcom

3D extrusion printing of magnesium aluminate spinel ceramic parts using thermally induced gelation of methyl cellulose

Papiya Biswas [a], Sirisala Mamatha [a], Subhendu Naskar [b], Yabaluri Srinivasa Rao [a], Roy Johnson [a, *], Gadhe Padmanabham [a]

[a] International Advanced Research Centre for Powder Metallurgy and New Materials, Balapur, Hyderabad, 500 005, India
[b] Metallurgical and Materials Engineering, National Institute of Technology, Warangal, 506004, India

ARTICLE INFO

Article history:
Received 5 April 2018
Received in revised form
10 August 2018
Accepted 16 August 2018
Available online 17 August 2018

Keywords:
Magnesium aluminate spinel
3D printing
Methyl cellulose
Thermal gelation

ABSTRACT

Additive manufacturing (AM) is an innovative complex shaping technique with unlimited freedom and flexibility in fabrication. Though the majority of AM processes were focused in polymers, it is later extended to metals and very recently to ceramics. Conventional prototyping of ceramics, especially complex parts proceeds through several iterations of design and fabrication of dies, moulds, fixtures etc. which are cost intensive and also time taking to arrive at the final designs. Often the finished parts also needs machining to achieve the micro-features. 3D printing of ceramics with its inherent advantages simplifies above issues especially for fabrication of prototypes leading to the selection of optimum designs in a very short time. Further, as the same infrastructure is based on the printing of ceramic shapes using software generated virtual images it also results in lower cost. In the present study, unlike generally employed UV or visible curable resins to 3D print the green ceramic parts, a new concept of thermally induced gelation of methyl cellulose is used to retain the shape while printing of the parts. In this process, magnesium aluminate spinel paste formulated with 0.25% by weight of methyl cellulose (MC) having optimized rheology was 3D printed simultaneously exposing to the hot air flow close to the MC gelation temperature. Magnesium aluminate spinel test specimens are also shaped using generally practiced slip casting process for the sake of comparison, as slip casting process is not adaptable to fabricate the parts micro-features 3D printed in the present study. The formed parts by both the techniques were pressureless sintered at 1650 °C. 3D printed spinel specimens have shown comparable density, hardness and flexural strength with respect to the slip cast specimens complemented by fractographic analysis.

1. Introduction

Additive manufacturing (AM) is rather simple and a versatile process for complex shaping of materials that provides flexibility in prototyping [1–5]. The major application of AM process is well known for polymers and is being extended to metal powders [6–8]. Very recently a lot of interest has been generated in the printing of 3D shapes using ceramic powders [9–11]. Prototyping of ceramics proceeds through several iterations of green shaping involving design and fabrication of dies, fixtures or moulds, followed by machining in the green stage or after sintering to achieve critical micro geometries. These conventional prototyping processes is time taking and cost intensive due to several iterations especially for prototyping before arriving at the final design. AM processing of ceramics generally divided into two categories based on the macroscopic properties. The components 3D printed can be dense or porous parts [12]. Currently explored major AM processing techniques for ceramic shaping are stereolithography (SLA), extrusion of ceramic pastes, selective laser sintering (SLS), laminated object manufacturing (LOM) and binder jetting. Powder based SLS employs an inbuilt laser beam for direct sintering of the printed ceramic parts [13–15]. LOM is an alternative for lamination of individual green ceramic tapes to form three dimensional sintered ceramic parts [16–19]. SLA is based on a liquid resin which undergoes photopolymerization along with ceramic particles printed layer by layer [20–22]. Extrusion of ceramic paste generally also known as robocasting or direct ink writing uses a ceramic suspension or paste with controlled rheology exhibiting

* Corresponding author.
E-mail address: royjohnson@arci.res.in (R. Johnson).

https://doi.org/10.1016/j.jallcom.2018.08.152
0925-8388/

pseudoplastic behavior [23–25]. Binder jetting or powder based 3D printing realizes the component through deposition of the layer of flowable powder followed by the binder gluing which is repeated till the object is realized [26–28]. These parts are binder removed and sintered to form the final component.

Shaping of ceramics by thermally induced gelation of methyl cellulose (MC) is attracted interest due to its advantages of eco-friendliness as it is a naturally occurring polymer and further due to effectiveness in very low concentrations [29,30]. However, ceramic AM process hitherto reported are not so far used thermal gelation process for the 3D printing shapes. This paper describes the preparation of printable MC based homogeneous magnesium aluminate ($MgAl_2O_4$) spinel. Spinel is a well-known refractory ceramics and recently emerged as a transparent ceramic for strategic applications such as transparent windows and domes [31–33]. Spinel is also achieving importance as complex shaped scaffolds for bio-medical applications [34,35]. 3D printing being an ideal route for complex shaped products, the developed technique can be employed for above application.

The spinel paste with optimum rheological properties using MC followed by 3D printing with in-situ hot air flow for thermal gelation. Thermal gelation process is found to be very effective in retaining the shapes of the formed ceramic parts. For the sake of comparison, the formulations were only shaped into test specimens by conventional slip casting due to the limitation of this process to produce the samples with micro-features printed in the current research. The parts are binder removed and sintered at 1650 °C under identical conditions to study the densification behavior. Both the samples processed through 3D printing and slip casting have shown density of 3.47 and 3.51 g/cm^3, a hardness of 11.5 and 12.6 GPa and flexural strength of 182 and 205 MPa, respectively, complementing each other with respective fractographs.

2. Experimental procedure

Spinel powder (S30CR, Baikowski, France) has been characterized for the phase purity using XRD (D8-Bruker, Germany) and particle size by Laser Diffraction technique (Malvern Instruments, UK) and were used for 3D printing after thermal passivation [36]. Spinel powder was further blended with 0.25% (by wt.) of methyl cellulose (MC) aqueous solution as binder in water medium (approximately 40 wt%). The mix was subsequently kneaded in a vacuum sigma kneader for about 30 min. The specific gravity of the paste was found to be 1.95. Rheological behavior of the paste was measured at varying shear rates (MCR 51, Anton Paar, Austria) to determine the flow properties. The variation in viscosity as a

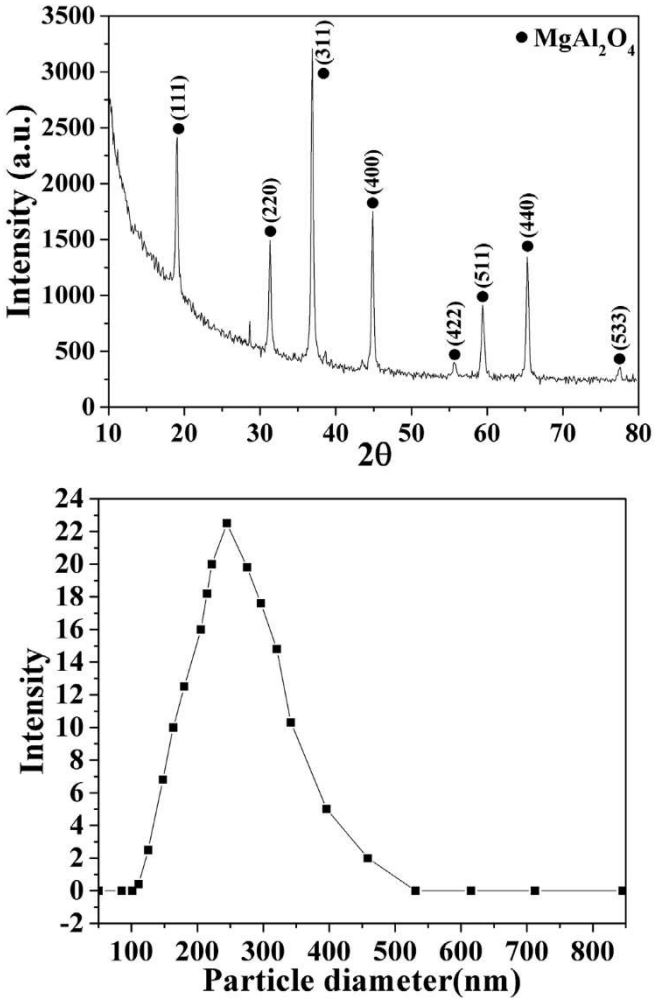

Fig. 1. (a) X-ray diffraction pattern and (b) particle size distribution of magnesium aluminate spinel powder.

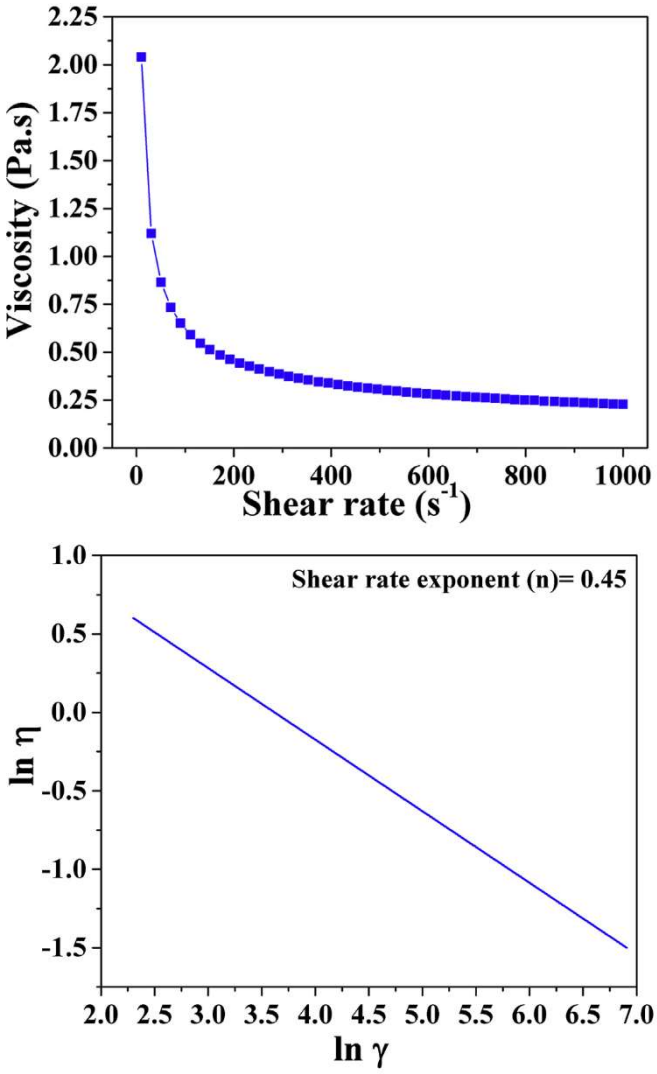

Fig. 2. (a) Variation of viscosity with shear rate of the paste with methyl cellulose and (b) shear rate exponent.

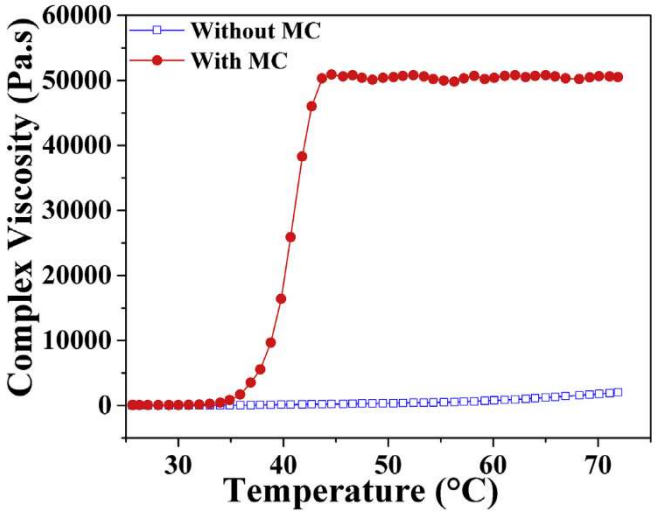

Fig. 3. Variation of viscosity of the paste with and without methyl cellulose with respect to temperature.

function of temperature was also studied at low shear rates of 10 s^{-1} in the temperature range of 25–72 °C at the heating rate of 1 °C/min. In order to bring out the gelation behavior, the paste without MC was also subjected to the rheological measurements with respect to temperature.

Table 1
Density, hardness and flexural strength of both the samples.

Properties	3D printed specimens	Slip cast specimens
Density (g/cm^3)	3.47	3.51
[a]Hardness (GPa)	11.5	12.5
[b]Flexural Strength (MPa)	182	205

[a] Average of 10 readings.
[b] Average of 5 readings.

Formable spinel paste with optimum rheology was printed using a ram type 3D printer (3D Ceramic, Maker City, India) fitted with 1.0 mm nozzle. The printing of the ceramic parts were based on a virtual CAD design which in turn converted into a STL file with all printing parameters (layer thickness, printing speed, number of layers etc.) and transferred to a microprocessor which will dictate the tailored nozzle path for printing leading to the formation of physical object. The component while printing was exposed to the MC gelation temperature of 45–60 °C by means of a honeycomb based energy efficient air heater which ensure the temperature uniformity [37]. Test specimen were casted for the comparative evaluation of the properties through slip casting. The dried samples shaped through both the techniques were characterized for their green density and were subjected to the binder removal at a heating rate of 1 °C/min upto 550 °C followed by sintering at the temperature of 1650 °C in a muffle furnace (Deltech, USA) at the ramp rate of 100 °C/h with a soaking period of 1 h to achieve the

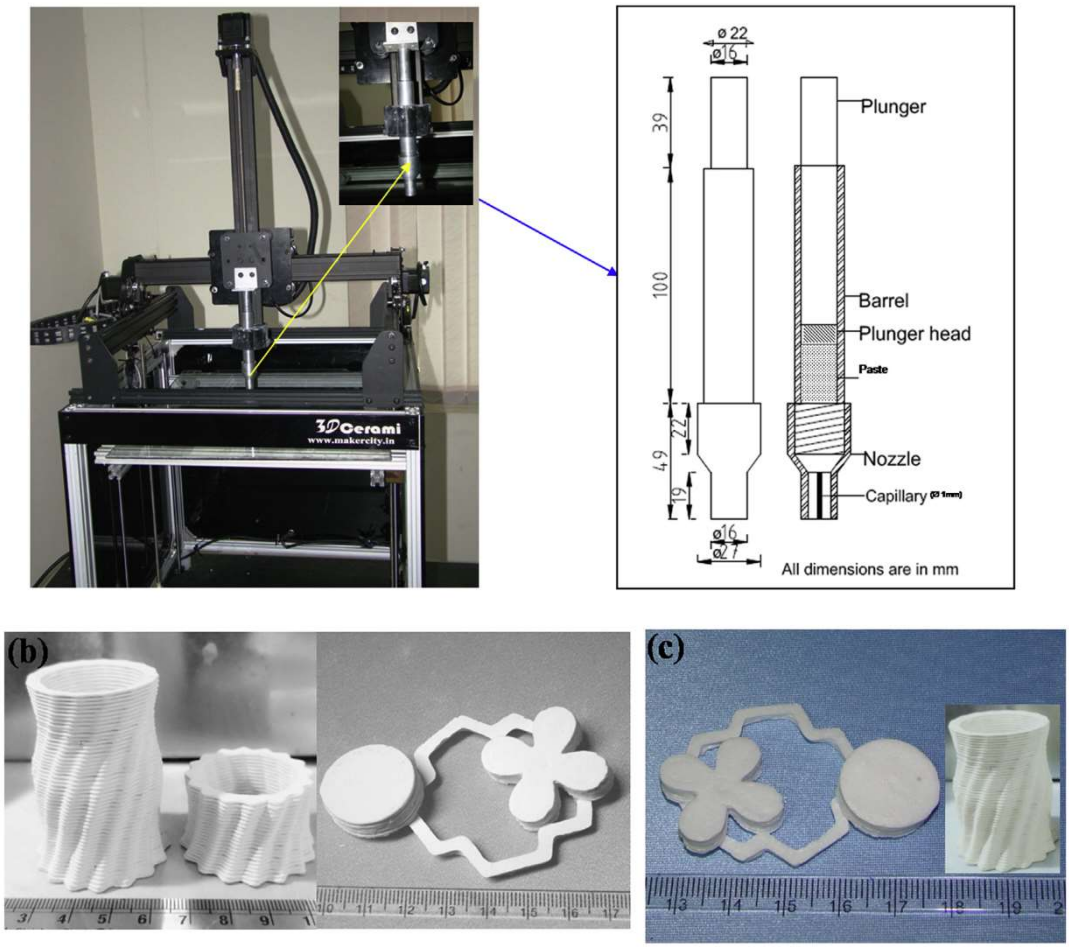

Fig. 4. (a) 3D printer, (b) printed green parts and (c) sintered parts.

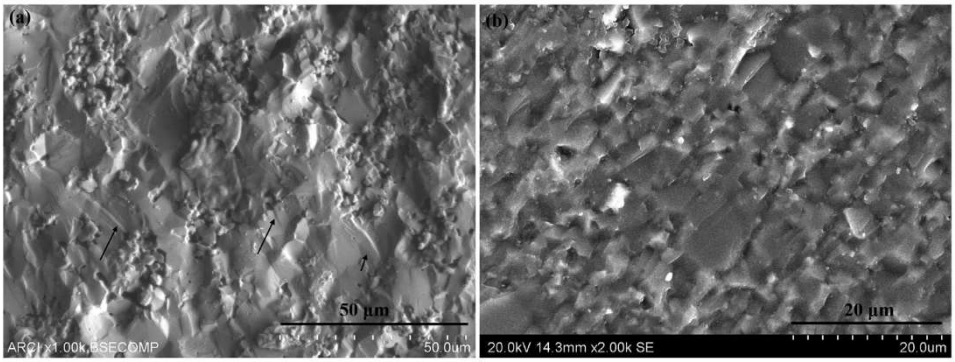

Fig. 5. Fractography of (a) 3D printing sample and (b) slip casted sample.

density. These heating conditions were optimized based on several trials at our laboratory.

Density of the sintered samples was evaluated by widely used Archimedes principle (ASTM C792) and the samples were also subjected to hardness measurement (ASTM C1327) using a Vickers hardness tester (Leco, St. Joseph, MI) at 5 kg load. Flexural strength specimens ($45 \times 4 \times 3$ mm) were also prepared and subjected to 3-point bend test (ASTM C1161) in Universal testing machine (Instron-5584) and fractographs were recorded by scanning electron microscope (S-4300SE/N, Hitachi, Tokyo, Japan).

3. Results and discussion

As evident from Fig. 1 (a) and (b) the spinel powder have exhibited high phase purity and average particle sizes of 0.25 µm. Variation of viscosity of the paste with methyl cellulose and shear rate exponent (n) is shown in Fig. 2 (a) and (b), respectively. The paste used for 3D printing should optimally flow under minimum shear forces and must have sufficient mechanical strength to maintain the shape integrity after printing. The viscosity vs. shear rate plot clearly indicates a non-linear trend, suggesting that the mix behaves like a non-Newtonian shear thinning fluid with a storage modulus of 243 Pa which is found suitable for 3D printing.

Variation of viscosity of the paste with and without methyl cellulose with respect to temperature is shown in Fig. 3. It is evident that, slurry viscosity is almost constant in both cases in the temperature range of 25–35 °C; however, in the case of paste with methyl cellulose, there is a steep increase in viscosity in the temperature range of 40 °C onwards indicating the dehydration of hydrated methoxy groups. This results in hydrophobic association of monomer molecules leading to polymerization resulting in gel formation. On the contrary, in the case of paste without methyl cellulose no such increase in paste viscosity is seen in similar temperature ranges. However, a gradual raise in the viscosity at around 60 °C can be attributed to the evaporation of water.

Fig. 4(a) shows 3D printing process using the above viscoplastic paste which flows under shear and form the parts. The parts was simultaneously exposed to hot air while printing resulting in immediate gelation of methyl cellulose leading to retention of shapes. Fig. 4(b) shows a few of the simple and complex parts 3D printed and in-situ dried in the present study and Fig. 4(c) shows the sintered samples. A paste feed rate of 9 mm/s is found to be optimum based on the several experiments in our laboratory. Density, hardness and flexural strength of 3D printed and slip cast samples are shown in Table 1.

Fig. 5 (a) and (b) are showing the fracture surface of sintered 3D printed sample and slip cast sample, respectively. Fractograph shows the formation of layered structure while printing; however, the samples have shown comparable density values of 3.47 and 3.51 g/cm^3, respectively with slip cast specimens. Hardness and flexural strength values are found to be 11.5 GPa and 182 MPa for printed and 12.6 GPa and 205 MPa for slip casted samples respectively.

4. Conclusions

Thermally induced gelation behavior of methyl cellulose has been successfully applied to 3D printing of advanced ceramic (magnesium aluminate spinel) for the first time and complex shaped magnesium aluminate spinel specimens are produced.

In-situ thermally induced gelation process currently employed in the present study is advantageous as the methyl cellulose is used only at a very low concentration of 0.25% by weight. This process is eco-friendly and offers flexibility in post processing as in the case of conventional ceramic processing employing binders.

Further, as the in-situ drying occurs while printing of the specimens substantial reduction in the duration of drying is also observed in comparison to slip casting employed in the present study.

3D printed and sintered spinel specimens have shown comparable density of 3.47 g/cm^3 and hardness of 11.5 GPa as compared to 3.51 g/cm^3 and 12.5 GPa observed with slip cast specimens. Flexural strength of the samples was also found to be 182 and 205 for 3D printed and slip cast samples, respectively. The fractographs complements with the reported density and mechanical property values. The observations can be attributed to the processing parameters optimized in the current study for 3D printing of spinel ceramics.

References

[1] Z. Zhua, N. Anwer, L. Mathieu, Deviation modeling and shape transformation in design for additive manufacturing, Proc. CIRP 60 (2017) 211–216.
[2] B.H. Jared, M.A. Aguilo, L.L. Beghini, B.L. Boyce, B.W. Clark, A. Cook, B.J. Kaehr, J. Robbins, Additive manufacturing: toward holistic design, Scripta Mater. 135 (2017) 141–147.
[3] X. Ren, H. Shao, T. Lin, H. Zheng, 3D gel-printing—an additive manufacturing method for producing complex shape parts, Mater. Des. 101 (2016) 80–87.
[4] M. Schmidt, M. Merklein, D. Bourell, D. Dimitrov, T. Hausotte, K. Wegener, L. Overmeyer, F. Vollertsen, G.N. Levy, Laser based additive manufacturing in industry and academia, CIRP Ann. - Manuf. Technol. 66 (2017) 561–583.
[5] L. Li, B. Post, V. Kunc, A.M. Elliott, M.P. Paranthaman, Additive manufacturing of near-net-shape bonded magnets: prospects and challenges, Scripta Mater. 135 (2017) 100–104.
[6] J.N. Haigh, T.R. Dargaville, P.D. Dalto, Additive manufacturing with polypropylene microfibers, Mater. Sci. Eng. C 77 (2017) 883–887.
[7] B.G. Compton, B.K. Post, C.E. Duty, L. Love, V. Kunc, Thermal analysis of additive manufacturing of large-scale thermoplastic polymer composites, Addit. Manuf. 17 (2017) 77–86.
[8] B.M. West, N.E. Capps, J.S. Urban, J.D. Pribe, T.J. Hartwig, T.D. Lunn, B. Brown, D.A. Bristow, R.G. Landers, E.C. Kinzel, Modal analysis of metal additive

manufactured parts, Manuf. Lett. 13 (2017) 30–33.
[9] W. Harrer, M. Schwentenwein, T. Lube, R. Danzer, Fractography of zirconia-specimens made using additive manufacturing (LCM) technology, J. Eur. Ceram. Soc. 37 (2017) 4331–4338.
[10] Y. Li, Y. Hu, W. Cong, L. Zhi, Z. Guo, Additive manufacturing of alumina using laser engineered net shaping: effects of deposition variables, Ceram. Int. 43 (2017) 7768–7775.
[11] M. Dehurtevent, L. Robberecht, J.-C. Hornez, A. Thuault, E. Deveaux, P. Béhin, Stereolithography: a new method for processing dental ceramics by additive computer-aided manufacturing, Dent. Mater. 33 (2017) 477–485.
[12] A. Zocca, P. Colombo, C.M. Gomes, J. Gunster, Additive manufacturing of ceramics: issues, potentialities, and opportunities, J. Am. Ceram. Soc. 98 (2015) 1983–2001.
[13] S.L. Sing, W.Y. Yeong, Direct selective laser sintering and melting of ceramics: a review, Rapid Prototyp. J. 23 (3) (2017) 611–623.
[14] K. Shahzad, J. Deckers, J.P. Kruth, J. Vleugels, Additive manufacturing of alumina parts by indirect selective laser sintering and post processing, J. Mater. Process. Technol. 213 (2013) 1484–1494.
[15] J. Deckers, S. Meyers, J.P. Kruth, J. Vleugels, Direct selective laser Sintering/Melting of high density alumina powder layers at elevated temperatures, Phys. Proced. 56 (2014) 117–124.
[16] D. Klosterman, R. Chartoff, G. Graves, N. Osborne, B. Priore, Interfacial characteristics of composites fabricated by laminated object manufacturing, Compos. Appl. Sci. Manuf. 29 (1998) 1165–1174.
[17] L. Weisensel, N. Travitzky, H. Sieber, P. Greil, Laminated object manufacturing (LOM) of SiSiC composites, Adv. Eng. Mater. 6 (2004) 899–903.
[18] H. Windsheimer, N. Travitzky, A. Hofenauer, P. Greil, Laminated object manufacturing of preceramic-paper-derived SiSiC composites, Adv. Mater. 19 (2007) 4515–4519.
[19] Y. Zhang, X. He, J. Han, S. Du, Ceramic green tape extrusion for laminated object manufacturing, Mater. Lett. 40 (1999) 275–279.
[20] H. Wu, W. Liu, R. He, Z. Wu, Q. Jiang, X. Song, Y. Chen, L. Cheng, S. Wu, Fabrication of dense zirconia-toughened alumina ceramics through a stereolithography-based additive manufacturing, Ceram. Int. 43 (2017) 968–972.
[21] G. Mitteramskogler, R. Gmeiner, R. Felzmann, S. Gruber, C. Hofstetter, J. Stampfl, J. Ebert, W. Wachter, J. Laubersheime, Light curing strategies for lithography-based additive manufacturing of customized ceramics, Addit. Manuf. 1–4 (2014) 110–118.
[22] M.L. Griffith, J.W. Halloran, Freeform fabrication of ceramics via stereolithography, J. Am. Ceram. Soc. 79 (1996) 2601–2608.
[23] M. Faes, J. Vleugels, F. Vogeler, E. Ferraris, Extrusion-based additive manufacturing of ZrO2 using photo initiated polymerization, CIRP J. Manuf. Sci. Technol. 14 (2016) 28–34.
[24] J. Cesarano, P. D. Calvert, Inventor: Sandia Corporation, Assignee, Freeforming objects with low-binder slurry, US Patent 6027326 A (2000).
[25] J.A. Lewis, J.E. Smay, J. Stuecker, J. Cesarano, Direct ink writing of three-dimensional ceramic structures, J. Am. Ceram. Soc. 89 (2006) 3599–3609.
[26] J.A. Gonzalez, J. Mireles, Y. Lin, R.B. Wicker, Characterization of ceramic components fabricated using binder jetting additive manufacturing technology, Ceram. Int. 42 (2016) 10559–10564.
[27] A. Butscher, M. Bohner, N. Doebelin, L. Galea, O. Loeffel, R. Muller, Moisture based three-dimensional printing of calcium phosphate structures for scaffold engineering, Acta Biomater. 9 (2013) 5369–5378.
[28] R. Chumnanklang, T. Panyathanmaporn, K. Sitthiseripratip, J. Suwanprateeb, 3D printing of hydroxyapatite: effect of binder concentration in pre-coated particle on part strength, Mater. Sci. Eng. C 27 (2007) 914–921.
[29] U.S. Hareesh, R. Anantharaju, P. Biswas, K. Rajeswari, R. Johnson, Colloidal shaping of alumina ceramics by thermally induced gelation of methylcellulose, J. Am. Ceram. Soc. 94 (2011) 749–753.
[30] P. Biswas, K. Rajeswari, P. Ramavath, R. Johnson, H.S. Maiti, Fabrication of transparent spinel honeycomb structures by methyl cellulose based thermal gelation processing, J. Am. Ceram. Soc. 96 (2013) 3042–3045.
[31] T. Mroz, L.M. Goldman, A.D. Gledhill, D. Li, N.P. Padture, Nanostructured, infrared-transparent magnesium aluminate spinel with superior mechanical properties, Int. J. Appl. Ceram. Technol. 9 (2012) 83–90.
[32] M. Ramisetty, S. Sastri, U. Kashalikar, L.M. Goldman, N. Nag, Transparent polycrystalline cubic spinels: protect and defend, Am. Ceram. Soc. Bull. 92 (2013) 20–25.
[33] N. Frage, S. Cohen, S. Meir, S. Kalabukhov, M.P. Dariel, Spark plasma sintering (SPS) of transparent magnesium-aluminate spinel, J. Mater. Sci. 42 (2007) 3273–3275.
[34] M. Krishnan, Brijesh, V. Arora, P. Biswas, K. Rajeswai, M.B. Suresh, R. Johnson, Transparent magnesium aluminate spinel: a prospective biomaterial for esthetic orthodontic brackets, J. Mater. Sci. Mater. Med. 25 (2014) 2591–2599.
[35] P. Biswas, A. Sharma, M. Krishnan, R. Johnson, Mantravadi Krishna Mohan, Fabrication of $MgAl_2O_4$ spinel scaffolds and sonochemical synthesis and deposition of hydroxyapatite nanorods, J. Am. Ceram. Soc. 99 (2016) 1544–1549.
[36] K. Rajeswari, P. Biswas, R. Johnson, S. Prabhudesai, V.K. Sharma, S. Mitra, R. Mukhopadhayay, Effect of surface passivation in spinel slurry towards hydrolysis: neutron scattering and rheological studies, J. Dispersion Sci. Technol. 35 (2014) 1442–1448.
[37] V. V. S. Rao, R. Johnson, B. P. Saha, Y. R. Mahajan, Ceramic Honeycomb Based Energy Efficient Air Heater, Indian Patent 2007787 (1999).

Journal of Water Process Engineering 37 (2020) 101503

Contents lists available at ScienceDirect

Journal of Water Process Engineering

journal homepage: www.elsevier.com/locate/jwpe

3D printing of high surface area ceramic honeycombs substrates and comparative evaluation for treatment of sewage in Phytorid application

Papiya Biswas[a], Sirisala Mamatha[a], Kezil Varghese[a], Roy Johnson[a,*], Ritesh Vijay[b], Rakesh Kumar[b]

[a] International Advanced Research Centre for Powder Metallurgy and New Materials (ARCI), Hyderabad, 500005, India
[b] National Environmental Engineering Research Institute (NEERI), Nagpur, 400020, India

ARTICLE INFO

Keywords:
3D printing
Ceramic honeycombs
Phytorid
Bioreactor

ABSTRACT

Substrates properties play an important role in immobilization of bio-organisms and hence in optimizing design of the bioreactor to maximize the performance. Highly flexible 3D printing process based on virtual Computer Aided Design (CAD) is used for producing honeycomb substrates with desired properties. Clay based honeycomb with square, triangular and hexagonal configurations are 3D printed in order to achieve substrates with pre-designed geometrical surface areas. Laboratory reactors were fabricated with engineered properties using 3D printed honeycombs and a combination of honeycombs and commonly used stones for performance evaluation. Additionally, reactor based on commonly used gravel stones also fabricated for sake of comparison of performance. In order to elucidate the performance, sewage mix was fed into the reactors and the space velocity of all the three reactors were maintained at 0.041 h^{-1}. The sewage before and after treatment was tested for the performance markers such as pH, TSS, BOD and COD. Treated water met the stipulated standards prescribed by American Public Health Association with respect to all parameters studied. Though the difference in the performance of the reactors was marginal, with honeycombs a substantial reduction in the weight of the reactor can be accrued along with high mass transfer due to low pressure drop which can be attributed to the inherent higher surface to volume ratio. Further, by engineering the surface porosity of the honeycombs, it is possible reduce TSS as demonstrated in this study. These advantages offer flexibility in scaling up the reactors for larger capacities for de-centralized requirements.

1. Introduction

Sewage is the contaminated water containing constituents such as organic wastes, suspended solids and pathogenic micro-organisms generated from toilets, kitchens, farming etc. Sewage pollutes the primary source of water. Hence, it is necessary to treat the sewage before it is discharged to the environment to use the water efficiently. Sewage is generally treated by physical, biological and sometimes chemical or combined processes to convert into water suitable for disposal or reuse. However, economics and energy related to these treatments is a major concern. Among the advanced technologies [1–10], patented Phytorid technology developed by CSIR-NEERI (National Environmental Engineering Research Institute) which mimics the natural wetland ecosystem is gaining prominence. Gravel stone / aggregates substrates used in the Phytorid technology which not only act as a filter media but also immobilise the micro-organisms that consumes the organic wastes through the metabolic activities [11,12].

Concept of using solid substrate for Phytorid reactors to immobilise the micro-organisms to achieve high culture densities for effective treatments are being recently investigated by various researchers [13,14]. Phytorids with gravel-based substrates are in operation from 1000 L to 5 Million litre. However, use of gravel-based substrates make the system heavy and requires Reinforced Cement Concrete (RCC) structures to support such heavy substrates. The scope of this paper is to evaluate the performance of the reactor with the light weight 3D printed clay-based honeycomb substrate on a laboratory scale in place of gravel-based substrate currently used.

Substrates with optimum surface to volume ratio provides the scope for miniaturisation, weight reduction and high mass transfer offering flexibility to design the bio-reactors on economic scale. In the current study, additive manufacturing (AM) is also known as 3D printing or rapid prototyping is used for the fabrication of naturally occurring clay-based substrates. As the 3D printing process generates part from the virtual model directly, it offers prototyping of substrates with various

* Corresponding author.
E-mail address: royjohnson@arci.res.in (R. Johnson).

https://doi.org/10.1016/j.jwpe.2020.101503
Received 1 June 2020; Received in revised form 2 July 2020; Accepted 6 July 2020

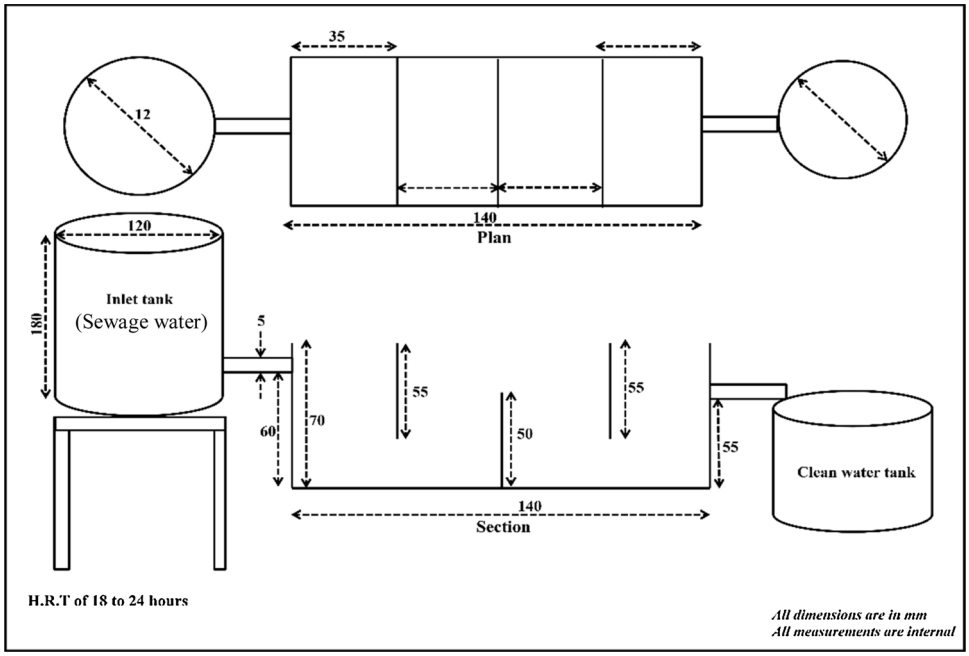

Fig. 1. Design of Phytorid reactor.

configurations and cellular parameters to achieve varying surface to volume ratio [15–20]. Naturally occurring clay-based honeycombs with square (HCS), triangular (HCT) and hexagonal (HCH) configurations with different cellular parameters are 3D printed to achieve substrates with pre-designed geometrical surface areas. Further, the substrates are also evaluated for their physico-chemical and mechanical properties. Material of fabrication of substrates being a clay-based ceramic, the substrates are stable in various chemical environments and is re-usable for several cycles of operations. Reactors were fabricated with 3D printed honeycomb substrates (designated as Reactor-I) and a reactor with the combination of gravel stones and honeycombs substrates (designated as Reactor-II). Further, for the sake of comparison conventional reactor with gravel stone substrates (designated as Reactor-III) were also experimented. Space velocity of all the reactors were maintained at 0.041 h^{-1}. Performance markers such as pH, Total Suspended Solid (TSS), Biochemical Oxygen Demand (BOD) and Chemical Oxygen Demand (COD) are comparatively evaluated.

All the parameters such as pH, TSS, BOD and COD were found to be within the stipulated values irrespective of the inlet concentration and reactor configurations. However, marginal differences were observed with respect to the performance of the reactors. Use of honeycombs as substrates has demonstrated substantial reduction in the weight by 50 %. Further, due to its inherent configurations low-pressure drop incombination with high mass transport can be achieved. Additionally, since honeycomb permits engineering the porosity and pore size distribution, an approach of gradation of porosity with respect to the reactor compartments can results in desired TSS removal without tortuosity. Functionalization with desired coating is also an option for the selective chemical/biological degradation [21].

2. Experimental procedure

2.1. 3D printing of honeycomb substrates

Clay based ceramic formulation was characterized for the phase purity using XRD (D8-Bruker, Germany) and particle size distribution by Laser Diffraction technique (Malvern Instruments, UK). The formulation was kneaded with water into a homogeneous paste using a sigma kneader with methyl cellulose (0.2 % by weight) as a binder and polyethylene glycol (0.75 % by weight) as a plastiziser. Rheological behavior of the paste was studied at varying shear rates using Anton Paar rheometer (MCR 51, Anton Paar, Austria) to determine the flow properties. Based on predesigned surface area, CAD models were generated and a ram type 3D printer (3D Cerami, Maker City, India) fitted with a nozzle was used for the printing of the honeycomb substrates with varying configurations, cellular parameters (such as unit cell length (l) and wall thickness (t)), shapes and sizes. The honeycombs were sintered at 1100 °C using air sintering furnace (Deltech, USA) and were also characterized for their density (ASTM-B962) using high precision electronics balance with density kit (ME204E/A04, Mettler-Toledo AG, Switzerland), specific surface area using BET-N_2 adsorption technique (Gemini, Micromeritics Instruments Corp, USA), compressive strength using a Universal Testing Machine (5584, Instron, USA) and further, surface volume ratio was also calculated.

2.2. Designing of Phytorid reactors

Phytorid is a Sub-Surface Flow Constructed Wetland System (SSFCW). Point and non-point water pollution sources can be treated using Phytorid technology. Phytorid system is generally provided with a basin or a channel with a barrier to eliminate seepage and the filter media is placed to a certain depth within the compartments and also supports the roots of the vegetation [22–24]. Initial filtration of suspended solids and a marginal reduction of BOD can be achieved through primary treatments. Various species of aquatic plants *Phalarisarundinacea*, *Glyceria maxima*, *Phramitesaustralis*, *Typha spp* and other common grasses are found to be very effective in maximizing the treatment efficiencies. The design of the Phytorid should ensure subsurface flow and the water level in the cells should remain below the top of the filter media.

Phytorid reactor designed for the proposed study is shown in Fig. 1. The reactor consists of three units such as inlet tank, Phytorid bed and treated water tank. Considering the quantity of wastewater to be treated, the inlet tank, Phytorid bed and treated water tank is designed. The inlet tank works as sedimentation unit in order to provide preliminary treatment to wastewater similar to what is available for Phytorid Treatment Plant. The design of Phytorid bed depends upon its ratio of length to breadth which is 3:1. Phytorid bed consists of odd

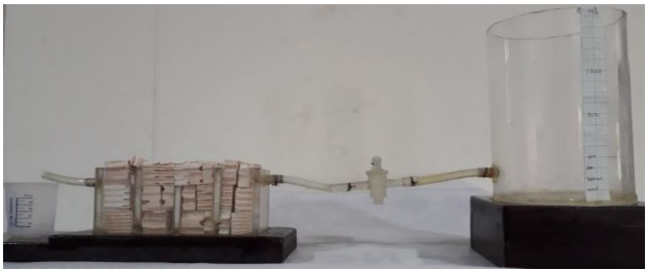

Fig. 2. Phytorid reactor fabricated as per design.

numbers of baffle walls in order to provide sinusoidal flow to the wastewater. These baffles are also responsible for eliminating the short-circuiting of wastewater and treat water more efficiently. The Phytorid reactor fabricated as per the design shown in Fig. 2. Phytorid reactors along with porous honeycomb substrates and gravel stone substrates are shown in Fig. 3.

2.3. Reactor configuration

3D printed honeycombs of various configurations were loaded in all the compartments of Reactor-I and Reactor-II has a combination of gravel stones in the 1st compartment followed by honeycombs in 2nd, 3rd and 4th compartments and further, all the compartments of Reactor-III were loaded with gravel stones. All the reactors volume and the flow conditions were identical for the sake of one to one comparison of the performance of the substrates in the reactors. Since 3D printed substrate was used in small Phytorid tank and a 15 days' time is required to get acclimatize with the bacteria available in sewage and generate very thin bio layers to treat the incoming sewage. Treated water samples were collected for analysis on 15th, 30th and 45th day.

A minimum of five samples are evaluated in each case. TSS, pH, BOD and COD are the mandatory parameters to evaluate quality of the treatment of wastewater or sewage as per Indian guidelines. These parameters are analyzed by standard method as prescribed by American Public Health Association (APHA) [25]. An instrumental method was used for monitoring of pH, evaporation method was used for TSS, iodometeric titration was used for BOD and dichrometric refluxing was employed for measurement of COD. Acidic or basic nature of waste water is determined by pH and has an effect on the microbial growth rate but it largely depends on types of microorganisms. Most of the micro-organisms perform well within pH range of 6.5–8.5.

3. Results and discussions

XRD [26,27] studies of the raw material confirmed the kaolinite phase inherently present in the clay as is evident from the XRD pattern (Fig. 4(a)). All peaks are indexed by using Match software and Entry no. 96-901-5000. The particle size [28] D_{50} was found to be 620 nm with a distribution of 200 − 1500 nm from the particle size distribution plot as depicted in Fig. 4(b). Though the clay exhibit plasticity with addition of 38 % by weight of water as a medium in order to derive optimum pseudo-plastic behaviour the flow properties required to be modified using organic additives. These additives such as polyethylene glycol 0.75 % by weight promotes the flow under shear while 3D printing and 0.2 % by weight methyl cellulose as a binder aids to retain the shape after shear forces are removed. The paste with has clearly indicated a shear thinning behavior (Fig. 5(a)) with respect to shear rate. The type and concentration of additives are optimized based on several experiments in our laboratory [29]. Further shear rate exponent (n) was calculated and is found to be 0.77 (Fig. 5(b)) signifying shear thinning behavior which can be attributed to the optimum additives concentrations added during the paste preparation.

A typical CAD model generated, 3D printed green honeycomb and the printed honeycombs sintered at 1100 °C are shown in Fig. 6. Further, the properties of the printed honeycombs along with gravel stone substrates are shown in Table 1.

It is evident from the Table 1 that, double the wall thickness (2 mm) of hexagonal configuration in comparison to square and triangular honeycombs (1 mm) is due to the common edge sharing while printing the hexagonal geometry. Surface to volume ratio of the honeycombs of different configurations are 4.34–15.16 which is further depends on respective cellular properties. Accordingly, the compressive strength of the hexagonal honeycombs are higher and exhibits superior load bearing capacity. Specific surface area and density being the material properties are similar as they are processed under identical conditions. Samples also exhibited an identical density of 1.68 g/cc and 32–35 % porosity due to the identical sintering schedules and same peak temperature followed for these substrates.

The properties of the reactors with respect to geometrical and specific surface area, space velocity, retention time and total weight of the reactor are presented in Table 2. It is evident from Table 2 that the geometrical surface area in Reactor-I (0.1850 m^2) is almost 2 times than that of Reactor-III (0.0945 m^2) which is based on the stone substrates and in case of Reactor-II geometrical surface area (0.1623 m^2) is designed to have about 1.7 times of Reactor-III. The space velocity was kept identical by engineering the flow regulation at the outlet of the sewage storage tank in order to maintain the chemical environment similar for better comparison of the results. A substantial reduction is observed in weight almost by 50 % in case of Reactor-I and 37 % for the Reactor-II with respect to Reactor-III.

The performane markers (as an average of 5 measurements) of the bioreactor have presented in Table 3. The efficiency of treatment with respect to the parameters are improving over the period of time from 15th to 45th day which can be attributed to the acclimatization of the bacteria with the sewage and formation of bio-layers for the effective treatment of incoming sewage. In case of all parameters a combination of gravel stones and honeycombs (Reactor-II) have exhibited relatively low values with respect to the prescribed standards followed by honeycombs-based reactor (Reactor-I) and relatively lowest performance with stone-based reactor (Reactor-III). The highest efficiency in case of TSS, BOD and COD in Reactor-II can be attributed to the synergistic effect of the tortuous path offered by the gravel stones in combination with the laminar flow occurred in the channeled honeycombs structure. Honeycombs have exhibited better performance with respect to

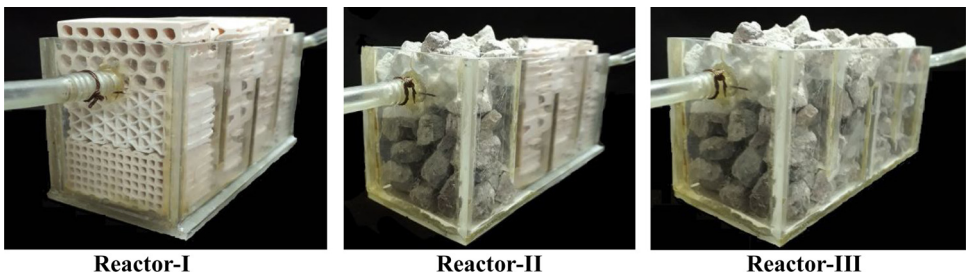

Fig. 3. Phytorid reactors (Reactor-I, II and III) with porous ceramic honeycombs and gravel stones.

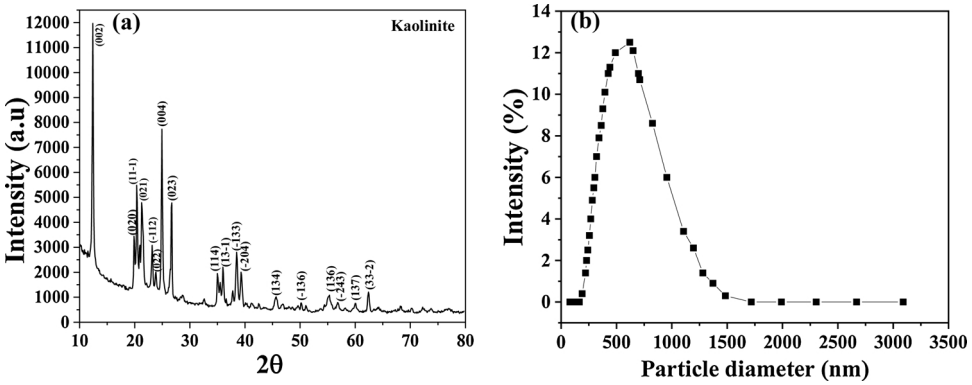

Fig. 4. (a) X- Ray diffraction pattern and (b) Particle size distribution of clay powder.

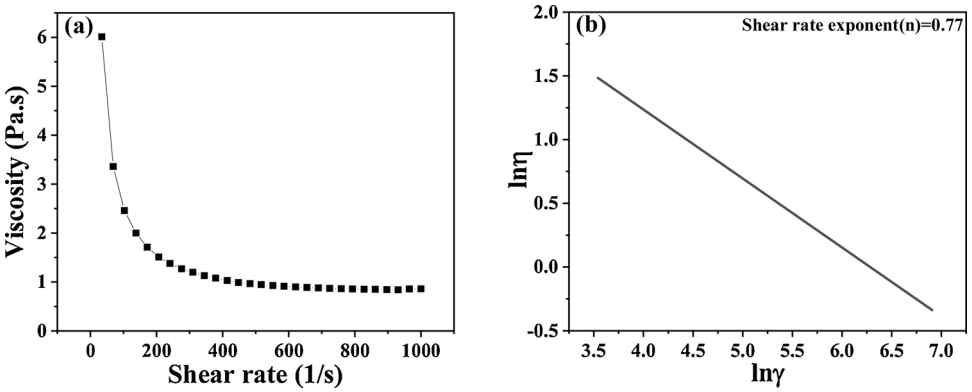

Fig. 5. Plots of (a) Shear rate vs Viscosity and (b) lnγ vs lnη of clay paste.

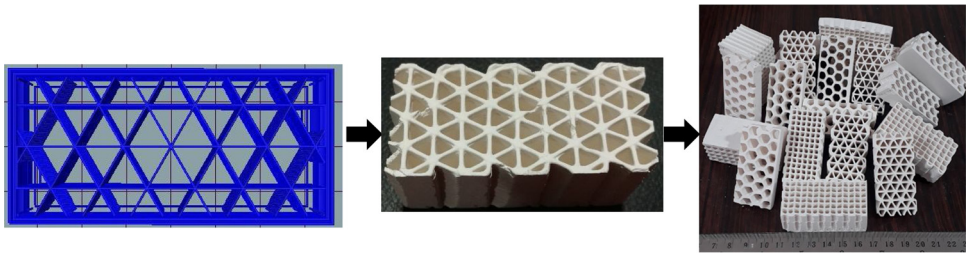

Fig. 6. A typical CAD model along with printed honeycombs.

Table 1
Properties of 3D printed clay based honeycombs and gravel stones grits.

Properties	Ceramic honeycombs			Gravel stones
	Square channel	Hexagonal channel	Triangular channel	
Honeycomb cellular parameters (mm) (Edge length (l), Wall thickness (t))	l = 6.52 and t = 1	l = 5.53 and t = 2	l = 13.40 and t = 1	–
Surface to volume ratio	15.16	8.41	4.34	3.78
Specific surface area (m^2/g)	53.05	53.05	53.05	1.4 [30]
Compressive strength (MPa)	3.64	5.13	3.31	–
Material density (g/cc)	1.68	1.68	1.68	2.59

Table 2
Properties of Phytorid reactors.

	Reactor-I	Reactor-II	Reactor-III
Geometrical surface areaof reactor bed (m^2)	0.1850	0.1623	0.0945
Specific surface area of reactor bed (m^2)	10,494	8104	934
Space velocity (hr^{-1})	0.041	0.041	0.041
Retention time (hr)	24.3	24.3	24.3
Total weight of reactor (g)	478	595	947

conventional gravel stones reactor because of the layered structure generated due to the inherent layer by layer formation (as shown in Fig. 7(a)) of 3D printing process in combination with the highly porous surface morphology of honeycomb (as shown in Fig. 7(b)). This surface features results in the boundary layer formation close to the surface which act as the subsequent filter medium in case of 1st compartment. However, the biological degradation of sewage is better than the conventional reactor as the effective boundary layer formation due to sedimentation is limited to the first compartment. In the case of

Table 3
Performance of Bio reactors: Comparative Evaluation.

		After 15 days				After 30 days				After 45 days			
		pH	TSS	BOD	COD	pH	TSS	BOD	COD	pH	TSS	BOD	COD
Inlet		5.39	255	150	480	6.88	250	145	450	6.55	258	140	440
Outlet	Reactor I	7.83	57	86	224	8.02	56	81	224	7.36	54	77	156
	Reactor II	7.54	53	73	215	7.86	51	72	220	7.25	50	65	156
	Reactor-III	7.73	111	110	252	8.08	61	85	244	7.48	50	79	212
Standard		**5.5 − 9.0**	**200**	**100**	**250**	**5.5 − 9.0**	**200**	**100**	**250**	**5.5 − 9.0**	**200**	**100**	**250**

*Values are average of 5 measurements.

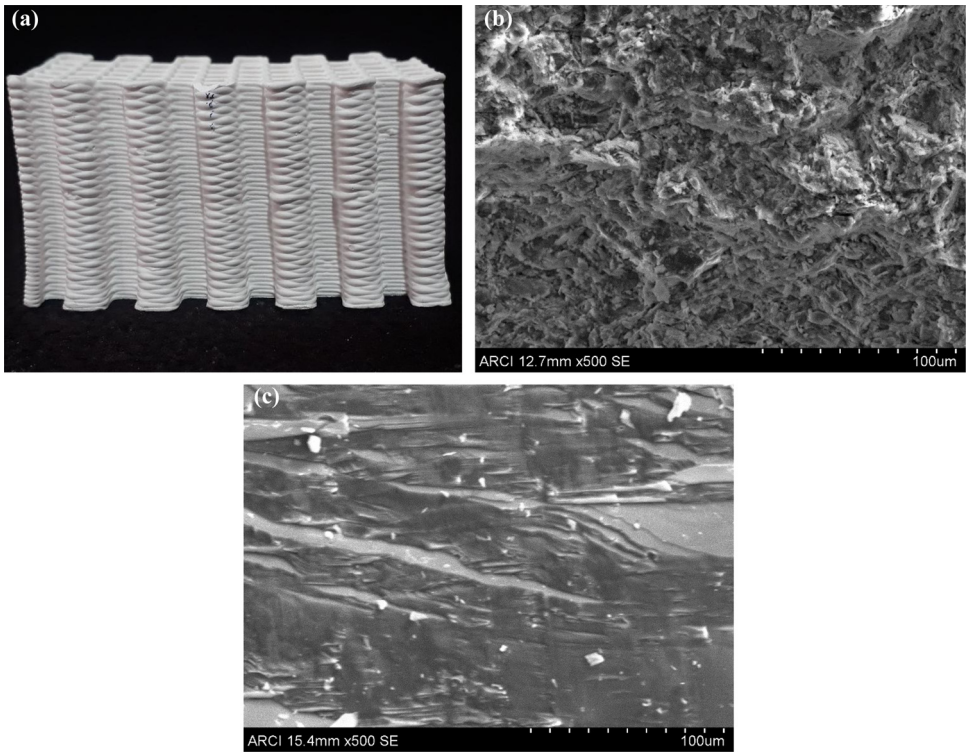

Fig. 7. (a) Layer by layer formation in 3D printed honeycomb sample, (b) Microstructure of 3D printed honeycomb substrate and (c) Microstructure of stone substrate.

conventional reactor though the gravel stones have irregular features, the surfaces are not porous (as shown in Fig. 7(c)) for effective filtration through boundary layer formation even with the tortuous flow leading to higher values in TSS and lower efficiencies in case of BOD and COD. The pH of the treated sewage remains similar irrespective of the reactor configurations. The study reveals that the Phytorid system with a combination of natural stone and 3D printed honeycomb structures may yield better efficiencies with respect to the biological parameters in the sewage treatment. Additionally, substantial weight reduction can be achieved by the use of 3D printed honeycomb substrates providing flexibility for using the constructions other than reinforced cement concrete (RCC) structures to support such heavy stone or gravel-based substrates. Scale up parameters with respect to self-weight of the substrates and flow parameters are being studied to identify the optimum surface to volume ratio and to explore the scope for miniaturisation, weight reduction and high mass transfer offering flexibility to design the bio-reactors on an economic scale.

4. Conclusion

Clay based honeycomb substrates were 3D printed with channel configurations of square, hexagonal and triangular with varying cellular parameters and desirable microstructure and structural properties.

A comparative evaluation of the performance of Phtyorid reactors with honeycomb substrates along with conventional gravel stones and their combination in treating the sewage is studied. Performance markers such as TSS, BOD and COD have shown substantial reduction confirming with highest efficiency in case of reactor with a combination of gravel stones and honeycomb substrates due to the probable mechanisms elucidated.

The study reveals the possibility of exploring honeycomb substrates with optimum surface to volume ratio for miniaturisation, weight reduction and high mass transfer offering flexibility to design the Phytorid reactors economically.

Declaration of Competing Interest

The authors declare that they have no known competing financial interests or personal relationships that could have appeared to influence the work reported in this paper.

References

[1] N.A. Akhade, A.R. Mhaske, B. Punde, Modeling of COD using phytorid sewage treatment plant, Int. J. Innov. Res. Sci. Eng. Technol. 4 (2019) 35–45.
[2] S.S. Patil, V.P. Dhulap, G. Kaushik, Application of constructed wetland using

eichhornia crassipes for sewage treatment, J. Mater. Environ. Sci. 7 (2019) 3256–3263.
[3] D.M. Koranne, D.G. Patil, K.P. Barne, A.S. Pasalkar, D.A. Narayankar, Urban wastewater treatment using phytorid, Int. J. Adv. Sci. Res. Dev. 6 (2018) 1100–1102.
[4] A.M. Patil, S. Gawande, Implementation of sewage treatment plant by using phytorid technology, Inter. J. Innovative Res. Tech. 3 (2016) 121–123.
[5] A.R. Mhaske, G.R. Atal, S.P. Gawande, Optimization of potassium from domestic sewage water phytorid sewage treatment plant: a study using Box-Behenken design, J. Soils Crops 27 (2017) 169–177.
[6] J. Teng, L. Shen, Y. Xu, Y. Chen, X.-L. Wu, Y. He, J. Chen, H. Lin, Effects of molecular weight distribution of soluble microbial products (SMPs) on membrane fouling in a membrane bioreactor (MBR): novel mechanistic insights, Chemosphere 248 (2020) 1260131-11.
[7] M. Wu, Y. Chen, H. Lin, L. Zhao, L. Shen, R. Li, Y. Xu, H. Hong, Y. He, Membrane fouling caused by biological foams in a submerged membrane bioreactor: mechanism insights, Water Res. 181 (115932) (2020) 1–11.
[8] W. Yu, Y. Liu, L. Shen, Y. Xu, R. Li, T. Sun, H. Lin, Magnetic field assisted preparation of PES-Ni@MWCNTs membrane with enhanced permeability and anti fouling performance, Chemosphere 243 (125446) (2020) 1–10.
[9] L. Rao, J. Tang, S. Hu, L. Shen, Y. Xu, R. Li, H. Lin, Inkjet printing assisted electroless Ni plating to fabricate Ni plated polypropylene membrane with improved performance, J. Colloid Interface Sci. 565 (2020) 546–554.
[10] R. Li, H. Fan, L. Shen, L. Rao, J. Tang, S. Hu, H. Lin, Inkjet printing assisted fabrication of polyphenol-based coating membranes for oil/water separation, Chemosphere 250 (126236) (2020) 1–8.
[11] R. Kaalipushpa, S. Karthika, S. Revathi, Domestic wastewater treatment using Phytorid technology, Int. J. Eng. Res. Technol. 5 (2017) 1–4.
[12] M. Kejariwal, Effect on Growth of Plants Under “Phytorid Technology Based” Treated Water at Education Institute: A Case Study at RD National College, Technol Renewable Energy Water, Harshvardhan Publication Pvt. Ltd., 2016, pp. 207–216 ISBN 978-93-85882-53-1.
[13] R. Kumar, S. Tayade, R.N. Singh, System and Method for the Treatment of Wastewater Using Plant, WO 2004/087584A1 (2004).
[14] J. Zur, D. Wojcieszyńska, U. Guzik, Metabolic responses of bacterial cells to immobilization, Molecules 21 (2016) 958–961.
[15] P. Biswas, S. Mamatha, S. Naskar, Y. Srinivasa Rao, R. Johnson, G. Padmanabham, 3D extrusion printing of Magnesium aluminate spinel ceramic parts using thermally induced gelation of methyl cellulose, J. Alloys Compd. 770 (2019) 419–423.
[16] S. Mamatha, P. Biswas, P. Ramavath, D. Das, R. Johnson, 3D Printing of complex shaped alumina parts, Ceram. Int. 44 (2018) 19278–19281.
[17] J. Maurath, N. Willenbacher, 3D printing of open porous cellular ceramics with high specific strength, J. Eur. Ceram. Soc. 37 (2017) 4833–4842.
[18] S. Mamatha, P. Biswas, D. Das, R. Johnson, Fabrication of complex shaped ceramic articles from 3D printed polylactic acid templates by replication process, Ceram. Int. 45 (2019) 19577–19580.
[19] S. Mamatha, P. Biswas, D. Das, R. Johnson, 3D printing of cordierite honeycomb structures and evaluation of compressive strength under quasi-static condition, Int. J. Appl. Ceram. Technol. 17 (2020) 211–216.
[20] Z. Chen, Z. Li, J. Li, C. Liu, C. Liu, Y. Li, P. Wang, Y. He, 3D printing of ceramics: a review, J. Eur. Ceram. Soc. 39 (2018) 661–687.
[21] S.A.A. El-Gawad, H.M.A. El-Aziz, Effective removal of chemical oxygen demand and phosphates from aqueous medium using entrapped activated carbon in alginate, MOJ Bio. Med. 3 (2018) 227–236.
[22] S.S. Balpande, A. Mhaske, Quality of sewage water and phytorid technology for its reuse in agriculture, J. Global Biosci. 6 (2017) 5114–5119.
[23] A.R. Mhaske, S.M. Taley, R.B. Biniwale, Removal of turbidity from sewage water by phytorid sewage treatment plant: a study using the response surface methodology, Int. J. Agric. Eng. 7 (2014) 365–372.
[24] A.R. Mhaske, K.G. Jayade, R.N. Katkar, P.C. Pagar, Removal of Phosphorous (P) from sewage water using phytorid sewage treatment plant: a study using response surface methodology, Int. J. Innov. Res. Sci. Eng. Technol. 6 (2017) 2319–8753.
[25] American Public Health Association, https://www.apha.org/.
[26] A.A. Bunaciu, E.G. Udristioiu, H.Y. Aboul-Enein, X-ray diffraction: instrumentation and applications, Critical Rev. Anal. Chem. 45 (2015) 289–299.
[27] C. Giannini, M. Ladisa, D. Altamura, D. Siliqi, T. Sibillano, L.D. Caro, X-ray diffraction: a powerful technique for the multiple-length-scale structural analysis of nanomaterials, Crystals 6 (87) (2016) 2–22.
[28] Particle Size Distribution, (2020) https://en.wikipedia.org/wiki/Particle-size_distribution.
[29] M. Swathi, R. Papitha, U.S. Hareesh, B.P. Saha, R. Johnson, M. Vijayakumar, Rheological studies on aqueous alumina extrusion mixes, Trans. Indian Inst. Met. 64 (2011) 541–547.
[30] S.O. Alayande, M.P. Mubiayi, R. Derek, Experimental characterization of physico-chemical and geological properties of granite from Olowu, Ibadan, Oyo State, Nigeria, Proc. World Cong. Mech. Chem. Mater. Eng. 20–21 (337) (2015) 1–9.

3D Printing and Additive Manufacturing, Ahead of Print |

3D Printing of $MgAl_2O_4$ Spinel Mesh and Densification Through Pressure-Less Sintering and Hot Isostatic Pressing

Aparna Adumbumkulath, Crystal Shin, Ghanashyam S. Acharya, Papiya Biswas, Mamatha Sirisala, Roy Johnson, and Padmanabham Gade

Published Online: 14 Jun 2021 | https://doi.org/10.1089/3dp.2021.0034

View Article

Abstract

$MgAl_2O_4$ spinel mesh with micro-features of 410 and 250 μm unit cell length and rib thickness, respectively, was three-dimensional (3D) printed and sintered followed by Hot Isostatic Pressing (HIPing). A stable colloidal dispersion of spinel in polymer-water solution was prepared and 3D-printed using a 30-gauge needle (~100 μm inner diameter) on a regenHU 3D-Discovery bioprinter. Samples were characterized for their density and microstructure. Samples with near theoretical density after HIPing was subjected to mechanical property evaluation such as hardness by Vickers indentation and elastic modulus using nanoindentation technique. Microstructure of sintered samples across the ribs have shown graded grain structure with finer grains near the edges (0.7 μm average) with occasional porosity and coarser grains toward the center of the rib (5.2 μm average). HIPing resulted in substantial grain growth and the average grain size was found to be 10.9 μm (with a variation in the grain size of 2.2 μm along the edges and 13.1 μm at the center of the rib) exhibiting close packed and dense microstructure. Finer grains toward the edges may probably be due to the flow behavior during printing process and lower distribution of the powder loading along the edges resulting in low green density. This relatively higher porosity pining the grain growth under the extremely low heating rate employed for the controlled shrinkage to maintain the integrity of the sample. 3D printed samples after HIPing exhibited a density of 3.57 g/cc and hardness of 12.95 GPa, which are at par with the samples processed through conventional ceramic processing techniques. Nanoindentation studies employing maximum load of 45 mN with depth have shown an elastic modulus of 238 ± 15 GPa. $MgAl_2O_4$ spinel mesh 3D printed in this study is a potential prospective candidate that can be explored for cranioplasty procedures and other biomedical applications.

Dr. Dibakar Das
Professor and Dean,
School of Engineering Sciences and Technology (SEST)
University of Hyderabad
Hyderabad - 500046, INDIA
E-mail: ddse@uohyd.ernet.in or dibakar1871@gmail.com
Tel: 91 - 040 - 23134454 (Office), 91-958104879 (Mobile)

Date: 08th September, 2021

To
The Controller of Examination (CE),
University of Hyderabad
Hyderabad – 500046

Through
Dean. SEST,
University of Hyderabad

Subject – Submission of thesis of S. Mamatha (Regn. No. 18ETPM02) – reg.

Dear Sir,
Please find enclosed the Ph.D. thesis titled "Near-net Shaping of Simple and Complex Ceramic Parts by 3D Printing and Investigations on the Physico-Chemical, Thermal, Mechanical and Microstructural Properties" by S. Mamatha (Regn. No. 18ETPM02). The thesis has been checked for plagiarism from the central library and the report shows a similarity index of 12%, out of which 3-4% is from our own work. So, an effective similarity index of 8-9% (12-3/4) has been found for the thesis, which is within the acceptable limit. Hope you will find everything in order.

Please let me know if you need anything else in this regard.

Thanking you in anticipation,

Sincerely yours,

(Dibakar Das, Supervisor and Dean)

DIBAKAR DAS, Ph.D., FIIC
Professor
School of Engineering Sciences and Technology
University of Hyderabad, Prof. C. R. Rao Road,
Gachibowli, Hyderabad 500 046, INDIA

Near-net Shaping of Simple and Complex Ceramic Parts by 3D Printing and Investigations on the Physico-chemical, Thermal, Mechanical and Microstructural Properties

by Mamatha S

Submission date: 07-Sep-2021 10:29AM (UTC+0530)
Submission ID: 1642855083
File name: amatha_18ETPM02_-Ph.D_thesis_for_Plagiarism-30082021-UOH_Lib.pdf (5.57M)
Word count: 44621
Character count: 234842

Near-net Shaping of Simple and Complex Ceramic Parts by 3D Printing and Investigations on the Physico-chemical, Thermal, Mechanical and Microstructural Properties

ORIGINALITY REPORT

12%	5%	10%	3%
SIMILARITY INDEX	INTERNET SOURCES	PUBLICATIONS	STUDENT PAPERS

PRIMARY SOURCES

1	Sirisala Mamatha, Papiya Biswas, Pandu Ramavath, Dibakar Das, Roy Johnson. "Effect of parameters on 3D printing of alumina ceramics and evaluation of properties of sintered parts", Journal of Asian Ceramic Societies, 2021 Publication	1%
2	Papiya Biswas, Sirisala Mamatha, Kezil Varghese, Roy Johnson, Ritesh Vijay, Rakesh Kumar. "3D printing of high surface area ceramic honeycombs substrates and comparative evaluation for treatment of sewage in Phytorid application", Journal of Water Process Engineering, 2020 Publication	1%
3	Submitted to National Institute of Technology Warangal Student Paper	1%

DIBAKAR DAS, Ph.D., FIC
Professor
School of Engineering Sciences and Technology
University of Hyderabad, Prof. C. R. Rao Road,
Gachibowli, Hyderabad 500 046, INDIA

4	"Handbook of Advanced Ceramics and Composites", Springer Science and Business Media LLC, 2020 Publication	1 %
5	shodhganga.inflibnet.ac.in Internet Source	1 %
6	Sirisala Mamatha, Papiya Biswas, Pandu Ramavath, Dibakar Das, Roy Johnson. "3D printing of complex shaped aluminia parts", Ceramics International, 2018 Publication	1 %
7	Sirisala Mamatha, Papiya Biswas, Dibakar Das, Roy Johnson. "3D printing of cordierite honeycomb structures and evaluation of compressive strength under quasi - static condition", International Journal of Applied Ceramic Technology, 2019 Publication	1 %
8	Sirisala Mamatha, Papiya Biswas, Dibakar Das, Roy Johnson. "Fabrication of complex shaped ceramic articles from 3D printed polylactic acid templates by replication process", Ceramics International, 2019 Publication	<1 %
9	Papiya Biswas, Sirisala Mamatha, Subhendu Naskar, Yabaluri Srinivasa Rao, Roy Johnson, Gadhe Padmanabham. "3D extrusion printing	<1 %

DIBAKAR DAS, Ph.D., FIIC
Professor
School of Engineering Sciences and Technology
University of Hyderabad, Prof. C. R. Rao Road,
Gachibowli, Hyderabad 500 046, INDIA

of magnesium aluminate spinel ceramic parts using thermally induced gelation of methyl cellulose", Journal of Alloys and Compounds, 2018
Publication

10	www.cosmosscholars.com Internet Source	<1 %
11	engineeringproductdesign.com Internet Source	<1 %
12	mafiadoc.com Internet Source	<1 %
13	Elham Babaie, Sarit B. Bhaduri. "Fabrication Aspects of Porous Biomaterials in Orthopedic Applications: A Review", ACS Biomaterials Science & Engineering, 2017 Publication	<1 %
14	Priya Anish Mathews, Swati Koonisetty, Sanjay Bhardwaj, Papiya Biswas, Roy Johnson, Padmanabham Gadhe. "Chapter 57-1 Patent Trends in Additive Manufacturing of Ceramic Materials", Springer Science and Business Media LLC, 2020 Publication	<1 %
15	new.esp.org Internet Source	<1 %
16	Junyong He, Ya Yang, Zijian Wu, Chao Xie, Kaisheng Zhang, Lingtao Kong, Jinhuai Liu.	<1 %

	"Review of fluoride removal from water environment by adsorption", Journal of Environmental Chemical Engineering, 2020 Publication	
17	www.mdpi.com Internet Source	<1 %
18	"Advances in Additive Manufacturing and Joining", Springer Science and Business Media LLC, 2020 Publication	<1 %
19	dokumen.pub Internet Source	<1 %
20	ethesis.nitrkl.ac.in Internet Source	<1 %
21	Submitted to Associatie K.U.Leuven Student Paper	<1 %
22	He Li, Yongsheng Liu, Yansong Liu, Kehui Hu, Zhigang Lu, Jingjing Liang. "Effects of Solvent Debinding on the Microstructure and Properties of 3D-Printed Alumina Ceramics", ACS Omega, 2020 Publication	<1 %
23	worldwidescience.org Internet Source	<1 %
24	Submitted to Waikato Institute of Technology Student Paper	<1 %

25	I. Ganesh. " A review on magnesium aluminate (MgAl O) spinel: synthesis, processing and applications ", International Materials Reviews, 2013 Publication	<1 %
26	www.britannica.com Internet Source	<1 %
27	dns2.asia.edu.tw Internet Source	<1 %
28	Zhangwei Chen, Ziyong Li, Junjie Li, Chengbo Liu, Changshi Lao, Yuelong Fu, Changyong Liu, Yang Li, Pei Wang, Yi He. "3D printing of ceramics: A review", Journal of the European Ceramic Society, 2019 Publication	<1 %
29	silo.pub Internet Source	<1 %
30	www.substech.com Internet Source	<1 %
31	Submitted to Hong Kong Baptist University Student Paper	<1 %
32	Halloran, John W.. "Ceramic Stereolithography: Additive Manufacturing for Ceramics by Photopolymerization", Annual Review of Materials Research, 2016. Publication	<1 %

33	Submitted to University of Nottingham Student Paper	<1 %
34	repositories.lib.utexas.edu Internet Source	<1 %
35	digital.ub.uni-paderborn.de Internet Source	<1 %
36	Guotian Ye. "Synthesis of MgAl2O4 Spinel Powder by Combination of Sol-Gel and Precipitation Processes", Journal of the American Ceramic Society, 11/2005 Publication	<1 %
37	Ian Gibson, David Rosen, Brent Stucker, Mahyar Khorasani. "Additive Manufacturing Technologies", Springer Science and Business Media LLC, 2021 Publication	<1 %
38	en.wikipedia.org Internet Source	<1 %
39	lppm-unissula.com Internet Source	<1 %
40	3dadditive4.com Internet Source	<1 %
41	Inbaraj, S.R.. "Processing and properties of sol gel derived alumina-carbon nano tube composites", Ceramics International, 201207 Publication	<1 %

42	ntrs.nasa.gov Internet Source	<1%
43	Schwentenwein, Martin, and Johannes Homa. "Additive Manufacturing of Dense Alumina Ceramics", International Journal of Applied Ceramic Technology, 2014. Publication	<1%
44	Submitted to University of Kent at Canterbury Student Paper	<1%
45	Guiyuan Wu, Wen Yan, Stefan Schafföner, Xiaoli Lin, Sanbao Ma, Yaojie Zhai, Xijun Liu, Linlin Xu. "Effect of magnesium aluminate spinel content of porous aggregates on cement clinker corrosion and adherence properties of lightweight periclase-spinel refractories", Construction and Building Materials, 2018 Publication	<1%
46	Lisa Rueschhoff, William Costakis, Matthew Michie, Jeffrey Youngblood, Rodney Trice. "Additive Manufacturing of Dense Ceramic Parts via Direct Ink Writing of Aqueous Alumina Suspensions", International Journal of Applied Ceramic Technology, 2016 Publication	<1%
47	scholar.uwindsor.ca Internet Source	<1%

48	spectrum.library.concordia.ca Internet Source	<1%
49	www.cisco.com Internet Source	<1%
50	Submitted to Hong Kong University of Science and Technology Student Paper	<1%
51	Junyong He, Xingguo Cai, Kai Chen, Yulian Li et al. "Performance of a novelly-defined zirconium metal-organic frameworks adsorption membrane in fluoride removal", Journal of Colloid and Interface Science, 2016 Publication	<1%
52	Sa Liu, Lina Mo, Gangyuan Bi, Shenggui Chen, Diwei Yan, Junzhong Yang, Yong-Guang Jia, Li Ren. "DLP 3D printing porous β-tricalcium phosphate scaffold by the use of acrylate/ceramic composite slurry", Ceramics International, 2021 Publication	<1%
53	X.P. Tan, Y.J. Tan, C.S.L. Chow, S.B. Tor, W.Y. Yeong. "Metallic powder-bed based 3D printing of cellular scaffolds for orthopaedic implants: A state-of-the-art review on manufacturing, topological design, mechanical properties and biocompatibility", Materials Science and Engineering: C, 2017 Publication	<1%

54	Advances in Superconductivity X, 1998. Publication	<1 %
55	Haomin Wang, Li Ying Liu, Pengcheng Ye, Zhangyi Huang, Andrew Yun Ru Ng, Zehui Du, Zhili Dong, Dingyuan Tang, Chee Lip Gan. "3D Printing of Transparent Spinel Ceramics with Transmittance Approaching the Theoretical Limit", Advanced Materials, 2021 Publication	<1 %
56	Submitted to National Institute of Technology, Rourkela Student Paper	<1 %
57	P. G. Lampropoulou, C. G. Katagas, I. Iliopoulos, D. Papoulis. "New periclase-spinel refractories from densely sintered high purity magnesite and new synthetic compositions based on spinel. Part 1. Study of mineral composition, microstructure, thermal expansion, and ultimate strength in compression", Refractories and Industrial Ceramics, 2013 Publication	<1 %
58	Submitted to Universiti Malaysia Pahang Student Paper	<1 %
59	Zhenyu Ye, Chengyi Chu, Diwei Zhang, Siwei Ma, Jianjun Guo, Yuchuan Cheng, Gaojie Xu, Zhixiang Li, Aihua Sun. "Study on 3D-Direct	<1 %

Ink Writing based on adding silica submicron-particles to improve the rheological properties of alumina ceramic ink", Materials Today Communications, 2021
Publication

60	eprints.whiterose.ac.uk Internet Source	<1 %
61	webitc.itc.uji.es Internet Source	<1 %
62	www.manchester.ac.uk Internet Source	<1 %
63	Ruth Felzmann, Simon Gruber, Gerald Mitteramskogler, Passakorn Tesavibul, Aldo R. Boccaccini, Robert Liska, Jürgen Stampfl. "Lithography-Based Additive Manufacturing of Cellular Ceramic Structures", Advanced Engineering Materials, 2012 Publication	<1 %
64	S. Iyer. "Microstructural Characterization and Mechanical Properties of Si_3N_4 Formed by Fused Deposition of Ceramics", International Journal of Applied Ceramic Technology, 2/25/2008 Publication	<1 %
65	Samuel Clark Ligon, Robert Liska, Jürgen Stampfl, Matthias Gurr, Rolf Mülhaupt. "Polymers for 3D Printing and Customized	<1 %

	Additive Manufacturing", Chemical Reviews, 2017 Publication	
66	edoc.pub Internet Source	<1 %
67	epdf.pub Internet Source	<1 %
68	etheses.whiterose.ac.uk Internet Source	<1 %
69	studentsrepo.um.edu.my Internet Source	<1 %
70	He Li, Yongsheng Liu, Yansong Liu, Qingfeng Zeng, Kehui Hu, Zhigang Lu, Jingjing Liang, Jinguo Li. "Influence of debinding holding time on mechanical properties of 3D-printed alumina ceramic cores", Ceramics International, 2020 Publication	<1 %
71	Zhuohao Xiao, Shijin Yu, Yueming Li, Shuangchen Ruan et al. "Materials development and potential applications of transparent ceramics: A review", Materials Science and Engineering: R: Reports, 2020 Publication	<1 %
72	qmro.qmul.ac.uk Internet Source	<1 %

73	"Recent Trends in Civil Engineering", Springer Science and Business Media LLC, 2021 Publication	<1 %
74	Submitted to Bellarmine University Student Paper	<1 %
75	Submitted to Higher Education Commission Pakistan Student Paper	<1 %
76	Submitted to University of Wales Swansea Student Paper	<1 %
77	iesgeneralstudies.com Internet Source	<1 %
78	res.mdpi.com Internet Source	<1 %
79	Submitted to Curtin University of Technology Student Paper	<1 %
80	Submitted to University of Sheffield Student Paper	<1 %
81	Submitted to Loughborough University Student Paper	<1 %
82	Submitted to University of Newcastle upon Tyne Student Paper	<1 %
83	pure-oai.bham.ac.uk Internet Source	<1 %

84	www.uwu.ac.lk Internet Source	<1%

Exclude quotes	On	Exclude matches	< 14 words
Exclude bibliography	On		